

AD-A192 296

THREE-DIMENSIONAL ASPECTS OF FATIGUE CRACK CLOSURE(U)  
PURDUE UNIV LAFAYETTE IN SCHOOL OF AERONAUTICS AND  
ASTRONAUTICS A F GRANDT ET AL. FEB 89 RAE-88-1

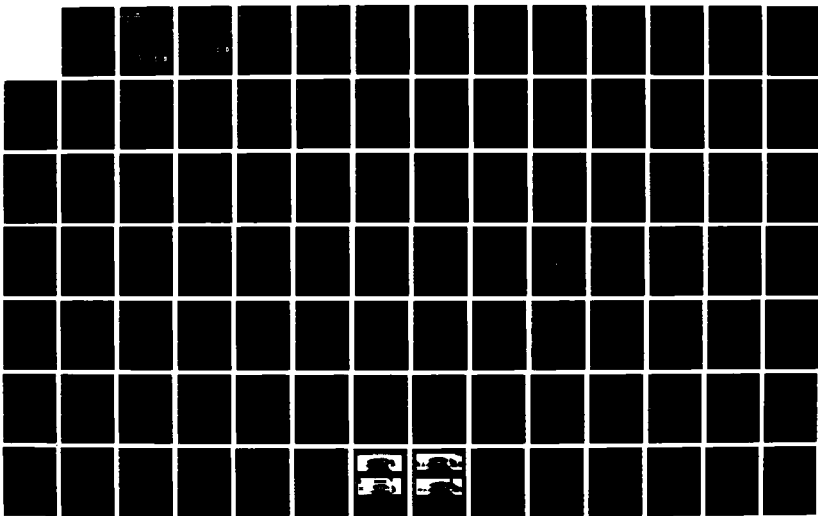
1/3

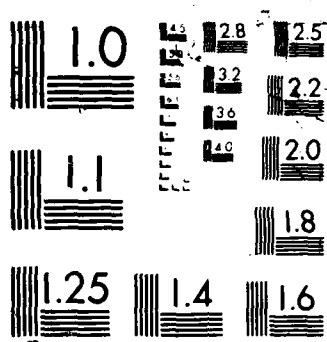
UNCLASSIFIED

AFOSR-TR-88-0266 AFOSR-85-0106

F/G 20/11

ML



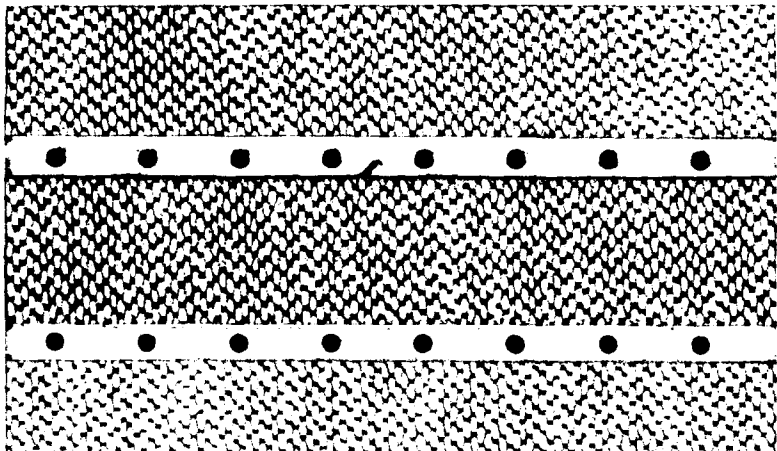


AD-A192 296

AFOSR - TR. 68 - UZ66  
②

DTIC FILE COPY

**PURDUE UNIVERSITY**  
**SCHOOL OF AERONAUTICS AND ASTRONAUTICS**



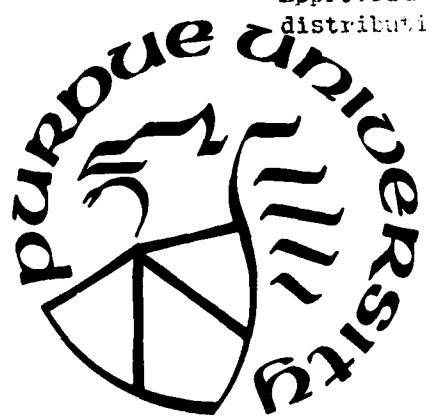
AIR FORCE OFFICE OF SCIENTIFIC RESEARCH (AFSC)  
NOTICE OF TRANSMITTAL TO DTIC

This technical report has been reviewed and is  
approved for public release via AFR 190-12.

Distribution is unlimited.

MATTHEW J. KEPER  
Chief, Technical Information Division

Approved for public release;  
distribution unlimited.



DTIC  
SELECTED  
MAR 11 1988  
S D  
O H

West Lafayette, Indiana 47907

88 3 7 11 6

2

**THREE-DIMENSIONAL ASPECTS OF  
FATIGUE CRACK CLOSURE**

by

**A.F. Grandt, Jr., J.E. Pope,  
and S.K. Ray**

**February 1988**

**Final Technical Report  
for  
AFOSR Grant Number 85-0106**

**School of Aeronautics and Astronautics  
Grissom Hall  
Purdue University  
West Lafayette, IN 47907**

**DTIC  
SELECTED  
MAR 11 1988  
S D  
H**

**School of Aeronautics & Astronautics Technical Report  
AAE-88-1**

**DISTRIBUTION STATEMENT A**

Approved for public release;  
Distribution Unlimited

Unclassified

SECURITY CLASSIFICATION OF THIS PAGE

ADA192296

## REPORT DOCUMENTATION PAGE

| 1a. REPORT SECURITY CLASSIFICATION<br>Unclassified  |  | 1b. RESTRICTIVE MARKINGS  |                          |                        |                |             |                  |        |      |    |     |  |  |   |  |
|---|--|---|--------------------------|------------------------|----------------|-------------|------------------|--------|------|----|-----|--|--|---|--|
| 2a. SECURITY CLASSIFICATION AUTHORITY   |  | 3. DISTRIBUTION/AVAILABILITY OF REPORT<br>Approved for public release;<br>distribution is unlimited   |                          |                        |                |             |                  |        |      |    |     |  |  |   |  |
| 2b. DECLASSIFICATION/DOWNGRADING SCHEDULE   |  |   |                          |                        |                |             |                  |        |      |    |     |  |  |   |  |
| 4. PERFORMING ORGANIZATION REPORT NUMBER(S)<br>School of Aeronautics and Astronautics<br>Technical Report No. AAE-88-1  |  | 5. MONITORING ORGANIZATION REPORT NUMBER(S)<br><b>AFOSR-TR-88-U266</b>  |                          |                        |                |             |                  |        |      |    |     |  |  |   |  |
| 6a. NAME OF PERFORMING ORGANIZATION<br>Purdue University  | 6b. OFFICE SYMBOL<br>(If applicable)       | 7a. NAME OF MONITORING ORGANIZATION<br>AFOSR/NA   |                          |                        |                |             |                  |        |      |    |     |  |  |   |  |
| 6c. ADDRESS (City, State and ZIP Code)<br>School of Aeronautics and Astronautics<br>Grissom Hall, Purdue University<br>West Lafayette, IN 47907   |  | 7b. ADDRESS (City, State and ZIP Code)<br>Building 410<br>Bolling AFB, DC 20332-6448  |                          |                        |                |             |                  |        |      |    |     |  |  |   |  |
| 8a. NAME OF FUNDING/SPONSORING<br>ORGANIZATION<br>AFOSR   | 8b. OFFICE SYMBOL<br>(If applicable)<br>NA | 9. PROCUREMENT INSTRUMENT IDENTIFICATION NUMBER<br>AFOSR-85-0106  |                          |                        |                |             |                  |        |      |    |     |  |  |   |  |
| 8c. ADDRESS (City, State and ZIP Code)<br>AFOSR/NA<br>Building 410<br>bolling AFB, DC 20332-6448  |  | 10. SOURCE OF FUNDING NOS.<br><table border="1"> <tr> <th>PROGRAM<br/>ELEMENT NO.</th> <th>PROJECT<br/>NO.</th> <th>TASK<br/>NO.</th> <th>WORK UNIT<br/>NO.</th> </tr> <tr> <td>61102F</td> <td>2302</td> <td>B2</td> <td>205</td> </tr> </table> |                          | PROGRAM<br>ELEMENT NO. | PROJECT<br>NO. | TASK<br>NO. | WORK UNIT<br>NO. | 61102F | 2302 | B2 | 205 |  |  |   |  |
| PROGRAM<br>ELEMENT NO.  | PROJECT<br>NO.                             | TASK<br>NO.   | WORK UNIT<br>NO.         |                        |                |             |                  |        |      |    |     |  |  |   |  |
| 61102F  | 2302                                       | B2  | 205                      |                        |                |             |                  |        |      |    |     |  |  |   |  |
| 11. TITLE (Include Security Classification)<br>Three-Dimensional Aspects of Fatigue Crack Closure   |  |   |                          |                        |                |             |                  |        |      |    |     |  |  |   |  |
| 12. PERSONAL AUTHORIS<br>A.F. Grandt, J.E. Pope, S.K. Ray   |  |   |                          |                        |                |             |                  |        |      |    |     |  |  |   |  |
| 13a. TYPE OF REPORT<br>Final Report   | 13b. TIME COVERED<br>FROM _____ TO _____   | 14. DATE OF REPORT (Yr., Mo., Day)<br>1988 February   | 15. PAGE COUNT           |                        |                |             |                  |        |      |    |     |  |  |   |  |
| 16. SUPPLEMENTARY NOTATION  |  |   |                          |                        |                |             |                  |        |      |    |     |  |  |   |  |
| 17. COSATI CODES<br><table border="1"> <tr> <th>FIELD</th> <th>GROUP</th> <th>SUB GR.</th> </tr> <tr> <td> </td> <td> </td> <td> </td> </tr> <tr> <td> </td> <td> </td> <td> </td> </tr> <tr> <td> </td> <td> </td> <td> </td> </tr> </table>   |  | FIELD   | GROUP                    | SUB GR.                |                |             |                  |        |      |    |     |  |  | 18. SUBJECT TERMS (Continue on reverse if necessary and identify by block number)<br>Cracks. Fatigue, Fracture Mechanics, Closure |  |
| FIELD   | GROUP                                      | SUB GR.   |                          |                        |                |             |                  |        |      |    |     |  |  |   |  |
|   |  |   |                          |                        |                |             |                  |        |      |    |     |  |  |   |  |
|   |  |   |                          |                        |                |             |                  |        |      |    |     |  |  |   |  |
|   |  |   |                          |                        |                |             |                  |        |      |    |     |  |  |   |  |
| 19. ABSTRACT (Continue on reverse if necessary and identify by block number)<br>This final report summarizes progress on a basic research effort to determine three-dimensional aspects of the relationship between applied load and fatigue crack face separation. The research was motivated by the well known crack closure phenomenon, which indicates that naturally occurring fatigue cracks are physically held shut (or propped open) at zero load, so that crack surfaces do not separate in a linear elastic manner. Although prediction of fatigue crack opening behavior is of fundamental importance to many aspects of crack growth, relatively little is known about the three-dimensional character of closure. The research employed experimental and numerical procedures to develop predictive techniques for this important aspect of crack closure. Optical interference was used to measure crack opening in transparent polymer specimens, along with conventional crack opening and back face strain techniques for measuring crack closure. A numerical algorithm was developed to predict opening loads in surface flawed plates, and was compared with the experimental results. |  |   |                          |                        |                |             |                  |        |      |    |     |  |  |   |  |
| 20. DISTRIBUTION/AVAILABILITY OF ABSTRACT<br>UNCLASSIFIED/UNLIMITED <input checked="" type="checkbox"/> SAME AS RPT. <input type="checkbox"/> DTIC USERS <input type="checkbox"/>   |  | 21. ABSTRACT SECURITY CLASSIFICATION<br>Unclassified  |                          |                        |                |             |                  |        |      |    |     |  |  |   |  |
| 22a. NAME OF RESPONSIBLE INDIVIDUAL<br>Lt. Col. George K. Haritos   |  | 22b. TELEPHONE NUMBER<br>(Include Area Code)<br>202/767-0463  | 22c. OFFICE SYMBOL<br>NA |                        |                |             |                  |        |      |    |     |  |  |   |  |

Unclassified

SECURITY CLASSIFICATION OF THIS PAGE

## TABLE OF CONTENTS

|  | Page |
|--|------|
| LIST OF TABLES .....                           | v    |
| LIST OF FIGURES .....                          | vi   |
| LIST OF SYMBOLS .....                          | xiv  |
| CHAPTER 1 - BACKGROUND .....                   | 1    |
| 1.1 INTRODUCTION.....                          | 1    |
| 1.2 REVIEW OF PRIOR WORK .....                 | 4    |
| 1.2.1 Numerical Studies .....                  | 4    |
| 1.2.2 Experimental Studies.....                | 6    |
| 1.3 OBJECTIVE OF CURRENT RESEARCH .....        | 8    |
| CHAPTER 2 - EXPERIMENTAL PROCEDURE.....        | 13   |
| 2.1 OPTICAL INTERFERENCE TECHNIQUE.....        | 13   |
| 2.2 THROUGH-THICKNESS FLAW.....                | 14   |
| 2.3 CORNER CRACKED HOLES .....                 | 16   |
| 2.4 SURFACE FLAWED PLATES .....                | 17   |
| CHAPTER 3 - SURFACE CRACK CLOSURE MODEL .....  | 23   |
| 3.1 PLASTIC ZONE SIZE.....                     | 24   |
| 3.2 DEFORMATION WITHIN THE PLASTIC ZONE.....   | 25   |
| 3.3 CONTACT STRESSES AT MINIMUM LOAD .....     | 25   |
| 3.4 CRACK OPENING STRESS INTENSITY FACTOR..... | 27   |
| 3.5 FATIGUE CRACK GROWTHII .....               | 29   |
| CHAPTER 4 - EXPERIMENTAL RESULTS .....         | 39   |
| 4.1 THROUGH CRACKS IN PMMA .....               | 39   |
| 4.1.1 Interferometric Measurements.....        | 39   |
| 4.1.2 CMOD and BFS Measurements.....           | 40   |
| 4.1.3 Sensitivity Analysis.....                | 45   |
|  | 46   |



|                    |   |
|--------------------|---|
| On For             |   |
| 39                 | A&I <input checked="" type="checkbox"/> |
| 39                 | <input type="checkbox"/>                |
| 40                 | ced <input type="checkbox"/>            |
| 45                 | ation <input type="checkbox"/>          |
| 46                 |   |
| Distribution/      |   |
| Availability Codes |   |
| Dist               | Avail and/or<br>Special                 |
| A-1                |   |

|  | Page    |
|--|---------|
| 4.1.3.1 Thickness Effect.....  | 47      |
| 4.1.3.2 Cyclic $K_{max}$ and Stress Ratio (R) Effect.....                      | 50      |
| 4.2 THROUGH-THICKNESS FLAWS IN PC.....   | 52      |
| 4.3 CORNER CRACKED HOLES .....   | 55      |
| 4.3.1 Cyclic Tension Results.....  | 55      |
| 4.3.2 Cyclic Bend Results.....   | 58      |
| 4.4 SURFACE FLAWS UNDER CYCLIC BENDING.....                                    | 60      |
| 4.4.1 Interferometric Measurements .....                                       | 60      |
| 4.4.2 CMOD Measurements.....   | 63      |
| <br>CHAPTER 5 - ANALYTICAL RESULTS.....  | <br>125 |
| 5.1 TESTING BY RAY .....   | 126     |
| 5.2 TESTING BY TROHA.....  | 127     |
| 5.3 TENSION TESTING.....   | 128     |
| 5.4 SENSITIVITY ANALYSIS.....  | 130     |
| 5.4.1 Flow Stress.....   | 130     |
| 5.4.2 Maximum Load.....  | 132     |
| 5.4.3 R Ratio .....  | 132     |
| 5.4.4 Constraint Factor Alpha .....  | 133     |
| 5.4.5 Weight Function Reference Case.....                                      | 135     |
| <br>CHAPTER 6 - SUMMARY.....   | <br>161 |
| 6.1 SUMMARY OF POLYMER RESULTS .....   | 161     |
| 6.2 CRACK OPENING IN METALS.....   | 164     |
| 6.3 SUMMARY OF ANALYTICAL RESULTS .....  | 168     |
| <br>LIST OF REFERENCES.....  | <br>179 |
| <br>APPENDIX A - SUMMARY OF PERSONNEL, PUBLICATIONS,<br>AND PRESENTATIONS..... | <br>187 |

## LIST OF TABLES

| Table   | Page |
|---|------|
| 3.1 Test cases for closure K algorithm .....  | 31   |
| 4.1 Test matrix for the through-thickness flaw experiments<br>with PMMA .....                 | 66   |
| 4.2 Test matrix for the Polycarbonate through-thickness<br>flaw experiments .....             | 67   |
| 4.3 Test matrix for the corner cracked hole experiments.....                                  | 68   |
| 4.4 Test matrix for the surface flawed plates.....  | 69   |
| 5.1 Load levels and specimen dimensions of experiments which<br>were modeled numerically..... | 136  |
| 5.2 Summary of sensitivity analysis runs.....   | 137  |

## LIST OF FIGURES

| Figure   | Page |
|--|------|
| 1.1 Schematic view of the crack tip plastic wake formation behind the crack tip, resulting in compressive residual stress, which hold the crack faces closed during portions of positive applied load..... | 10   |
| 1.2 A schematic representation of the effective cyclic K level that the specimen experiences in a typical load cycle .....   | 11   |
| 1.3 Schematic presentation of 3-D crack tip plastic zone showing transition from large plane stress plastic zone at specimen surface to smaller plane strain zone size at the center of the specimen ..... | 12   |
| 2.1 Schematic of interferometry method which gives 3-D crack surface displacement in transparent specimens.....  | 19   |
| 2.2 Schematic representation of four-point bend specimen containing back face strain gage and clip gage for crack opening measurements .....   | 20   |
| 2.3 Schematic view of corner cracked hole specimen.....  | 21   |
| 2.4 Schematic view of the surface flawed rectangular plate.....  | 22   |
| 3.1 Crack elements under minimum load .....  | 32   |
| 3.2 Surface crack dimensions.....  | 33   |
| 3.3 Equivalent crack lengths.....  | 34   |
| 3.4 Surface crack coordinates .....  | 35   |

| Figure  | Page |
|---|------|
| 3.5 Crack surface sections .....  | 36   |
| 3.6 Test of closure K algorithm at point A,<br>maximum bending stress = 1000 psi, $a/c = 2/3$ .....   | 37   |
| 3.7 Test of closure K algorithm at point C,<br>maximum bending stress = 1000 psi, $a/c = 2/3$ .....   | 38   |
| 4.1 Crack length versus elapsed cycles response for Test PX-6.<br>Mid-plane and free surface crack lengths are shown to<br>characterize the tunnelling phenomenon .....                   | 70   |
| 4.2 Interference fringe pattern obtained for various applied<br>loads showing the three-dimensional crack opening profile<br>of PMMA specimen subjected to constant cyclic K loading..... | 71   |
| 4.3 Crack opening perimeter as a function of applied load,<br>obtained by overlapping the zero order fringe pattern<br>from Figure 4.2 .....  | 73   |
| 4.4 Mid-plane crack opening profile for increasing load. The<br>crack opening displacement is expressed here in fringe<br>order units .....   | 74   |
| 4.5 Free surface crack opening profiles for increasing load.<br>$K_{01}$ represents the K value which causes complete<br>crack separation at the free surface.....                        | 75   |
| 4.6 Interferometric crack tip opening load as a function of<br>dimensionless distance from the free surface.....  | 76   |
| 4.7 Interferometric zero load mid-plane opening profiles for<br>various crack lengths.....  | 77   |
| 4.8 Load-displacement record obtained from a clip gage mounted<br>across the crack mouth. $K_{0C}$ refers to the load<br>where the load-displacement becomes linear.....                  | 78   |
| 4.9 Load-strain record obtained from a strain gage mounted on<br>the back face of the PMMA specimen. $K_{0E}$ refers to the<br>load where the crack opens in a linear manner.....         | 79   |

| Figure  | Page |
|---|------|
| 4.10 Comparison of crack opening loads obtained from interferometry, CMOD, and BFS measurements for various crack lengths.....                          | 80   |
| 4.11 Comparison of the magnitude of crack tunnelling with changing specimen thickness .....   | 81   |
| 4.12 Comparison of zero-load (residual) interference fringe photographs obtained for the 25 mm and 5 mm thick specimens .....                           | 82   |
| 4.13 Comparison of zero load mid-plane opening profile for varying specimen thickness .....   | 83   |
| 4.14 Interferometric opening load as a function of absolute distance $x$ from the free surface for varying specimen thickness .....                     | 84   |
| 4.15 Interferometric free surface opening load as a function of crack length for varying specimen thickness.....  | 85   |
| 4.16 Interferometric free surface opening loads for 19 mm thick experiments with various cyclic $K_{max}$ levels.....                                   | 86   |
| 4.17 Interferometric free surface opening loads for 25 mm thick experiments with various cyclic $K_{max}$ levels.....                                   | 87   |
| 4.18 Comparison of crack tunnelling with varying cyclic $K_{max}$ levels .....  | 88   |
| 4.19 Interferometric opening load versus normalized distance from the free surface with varying cyclic $K_{max}$ levels for 25 mm thick specimens ..... | 89   |
| 4.20 Crack opening loads obtained from various measurements for increasing crack length for Test PX-5, $R = 0.1$ .....                                  | 90   |
| 4.21 Crack opening loads obtained from various measurements for increasing crack length for Test PX-7, $R = 0.3$ .....                                  | 91   |
| 4.22 Comparison of crack tunnelling magnitude for various PC specimen thickness.....  | 92   |

| Figure   | Page |
|--|------|
| 4.23 Crack opening perimeter as a function of applied load<br>for the 25 mm thick PC specimen .....  | 93   |
| 4.24 Crack opening perimeter as a function of applied load<br>for the 19 mm thick PC specimen .....  | 94   |
| 4.25 Mid-plane crack opening profile for 19 mm thick PC specimen<br>under steady state cycling .....   | 95   |
| 4.26 Free surface crack opening profile for a 19 mm thick PC<br>specimen under steady state cycling.....   | 96   |
| 4.27 Mid-plane crack opening profile for a 25 mm thick PC<br>specimen under steady state cycling.....  | 97   |
| 4.28 Near free surface opening profile for a 25 mm thick PC<br>specimen under steady state cycling.....  | 98   |
| 4.29 Interferometric crack opening load as a function of<br>normalized distance from the free surface for a 25 mm<br>thick PC specimen .....                     | 99   |
| 4.30 Interferometric crack opening load as a function of<br>normalized distance from the free surface for a 19 mm<br>thick PC specimen .....                     | 100  |
| 4.31 Comparison of opening loads obtained from optical<br>interferometry, CMOD, and back face strain measure-<br>ments for Test PC-1 tested with $R = 0.1$ ..... | 101  |
| 4.32 Comparison of zero load (residual) mid-plane opening for<br>varying specimen thickness .....  | 102  |
| 4.33 Comparison of interferometric free surface opening load<br>for varying specimen thickness .....   | 103  |
| 4.34 Typical interference fringe patterns for various applied<br>remote tensile stresses.....  | 104  |
| 4.35 Crack opening perimeters as a function of applied load,<br>obtained by overlapping the zero order fringe patterns<br>from Figure 4.34.....                  | 105  |

| Figure   | Page |
|--|------|
| 4.36 Crack opening profiles under remote tension of 263 KPa for varying parametric angle $\phi$ .....  | 106  |
| 4.37 Crack opening profiles for varying applied load at the free surface ( $\phi = 0^\circ$ ).....   | 107  |
| 4.38 Crack opening profiles for varying applied load along the hole bore ( $\phi = 90^\circ$ ).....  | 108  |
| 4.39 Interferometric crack tip opening load as a function of angle $\phi$ for Test CTB-1.....  | 109  |
| 4.40 Interference fringe pattern photographed during steady state cyclic bending.....  | 110  |
| 4.41 Crack opening perimeters as a function of applied bending stress, obtained by overlapping the zero order fringe patterns from Figure 4.40 ..... | 111  |
| 4.42 Crack opening profile under remote bending stress of 862 KPa for varying parametric angle $\phi$ .....  | 112  |
| 4.43 Crack opening profiles obtained at the free surface for varying remote bending stress .....   | 113  |
| 4.44 Crack opening profile obtained along the hole bore for varying remote bending stress .....  | 114  |
| 4.45 Interferometric crack tip opening load as a function of parametric angle $\phi$ for Test CTB-1 .....  | 115  |
| 4.46 Photographs of typical interference fringe patterns for various applied remote bending stresses for specimen SB-1 .....                         | 116  |
| 4.47 Crack opening perimeters as a function of applied load obtained by overlapping the zero order fringe patterns in Figure 4.46 .....              | 117  |
| 4.48 Crack opening profiles for various angles $\phi$ obtained for applied stress of 20% the maximum remote cyclic stress.....                       | 118  |

| Figure  | Page |
|---|------|
| 4.49 Crack opening profiles for various angles $\phi$ obtained for applied stress of 28% the maximum remote cyclic stress .....   | 119  |
| 4.50 Interferometric crack tip opening load as a function of parametric angle $\phi$ for Test SB-2 .....  | 120  |
| 4.51 Interferometric free surface crack opening stresses as a function of dimensionless crack size for five cyclic bend experiments .....   | 121  |
| 4.52 Fatigue crack growth rates $da/dN$ and $dc/dN$ versus nominal applied $\Delta K$ .....   | 122  |
| 4.53 Fatigue crack growth rates $da/dN$ and $dc/dN$ versus closure corrected effective $\Delta K$ .....   | 123  |
| 4.54 Comparison of interferometric free surface opening load with the bulk measurements via crack mouth opening displacement for Tests SB-1 and SB-2. The maximum remote cyclic bending stress was kept at 8790 KPa ..... | 124  |
| 5.1 Interior closure for test SB-1 max bending stress=1275 psi.....   | 138  |
| 5.2 Free surface closure for test SB-1 max bending stress=1275 psi .....  | 139  |
| 5.3 Free surface closure for test SB-3 max bending stress=1500 psi .....  | 140  |
| 5.4 Aspect ratios for test SB-7 .....   | 141  |
| 5.5 Type II crack .....   | 142  |
| 5.6 Type III crack .....  | 143  |
| 5.7 Free surface closure for test 3-15 constant load .....  | 144  |
| 5.8 Interior closure for test 3-15 constant load.....   | 145  |
| 5.9 Free surface closure for test 3-16 block loading.....   | 146  |
| 5.10 Interior closure for test 3-16 block loading.....  | 147  |

| Figure   | Page |
|--|------|
| 5.11 Effect of simulated growth on free surface closure<br>for test 3-16.....  | 148  |
| 5.12 Free surface closure for test T-2.....  | 149  |
| 5.13 Effect of flow stress on closure at the free surface.....   | 150  |
| 5.14 Effect of flow stress on closure in the interior.....   | 151  |
| 5.15 Plastic wake due to pre-cracking .....  | 152  |
| 5.16 Effect of R ratio on closure at the free surface<br>when $K_{max}$ is kept constant.....                                  | 153  |
| 5.17 Effect of R ratio on closure at the interior<br>when $K_{max}$ is kept constant .....                                     | 154  |
| 5.18 Effect of R ratio on closure at the free surface<br>when $\Delta K$ is kept constant .....                                | 155  |
| 5.19 Effect of R ratio on closure at the interior<br>when $\Delta K$ is kept constant .....                                    | 156  |
| 5.20 Effect of alpha on closure at the free surface.....   | 157  |
| 5.21 Effect of alpha on closure at the interior .....  | 158  |
| 5.22 Effect of weight function reference case on closure at<br>the free surface .....  | 159  |
| 5.23 Effect of weight function reference case on closure at<br>the interior .....  | 160  |
| 6.1 Comparison of crack opening loads obtained from IDG, CMOD,<br>and BFS measurements for 10 mm thick Rene 95 specimens ..... | 173  |
| 6.2 Comparison of crack opening loads obtained from IDG, CMOD,<br>and BFS measurements for a 5 mm thick Rene 95 specimen ..... | 174  |
| 6.3 Comparison of crack opening loads obtained from IDG, CMOD,<br>and BFS measurements for a 2 mm thick Rene 95 specimen ..... | 175  |

| Figure   | Page |
|--|------|
| 6.4 Crack plane view showing the opening perimeters as a function of increasing load obtained from Reference [18].<br>$S_{\max}$ represents the maximum cyclic stress..... | 176  |
| 6.5 Experimental and predicted contact of crack surfaces.....  | 177  |
| 6.6 Plastic zone for an edge crack .....   | 178  |
| 6.7 Discontinuous closure .....  | 178  |

## LIST OF SYMBOLS

a, c: Crack dimensions  
b: Half-width for surface flawed plate  
d: Indentation spacing in the IDG measurement  
h: Half-length for surface flawed plate  
m: Orange's coefficient in crack opening solution  
n: Orange's exponent in crack opening solution  
n: Fringe order  
r: Distance from crack tip  
t: Thickness of surface flawed plate  
u: Node deflection in finite element study  
B: Specimen thickness for through cracks  
C: Crack mouth compliance  
D: Hole diameter for corner cracked plate  
E: Elastic modulus  
G: Shear modulus  
K: Stress intensity factor  
L: Specimen length for corner cracked holes  
M: Applied remote bending load  
P: Applied remote force  
R: Stress ratio = minimum/maximum stress per cycle  
T: Specimen thickness for corner cracked plate  
U: Strain energy

V: Half crack separation at a specific location

W: Specimen width for corner & through-thickness flaws

$a_{avg}$ : Average through-thickness crack dimension

$a_{eff}$ : Closure corrected effective crack length

$a_m$ : Mid-plane crack dimension for through flaw

$a_s$ : Free surface crack dimension for through flaw

$g_f$ : Strain energy release rate

$E'$ : Effective modulus

$K_I$ : Mode I stress intensity factor

$K_{max}$ : Cyclic maximum  $K$  for a load cycle

$K_o$ :  $K$  needed to separate the crack faces at the tip

$K_{OC}$ : Global crack opening load obtained from CMOD reading

$K_{OE}$ : Global crack opening load from back face strain reading

$K_{OI}$ : Local crack opening load from optical interference

$S_{maj}$ : Major span in the four-point bend fixture

$S_{min}$ : Minor span in the four-point bend fixture

$V_o$ : Crack mouth separation

$\Delta a$ : Change in crack length

$\Delta u$ : Change in nodal deflection

$\Delta K$ : Cyclic range in stress intensity factor

$\Delta K_b$ : Applied  $\Delta K$  for steady state crack growth

$\Delta U$ : Change in strain energy

$\nu$ : Poisson's ratio

$\lambda$ : Wavelength of light

$\delta$ : Crack mouth opening

$\alpha$ : Non-dimensional crack length

$\theta$ : Angle defining points near the crack tip

$\phi$ : Parametric angle in part-through flaws  
 $\sigma$ : Applied remote stress  
 $\epsilon_{BF}$ : Back face strain  
 $\alpha_0$ : Reflection angle in IDG measurement  
 $\sigma_0$ : Stress needed to separate the crack faces at the tip  
 $\sigma_{max}$ : Maximum applied remote stress per load cycle

## CHAPTER 1

### BACKGROUND

#### 1.1 INTRODUCTION:

The objective of this research program was to characterize three-dimensional aspects of fatigue crack closure relative to part-through and through-thickness flaws. Personnel who contributed to the three year research grant, along with publications and presentations resulting from this effort are summarized in Appendix A.

The work is motivated by the well known fatigue crack closure phenomenon whereby naturally occurring fatigue cracks do not open in a linear elastic manner. Since proposed by Elber [1-3], considerable research has focused on developing the closure mechanism for fatigue life prediction schemes. As emphasized in reviews by Paris [4], Banarjee [5], and Suresh and Ritchie [6], understanding crack closure is of fundamental importance for describing many aspects of fatigue crack growth.

One explanation for fatigue crack closure involves the plastically deformed region ahead of the crack tip. As the crack propagates through the successive plastic zones ahead of its tip, a plastic wake is formed which results in residual deformations. These deformations in turn hold the crack faces closed during portions of positive applied load cycle, and reduce the

effective load for the remainder of the cycle. Figure 1.1 schematically shows the development of the crack tip plastic zones as the crack propagates through the specimen and the resulting plastic wake containing the residual deformations. Figure 1.2 shows how the effective stress range is reduced in a typical load cycle by crack closure. Here  $K_{\text{open}}$  is the stress intensity factor necessary to open the crack tip and  $\Delta K_{\text{effective}}$  is the actual stress intensity factor range during which the crack tip is completely open. Since crack extension can not occur unless the crack tip is open, only  $\Delta K_{\text{effective}}$  contributes to further crack propagation. Thus, fatigue crack closure is one of the controlling factors in crack extension.

It is well known that the crack tip plastic zone is larger at the free surfaces, where plane stress conditions occur, than at the center of a thick specimen where plane strain conditions prevail [7]. Figure 1.3 schematically shows the through-the-thickness variation of the plastic zone in a thick specimen. This through-thickness plastic zone size variation has been used to explain phenomena such as thickness dependent fracture toughness, fracture surface appearance, and thickness related fatigue crack behavior. The larger plastic zone at the specimen surface would imply that the closure effect is more pronounced at the surface than at the interior, resulting in a slower crack growth rate at the free surface. This through-thickness variation in crack growth rates is commonly called the tunnelling effect. The effect of the state of stress on plastic zone size, and the resulting fatigue crack growth has been demonstrated with variable amplitude loading experiments, where thin specimens have longer crack growth lives than thick members [8-11].

In addition to crack closure associated with the plastic wake behind the crack tip, two other closure mechanisms have been proposed: asperity induced and oxide induced closure. The asperity induced closure model [12-14] states that crack surface roughness keeps the crack faces propped open under zero load. The maximum plastic zone size in this model is smaller than the grain size, while the size of the fracture surface roughness is on the same order as the crack tip displacement. In order to meet the requirement for a small plastic zone size, asperity induced closure is generally observed at low crack growth rates (on the order of  $10^{-6}$  mm/cycle). When the fracture surface size is the dominant factor, the crack tends to grow in a zig-zag, out of plane path, leading to significant Mode II displacements promoting asperity induced closure.

In the oxide induced closure mechanism [15-16], the formation of an oxide layer just behind the crack tip prevents the crack surfaces from closing. As in the asperity induced closure mechanism, the thickness of the oxide layer is comparable to the crack tip displacements. During the closing phase of the load cycle, early contact occurs between the two crack faces due to the presence of the oxide layer, resulting once more in the closure phenomenon. Oxide induced closure, like the asperity model, has also been observed at low crack growth rates. Since both asperity and oxide induced closure mechanisms keep the crack faces open under zero load, these are sometimes referred to as "Non-closure" models.

## **1.2 REVIEW OF PRIOR WORK:**

This section reviews techniques that have been employed to characterize fatigue crack closure. Both numerical and experimental methods are briefly discussed.

### **1.2.1 Numerical Studies:**

Newman studied crack closure in a center-cracked panel under cyclic loading with a two-dimensional, non-linear, finite element model [17]. In this study the material was assumed to be elastic-perfectly plastic, and the model was composed of two-dimensional constant-strain triangular elements. It was observed that the element-mesh size near the crack tip influenced the prediction of the magnitude of crack closure and opening loads. By choosing an appropriate finite-element-mesh, the actual experimental crack growth rate could be simulated. Although the finite-element method may work well for closure predictions, the analysis is often complicated and may require long computation times.

Chermahini [18] performed a three-dimensional elastic-plastic finite element analysis of a straight through crack under cyclic tensile loading. His analysis did not allow for any curvature of the crack front. The crack was simply extended at the maximum load of each cycle, and no attempt was made to calculate the amount of crack growth. The results of Chermahini's analysis appeared to agree well with experimental observation, and also gave some new insight into the stresses that develop behind the crack tip. Unfortunately, this type of analysis requires an enormous amount

of computer time even though the program was vectorized to run on the VPS-32 computer at NASA Langley Research Center.

Newman [19] developed a two-dimensional model that would calculate crack growth for a center cracked panel. The model was based on the Dugdale concept, but was modified to leave plastically deformed material in the crack wake. The model was used to predict crack growth in center cracked tension specimens of 2219-T851 aluminum alloy aluminum alloy material. Thirteen tests were performed, including five different types of spectrum loadings. The model's predictions were in good agreement with the experimental results. The ratio of predicted to experimental lives ranged from 0.66 to 1.48. The running times for this model ranged from 2 to 15 minutes on a CDC-6600 computer, which makes this method much more usable than finite element analysis.

Fleck [20] has employed the two-dimensional finite element analysis developed in reference [17] to study crack closure under plane strain conditions. From this study, it was noted that plasticity-induced closure under plane stress conditions is quite different from the plane strain closure behavior. Under plane stress conditions, the crack faces were found to open and close in a continuous manner (ie: crack closes continuously from its tip). Under plane strain conditions, a discontinuous closure phenomenon was observed, whereby the crack first closes at a location near the crack tip, and next closes far behind the crack tip, leaving a gap where no closure occurs.

### **1.2.2 Experimental Studies:**

Many experimental measurements of fatigue crack opening have been performed on various types of specimens, employing techniques such as crack mouth opening displacement (CMOD) measurements, strain gages, push-rod, etc. Some detailed aspects of these methods are discussed below.

The CMOD gage [21-23] measures the crack mouth opening displacement from a clip gage mounted across the mouth of the precracking notch. A plot of displacement versus applied load is obtained, and the load at which linear elastic behavior begins represents the closure load.

The strain gage measurement technique [24-25] involves bonding one or more strain gages at various locations across the crack surface. In some cases strain gages are also mounted on the back face of the specimen. The signal from the strain gages are then recorded as a function of applied load, and the closure load is again determined as the point where the load versus strain record becomes linear.

The ultrasonics method [26-27] measures the changing acoustic resistance of a specimen as the crack opens or closes. The intensity of the ultrasonic signal reflected from the fatigue crack varies depending on the amount of crack closure present. In this technique, an ultrasonic transmitter is placed on the top of the cracked member, and a receiver is placed opposite the transmitter on the bottom of the specimen. As before, the received signal intensity is plotted versus load, and the closure load is determined.

The potential difference approach [28-29] measures the electrical resistance of a specimen, which is also proportional to opening of the crack.

In this instance the metal specimen acts as a part of an electrical circuit. A constant current supply is provided across the specimen, and the signal obtained from potential probes placed on both sides of the crack is recorded as a function of applied load. It has been observed in some applications that the received signal may be misled by the presence of a layer of insulating oxide on the crack faces which prevent electrical contact. Other complicating factors may include the change of electrical properties of the material in the crack tip yield zone.

The push-rod displacement gage [30-31] has been used to determine the closure load at a single point inside the specimen. For this method a push-rod assembly is fastened to the specimen by drilling two parallel holes just behind the fatigue crack front. The relative displacement of the hole bottoms is measured with a twin cantilever clip gages via the push-rods. The closure load is then determined by locating the linear point on the load-displacement curve.

The Elber gage [32-33] measures the crack opening at a certain distance from the tip on the free surfaces of a specimen. Here the Elber gage (modified clip gage) is mounted across the crack plane and the closure load is determined from a load-displacement plot as before.

The interferometric displacement gage (IDG) [34-38] uses a laser to measure relative displacement between two shallow reflecting indentations or grooves located across the crack. Interference fringe patterns are created by the diffracted laser beams, and the motion of these fringes represent the crack surface displacement. This technique has proven to be an effective method for measuring crack surface displacements due to its high resolution

capability.

Other methods to obtain the closure loads include direct-observation using electron microscopy [39], and a vacuum infiltration technique [40]. It should be noted here that all of these techniques only determine the closure load at the specimen's surface, or at a single point inside the specimen, and can not determine the complete through-the-thickness variation of closure. Furthermore, since the closure levels observed for a single test specimen vary with the measurement location [41-42], the results obtained from the above technique can differ significantly.

While the above techniques reflect an average (global) or single point behavior of the entire specimen, optical interferometry has been employed to determine the complete through-the-thickness variation of crack closure in transparent polymer specimens [43-48]. These optical interference experiments have shown that for a through-thickness or part-through flaw, the crack opening loads vary along the crack front.

### **1.3 OBJECTIVE OF CURRENT RESEARCH:**

The main objective of the current research is to determine how through-the-thickness variation in crack tip plasticity affects fatigue crack opening, and alters fatigue crack growth in transparent model materials.

Both experimental and numerical approaches were employed. As described later, complete three-dimensional crack opening profiles were measured by the use of optical interferometry for through-thickness flaws, corner cracked holes, and surface flaws. These point wise measurements are

then compared to global (average) measurements obtained from CMOD and back face strain techniques. Two types of polymer model materials, namely Polymethylmethacrylate (PMMA) and Polycarbonate (PC), are included in this research program. Although this project did no testing of metals, the polymer data are compared to results of rene-95 (a nickel based alloy) testing by Ashbaugh [49] in section 6.2. Differences in fatigue crack growth mechanisms of metals and polymers are discussed in section 1.4 of reference 50.

An algorithm was also developed here to analyze crack growth and crack closure of a surface flaw. This algorithm was based on Newman's model for center cracked plates, but was modified for the three-dimensional surface crack case. The model was used to analyze the surface crack experiments and the results are compared to the experimental values.

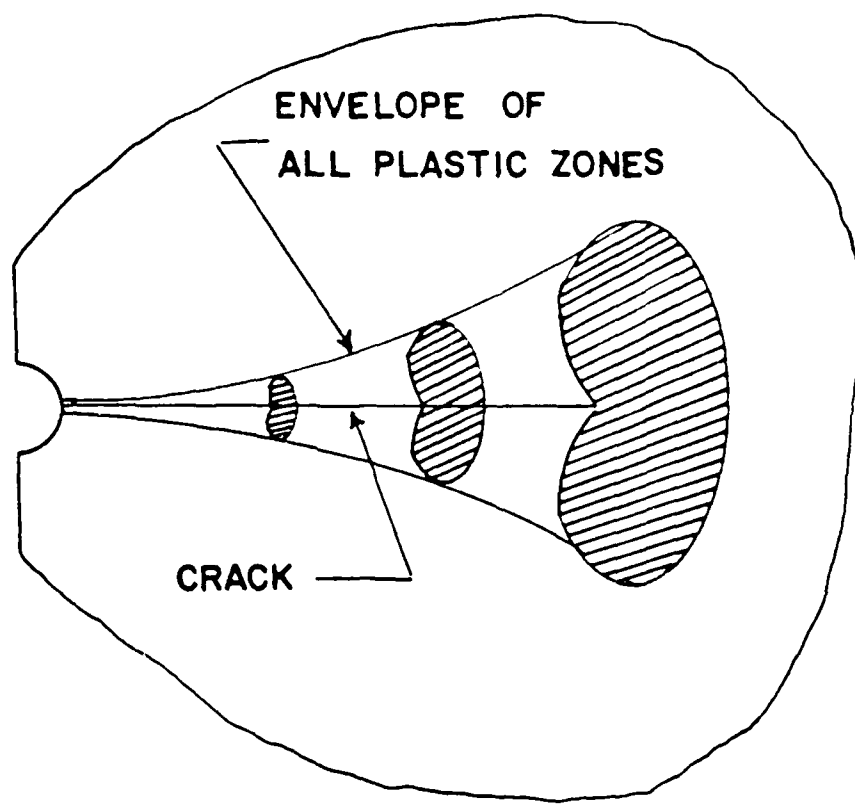


Figure 1.1: Schematic view of the crack tip plastic wake formation behind the crack tip, resulting in compressive residual stress, which hold the crack faces closed during portions of positive applied load.

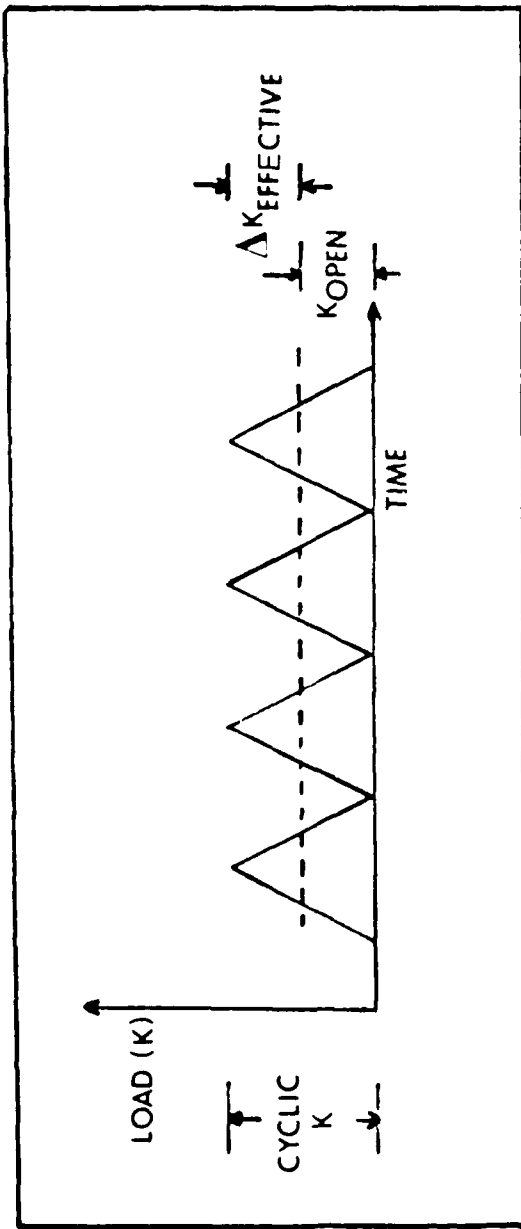


Figure 1.2: A schematic representation of the effective cyclic  $K$  level that the specimen experiences in a typical load cycle.

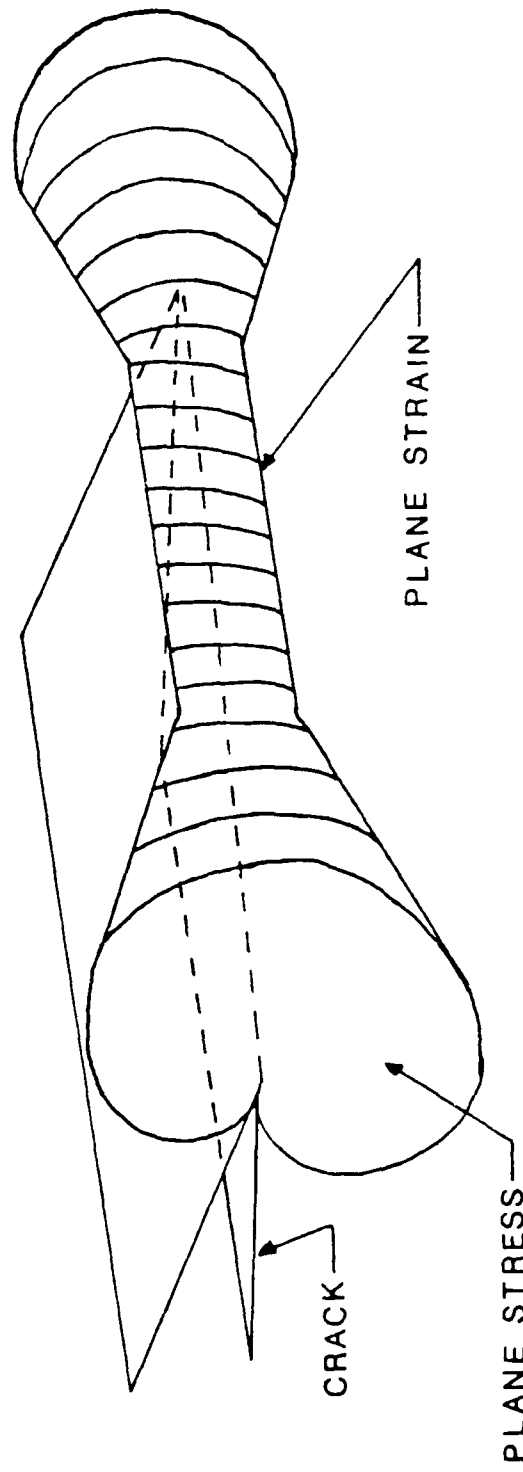


Figure 1.3: Schematic presentation of 3-D crack tip plastic zone showing transition from large plane stress plastic zone at specimen surface to smaller plane strain zone size at the center of the specimen.

## CHAPTER 2

### EXPERIMENTAL PROCEDURE

#### 2.1 OPTICAL INTERFERENCE TECHNIQUE:

This section describes the procedures used for the experimental portion of the research. The main experimental method employed for the current research involved optical interference measurements of crack opening in transparent polymer specimens. Both polymethylmethacrylate (PMMA) and polycarbonate (PC) model materials were employed.

Optical interference occurs in a thin transparent wedge when the reflection of light rays from the top and the bottom of the faces of the wedge have different path lengths [51-56]. When a crack is present in a transparent material, an air film wedge is formed between the two crack surfaces and may cause optical interference to take place. As schematically presented in Figure 2.1, some light waves travel through the transparent specimen and are reflected back by the top surface of the crack, whereas other waves, following a different path, penetrate the top surface and are reflected by the bottom surface of the crack. This difference in path lengths (phase difference) causes interference fringes to form. Each fringe represents a locus of points which have the same displacement between the crack faces. The interference fringes form an alternating pattern between dark and light

shades and are referred to as destructive and constructive fringes respectively. If the wavelength of the monochromatic light source is known, the crack surface displacements may be computed using either of the following optics equations [56].

For destructive interference (dark fringes):

$$V = \frac{n}{4} \lambda \quad (2.1)$$

For constructive interference (light fringes):

$$V = \frac{2n+1}{8} \lambda \quad (2.2)$$

Here  $V$  is half the crack surface separation at a specific constructive or destructive fringe location,  $n$  is the respective fringe order, and  $\lambda$  is the wavelength of the monochromatic light source. Here a sodium vapor lamp is employed for the interference study with a wavelength of  $8.89 \times 10^{-5}$  cm. The 0-order dark fringe is defined here as the first destructive fringe indicating the closed portion of the crack, while the 0-order light fringe corresponds to a total crack separation  $2V = \lambda/4$ .

## 2.2 THROUGH-THICKNESS FLAW:

The through-thickness flawed specimens studied here consisted of edge cracked beams loaded in four-point bending as shown in Figure 2.2. The test specimens were 38 mm high (W) and 178 mm long (L). The specimen

thickness (B) varied from 25 mm thick to 5 mm for PMMA and from 25 mm to 10 mm for PC. The specimen configuration for the 5 mm members was modified to avoid instability on the four-point bending fixtures. Here the test section of a 25 mm thick member was reduced to 5 mm with sufficient care being taken to avoid significant stress concentration build up at the test section.

A total of five different specimen thicknesses for PMMA and three for PC were studied. The specimens were cut from a single sheet of the respective material and each test member contained a 5 mm deep V-notch located midway along one specimen edge. The PMMA specimens were annealed at 100°C and the PC members at 138°C for 24 hours, and slowly cooled to room temperature to reduce potential residual stresses due to the machining process. One end of each specimen was then polished to transparency to allow crack plane observation. Two metal tabs were glued to each specimen at the starter V-notch to hold the clip gage (MTS Model 632.03B-30) at the crack mouth for the CMOD measurements. The back face strain measurement technique involved bonding of one or two 1000 ohm strain gages (Type MA-06-250BK-10C) on the top side of the four-point bend specimens (Figure 2.2).

Cyclic loads (Haversine function) were applied in a pure-bend configuration at 3Hz for PMMA and 4Hz for PC specimens. These relatively low test frequencies were chosen to avoid local crack tip melting due to the poor heat conductivity of the polymers. For these through-thickness flaw experiments, cracks were grown under constant  $\Delta K$  conditions, and constant stress ratio (R) was maintained, via automated computer controlled test

procedures which employed compliance measurements of crack length. When the crack grew to a suitable size, interferometry, CMOD, and BFS measurements were performed to determine the closure load. This procedure was repeated at different crack sizes for each specimen.

### **2.3 CORNER CRACKED HOLES:**

The corner cracked hole specimens consisted of PMMA rectangular plates, with a hole located midway along the specimen's length as shown in Figure 2.3(a). The specimens were 190 mm long ( $2h$ ), 89 mm wide ( $2b$ ), and 19 mm thick ( $T$ ) with a hole diameter ( $D$ ) of 19 mm. For the present study, the corner cracks were assumed to have a quarter-elliptic configuration as shown in Figure 2.3(b). Here the angle  $\phi$  is the elliptic angle commonly used to define points along the flaw border for analysis purposes [57]. The crack dimensions  $a$  and  $c$  represent the crack length along the hole bore and the free surface locations respectively.

Cyclic tensile loads were applied at 3Hz to the PMMA corner cracked hole specimens through grips glued and bolted to the specimen ends. Two strain gages were mounted on either side of the plate and monitored to ensure uniform tensile loading. All corner cracks were grown under constant amplitude load conditions with a fixed stress ratio of 0.1. The crack plane was viewed via a mirror mounted at  $45^\circ$  on the transparent end, and was photographed periodically. When the crack achieved a suitable length, the cycling was stopped and a set of optical interference fringe patterns were photographed for different applied tensile loads. This procedure was

repeated several times until a sufficiently large corner flaw appeared. At that time the loading condition was changed to pure-bending, keeping the same R value as that for the remote tension portion of the experiment. Interference fringe patterns were again periodically photographed for increasing crack lengths in the bending configuration.

#### 2.4 SURFACE FLAWED PLATES:

The surface flawed members consisted of PMMA rectangular plates with a surface flaw starter notch located midway along the specimen's length as shown in Figure 2.4 (a-b). The specimens were 200 mm long (2h), 102 mm wide (2b), and 25 mm thick (t). For the present study, the surface flaws were assumed to have a semi-elliptic configuration as shown in Figure 2.4 (c) with the elliptic angle  $\phi$  used to define the points along the flaw border. The crack dimensions a and c represent the crack depth and half the free surface length respectively. For the CMOD measurement purposes, two metal tabs were glued to each specimen at the starter notch to hold the clip gage at the crack mouth.

The surface flawed specimens were subjected to constant amplitude remote bending cyclic loads with a R value of 0.1. The crack plane was periodically photographed through the transparent end. When the surface flaw achieved a suitable dimension, the cycling was stopped and a set of interference fringe patterns were photographed for increasing applied bending stress. In addition to the optical interference measurements, readings from the CMOD gage were recorded as a function of applied load

to determine the average crack closure behavior. This procedure was repeated several times during the test period.

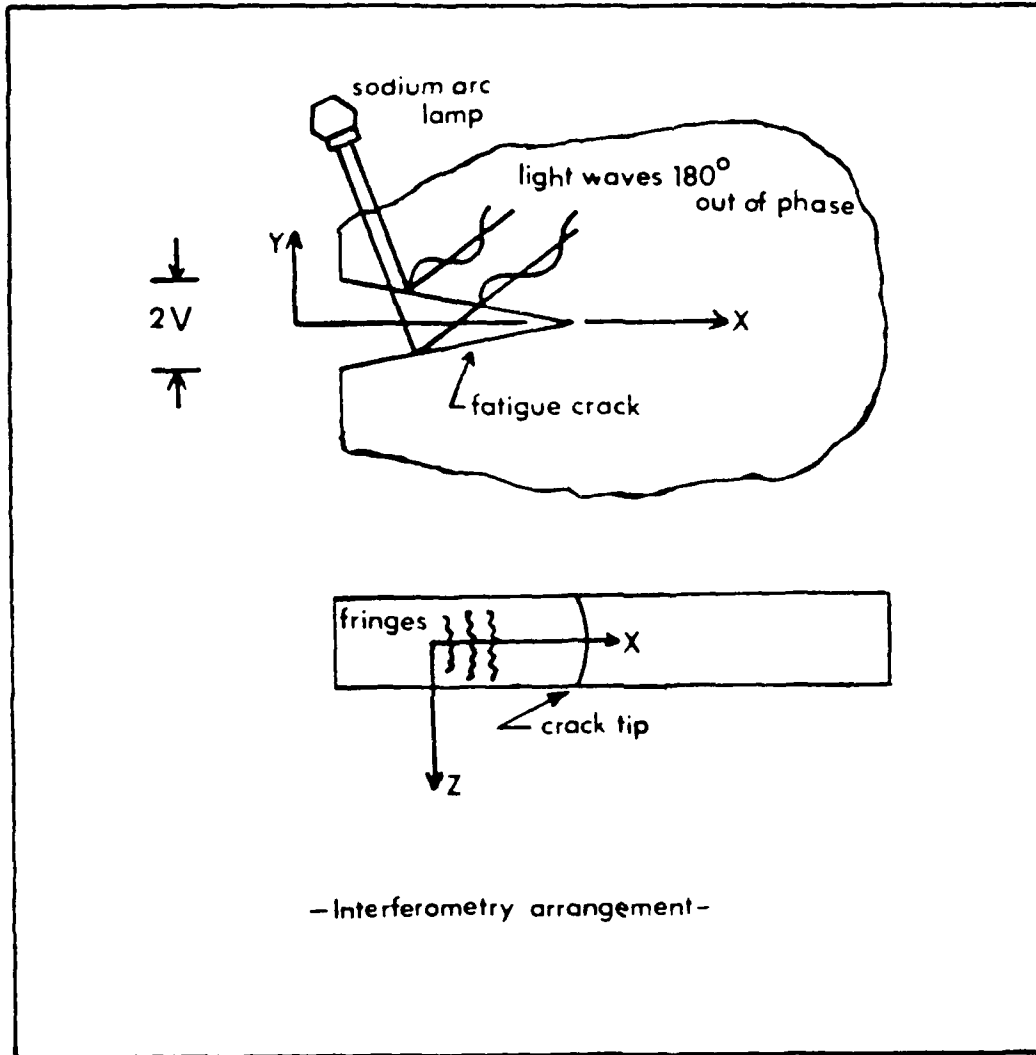


Figure 2.1: Schematic of interferometry method which gives 3-D crack surface displacements in transparent specimens.

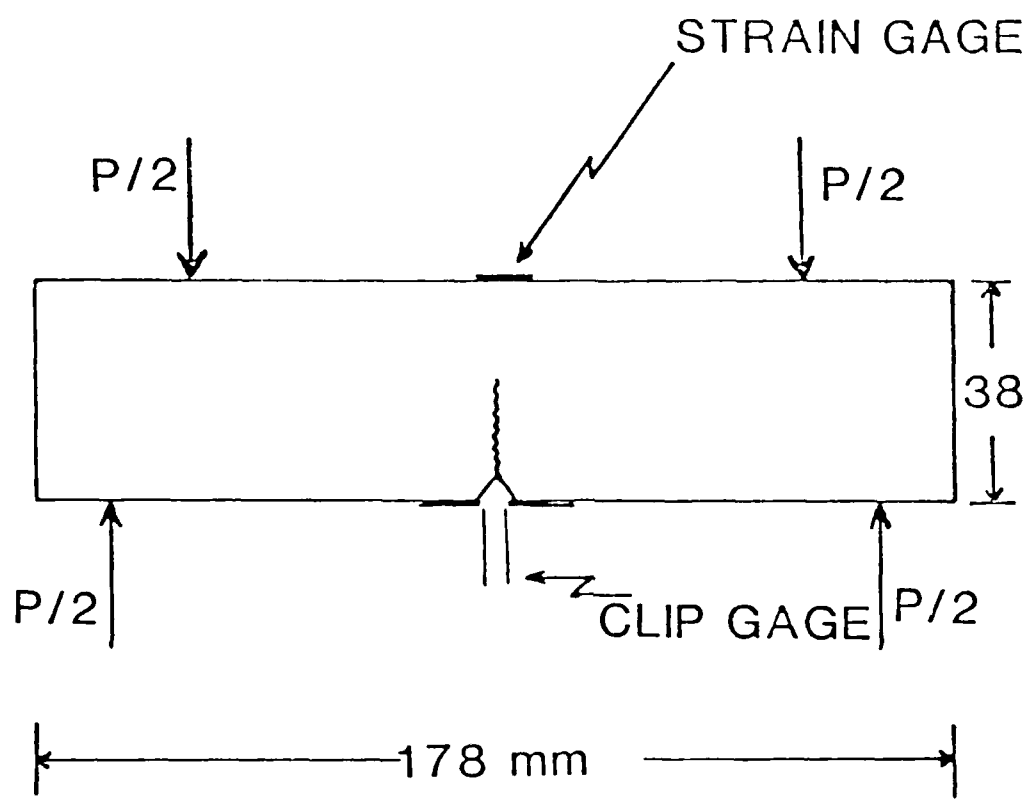


Figure 2.2: Schematic representation of four-point bend specimen containing back face strain gage and clip gage for crack opening measurements.

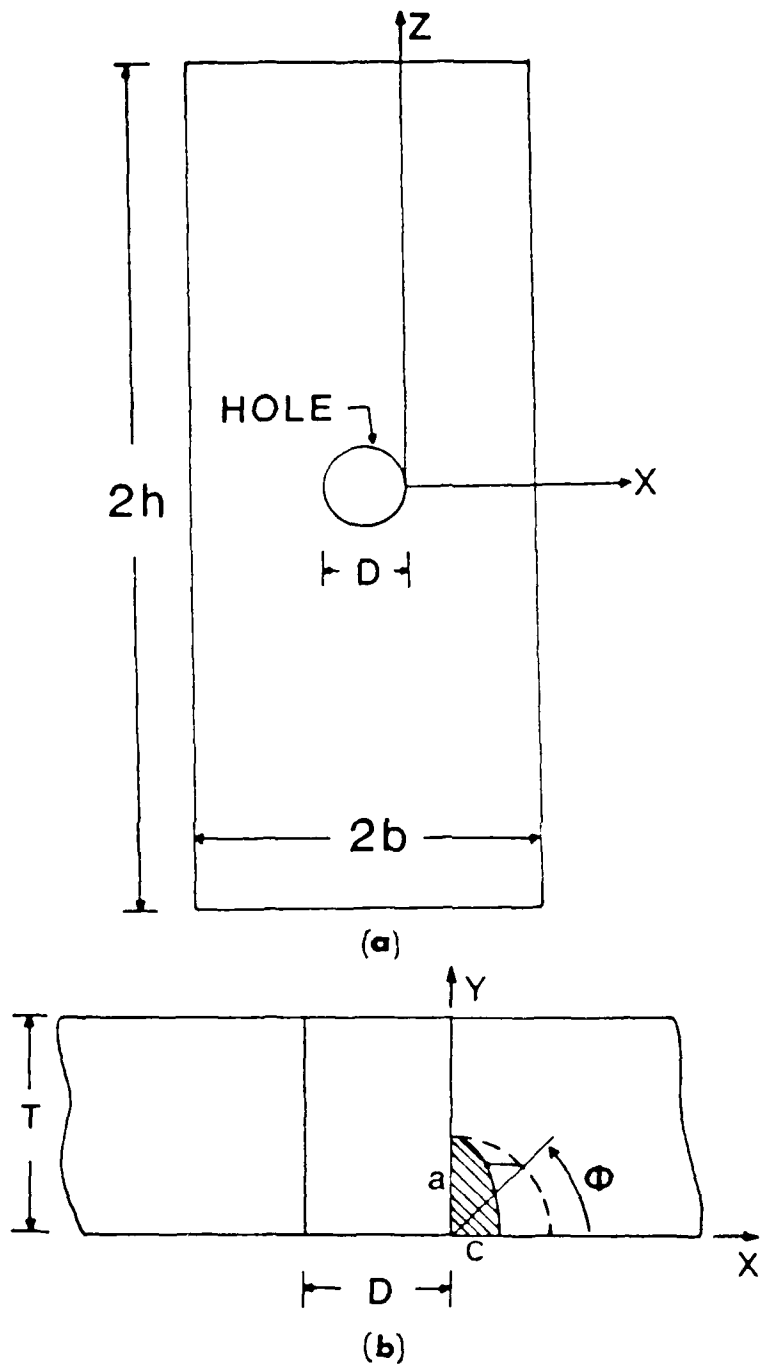


Figure 2.3: Schematic view of the corner cracked hole specimen.

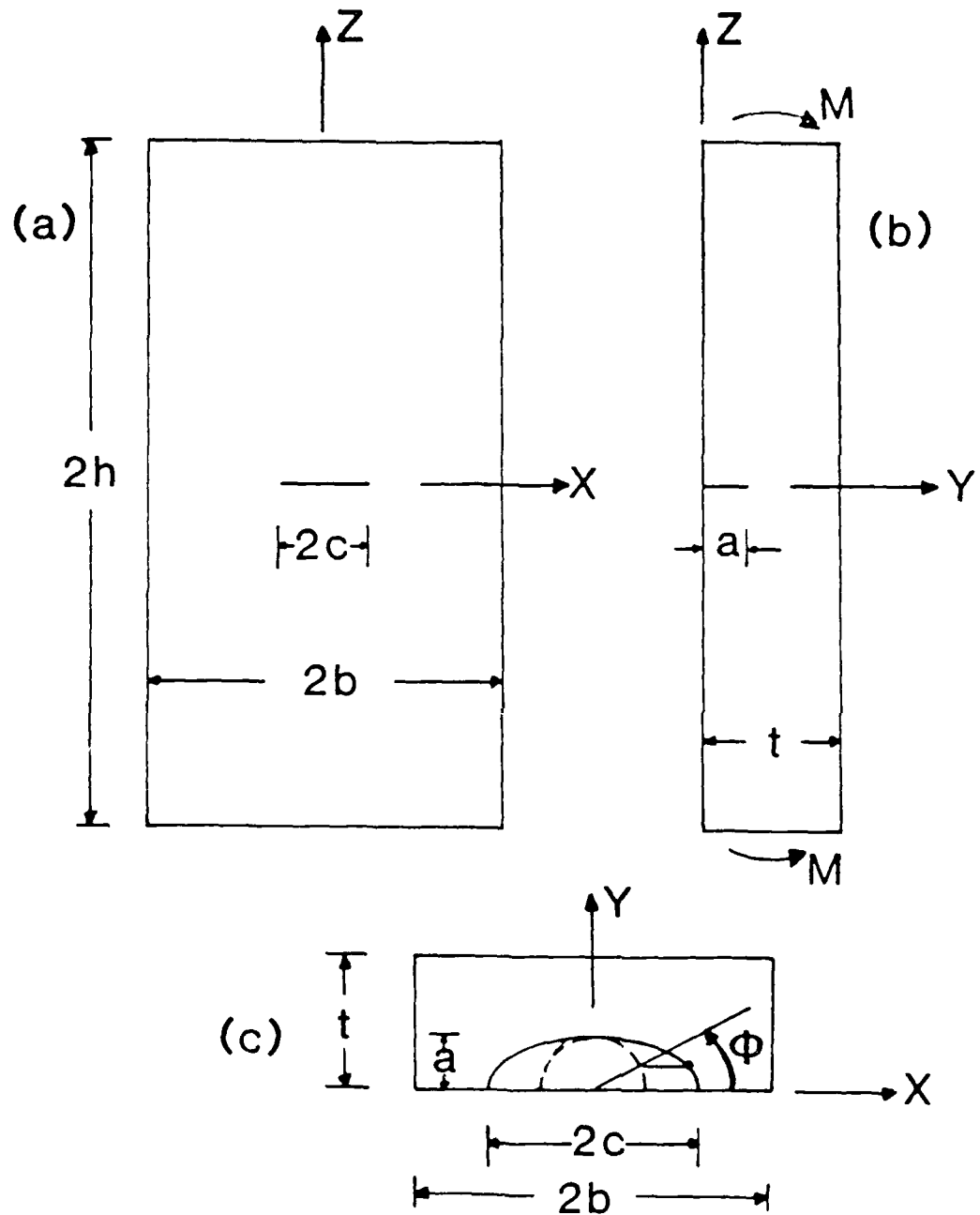


Figure 2.4: Schematic view of the surface flawed rectangular plate.

## CHAPTER 3

### SURFACE CRACK CLOSURE MODEL

This section describes the numerical approach employed to predict three-dimensional aspects of crack closure. The procedure used in this analysis for the calculation of fatigue growth of a surface crack is basically the same as Newman's method for a center cracked panel [19]. His method breaks the plastic zone and plastic wake into elements (see figure 3.1) which are created by yielding in the crack tip plastic zone. Unfortunately the tasks are greatly complicated by the three-dimensional nature of the surface flaw problem, and by the absence of appropriate crack surface displacement equations. Therefore many of Newman's center cracked panel equations are used. The major calculations in determining closure of a surface flaw are:

- 3.1 Plastic Zone Size
- 3.2 Deformation Within the Plastic Zone
- 3.3 Contact Stresses at Minimum Load
- 3.4 Crack Opening Stress Intensity Factor
- 3.5 Fatigue Crack Growth

Application of the method and equations used by Newman for the center crack problem are described in chapter 2 of reference 58. Chapter 3 of that thesis describes the surface crack closure model more explicitly and includes more details than are given in this report.

### 3.1 PLASTIC ZONE SIZE:

The plastic zone size around the periphery of a surface crack varies. This is due to two factors. The degree of constraint changes from plane stress at the free surface to near plane strain in the interior, and the stress intensity factor varies. An empirical stress intensity factor solution is available for a surface crack in bending and or tension. It was developed by Newman and Raju from three-dimensional finite element results, and is given below in its general form [59] (see figure 3.2):

$$K_I = (S_T + H S_B) \{ \gamma(a/Q) F(a/t), (a/c), (c/b), \dots \}^{1/2} \quad (3.1)$$

Here  $Q$  is the elliptical shape factor,  $F$  is the boundary correction factor for tension loading, and the product of  $H$  and  $F$  is the boundary correction factor for bending.

For this research the plastic zone size is calculated at discrete points around the crack edge by the following steps (see figure 3.3) :

1. Calculate  $K$  at flaw locations of interest by equation 3.1
2. Calculate an equivalent crack length ( $C_{eq}$ ) by
  - determining the length from the crack origin (point O) to the point of interest
3. Estimate the stress state coefficient ( $\gamma$ )
4. Solve for the crack tip plastic zone size ( $\rho$ ) by using the surface flaw values of  $K$ ,  $C_{eq}$  and  $\gamma$  in Newman's center cracked panel equations.

These steps are repeated for each point of interest (1,2,3,4,5,6 in figure 3.1) along the crack periphery.

### **3.2 DEFORMATION WITHIN THE PLASTIC ZONE:**

The plastic deformations ( $L_i$ ) within the plastic zone are calculated in a manner similar to the plastic zone size calculation. The surface flaw values of  $K$ ,  $C_{eq}$ , and  $\alpha$  are used in Newman's center cracked panel equations.

The transition from plane stress to plane strain was based on closure experiments performed on through-cracked PMMA specimens of various thicknesses (25, 19, 13, and 10 millimeters). As described in more detail in section 4.1, optical interferometry was used to determine the opening load at points along the crack front. The highest opening loads occurred at the free surface, where plane stress occurs. The opening loads for all thicknesses decreased linearly until reaching zero at a distance approximately 2.5 millimeters from the free surface.

In this model it is assumed that plane stress occurs at the free surface, plane strain occurs when the distance from the free surface is greater than 0.1 inches, and the stress state coefficient alpha is linearly interpolated for distances up to 0.1 inches. Since PMMA has a large poisson's ratio (approximately 0.4), this allows greater stresses to develop ahead of the crack tip. Therefore alpha was assigned a value of 5 where plane strain occurred [58]. In [19] Newman recommended a value of 3 for plane strain, but he was modeling the behavior of aluminum which has a poisson's ratio of 0.3.

### **3.3 CONTACT STRESSES AT MINIMUM LOAD:**

The method of determining the contact stresses in the plastic wake employed for this study utilizes Newman's center crack displacement formula along six radial lines which connect point O in figure 3.3 with crack perimeter points 1,2,3,4,5, and 6. This is done in the following manner:

1. The stress intensity factor at point 1 is calculated for the minimum load condition using equation 3.4.
2. Using the equivalent crack length ( $C_{eq}$ ) calculated earlier, and the stress intensity factor determined by step 1, the crack surface displacements due to the remote load are calculated by using the center cracked panel equations.
3. An iterative method is used to determine the element contact stresses. These stresses cause the crack surfaces to open up to the element lengths. When necessary, the stresses are modified to account for yielding and crack separation.
4. Proceed to the next radial line (2,3,4,5,6) and repeat until the contact stresses along all lines have been calculated.

Using this method appears to give reasonable contact stresses near the crack edge. The stresses near the surface crack origin (point O) are not expected to be accurate, however, since shear stresses will cause the displacement of a slice to be strongly affected by the displacements of its neighboring slices. This affect is less significant at the crack edge because the slices are farther apart. Inaccurate stresses near the crack origin are not expected to affect overall accuracy in most cases. Newman reported that only elements near the crack tip carried significant loads in his center cracked panels [19] for R ratios greater than zero. (Of course, his results were restricted to through-the-thickness flaws.) Also stresses away from the crack edge have a smaller effect on the crack opening stress intensity factor than stresses near the crack edge.

### 3.4 CRACK OPENING STRESS INTENSITY FACTOR:

When the element stresses have been determined, the crack opening stress intensity factor can then be calculated. By using the weight function method, Mattheck, et al [60] developed an algorithm to determine the stress intensity factors at points a and c ( $K_a$  and  $K_c$ ) due to arbitrary stresses on the crack surface. Their equations are given below and the coordinates are shown in figure 3.4.

$$K_a = [4h/K_{ra}\pi c] \int_{y=0}^c \int_{x=0}^{x(y)} \sigma_{new}(x,y) [\partial U_r / \partial a] dx dy \quad (3.2)$$

$$K_c = [4h/K_{rc}\pi a] \int_{y=0}^c \int_{x=0}^{x(y)} \sigma_{new}(x,y) [\partial U_r / \partial c] dx dy \quad (3.3)$$

Here  $h$  is a material constant equal to  $E$  for plane stress, and  $E/(1-\nu^2)$  for plane strain. The stress intensity factors at A and C due to the reference case load are  $K_{ra}$  and  $K_{rc}$ . The partial derivatives  $\partial U_r / \partial a$  and  $\partial U_r / \partial c$  are the changes in crack surface displacement ( $U_r$ ) due to the reference load with respect to changes in the crack dimensions  $a$  and  $c$ . The stress distribution  $\sigma_{new}(x,y)$  is the new loading for which  $K_a$  and  $K_c$  will be determined. The loading must be symmetric ( $\sigma_{new}(x,y) = \sigma_{new}(x,-y)$ ). Equations 3.2 and 3.3 are evaluated by the following steps:

1. Calculate  $\partial U_r / \partial a$  and  $\partial U_r / \partial c$  at element centers
2. Break crack surface into sections (figure 3.5)
3. Average  $\partial U_r / \partial a$ ,  $\partial U_r / \partial c$  and contact stress for each section.
4. Numerically evaluate integrals for each section.
5. Sum integrals and multiply by constants.

Calculating the partial derivatives is the most difficult step here. This is accomplished by calculating the displacements for the actual crack dimensions ( $a,c$ ), a slightly deeper crack ( $a + \delta a, c$ ) and a slightly wider crack ( $a, c + \delta c$ ). The derivatives are set equal to the change in

displacement divided by the change in crack size. The procedure for approximating the displacements is rather complex, and the details are given in reference [60]. The surface crack is assumed to displace like an edge crack along  $y = 0$ , and like a center crack along  $x = 0$ . The crack opening approximation developed by Petroski and Achenbach [61] for two-dimensional problems, was modified by Mattheck et al. [60] for the surface flaw problem. In this study an outer fiber bending stress of 100 psi was used as the reference load. This value is used internally by the algorithm to calculate displacements. It has no effect on the values of  $K_a$  and  $K_c$  in equations 3.2 and 3.3. The displacement ( $U_r$ ) and the reference stress intensity factors ( $K_{ra}$  and  $K_{rc}$ ) are directly proportional to the reference stress ( $\sigma_{new}(x,y)$ ), so the effects cancel. The type of reference case stress (bending or tension) does have some effect on the algorithm and this is discussed in section 5.4.5. The crack is broken into sections by connecting wake elements to their neighbors in adjacent slices. The stresses and partial derivatives of the two elements are averaged, and these values are assumed to be constant over the entire section. This allows easy evaluation of the double integral for each section. The stress intensity factor to cause crack opening is equal to the minimum  $K$  plus the  $K$  caused by the contact stresses, and is given by equations 3.4 and 3.5 for crack locations A and C.

$$KOP_a = K_{min}(at a) + \sum K(at a \text{ caused by contact stresses}) \quad (3.4)$$

$$KOP_c = K_{min}(at c) + \sum K(at c \text{ caused by contact stresses}) \quad (3.5)$$

This gives two opening stress intensity factors,  $KOP_a$  and  $KOP_c$ . These values are used to calculate the crack growth.

The algorithm for determining  $K$  due to contact stresses was evaluated by applying bending and tensile stresses over the crack surfaces. The results

from the algorithm were then compared to the Newman-Raju solutions. Although the Newman and Raju results are for either remote tension or bending, they may be used to evaluate the contact stress solutions when the crack faces are loaded with a uniform tension or linearly varying bending stress. This was done for various crack shapes and sizes (see table 3.1). Typical results are shown in figures 3.6 and 3.7. There is good agreement for small cracks, but the method is inadequate for large a/t ratios (above 0.3). This observation agrees with Mattheck's results [60]. There is slightly better agreement at point A than at the free surface. The largest a/t ratio used in the calculations shown in this report is 0.50, which is marked on the figures by a dotted line. It should be pointed out that while these figures provide a comparison of the algorithm to an accepted empirical solution, the loading is very different from what the crack faces would experience from surface contact due to closure. Therefore these figures may not necessarily reflect the accuracy of the algorithm due to actual loads.

### 3.5 FATIGUE CRACK GROWTH:

Newman [19] employed in his model a rather complex equation for crack growth. This equation utilized five constants that were needed to model crack growth at near threshold and near fracture conditions. Since this project did not analyze these situations, the simpler crack growth law proposed by Elber [3] (equation 3.6) should be sufficient.

$$da/dn = A(\Delta K_{eff})^n \quad (3.6)$$

Elber's equation (3.6) is integrated to determine the number of cycles required for the crack to grow 5 percent of the plastic zone size at point 6 (figure 3.3).

$$N = \int_a^{a+.05\rho} \{da/[A(\Delta K_{eff})^n]\} \quad (3.7)$$

In equation 3.3,  $\Delta K_{eff} = K_{max}(\text{at point 6}) - K_{OP_a}$ . While the crack is growing at point 6, it is also growing at all the other points along the crack edge. It is assumed that the crack will retain its semielliptical shape at all times. Therefore as the crack grows, it is only necessary to calculate new values of  $a$  and  $c$ . While the crack grows 5 percent of its plastic zone size at point 6, its growth at point 1 is calculated by:

$$\Delta c = N \frac{dc}{dn} = N A (\Delta K_{eff})^n \quad (3.8)$$

The  $N$  in equation 3.8 is the  $N$  (cycles) that was calculated in equation 3.7. The  $\Delta K_{eff} = K_{max}(\text{at point 1}) - K_{OP_c}$ . After these calculations are complete, the crack is extended ( $a = a + .05\rho$  and  $c = c + \Delta c$ ) and steps 3.1 through 3.5 are repeated.

Table 3.1: Test cases for closure K algorithm

| Figure | a/e<br>Ratio | Loading                          | Location | t<br>millimeters | 2b<br>millimeters |
|--------|--------------|----------------------------------|----------|------------------|-------------------|
| 3.5    | 1            | bending<br>max $\sigma=6890$ Kpa | A        | 19.1             | 38.1              |
| 3.6    | 1            | bending<br>max $\sigma=6890$ Kpa | C        | 19.1             | 38.1              |
| 3.7    | 2/3          | bending<br>max $\sigma=6890$ Kpa | A        | 19.1             | 38.1              |
| 3.8    | 2/3          | bending<br>max $\sigma=6890$ Kpa | C        | 19.1             | 38.1              |
| 3.9    | 1/2          | bending<br>max $\sigma=6890$ Kpa | A        | 19.1             | 38.1              |
| 3.10   | 1/2          | bending<br>max $\sigma=6890$ Kpa | C        | 19.1             | 38.1              |
| 3.11   | 1            | tension<br>$\sigma=6890$ Kpa     | A        | 19.1             | 38.1              |
| 3.12   | 1            | tension<br>$\sigma=6890$ Kpa     | C        | 19.1             | 38.1              |
| 3.13   | 2/3          | tension<br>$\sigma=6890$ Kpa     | A        | 19.1             | 38.1              |
| 3.14   | 2/3          | tension<br>$\sigma=6890$ Kpa     | C        | 19.1             | 38.1              |
| 3.15   | 1/2          | tension<br>$\sigma=6890$ Kpa     | A        | 19.1             | 38.1              |
| 3.16   | 1/2          | tension<br>$\sigma=6890$ Kpa     | C        | 19.1             | 38.1              |

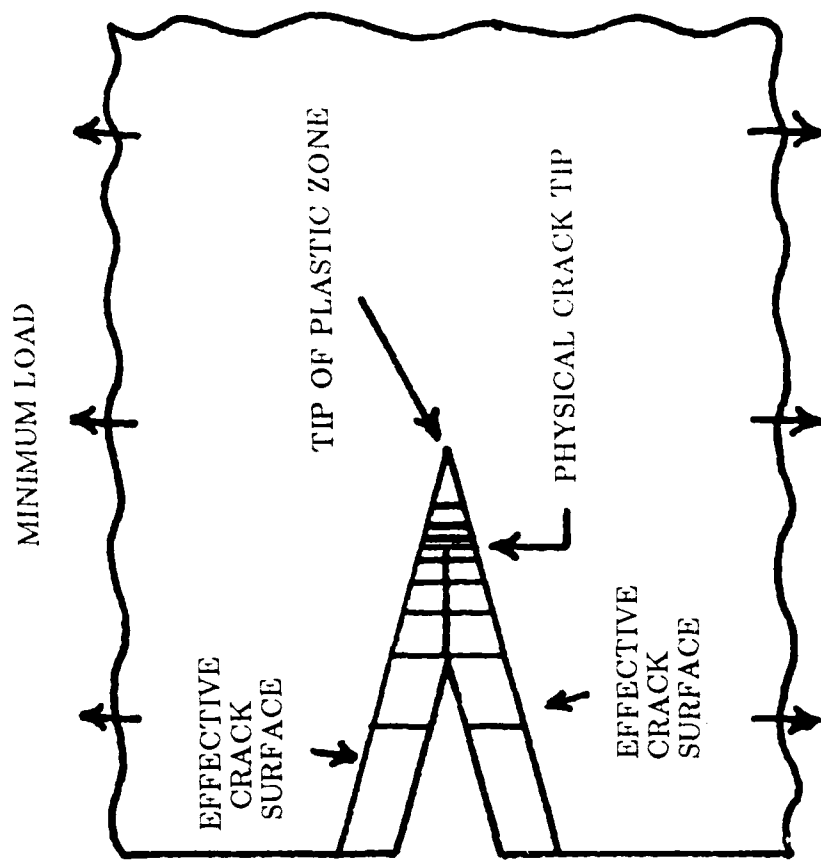


Figure 3.1: Crack elements under minimum load

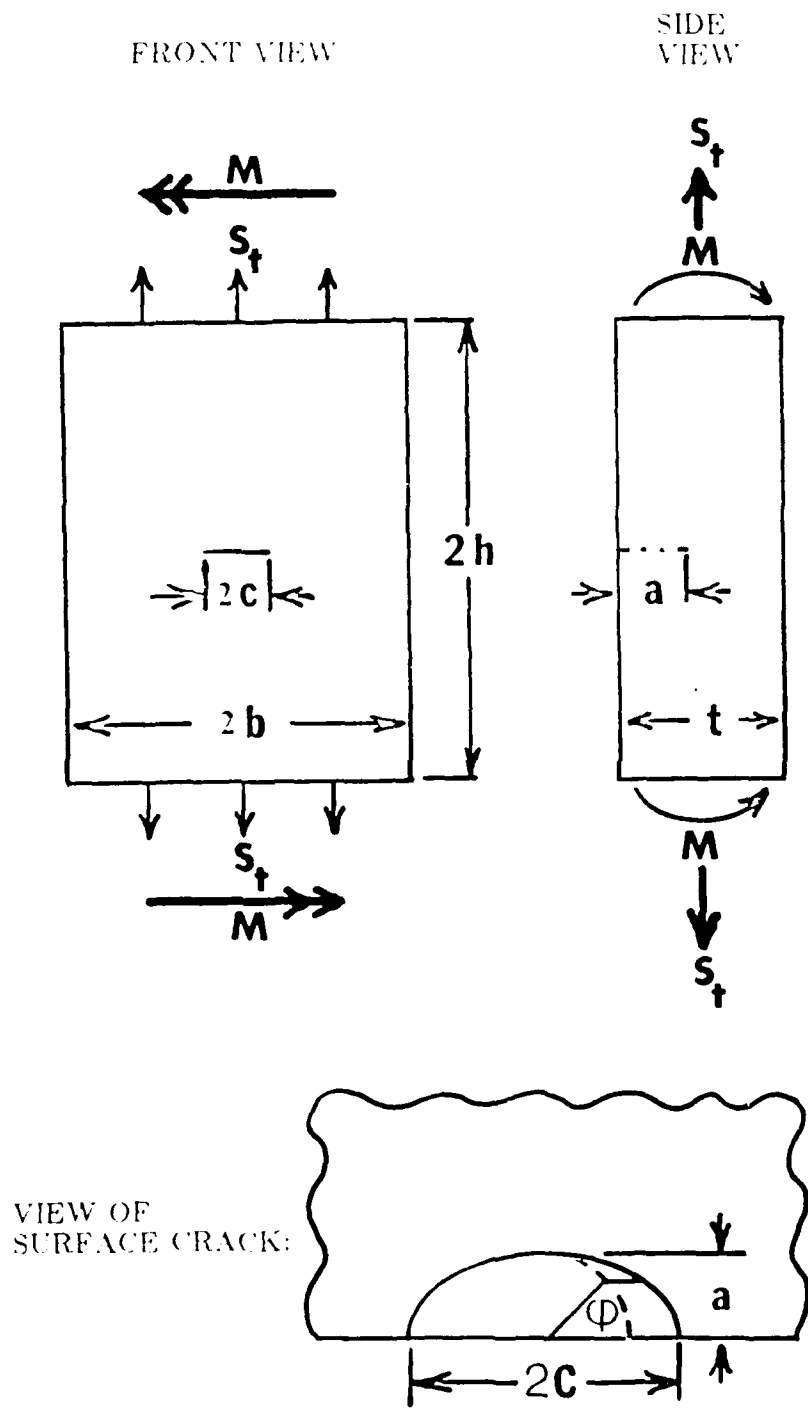


Figure 3.2: Surface crack dimensions

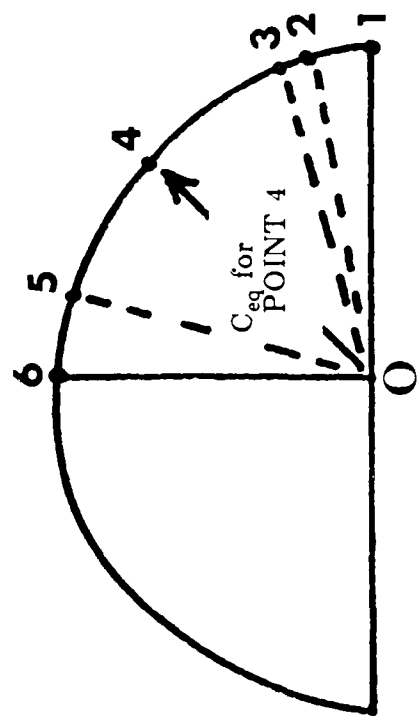


Figure 3.3: Equivalent crack lengths

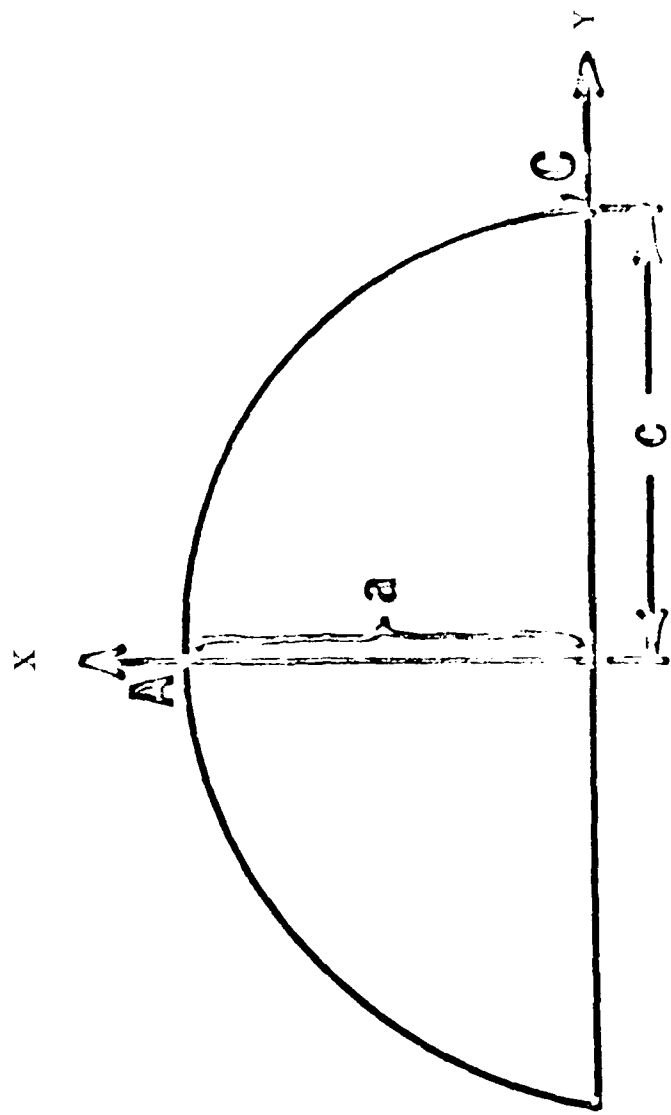


Figure 3.4: Surface crack coordinates

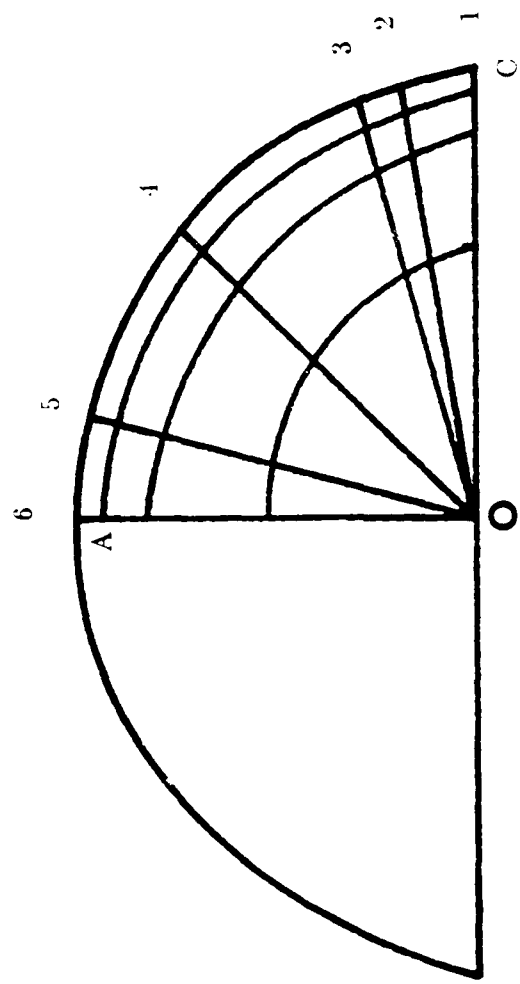


Figure 3.5: Crack surface sections

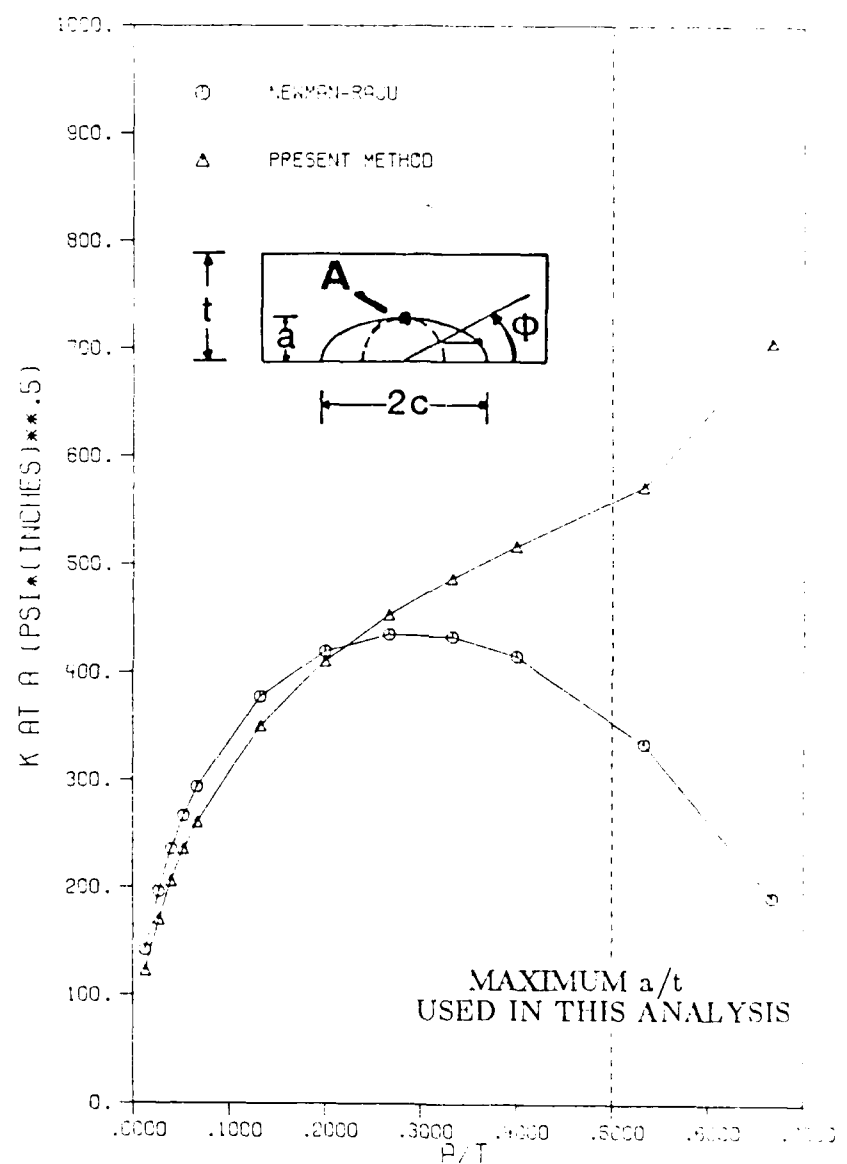


Figure 3.6: Test of closure  $K$  algorithm at point A,  
maximum bending stress = 1000 psi,  $a/c = 2/3$

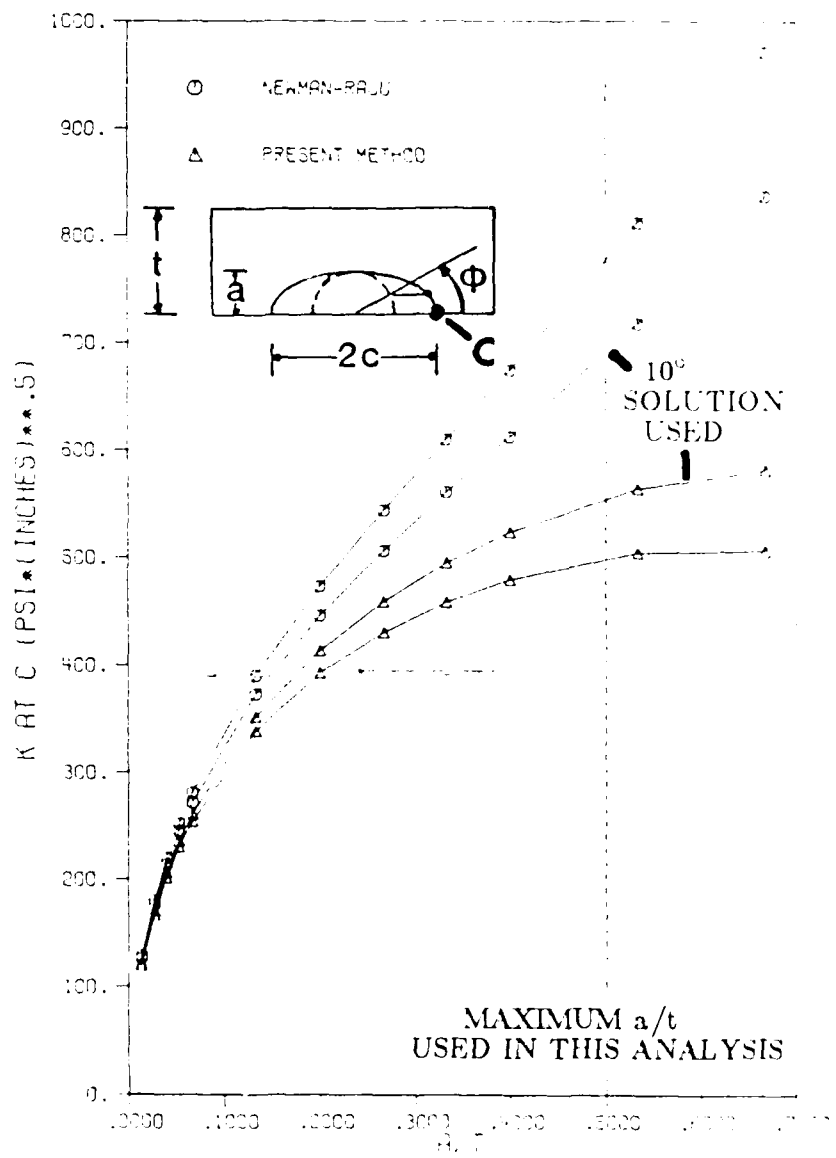


Figure 3.7: Test of closure K algorithm at point C,  
maximum bending stress = 1000 psi,  $a/c = 2/3$

## CHAPTER 4

### EXPERIMENTAL RESULTS

This chapter describes fatigue crack closure results obtained from various measurement techniques for four different crack types. These crack types are:

- 4.1 Through cracks in PMMA
- 4.2 Through cracks in polycarbonate
- 4.3 Corner cracked holes
- 4.4 Surface flaws in bending

These experiments are described in greater detail in chapters 4,5,6, and 7 of reference [50].

#### **4.1 THROUGH CRACKS IN PMMA:**

The test matrix for through thickness flaws is presented in Table 4.1. Sections 4.1.1 and 4.1.2 will focus on one particular test (PX-6) while section 4.1.3 examines the effect of varying thickness, R-ratio, and  $K_{max}$  on closure.

Experiment PX-6 was conducted at a cyclic baseline stress intensity ( $K_{max}$ ) of  $825 \text{ KPa-m}^{1/2}$ . When the crack length reached 11.6 mm, the cyclic stress intensity was reduced to  $550 \text{ KPa-m}^{1/2}$ . The stress ratio ( $R = K_{min} / K_{max}$ )

$K_{max}$ ) was kept constant at 0.1 for the entire experiment.

Figure 4.1 presents various measures of crack length versus elapsed cycles. Average through-thickness crack lengths obtained from both compliance and photographic measurements are shown along with the mid-plane and free surface crack dimensions obtained from the photographs. Note here that the drop in  $K_{max}$  from 825 to 550 KPa-m<sup>1/2</sup> when the crack length was 11.6 mm, gave a small crack retardation region (marked by  $N_d$ ) followed by steady state crack growth at  $K_{max}$  of 550 KPa-m<sup>1/2</sup>. Although the compliance (through-thickness) crack length is not significantly affected by the reduction in the cyclic stress intensity value, it can be seen from Figure 4.1 that the free surface crack dimension exhibits more retardation than the mid-plane crack length. This crack tunnelling behavior, where the crack grows faster in the mid-plane than the free surface location, was also observed in PC specimens subjected to tensile overloads [44]. For the present experiment, crack tunnelling continued well past the retardation period.

#### **4.1.1 Interferometric Measurements:**

Figure 4.2 presents a set of interference fringe patterns photographed during the steady state crack growth at an average (compliance) crack length of 10.3 mm. Recall that each fringe represents a locus of points of constant crack face displacement. Figure 4.2(a) shows the crack plane under zero load and clearly indicates a residual crack opening displacement field. Note here that the fringe pattern occupies the central portion of the

crack plane and a part of the interior crack front. Thus, that particular section of the interior crack plane is opened under zero load, while the region near the free surface remains closed. As the applied load is increased, the 0-order (outer-most) light fringe reaches the free surface crack tip at a  $K/K_{\max}$  value of 0.3, where  $K_{\max}$  is the peak value of  $K$  during the steady state cycling. The load required for this outer-most light fringe to reach the crack tip is one measure of the load required for the crack surfaces to separate, and is defined here as  $K_{OI}$  (interferometric opening load). The  $K_{OI}/K_{\max}$  value measured at the free surface was 0.3, while this value is zero for the mid-plane location, where the crack surfaces are propped open at zero load.

Figure 4.3 shows the open crack perimeter as a function of applied load. Recall that in Figure 4.2 (a-d) each photograph showed the opened crack area for a particular applied load. Figure 4.3 is obtained by overlapping the opened areas of the crack for increasing applied load for a given crack size. For example, the area enclosed between the crack front and the boundary line of  $K / K_{\max}$  of 0.04 represents the opened section of the crack under an applied  $K$  of  $0.04K_{\max}$ . Similarly the area enclosed between the crack front and any other boundary line represents the opened section of the crack under the respective applied  $K$  value. Note here that under a small load, portions of the crack faces are closed at the crack front and along the starter notch. Further applied load eventually separates the crack front at the free surfaces.

Crack opening displacements are examined in more detail by digitized measurements of the interference fringe patterns from Figure 4.2. One

means for presenting the crack opening profile is to plot the fringe order as a function of distance from the crack tip for different applied loads, as seen in Figure 4.4 and 4.5, giving the crack surface separation as a function of position. The displacements are expressed here in fringe order units, although other dimensions may be obtained from Equation 2.2 for light fringes. Two displacement profiles were obtained for each load sequence; one measured at the specimen's mid-plane, and another crack opening profile obtained at the free surface. In these crack opening profiles, the physical (original) crack tip serves as the plot origin.

Figure 4.4 presents the crack opening profiles measured at the specimen's mid-plane (interior) for an average crack size of 10.3 mm. Since it was difficult to determine the fringe number near the mid-plane crack tip due to close fringe spacing, as seen from Figure 4.2, the fringe order near this mid-plane crack tip was established by counting the fringe number from the specimen's free surface location. Each curve in Figure 4.4 represents a different applied load, and gives the total separation ( $2V$ ) between the two crack surfaces as a function of distance from the crack tip. The load which causes the curve to pass through the origin, giving complete crack tip separation, is referred to here as the interferometric opening load ( $K_{OI}$ ) for the particular crack location. In Figure 4.4, the crack tip in the specimen's interior is separated under zero applied load. Figure 4.5 shows the corresponding crack opening profiles measured at the specimen's free surface. Note here that crack surfaces are closed at the free surface until the applied  $K$  equals  $271 \text{ KPa-m}^{1/2}$  (ie:  $K_{OI} / K_{\max} = 0.3$ ). Crack mouth opening displacement for an applied  $K$  value of  $271 \text{ KPa-m}^{1/2}$ , obtained from

a clip gage mounted at the crack mouth is shown in Figure 4.5. The presence of the starter notch and rough precracking surfaces prevented the measurement of crack mouth opening via optical interference. In addition, elastic crack mouth separation computed from a finite element analysis 50 with both plane stress and plane strain assumptions are presented in Figure 4.5 along with the clip gage reading. Here the measurements obtained from the clip gage and finite element analysis are converted to fringe order units.

Note from Figure 4.4 that the crack surface separation is a maximum at a certain distance from the crack tip. This maximum crack surface separation location moves further away from the crack tip for increasing load as seen from Figure 4.4. Under a sufficiently high load, this 'bump', where the crack surface separation is a maximum, moves to the crack mouth. Thus under a large load, the crack surface separation only increases as one moves further away from the crack tip. Some possible factors contributing to the fact that crack separation does not attain its maximum value at the crack mouth under 'low' loads, may be the high closure stresses present at the precracking region and the effect of free surface closure on the mid-plane opening behavior. Figure 4.5 shows that unlike the crack opening profile at the mid-plane, crack surface separation reaches a maximum at the crack mouth. Furthermore, the magnitude of crack separation is much smaller for the free surface location than that measured at the mid-plane region. This difference in crack opening is presumably due to the larger plastic zone at the specimen's free surface.

Figure 4.6 presents the interferometric crack tip opening load determined at different locations through the specimen thickness for an

average (compliance) crack length of 10.3 mm. Here  $K_{OI}$  values are normalized with the maximum cyclic stress intensity ( $K_{max}$ ), and distances from the specimen's free surface are normalized with the specimen thickness (B). The abscissa origin represents the specimen's free surface location, while  $x/B = 0.5$  specifies the mid-plane (interior) location. Note from Figure 4.6 that the opening load decreases rapidly as one moves into the specimen thickness. Moreover about 70% of the specimen's thickness is open under zero load. One interpretation of Figure 4.6 may suggest that 30% of the specimen's thickness (15% from each free surface) serves as a transition region from plane stress to plane strain, while the remaining 70% is under nominally plane strain conditions.

Figure 4.7 presents the residual zero load mid-plane opening obtained from optical interference for increasing crack length. Note here that for a crack size of 10.3 mm the point of maximum opening (bump) is approximately 2 mm away from the mid-plane crack tip, and when the crack length reaches 19.1 mm, this bump lies 4.4 mm away from the local crack tip. As a result, an increase of 8.8 mm in crack size corresponds to an increase of 2.4 mm in the distance between the crack tip and the point of maximum opening. Thus this 'bump' where the crack surface separation is a maximum under zero load, moves in the direction of the advancing crack tip.

#### 4.1.2 CMOD and BFS Measurements:

As discussed earlier, CMOD and BFS measurements were also employed to determine the average (global) closure loads. For the CMOD gage measurement, a clip gage was mounted at the starter notch mouth and the signal from the gage was recorded as a function of applied load. Figure 4.8 shows the CMOD gage reading versus applied load for an average crack length of 16.8 mm. The left-most graph presents the load versus displacement curve obtained from the clip gage at the crack mouth during one cycle of loading (The right-hand curve is discussed later). Note that the displacement varies in a non-linear fashion up to a certain load, followed by larger linear region, and a slight non-linear region at the upper end of the load displacement record. As discussed earlier, the closure load may be determined from this data as the point where the load-displacement relation first becomes linear. The small non-linear region at the upper end of the load cycle may be due to large plastic deformation at the crack tip present at the high load levels of the cycle. Moreover, Figure 4.8 indicates that PMMA exhibits fairly large hysteresis. For the present study, the loading curve is used to determine the closure loads.

The closure load is determined here by an offset axis method, although there are various other techniques described in the literature to obtain this closure value. In this offset axis technique, one least squares line is calculated through the upper linear portion of the loading curve. The deviation of the actual displacement from the least squares line is plotted in an expanded scale (approximately 5X) in the right-half of Figure 4.8. The closure load is then determined as the point where the actual data deviates

from the least squares line, and is referred to here  $K_{OC}$ . Here  $K_{OC}$  is defined as the crack opening load obtained from the CMOD measurements, and from Figure 4.8, for an average crack size of 16.8 mm,  $K_{OC} / K_{max}$  equaled 0.34.

A similar procedure was used to obtain the crack closure load from the back face strain measurements as seen in Figure 4.9. Here the readings from a 1000 ohm strain gage mounted on the back face of the specimen were analyzed to determine a closure load. This measurement gave a  $K_{OE} / K_{max}$  value of 0.34, where  $K_{OE}$  is defined as the crack opening load determined from the BFS data.

Figure 4.10 compares the closure loads determined by interferometry, CMOD, and BFS measurements for increasing crack length. Here the crack opening loads increase slightly for increasing crack length up to a point before returning to a lower value for further crack extension. Note from Figure 4.10 that the interferometric free surface opening load is larger than the compliance (CMOD and BFS) opening load. Since interferometric measurements showed that the crack tip in the specimen interior was separated under zero load, the global closure loads obtained from the CMOD and BFS techniques should fall between zero and the interferometric free surface opening load.

#### **4.1.3 Sensitivity Analysis:**

The objective of this section is to describe the effects of specimen thickness, cyclic  $K_{max}$ , and stress ratio ( $R$ ) on the fatigue crack closure

behavior of through-thickness flaws in the PMMA specimens. Several experiments conducted in this test program are summarized in Table 4.1.

#### 4.1.3.1 Thickness Effect:

Five fatigue crack closure experiments were conducted to determine the effect of specimen thickness on crack opening behavior. The cyclic  $K_{max}$  for these tests was kept a constant at 600 KPa-m<sup>1/2</sup>, and the stress ratio (R) was kept at 0.1, while the specimen thickness ranged from 5 mm to 25 mm. As indicated in Table 4.1, the specimen thicknesses for tests PX-16, PX-13, PX-12, PX-11, and PX-10 were 5, 10, 13, 19, and 25 mm respectively. Recall that the PMMA specimens were cut from a single 25 mm thick sheet. The 19 mm thick test specimens were prepared by removing a 6 mm layer of material from one side of the 25 mm thick members. However, the thinner test specimens were prepared by removing an equal amount of material from both sides of the 25 mm thick sheet. As mentioned earlier, all specimens were annealed after machining to the prescribed thickness.

Figure 4.11 shows the crack tunnelling behavior for various thicknesses. Here the difference between the free surface and mid-plane crack lengths is plotted against the average (compliance) crack size. Note from Figure 4.11 that the amount of crack tunnelling remains relatively constant with respect to increasing crack size, but varies significantly with changing specimen thickness. For example, the difference between the free surface and the mid-plane crack dimensions for a 25 mm thick specimen under steady state cycling is about 4.5 mm, while for a 5 mm thick member the magnitude of

crack tunnelling is negligible.

Figure 4.12 compares the zero load optical interference fringe patterns for the 25 mm and 5 mm thick members. Note here that, although a major portion of both crack planes remain opened under zero load for both members, the crack tip in the mid-plane remains partially closed in the 5 mm thick specimen. Furthermore, the zero load fringe patterns for the 5 mm thick member are quite different from the 25 mm thick specimen. The fringes in the 25 mm thick member form an elliptical pattern in the middle portion of the crack plane indicating a large displacement gradient between the mid-plane and the free surface opening behavior, while for the 5 mm thick member, the fringe patterns are relatively straight across the crack plane indicating a more uniform through-thickness opening behavior. Furthermore, the 25 mm thick specimen clearly shows the closed portions of the crack plane near the free edges under zero load, while a major portion of the free surfaces for the 5 mm thick member remain open under zero load.

Figure 4.13 presents these zero load (residual) displacement fields quantitatively for various specimen thickness. Here the mid-plane displacement is plotted in terms of fringe order as a function of distance from the crack tip. Note in Figure 4.13 that the magnitude of the mid-plane opening decreases with a reduction in the specimen thickness. Furthermore, the zero load opening profile for the 5 mm member reflects the closed portion of the crack at the mid-plane location.

Figure 4.14 presents the interferometric opening load for different locations through the specimen thickness. Note from figure 4.14 that when the absolute distance ( $x$ ) from the free surface is considered, the width of the

transition region remains invariant with the specimen total thickness. For example, in figure 4.14, the transition region is confined to a strip approximately 2-3 mm from each free surface regardless of the specimen thickness. This width of the transition region is consistent with the fact that for a 5 mm thick specimen, portions of the mid-plane crack tip remained closed under zero load indicating that the entire specimen thickness served as the transition region for this thin member.

Figure 4.15 presents the interferometric free surface opening load as a function of the average (compliance) crack length for the various experiments discussed here. Note here that the opening loads do not differ significantly for the 25 mm and 19 mm thick members, however, these free surface opening values decrease with further reduction in the specimen thickness. This decrease in crack opening load for a 'thin' member is not consistent with the plasticity induced closure arguments. Since a major portion of a thin member is under plane stress conditions, the crack opening loads for these thin members should be higher than the thick specimens due to the presence of higher compressive residual stresses in the large plastic zones of the thin members. Since the experimental results showed that the crack opening load decreases with a sufficient decrease in specimen thickness, perhaps some other factors such as the crack surface roughness, which increases with a reduction in specimen thickness, plays an important role in the crack opening behavior of the thin members. However, this phenomenon where the crack opening load decreases with a reduction in specimen thickness is not clearly understood at the present time.

#### 4.1.3.2 Cyclic $K_{max}$ and Stress Ratio (R) Effect:

The objective of this section is to describe the effects of cyclic  $K_{max}$  and the stress ratio on the crack opening behavior. As shown in Table 4.1, the cyclic  $K_{max}$  for the 19 mm thick members PX-11, PX-02, PX-03, and PX-04 were 600, 660, 825, and 935 KPa-m<sup>1/2</sup>, and for the 25 mm thick members PX-15, PX-10, PX-05, PX-07, and PX-14 were 440, 600, 715, 715, and 770 KPa-m<sup>1/2</sup> respectively. Although the cyclic  $K_{max}$  levels for tests PX-05 and PX-07 were kept a constant at 715 KPa-m<sup>1/2</sup>, the R values for these tests were 0.1 and 0.3 respectively.

Figure 4.16 summarizes the interferometric free surface opening loads for the various experiments with 19 mm thick members, and Figure 4.17 presents the results for the 25 mm thick specimens. Note from these figures that the crack opening loads for the intermediate cyclic  $K_{max}$  experiments are somewhat higher than the experiments conducted under relatively 'low' or 'high'  $K_{max}$  levels. For example in Figure 4.17, the crack opening loads observed under steady state cycling  $K_{max}$  of 600 KPa-m<sup>1/2</sup> are higher than the experiments conducted under cyclic  $K_{max}$  of 440 and 770 KPa-m<sup>1/2</sup>. Although, it is expected that the crack opening loads should decrease with a reduction in the cyclic  $K_{max}$  level from plasticity arguments, another explanation is in order for the reduction in crack opening load at extremely high cyclic  $K_{max}$ . Perhaps the difference in the crack closure mechanisms with varying cyclic K ranges combined with the rough crack surfaces observed under high K levels, contribute to this crack opening behavior. For example, plasticity may dominate the crack opening behavior at 'low' and 'intermediate' cyclic  $K_{max}$  ranges, while crack surface roughness combined

with crack craze zone bundling have significant effect on the closure values under 'high' cyclic stress levels. The fact that the crack opening loads decreases with an increase in cyclic  $K_{max}$  level, is consistent with the results in the previous section, where the crack opening loads decrease with a sufficient decrease in specimen thickness due to the crack surface roughness arguments. Since the free surface crack separation load attained a maximum level for a specimen subjected to an intermediate cyclic  $K_{max}$ , the crack tunnelling magnitude under this  $K_{max}$  level is significantly higher than the specimens subjected to either 'high' or 'low' cyclic stress values as seen from Figure 4.18.

Figure 4.19 presents the interference opening load for various distances from the specimen's free surface for the 25 mm thick members. Note here that, although the free surface opening loads vary somewhat with the cyclic  $K_{max}$  levels, the width of the transition region (near the free surface) does not vary significantly with the  $K_{max}$ . For example, the closure phenomenon is confined to a region about 2-3 mm from the free edges.

Figures 4.20 and 4.21 compare the free surface opening loads with the opening values obtained from CMOD and BFS readings for tests PX-05 and PX-07 respectively. Recall that although, the cyclic  $K_{max}$  levels for these two experiments were set at 715 KPa-m<sup>1/2</sup>, the stress ratio (R) for these tests were kept a constant at 0.1 and 0.3 for the tests PX-05 and PX-07 respectively. Thus  $K_{min}$  for Test PX-05 was set at 72 KPa-m<sup>1/2</sup> while it equaled 215 KPa-m<sup>1/2</sup> for Test PX-07.

Note from figures 4.20 and 4.21 that, although the crack opening levels for these two experiments do not vary significantly, the crack opening loads

for Test PX-07 ( $R = 0.3$ ) are less than or near the cyclic  $K_{min}$ , so that the crack is almost always open during the baseline cycling. This fact is reflected in the observation that the  $R = 0.1$  crack growth rate ( $1.57 \times 10^{-4}$  mm/cycle) was less than the  $R = 0.3$  crack growth rate ( $1.94 \times 10^{-4}$  mm/cycle), although the baseline cyclic  $\Delta K$  for the  $R = 0.1$  test was higher ( $643 \text{ KPa}\cdot\text{m}^{1/2}$ ) than the  $R = 0.3$  experiment ( $\Delta K = 500 \text{ KPa}\cdot\text{m}^{1/2}$ ). Thus the effective cyclic  $\Delta K$  for these two experiments were nearly equal in magnitude, (free surface  $\Delta K = 415 \text{ KPa}\cdot\text{m}^{1/2}$ ) although the nominal applied cyclic  $\Delta K$  for tests PX-5 and PX-7 were kept at 643 and  $500 \text{ KPa}\cdot\text{m}^{1/2}$  respectively.

#### 4.2 THROUGH-THICKNESS FLAWS IN PC:

The objective of this section is to describe the three-dimensional aspects of fatigue crack closure observed in the polycarbonate members. As before, the point-wise measure of crack opening load obtained via optical interferometry is compared with the bulk measurements from CMOD and BFS reading. A total of six through-thickness flaw experiments were conducted with the polycarbonate material as summarized in Table 4.2. Figure 4.22 compares the crack tunnelling behavior among the 25, 19, and 10 mm thick specimens. Note here that as with the through-thickness flaws in the PMMA members, the magnitude of crack tunnelling decreases rapidly with a reduction in specimen thickness.

Figure 4.23 shows the crack opening perimeter as a function of applied load. Again the area enclosed between the crack front and the boundary

line for  $K / K_{\max} = 0$  represents the initial (residual) opened section of the crack plane. Note in Figure 4.23 that unlike the PMMA experiments, both the free surface and mid-plane locations of this 25 mm thick PC member remain opened under zero load, however, an area of the crack perimeter in the interior of the specimen remained closed under zero load. The residual free surface opening may suggest that the closure phenomenon is confined to a region near each free surface, but not at the free surface in these thick PC test members. This crack opening behavior, where the crack opens last at a point interior to the free surfaces, was also observed in surface flaw experiments subjected to cyclic bending in reference [48]. Figure 4.24 shows the crack opening perimeter as a function of applied load for a 19 mm thick member. The crack opening perimeter for this 19 mm thick specimen follows the same pattern observed in the PMMA experiments, where the maximum closure occurred at the free surface locations.

Recall from above that the test member PC-3 was prepared by removing a 3 mm layer of material from both sides of a 25 mm thick sheet, while test pieces PC-2 and PC-5 were constructed by removing a 6 mm layer from one side of the 25 mm thick member. Although these specimens were cut differently, the crack opening profiles observed in these three tests were similar.

Figures 4.25 and 4.26 present the digitized crack opening profiles obtained at the mid-plane and free surface locations respectively for a 19 mm thick member. Here the magnitude of crack opening in the specimen's interior is significantly larger than the free surface opening, consistent with the PMMA experiments described earlier. This difference in crack opening

between the free surface and the mid-plane is presumably due to the variation of plasticity present along the crack perimeter. Figures 4.27 and 4.28 show the crack opening behavior for a 25 mm thick member recorded at the mid-plane and near-free surface locations respectively. Recall that in the 25 mm thick members, the free surface remained open under zero load. Figure 4.28 shows the crack opening behavior at a depth  $x/B = 0.08$ , where  $x$  is the distance from the free surface, and  $B$  is the specimen thickness.

Figures 4.29 and 4.30 present the interferometric crack tip opening load as a function of distance from the free surface for the 25 mm and 19 mm thick specimens. Here the distance from the free surface ( $x$ ) is normalized with the specimen thickness ( $B$ ) and the opening load is normalized with the cyclic maximum load. Note in these figures that as before, the crack tip separation load decreases rapidly as one moves into the specimen thickness.

Figure 4.31 compares the interferometric free surface opening loads with the bulk measurements obtained from the CMOD and BFS reading. Recall that the bulk opening loads from the CMOD and BFS reading are determined as the point where the load-displacement curve first become linear during the initial opening phase of a load cycle. Note from figure 4.31 that these bulk measurements are again generally lower than the interferometric free surface opening load, although the difference between these loads are considerably less than the results obtained from the PMMA experiments, where the bulk opening loads were found to be significantly less than the free surface opening load.

Figure 4.32 compares the zero load mid-plane opening profile for three different specimen thicknesses. Note here that the magnitude of the residual

crack surface separation again decreases with a reduction in specimen thickness, consistent with the behavior exhibited with the PMMA through-flaw experiments.

Figure 4.33 presents the interferometric free surface opening loads for the various polycarbonate members reported here. Here the opening loads from the 25 and 19 mm specimens form a scatter band between 50 and 115 KPa-m<sup>1/2</sup>. The baseline cycling was at  $K_{max}$  of 330 KPa-m<sup>1/2</sup> with R equal to 0.1 for all cases.

#### **4.3 CORNER CRACKED HOLES:**

Table 4.3 presents the test matrix for the corner cracked hole experimental program. The cyclic maximum remote tensile stress for tests CTB-1 and CTB-4 was kept at 3150 KPa, and for tests CTB-3 and CTB-5 was at 4200 KPa. Following the tensile portion of the experiment, the maximum cyclic bending stress for tests CTB-1 and CTB-2 was maintained at 7360 KPa, and for tests CTB-3 and CTB-5 was kept at 5520 KPa. The stress ratio (R) for all tests was maintained at 0.1.

##### **4.3.1 Cyclic Tension Results:**

Optical interference was employed to obtain three-dimensional crack surface displacement profiles as a function of applied load. Figure 4.34 shows the fringe patterns obtained during steady state cycling for an increasing remote tensile stress when the crack dimensions  $a = 7.7$  mm and

$c = 4.6$  mm. Figure 4.34(a) shows the interference pattern at zero load, and indicates a residual opening displacement field. Recall that experiments conducted with through-flaws in both PMMA and PC edge cracked members showed a similar residual pattern under zero load. In Figure 4.34(a) the fringes in the middle portion of the crack plane indicate that particular section of the crack plane is open under zero load, while the crack surfaces at  $\phi = 0^\circ$  and  $90^\circ$  (the locations where the flaw intersects the free surface and the hole bore) remain closed. As the remote tensile load is increased, the 0-order light fringe reaches the  $0^\circ$  and  $90^\circ$  locations at a stress level of 331 KPa. Although the a and c crack locations open at the same remote stress level, the stress intensity value (K) at these two points are different. Here the stress intensity factor for a particular location is computed from the Newman and Raju solution [57] employing the nominally applied remote tensile stress.

Figure 4.35 shows the opened crack perimeter as a function of applied remote tensile stress. Recall that Figure 4.35 is obtained by overlapping the opened areas of the crack for increasing load for a particular crack geometry. Thus the area enclosed between the original crack front and the boundary line for a particular stress  $\sigma$  represents the opened section of the crack plane under the respective applied remote stress. Note here that the crack front first starts to open along the middle portion of the corner flaw, and then progresses outward to the hole and the free surface locations.

The fact that a larger load was required to open the crack faces at the free surfaces than at interior locations, was also observed for the through-crack experiments reported in earlier sections. Those experiments indicated

that the crack opens first at the specimen's mid-plane followed by opening at the free surfaces at a significantly higher load. This difference in crack opening is presumably due to the variation in plastic zone size along the crack front, as conditions change from plane stress to plane strain.

Crack opening displacements were examined quantitatively by the digitized measurements of the interference fringe patterns of Figure 4.34. Here the displacements are presented in both fringe order ( $n$ ) and corresponding metric ( $\mu\text{m}$ ) units. Figure 4.36 presents the crack surface separation under a given remote stress ( $\sigma$ ) for varying parametric angle  $\phi$ . In this figure, the local original crack tip serves as the plot origin. Here the displacement profiles are obtained perpendicular to the local crack front at various points along the crack perimeter defined by the elliptic angle  $\phi$ . For example, the displacement curve for  $\phi = 30^\circ$  represents the crack face separation along a line perpendicular to the crack front at a point defined by the elliptic angle  $\phi = 30^\circ$ . Note from Figure 4.36 that the magnitude of the displacement field tends to increase as one moves away from either the specimen's free surface or the hole location. The displacement curves for  $\phi = 0^\circ$  and  $90^\circ$  in Figure 4.36 indicate that those portions of the corner flaw are closed under the applied remote tensile stress of 263 KPa.

Figure 4.37 presents the crack opening profile measured at the free surface ( $\phi = 0^\circ$ ). Each curve here represents a different applied remote stress, and gives the total crack separation ( $2V$ ) between the two crack surfaces as a function of distance from the original crack tip. Recall that, the stress which causes the displacement curve to pass through the origin, giving complete crack separation, is referred here as the interferometric

opening load for the particular crack location. In Figure 4.37 the crack tips separate completely at the specimen's free surface under an applied local  $K$  of  $67 \text{ KPa}\cdot\text{m}^{1/2}$ . Figure 4.38 presents the corresponding crack opening profile measured along the hole bore. The opening  $K$  value determined from Figure 4.38 equals  $71 \text{ KPa}\cdot\text{m}^{1/2}$ . Thus portions of the interior crack plane are opened under zero load, while the free surface and hole locations require opening loads of  $67$  and  $71 \text{ KPa}\cdot\text{m}^{1/2}$  respectively. It is important to note that the local  $K$  values are computed from the Newman and Raju solution [57], and these depend on  $\phi$  as well as load. Thus for a particular bending stress,  $K$  varies along the crack perimeter with the elliptic angle  $\phi$ .

Figure 4.39 presents the interferometric crack tip separation load determined at different parametric angles for test CTB-1. Here the opening loads are normalized with the cyclic maximum remote load. Note that the opening load decreases rapidly as one moves away from either the free surface or the hole location. This decrease in opening load with increasing distance from the free surfaces was also observed with the through-thickness flaw experiments reported earlier.

#### 4.3.2 Cyclic Bend Results:

Figure 4.40 presents a typical set of fringe pattern photographed during the opening phase of a bending load cycle. Figure 4.41 shows the corresponding crack opening perimeter as a function of applied remote bending stress. Note in Figure 4.41 that, unlike the opening behavior under remote tension, the free surface opens earlier than the hole bore location.

For example, the crack surfaces at  $\phi = 0^\circ$  separate under a remote bending stress of 862 KPa, while the crack surfaces along the hole bore require an applied stress of 1734 KPa to separate. This difference in opening loads is caused by the sharp stress gradient present along the hole direction.

Figure 4.42 presents the crack opening profiles for various parametric angles  $\phi$  under a given remote bending stress of 862 KPa. Note here that the displacement magnitude again increases as one moves away from either the free surface or hole locations. Recall that similar opening behavior was observed earlier for the remote tension phase of the experiment. Here the free surface displacement field at  $\phi = 0^\circ$  is significantly larger than the  $90^\circ$  profile due to the fact that, under a remote bending stress of 862 KPa, the  $K$  level experienced at the free surface location is significantly higher than the  $K$  value at the  $90^\circ$  crack tip location. For the crack dimensions under consideration, a remote bending stress of 862 KPa corresponds to  $K$  levels of 123 and  $42 \text{ KPa}\cdot\text{m}^{1/2}$  at the free surface and the hole bore locations respectively.

Figure 4.43 presents the crack opening profile for increasing remote bending stress at the free surface location ( $\phi = 0^\circ$ ). Note here that an applied bending stress of 862 KPa ( $K = 123 \text{ KPa}\cdot\text{m}^{1/2}$ ) is needed for the crack opening curve to pass through the origin (crack tip) in order to give complete crack tip separation. Similar crack opening profile plots obtained along the hole bore ( $\phi = 90^\circ$ ) are shown in Figure 4.44. A remote bending stress of 1734 KPa ( $K = 84 \text{ KPa}\cdot\text{m}^{1/2}$ ) is required here to open the crack tip completely along the hole bore.

Figure 4.45 presents the remote bending opening stress ( $\sigma_o$ ) as a function of parametric angle  $\phi$ . The opening stress is normalized here with respect to the maximum cyclic remote bending stress ( $\sigma_{max}$ ). Note in these figures that as the crack grows, the  $\sigma_o/\sigma_{max}$  value is reduced, and a larger portion of the crack front remains propped open under zero load. For example, the residual displacement field for a crack with  $a = 7.7$  and  $c = 4.6$  mm is smaller than the residual field for a crack with  $a = 7.7$  and  $c = 8.8$  mm.

#### 4.4 SURFACE FLAWS UNDER CYCLIC BENDING:

The objective of this section is to describe experiments directed at determining three-dimensional aspects of fatigue crack closure for a surface flaw in a rectangular plate subjected to pure bending. As before, optical interference technique is employed here with the transparent PMMA specimens to determine the point-wise measurement of fatigue crack closure. These point-wise measurements are then compared with an average (bulk) crack opening load obtained via CMOD gage measurements. The test matrix is shown in Table 4.4.

##### 4.4.1 Interferometric Measurements:

Figure 4.46 presents a set of interference fringe patterns photographed for increasing load for tests SB-2 with crack dimensions  $a = 5.8$  mm and  $2c = 13.5$  mm. Here  $\sigma$  is the maximum remote stress computed by the

standard flexural stress formula. The fringe pattern at zero load again indicates a residual crack opening displacement field.

Note from Figure 4.46 that under zero load, fringes are present in the middle portion of the surface flaw, indicating that section of the crack plane is open, while the free surface crack tip locations require a stress level of 2482 KPa to open. Thus the effective cyclic stress varies along the crack front. Figure 4.47 shows the opened crack perimeter as a function of applied remote stress. As before, Figure 4.47 is obtained by overlapping the opened areas of the crack from Figure 4.46 for increasing applied load.

Figures 4.48 and 4.49 present the crack opening profiles at various points along the crack front. Here the crack surface displacement is presented in fringe order units as a function of distance from the original crack tip. Figure 4.48 shows the displacement profiles along slices made at different parametric angles ( $\phi$ ) under an applied load of 20% of the maximum remote cyclic stress. These slices were oriented in the radial direction. For example, the curve for  $\phi = 17^\circ$  in Figures 4.48 and 4.49 represents the crack surface displacement profile along a radial line connecting the crack origin ( $X = Y = 0.0$  in Figure 2.5) and the point on the crack front where  $\phi$  equals  $17^\circ$ . Recall that for the corner cracked hole specimens, the crack surface displacements were measured perpendicular to the local crack front. Note in these figures that the crack surface displacements tend to increase as one moves away from the specimen's free edge ( $\phi = 0^\circ$ ). The displacement curve for  $\phi = 0^\circ$  indicates that the region near the crack tip is closed under an applied load of 20% of the maximum cyclic remote stress. Figure 4.49 shows the opening profiles for a load level

which is 28% of the maximum remote cyclic load, and indicates that the entire crack is opened under this stress level.

Figure 4.50 shows the interferometric crack separation load determined at different parametric angles for test SB-2. Here the local opening stress ( $\sigma_o$ ) is normalized with respect to the maximum cyclic stress ( $\sigma_{max}$ ). As observed earlier for through-thickness and corner flaw experiments, Figure 4.50 shows that the opening stress decreases rapidly as one moves away from the free surface location.

Figure 4.51 presents the free surface interferometric opening stresses (at  $\phi = 0^\circ$ ) obtained at various crack geometries for all tests reported here. Recall that the interior 'a' location was always opened under zero load, while the free surface required a significant portion of the load cycle to open at the tips. Thus an effective cyclic stress level can be computed at each point where the 'a' and 'c' dimensions are defined. The effective stress level at a given point is defined here as the difference between the maximum applied cyclic stress and the stress required for crack tip separation at the point under consideration.

Note in Figure 4.51 that the free surface opening loads for the intermediate cyclic  $\sigma_{max}$  experiments are somewhat higher than the opening loads observed under relatively 'low' or 'high' cyclic  $\sigma_{max}$ . For example, in Figure 4.51 the crack opening loads observed under cyclic  $\sigma_{max}$  of 8790 KPa are higher than the opening loads obtained from experiments conducted at 10,340 or 7240 KPa. Similar observations were made with the through-thickness flaw experiments where the crack opening loads for an intermediate cyclic  $K_{max}$  were higher than the opening loads recorded for

either 'low' or 'high' cyclic  $K_{max}$  experiments.

Figure 4.52 shows the fatigue crack growth rates  $da/dN$  and  $dc/dN$  plotted versus the corresponding nominal applied  $\Delta K$  for the five cyclic bend experiments reported here. Here the cyclic stress intensity factors are computed from the Newman and Raju solution [59] employing the nominally applied cyclic load. A least square fit through the through-thickness crack growth rate data ( $da/dN$  versus nominal applied  $\Delta K$ ) is also presented in Figure 4.52 for comparison purposes. Note here that the through crack growth behavior lies close to the surface flaw growth rates. Figure 4.53 plots the surface crack growth rates as a function of the effective  $\Delta K$  at the respective points 'a' and 'c'. Here the 'effective'  $\Delta K$  is computed with the 'closure corrected' cyclic load which results when the crack faces are always separated at the points of interest.

Note from Figure 4.52 that  $da/dN$  and  $dc/dN$  show a systematic variation when plotted against the nominal applied  $\Delta K$ . For example in Figure 4.52, a least square power law (Paris) fit through the  $da/dN$  versus applied  $\Delta K$  data shows significant deviation from a similar curve fit with the  $dc/dN$  quantities. However, when the closure corrected effective  $\Delta K$  value is used in place of the nominal applied  $\Delta K$ , as in Figure 4.53, the crack growth rates  $da/dN$  and  $dc/dN$  indicate little difference.

#### 4.4.2 CMOD Measurements:

As discussed earlier, CMOD readings were also obtained in addition to the interferometric measurements during the crack propagation period. The

bulk (average) crack opening loads were determined from the load-displacement curves obtained from a clip gage mounted at the crack mouth.

Figure 4.54 compares the crack opening loads obtained from CMOD readings with the interferometric free surface opening values. Here the opening loads are plotted versus the crack aspect ratios ( $a/c$ ) to observe the effect of surface flaw shape on the comparison between the local (free surface) and global (CMOD) opening values. The dotted lines represent the minimum and maximum cyclic stress limits. Recall that at the specimen's depth location the crack tip was open under zero load. Note from figure 4.54 that the interferometric free surface opening load generally lies above the bulk (average) measurements obtained at the crack mouth, although the difference between these two types of opening loads is not significant. Similar comparisons for through-thickness flaws in PMMA members using CMOD, BFS, and optical interference measurements showed that the global crack opening loads (from CMOD and BFS) were significantly lower than the interferometric free surface opening load. Thus the bulk crack opening load is lower than the free surface opening value for through-thickness flaws, while for surface flaws, these two quantities do not vary significantly.

For a through-thickness flaw, the entire crack front is equidistant from the CMOD measurement location; thus the global opening load obtained from the CMOD reflects an average of the mid-plane and free surface opening values. On the other hand for the surface flaw, the CMOD measurement location is closer to the free surface crack tip than for the maximum crack depth point. Thus the opening load determined from CMOD readings should be significantly influenced by the free surface crack

tip behavior, and may not reflect the true global (average) quantity for the entire surface flaw.

Table 4.1: Test matrix for the through-thickness flaw experiments with PMMA.

| TEST  | $K_{max}$ (KPa-m <sup>1/2</sup> ) | R   | Thickness (mm) |
|-------|-----------------------------------|-----|----------------|
| PX-16 | 600                               | 0.1 | 5              |
| PX-13 | 600                               | 0.1 | 10             |
| PX-12 | 600                               | 0.1 | 13             |
| PX-11 | 600                               | 0.1 | 19             |
| PX-10 | 600                               | 0.1 | 25             |
| PX-15 | 440                               | 0.1 | 25             |
| PX-14 | 770                               | 0.1 | 25             |
| PX-6  | 825-550                           | 0.1 | 25             |
| PX-8  | 825-550                           | 0.1 | 19             |
| PX-5  | 715                               | 0.1 | 25             |
| PX-4  | 935                               | 0.1 | 19             |
| PX-3  | 825                               | 0.1 | 19             |
| PX-2  | 660                               | 0.1 | 19             |
| PX-7  | 715                               | 0.3 | 25             |

Table 4.2: Test matrix for the Polycarbonate through-thickness flaw experiments.

| TEST | $K_{max}$ (KPa-m <sup>1/2</sup> ) | R   | Thickness (mm) |
|------|-----------------------------------|-----|----------------|
| PC-1 | 330                               | 0.1 | 25             |
| PC-7 | 330                               | 0.1 | 25             |
| PC-2 | 330                               | 0.1 | 19             |
| PC-5 | 330                               | 0.1 | 19             |
| PC-3 | 330                               | 0.1 | 19             |
| PC-6 | 330                               | 0.1 | 10             |

Table 4.3: Test matrix for the corner cracked hole experiments.

| TEST  | Tension<br>$\sigma_{\max}$<br>KPa | Bending<br>$\sigma_{\max}$<br>KPa | R   | Thickness (mm) |
|-------|-----------------------------------|-----------------------------------|-----|----------------|
| CTB-1 | 3150                              | 7360                              | 0.1 | 19             |
| CTB-2 | --                                | 7360                              | 0.1 | 19             |
| CTB-3 | 4200                              | 5520                              | 0.1 | 19             |
| CTB-4 | 3150                              | --                                | 0.1 | 19             |
| CTB-5 | 4200                              | 5520                              | 0.1 | 19             |

Table 4.4: Test matrix for the surface flawed plates.

| TEST | Bending<br>$\sigma_{max}$ KPa | R   | Thickness (mm) |
|------|-------------------------------|-----|----------------|
| SB-1 | 8790                          | 0.1 | 25             |
| SB-2 | 8790                          | 0.1 | 25             |
| SB-3 | 10,340                        | 0.1 | 25             |
| SB-6 | 10,340                        | 0.1 | 25             |
| SB-7 | 7240                          | 0.1 | 25             |

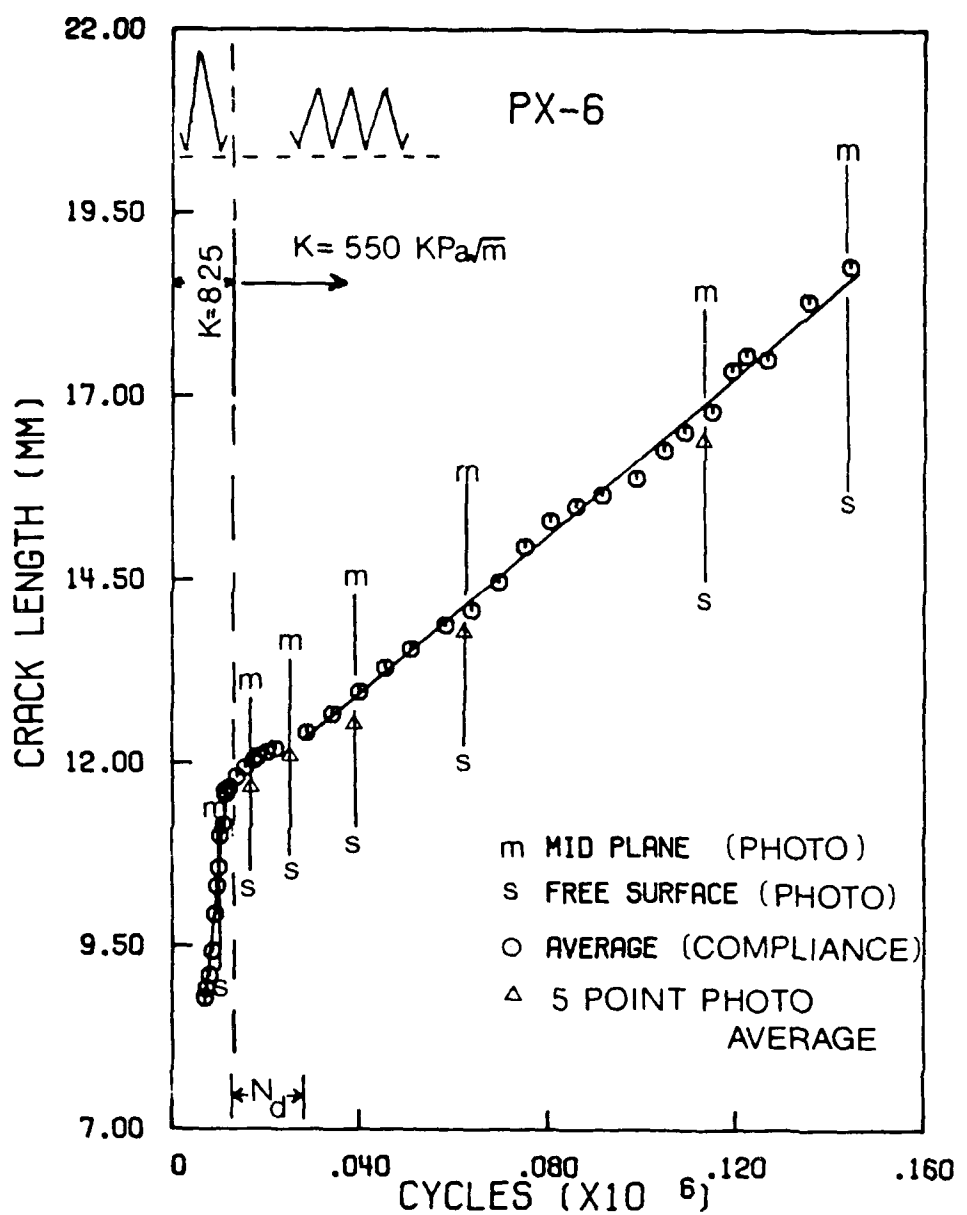
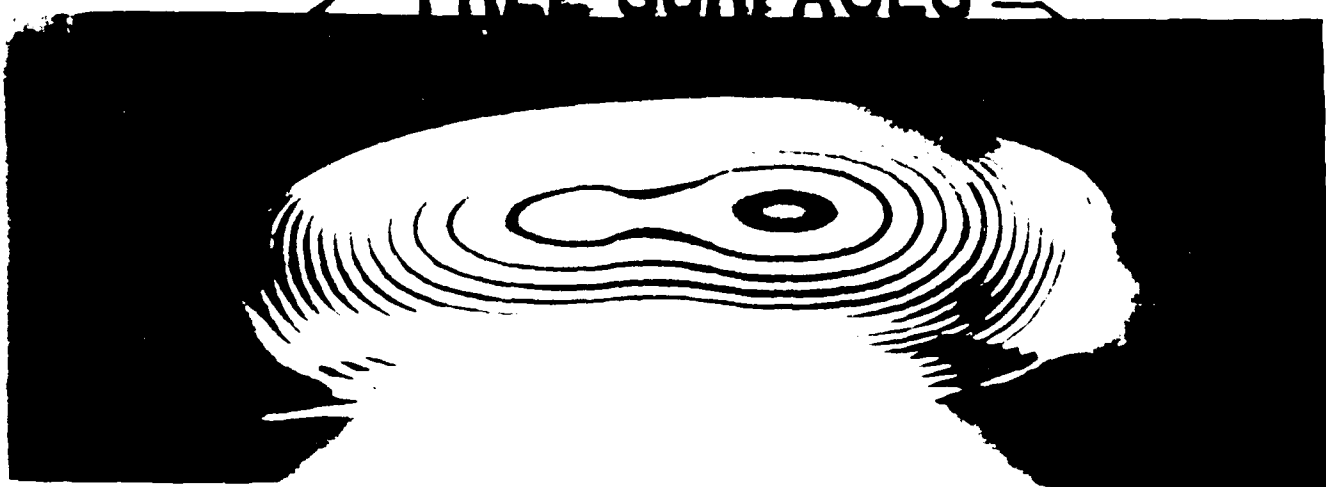
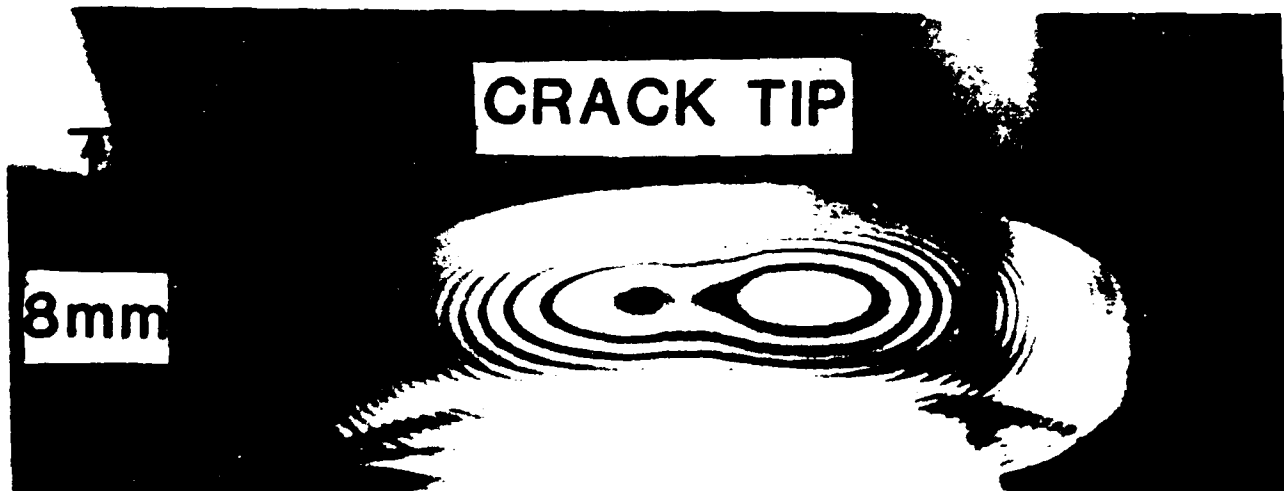


Figure 4.1: Crack length versus elapsed cycles response for test PX-6. Mid-plane and free surface crack lengths are also shown to characterize tunnelling phenomenon.

— FREE SURFACES —



(a)  $K/K_{\max} = 0$



(b)  $K/K_{\max} = 0.1$

$\longleftrightarrow B = 25 \text{ mm} \longrightarrow$

Figure 4.2: Interference fringe pattern obtained for various applied loads showing the three-dimensional crack opening profile of PMMA specimen subjected to constant cyclic  $K$  loading.



(c)

$$K/K_{\max} = 0.25$$



(d)

$$K/K_{\max} = 0.3$$

Figure 4.2: continued

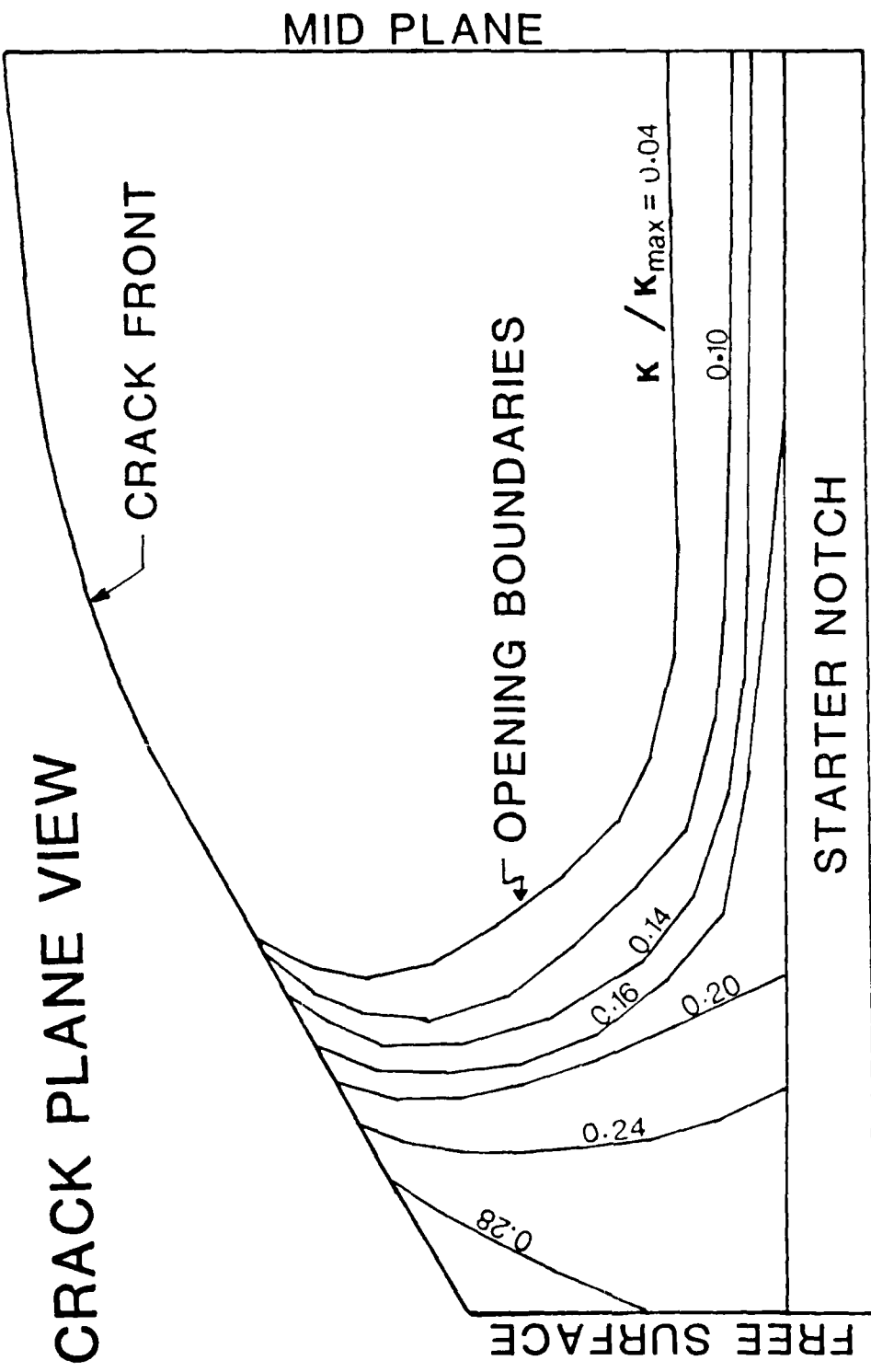


Figure 4.3: Crack opening parameters as a function of applied load, obtained by overlapping the zero order fringe pattern from Figure 4.2.

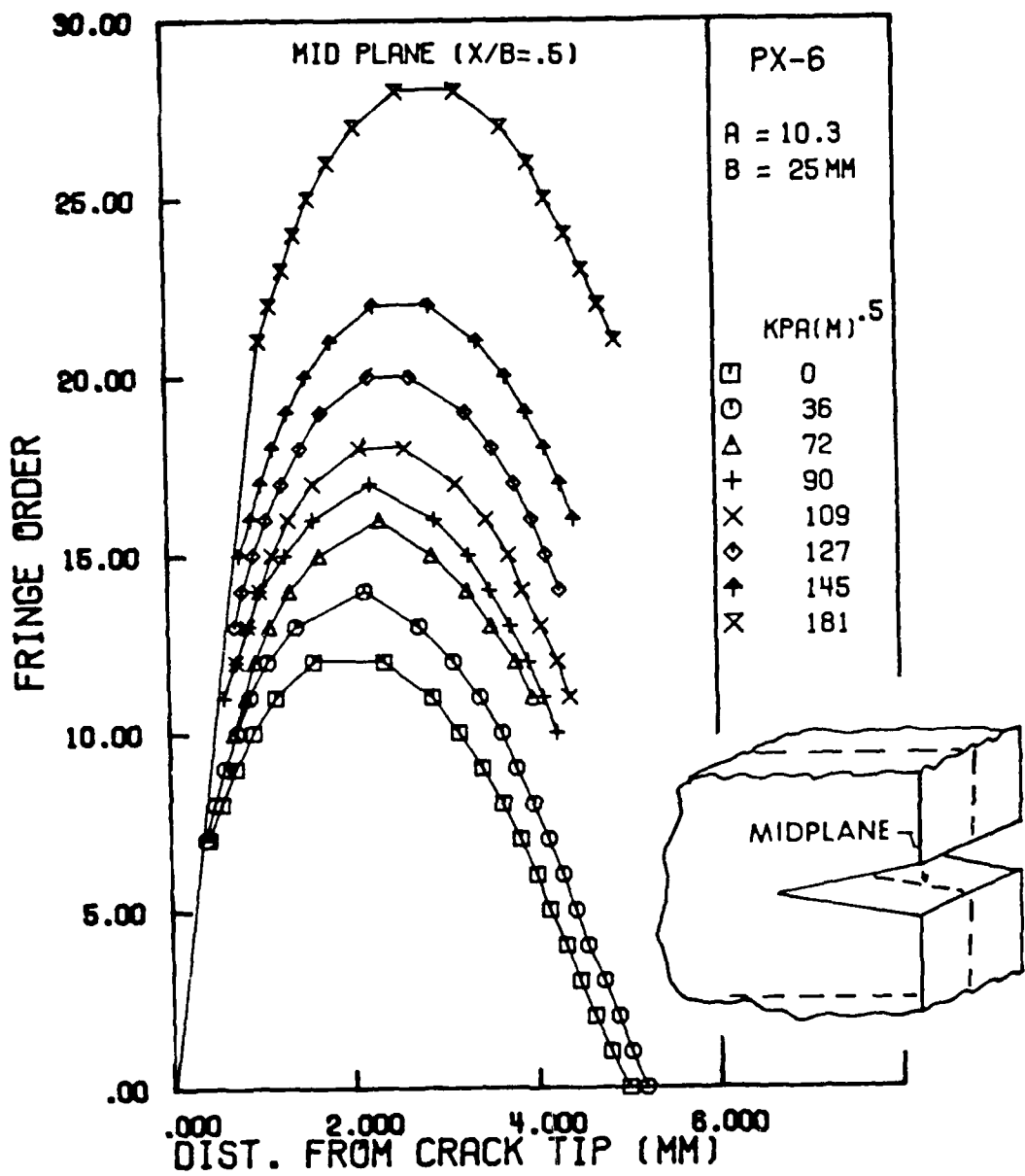


Figure 4.4: Mid-plane crack opening profile for increasing load. The crack opening displacement is expressed here in fringe order units.

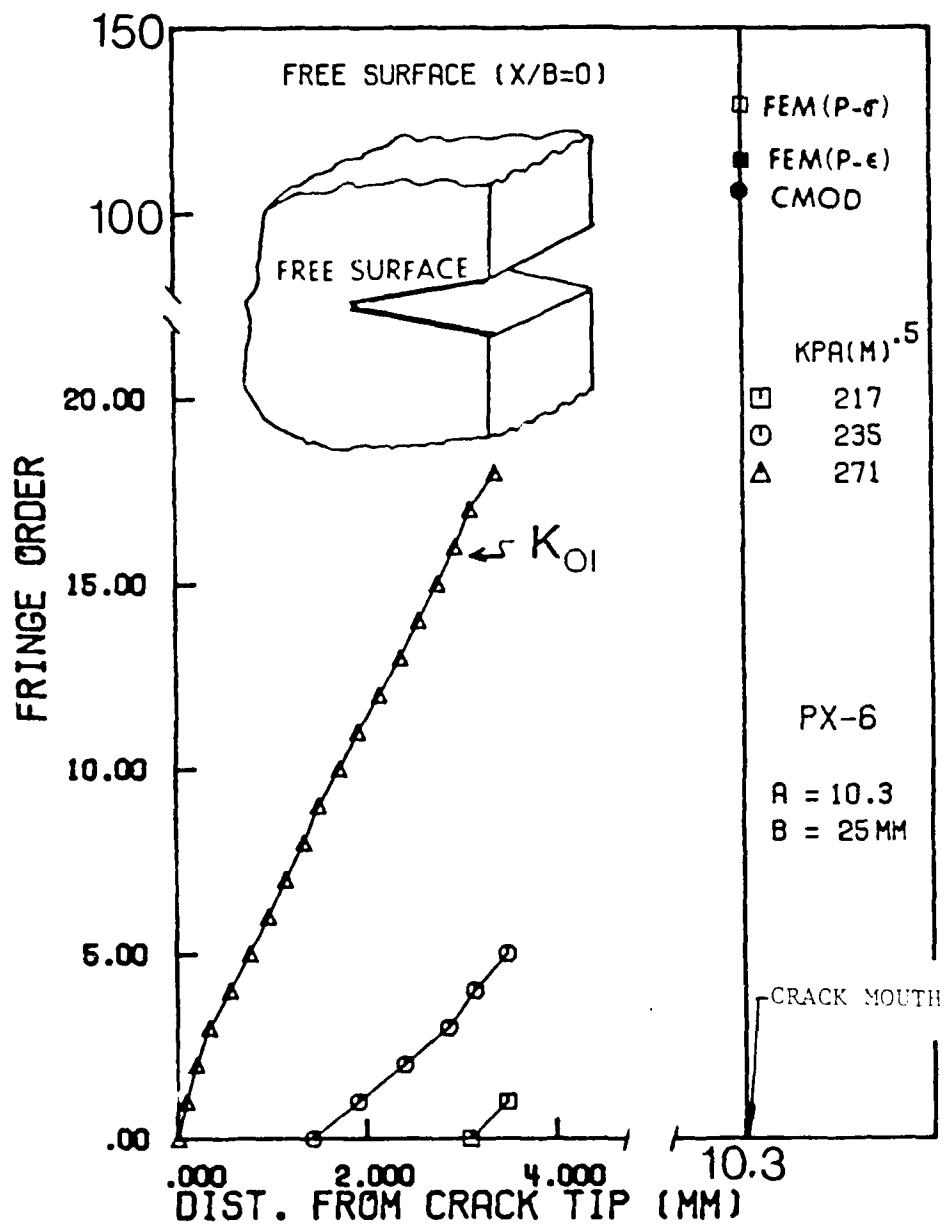


Figure 4.5: Free surface crack opening profiles for increasing load.  $K_{OI}$  represents the  $K$  value which causes complete crack separation at the free surface.

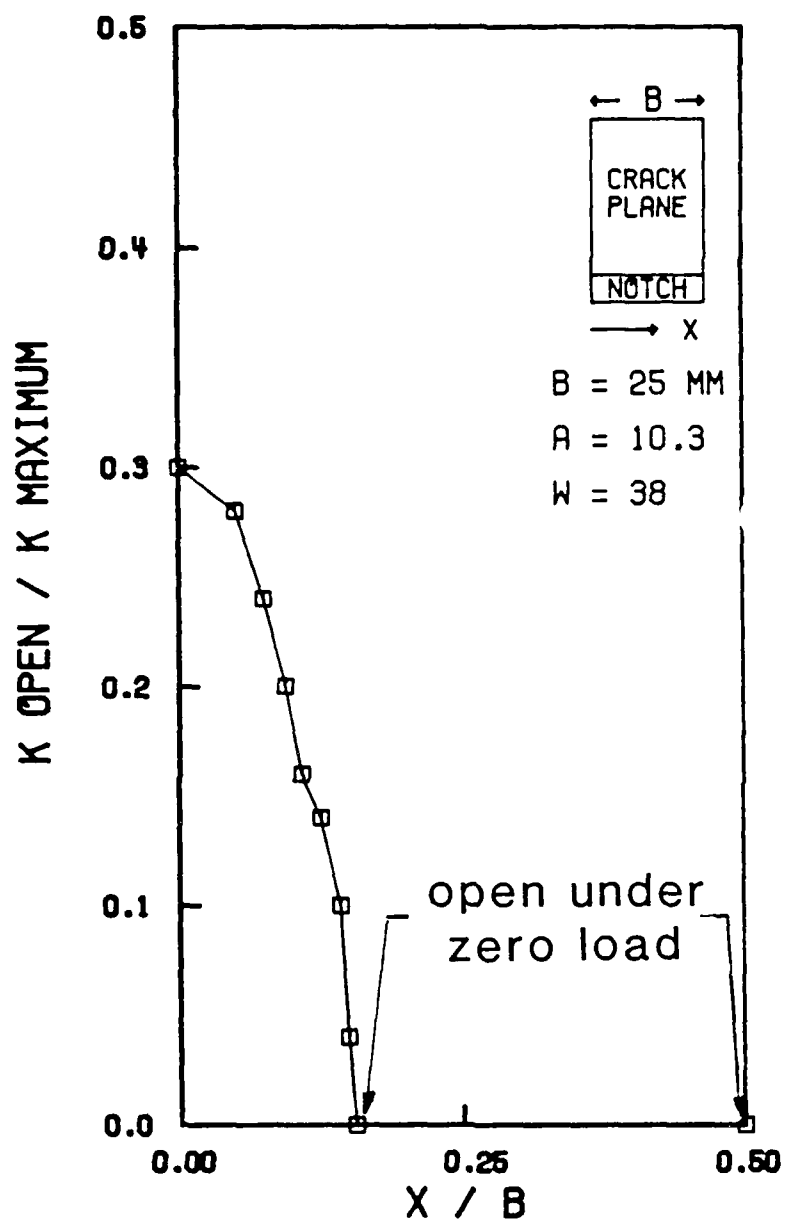


Figure 4.6: Interferometric crack tip opening load as a function of dimensionless distance from the free surface.

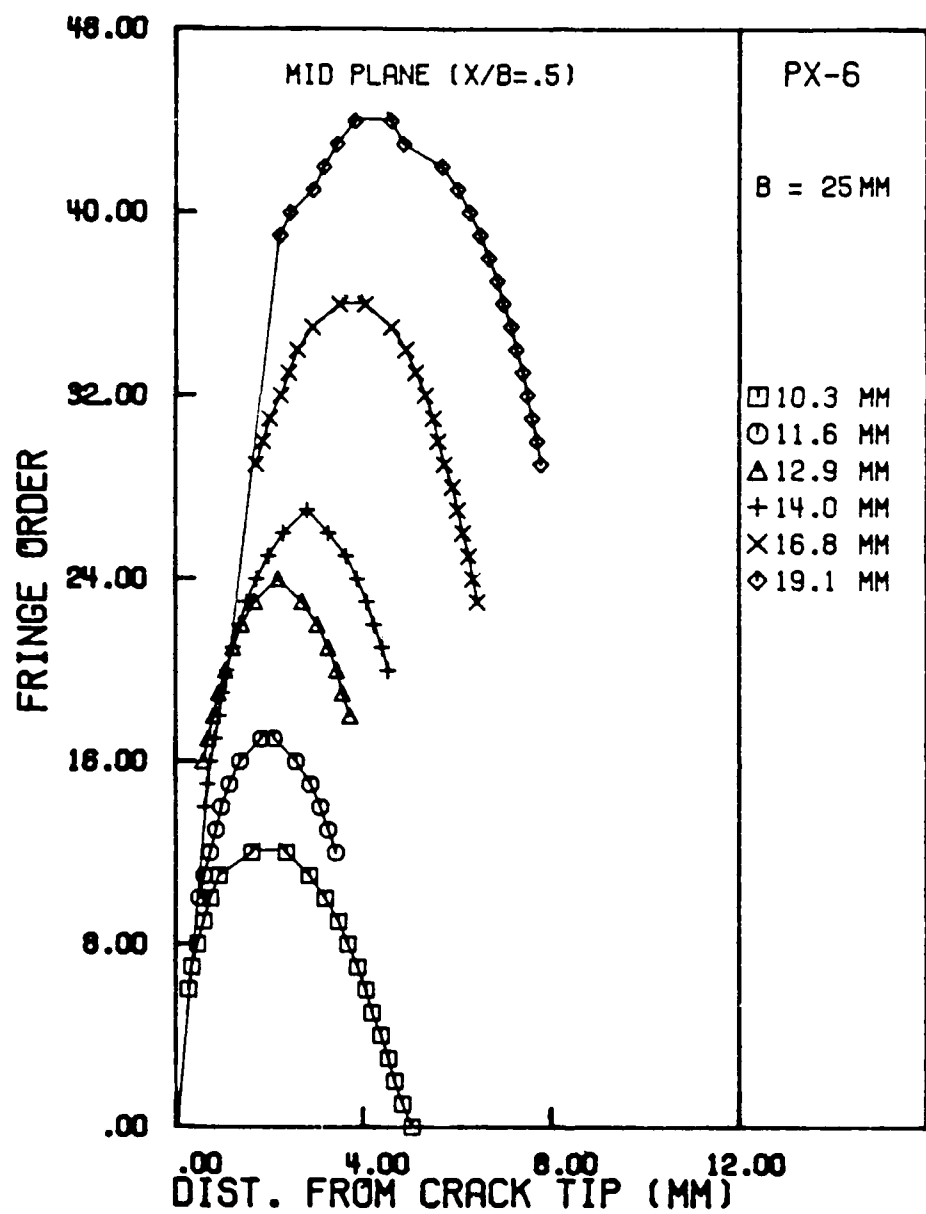


Figure 4.7: Interferometric zero load mid-plane opening profiles for various crack lengths.

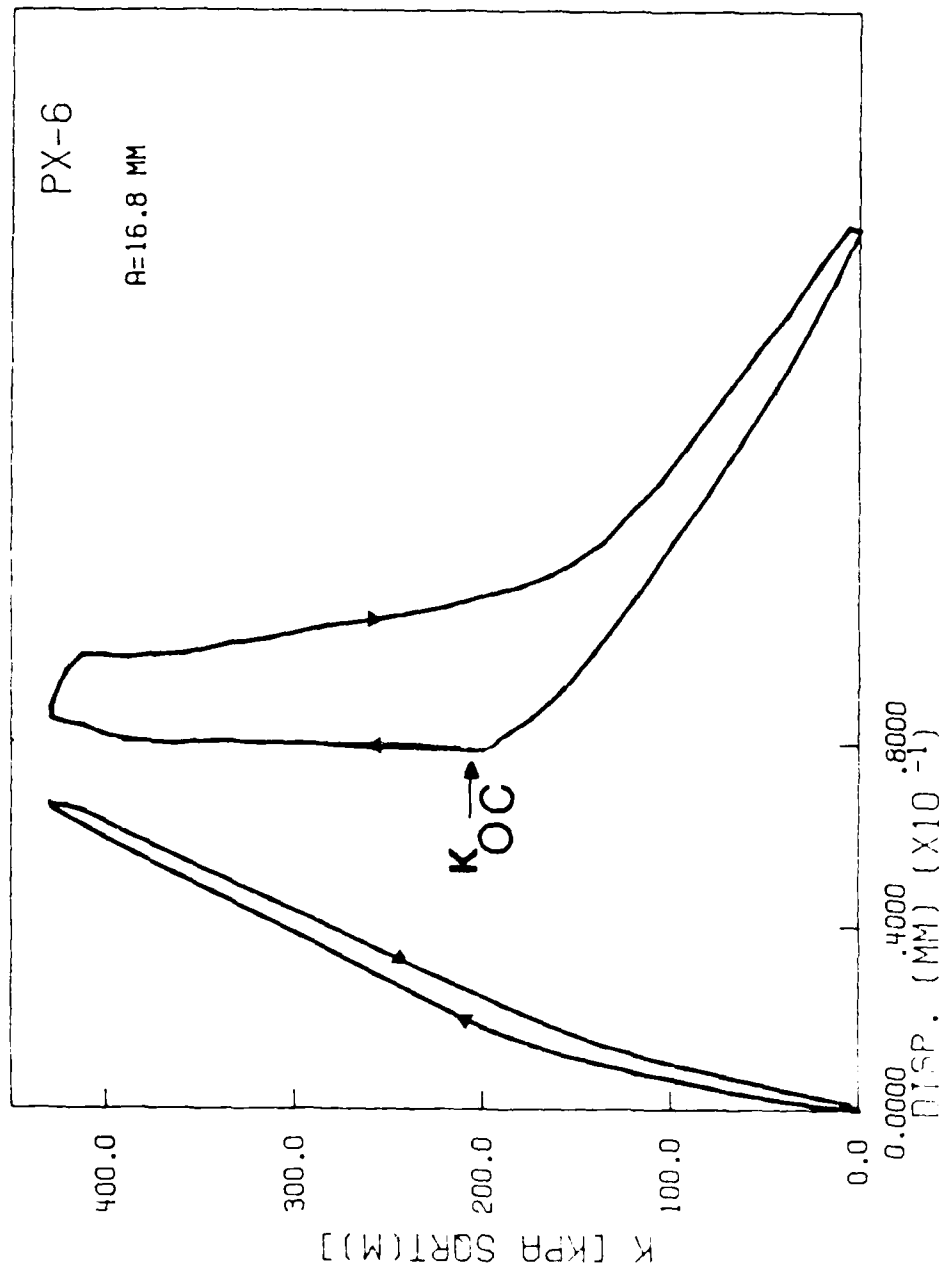


Figure 4.8: Load-displacement record obtained from a clip gage mounted across the crack mouth.  $K_{OC}$  refers to the load where the load-displacement becomes linear.

RD-R192 296

THREE-DIMENSIONAL ASPECTS OF FATIGUE CRACK CLOSURE(U)  
PURDUE UNIV LAFAYETTE IN SCHOOL OF AERONAUTICS AND  
ASTRONAUTICS A F GRANDT ET AL. FEB 88 AAE-88-1

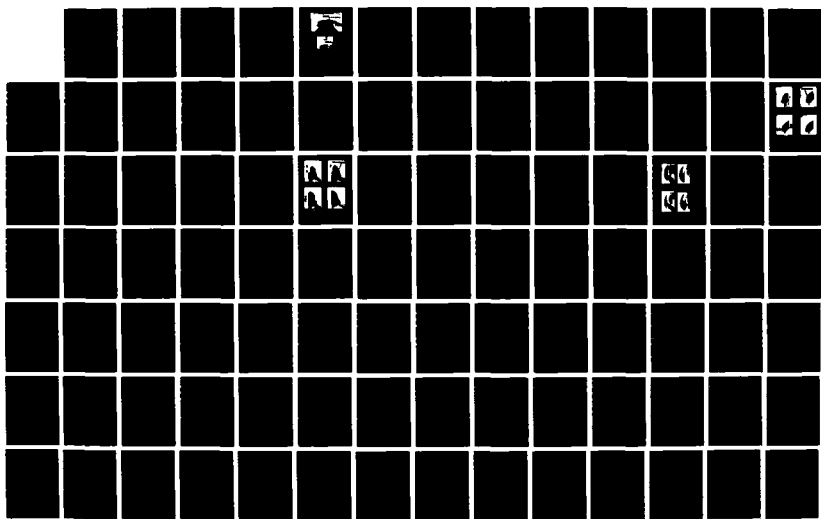
2/3

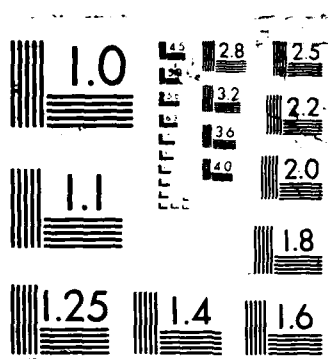
UNCLASSIFIED

AFOSR-TR-88-0266 AFOSR-85-0106

F/G 20/11

NL





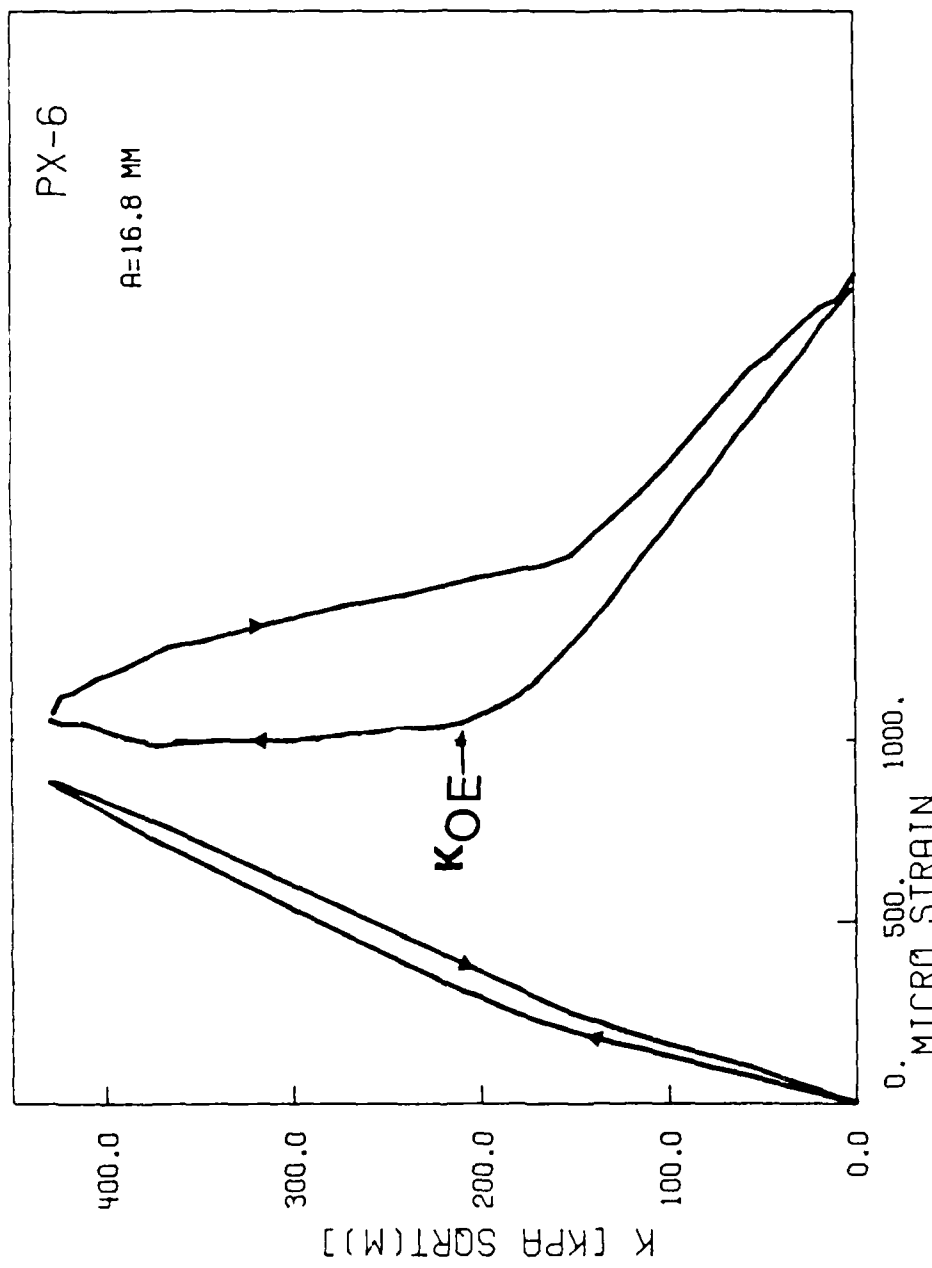


Figure 4.9: Load-strain record obtained from a strain gage mounted on the back face of the PMMA specimen.  $K_{OE}$  refers to the load where the crack opens in a linear manner.

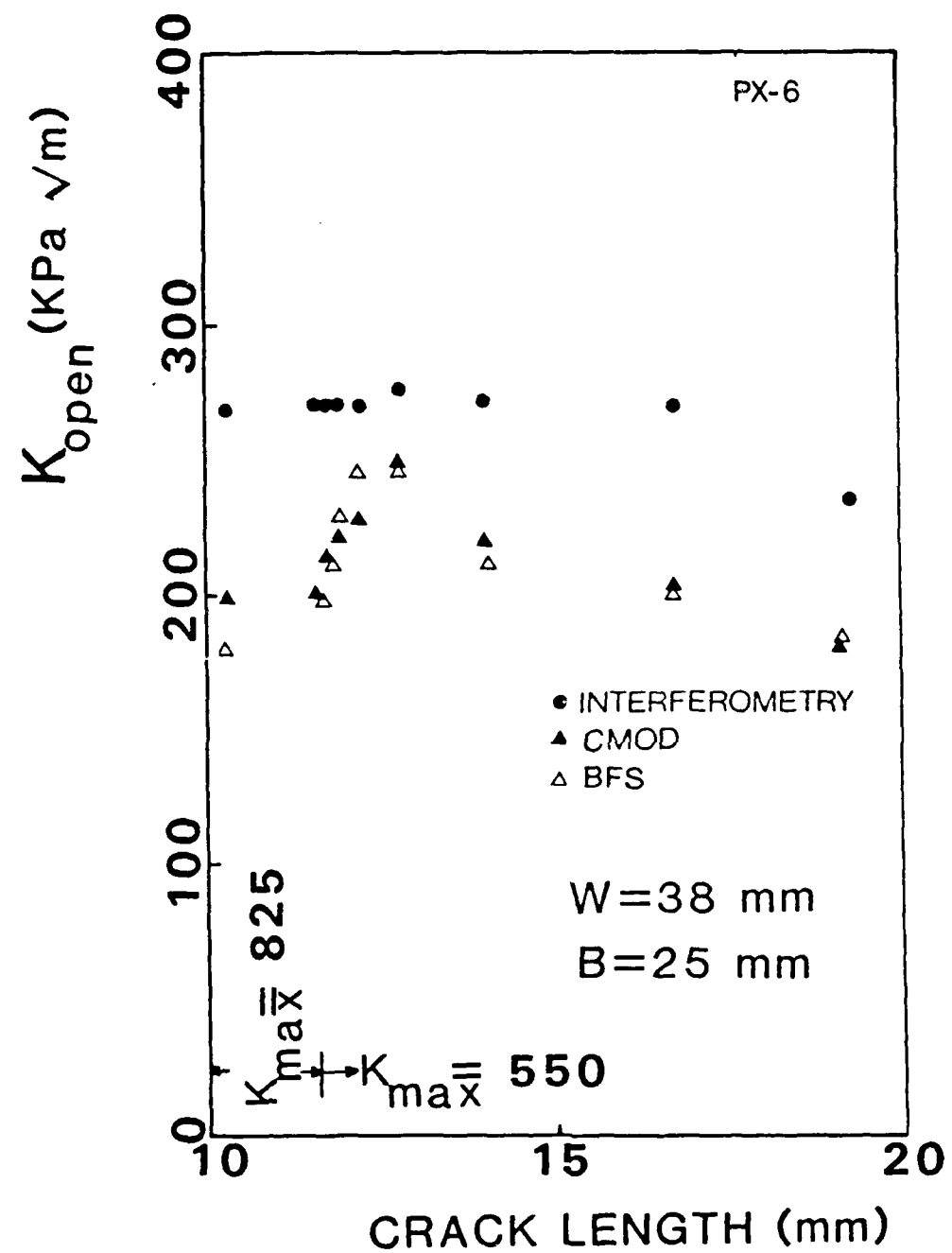


Figure 4.10: Comparison of crack opening loads obtained from interferometry, CMOD, and BFS measurements for various crack lengths.

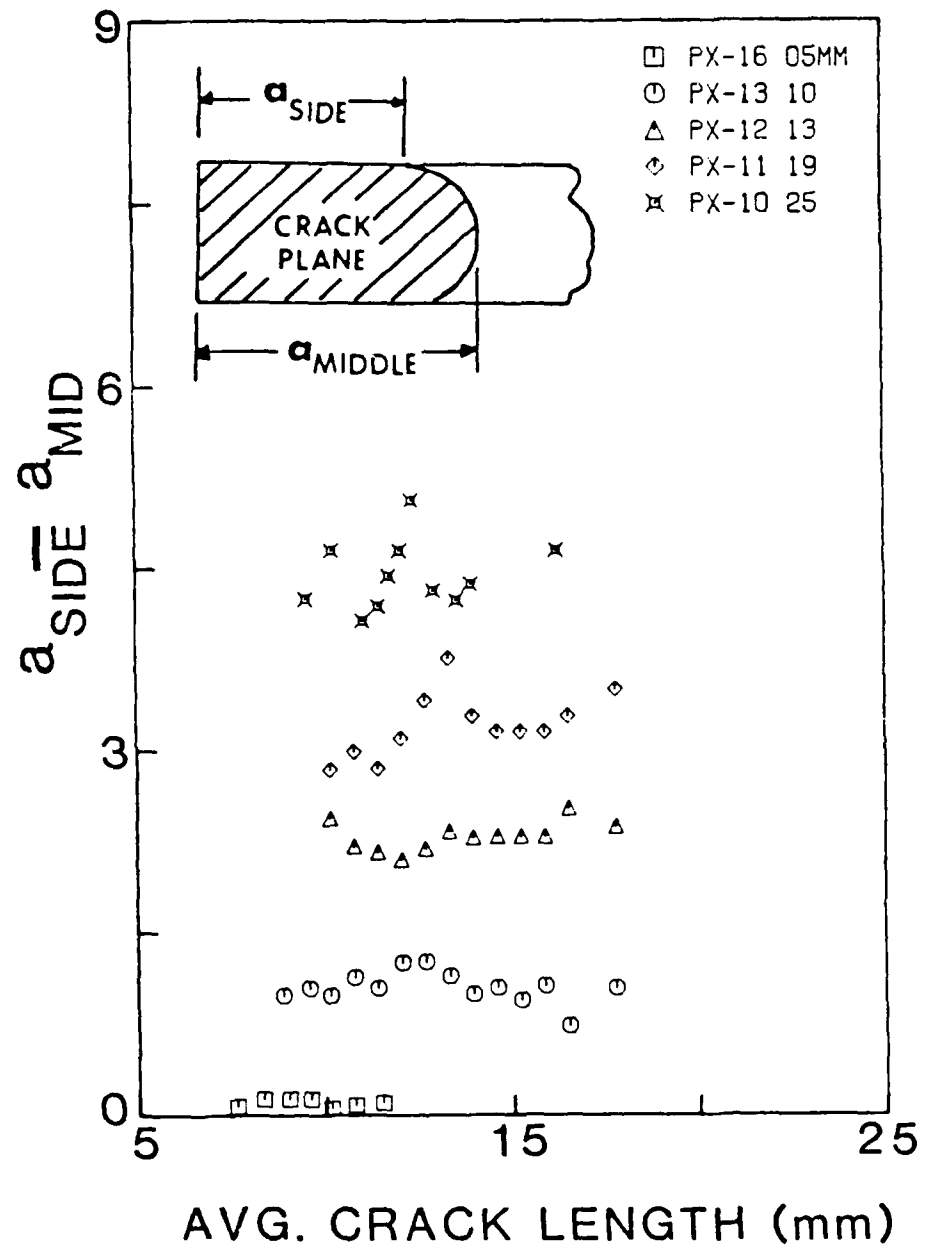
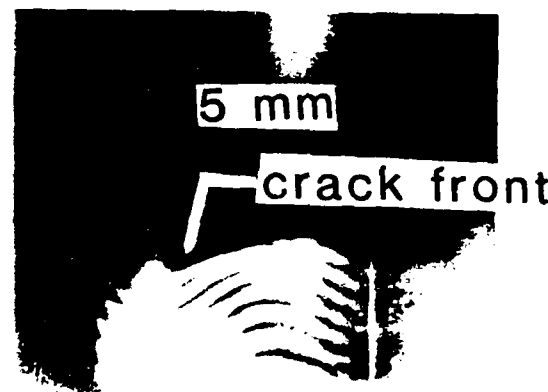
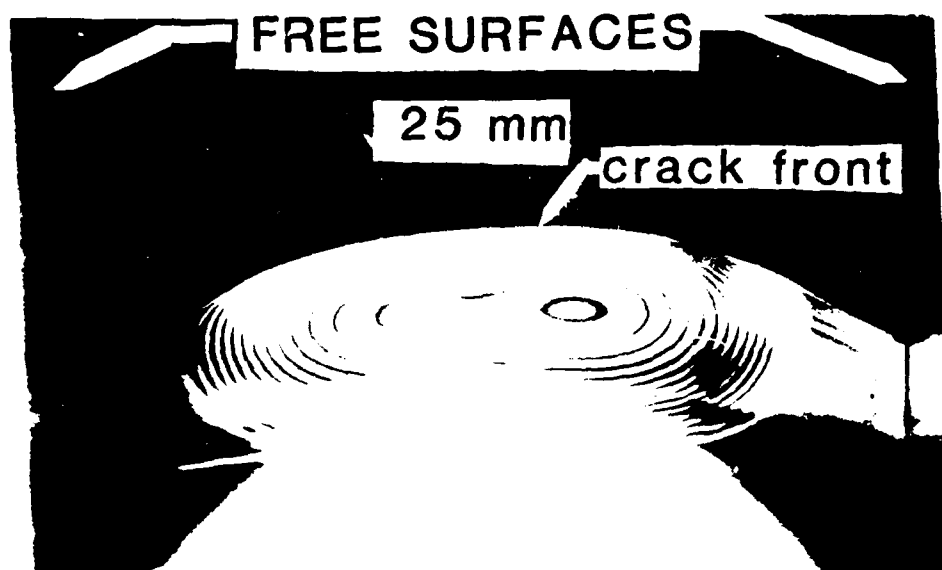


Figure 4.11: Comparison of the magnitude of crack tunnelling with changing specimen thickness.



### ZERO LOAD OPENING CRACK PLANE VIEW

Figure 4.12: Comparison of zero-load (residual) interference fringe photographs obtained for the 25 mm and 5 mm thick specimens.

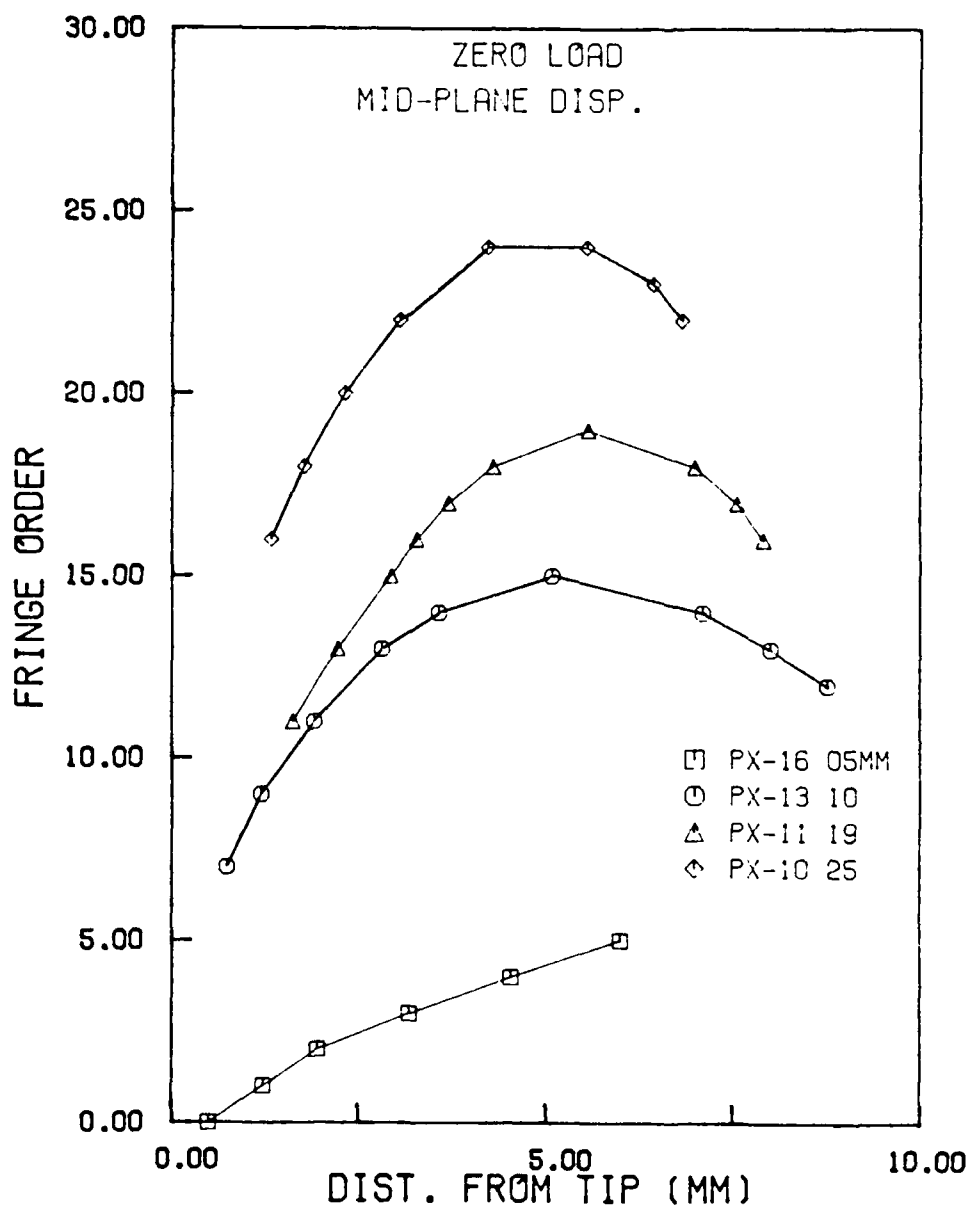


Figure 4.13: Comparison of zero load mid-plane opening profiles for varying specimen thickness.

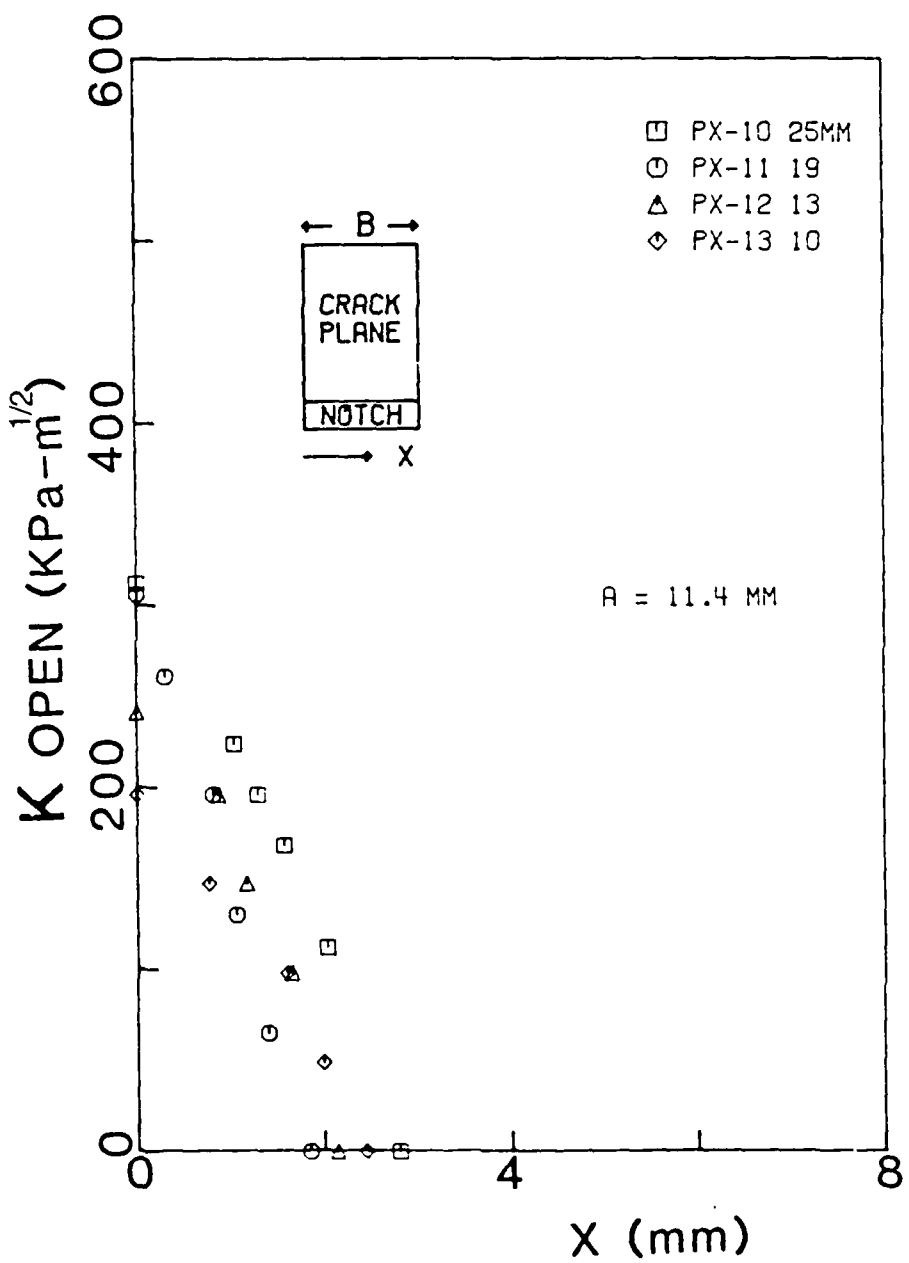


Figure 4.14: Interferometric opening load as a function of absolute distance  $x$  from the free surface for varying specimen thickness.

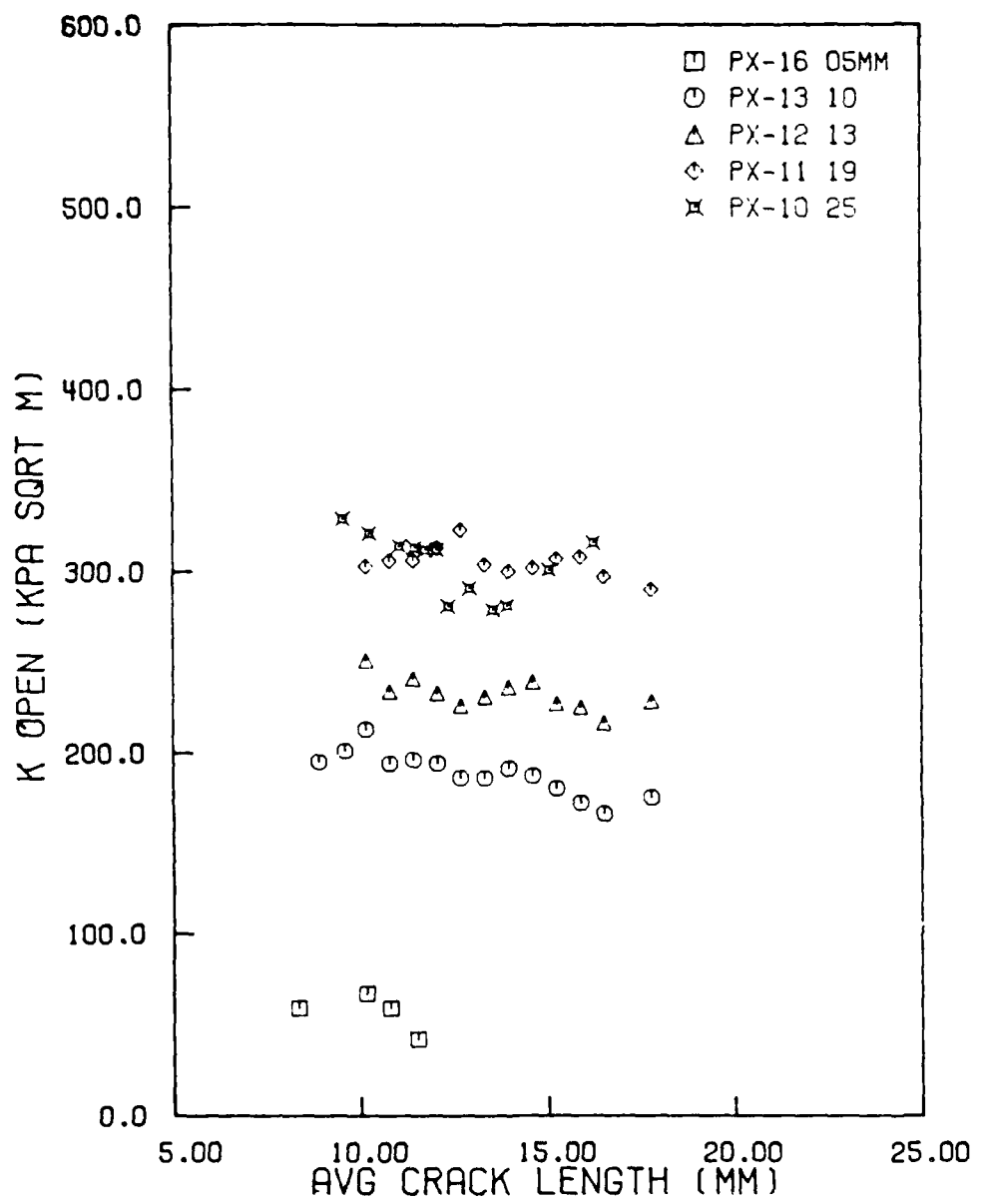


Figure 4.15: Interferometric free surface opening load as a function of crack length for varying specimen thickness.

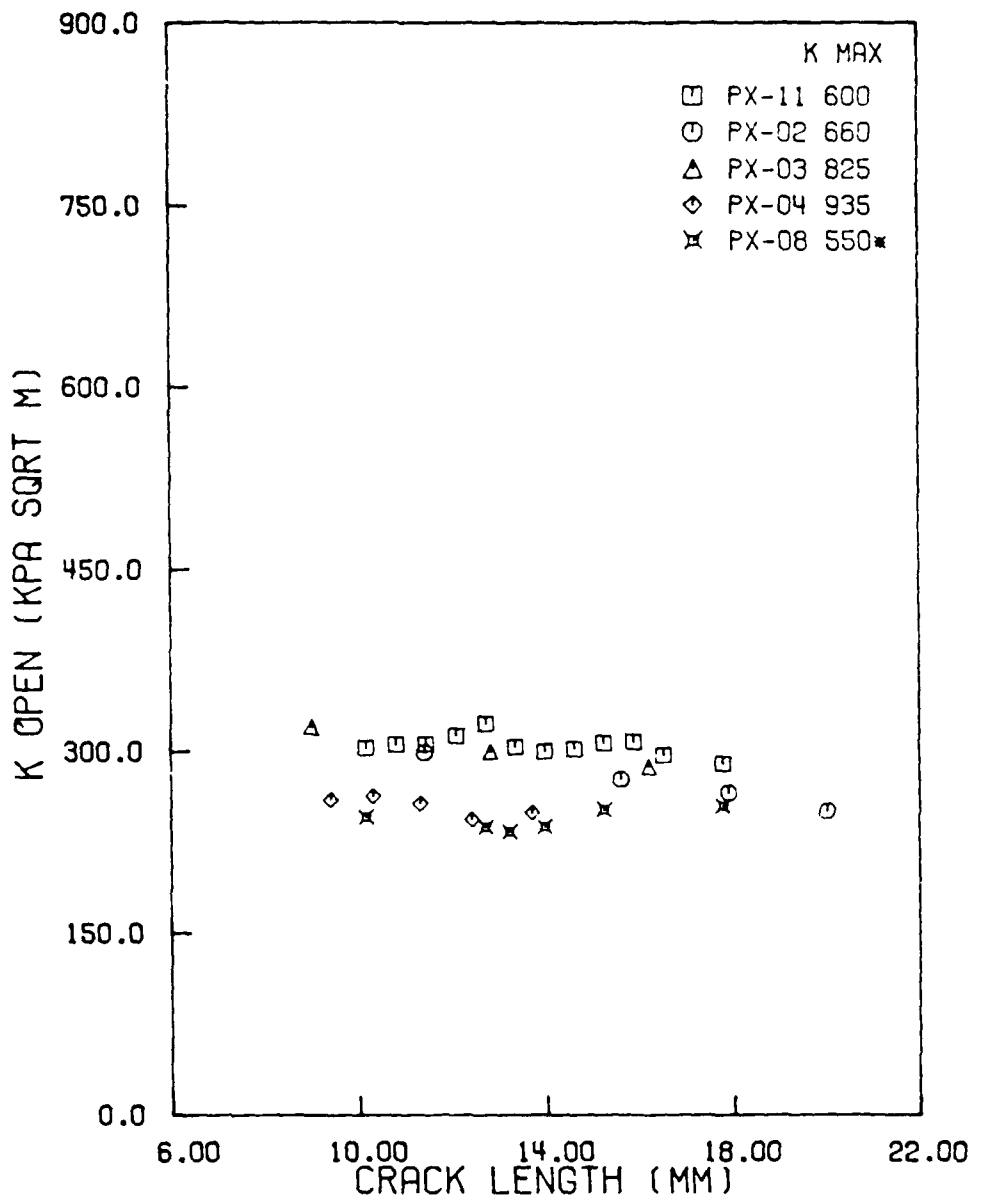


Figure 4.16: Interferometric free surface opening loads for 19 mm thick experiments with various cyclic  $K_{max}$  levels.

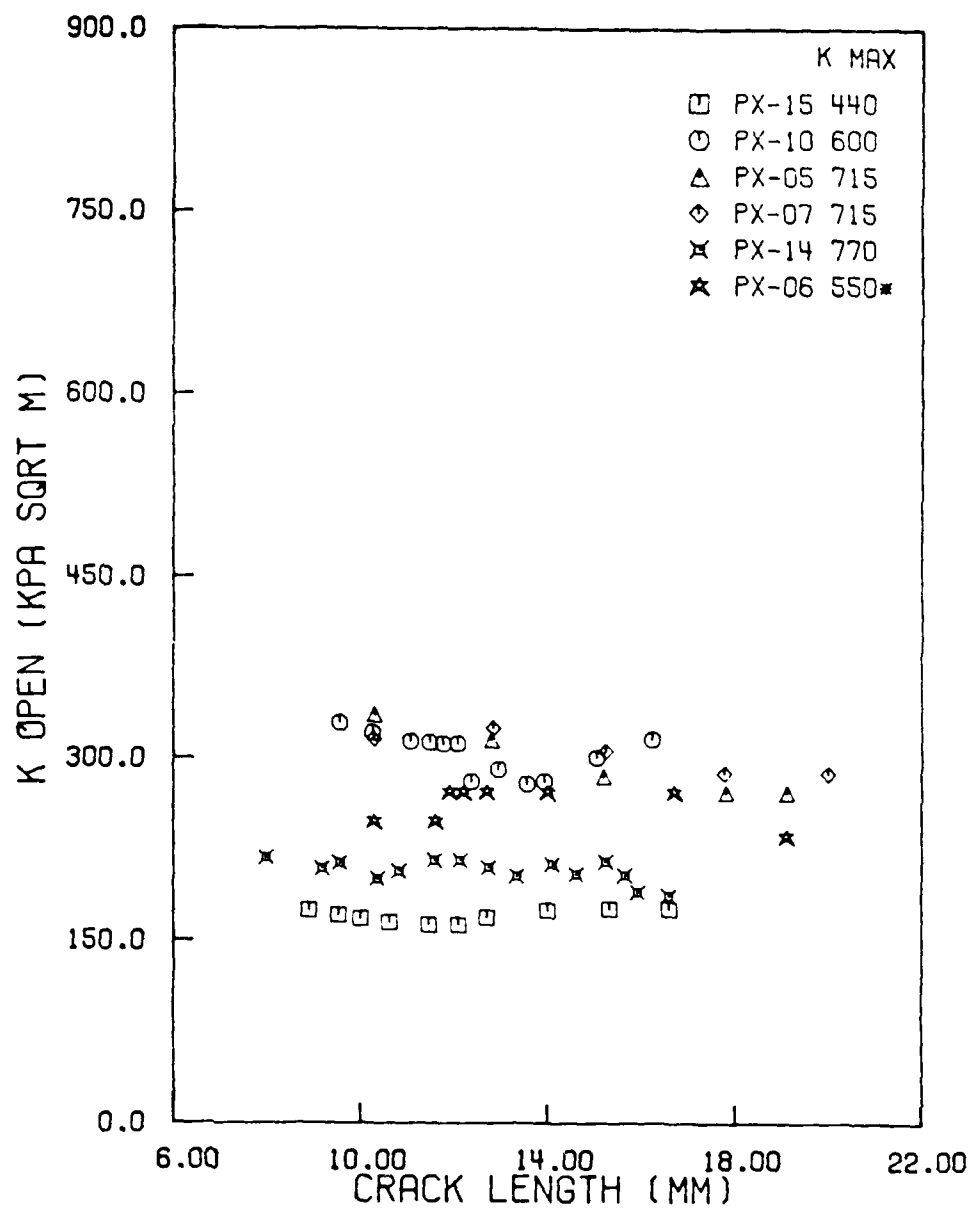


Figure 4.17: Interferometric free surface opening loads for 25 mm thick experiments with various cyclic  $K_{max}$  levels.

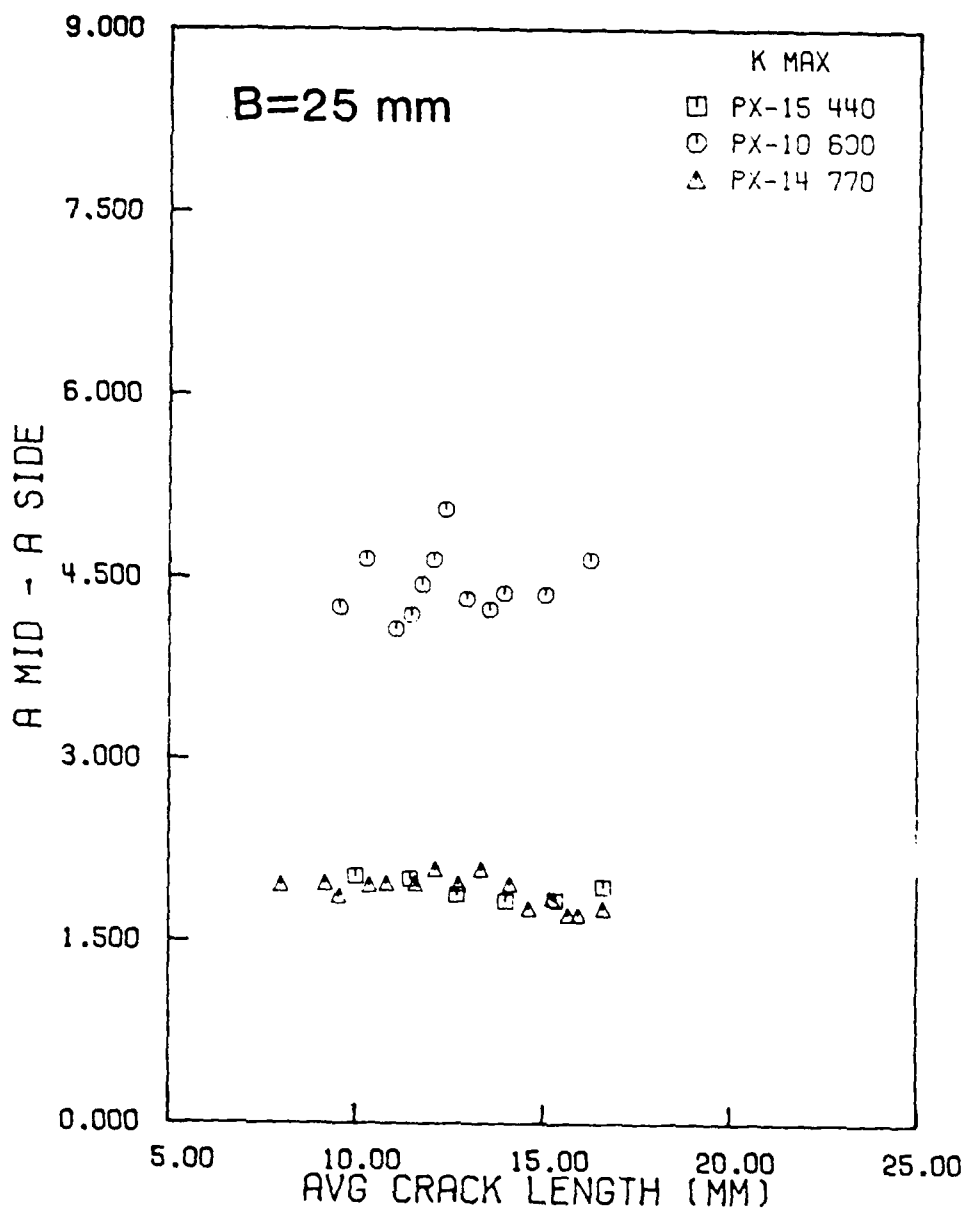


Figure 4.18: Comparison of crack tunnelling with varying cyclic  $K_{max}$  levels.

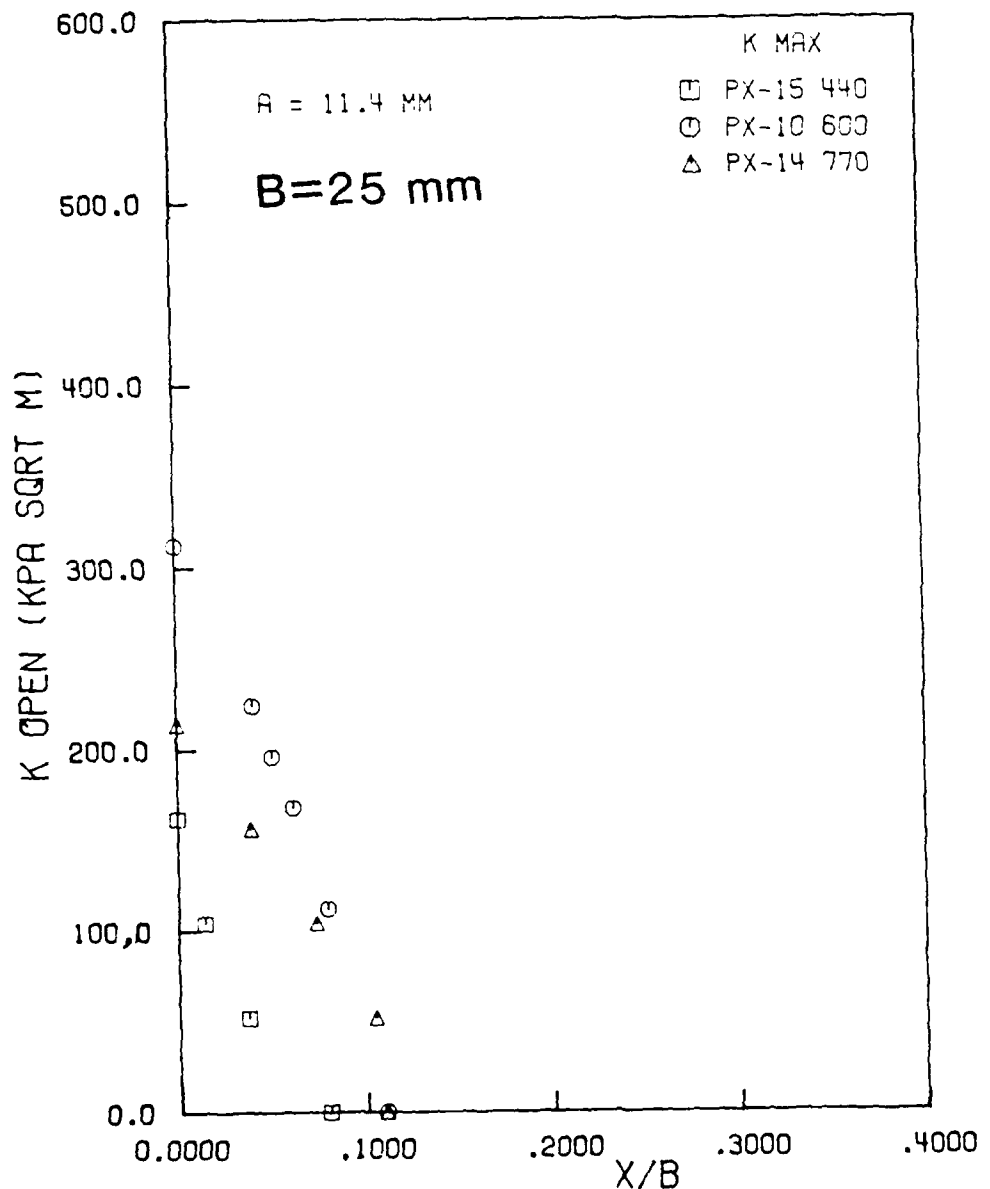


Figure 4.19: Interferometric opening load versus normalized distances from the free surface with varying cyclic  $K_{max}$  levels for 25 mm thick specimens.

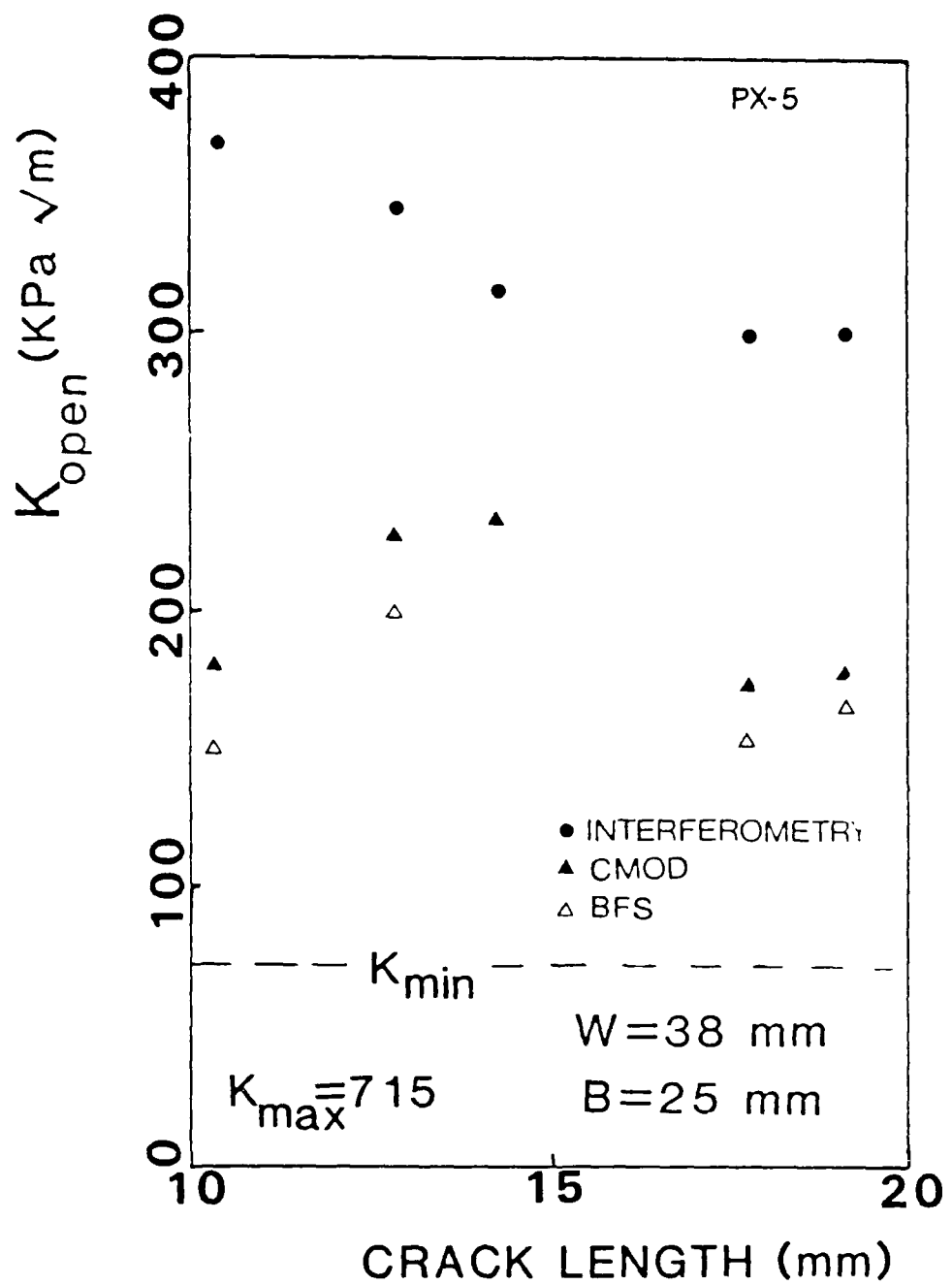


Figure 4.20: Crack opening loads obtained from various measurements for increasing crack lengths for Test PX-5,  $R = 0.1$ .

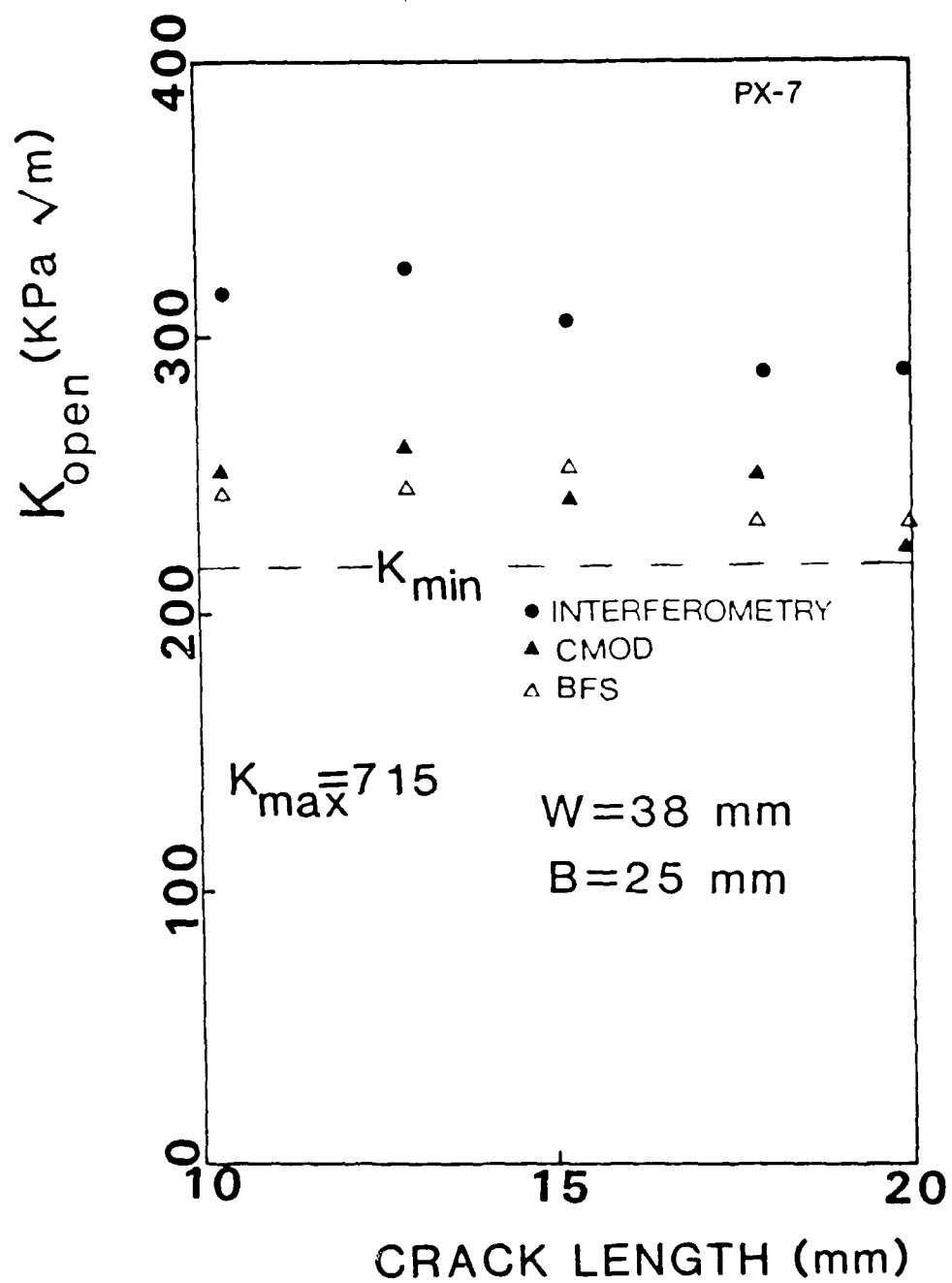


Figure 4.21: Crack opening loads obtained from various measurements for increasing crack length for Test PX-7,  $R = 0.3$ .

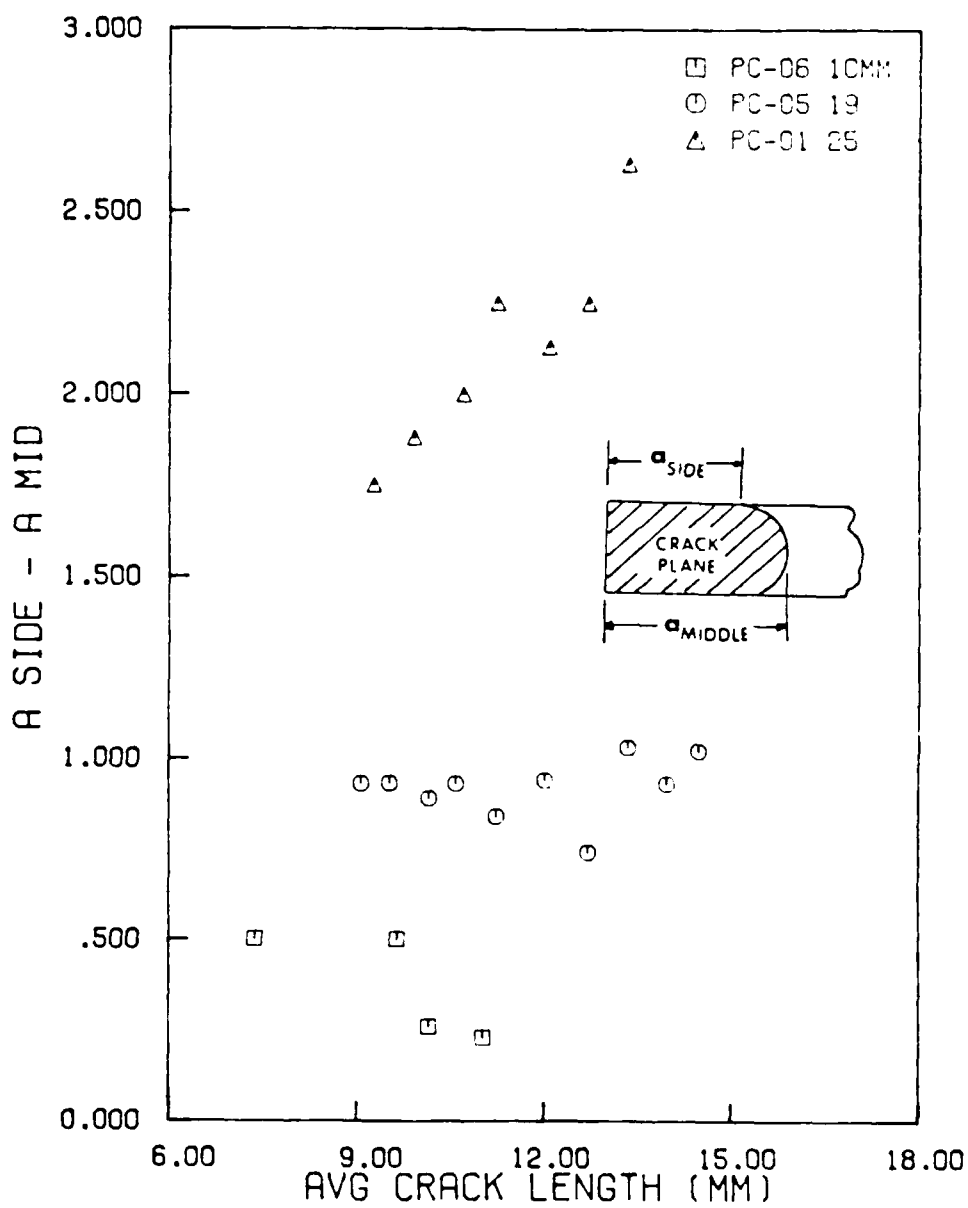


Figure 4.22: Comparison of crack tunnelling magnitudes for various PC specimen thickness.

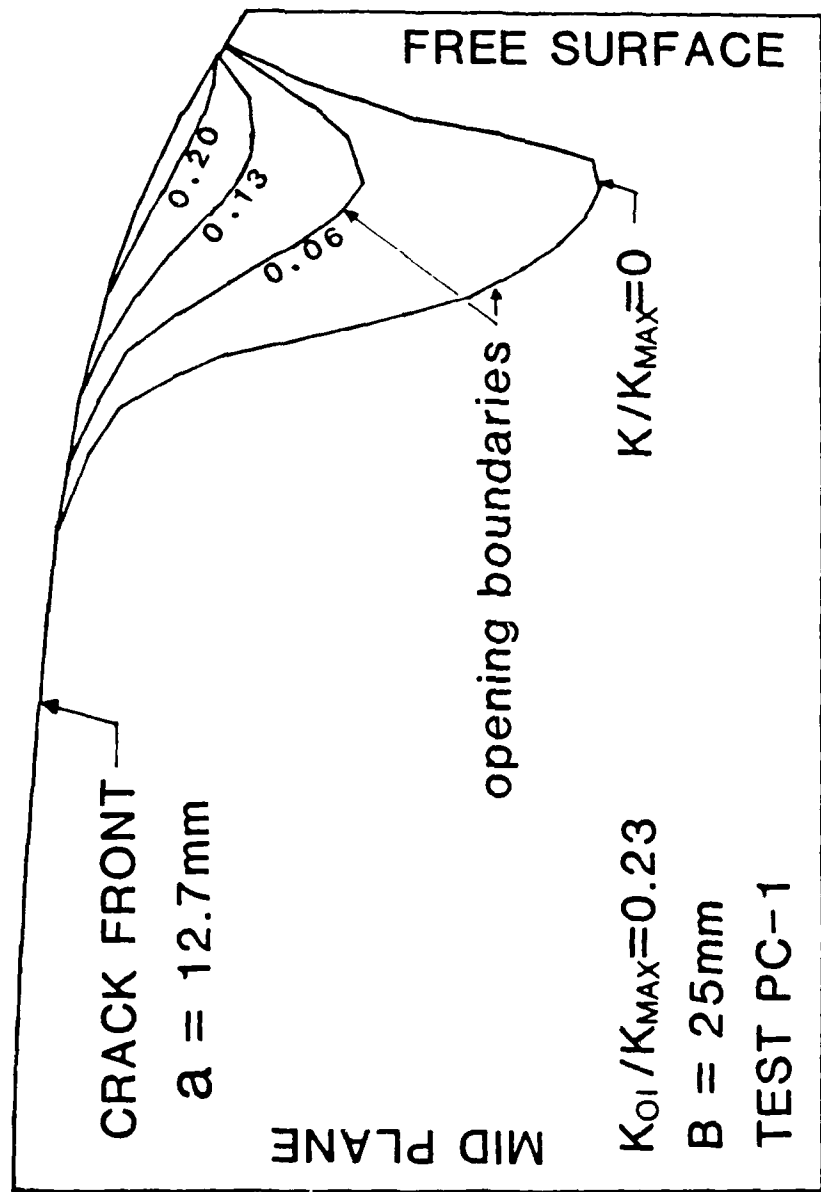


Figure 4.23: Crack opening perimeters as a function of applied load for the 25 mm thick PC specimen.

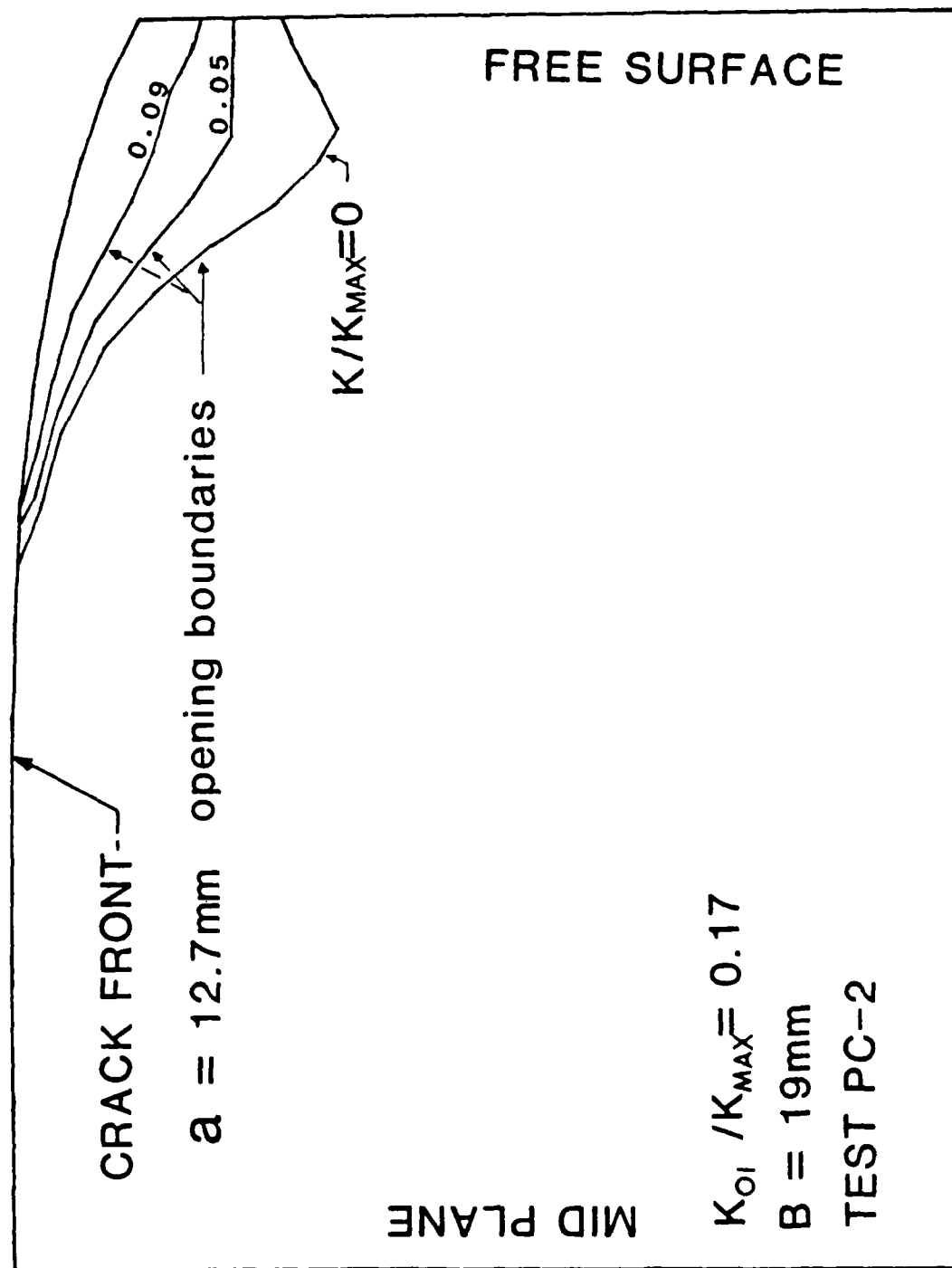


Figure 4.24: Crack opening parameters as a function of applied load for the 19 mm thick PC specimen.

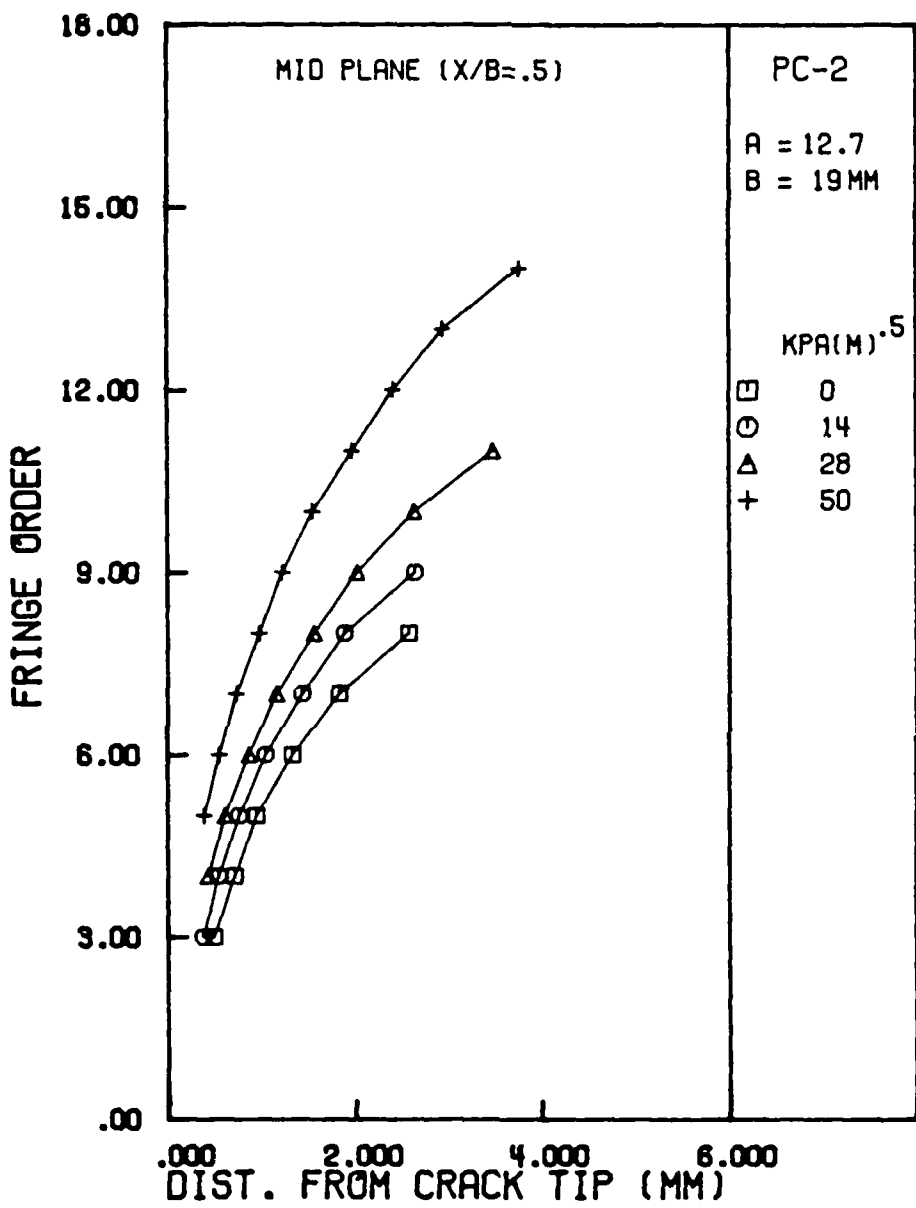


Figure 4.25: Mid-plane crack opening profile for 19 mm thick PC specimen under steady state cycling.

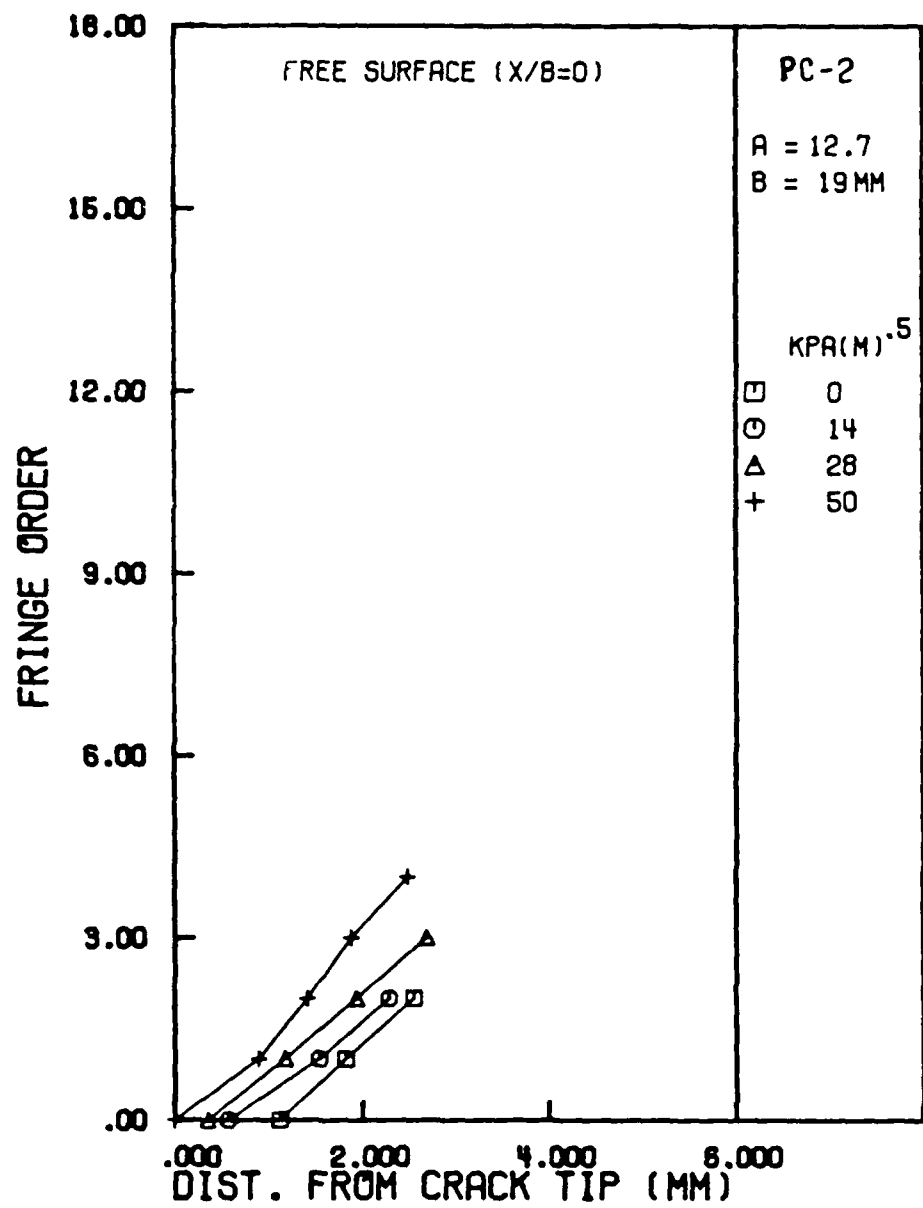


Figure 4.26: Free surface crack opening profile for a 19 mm thick PC specimen under steady state cycling.

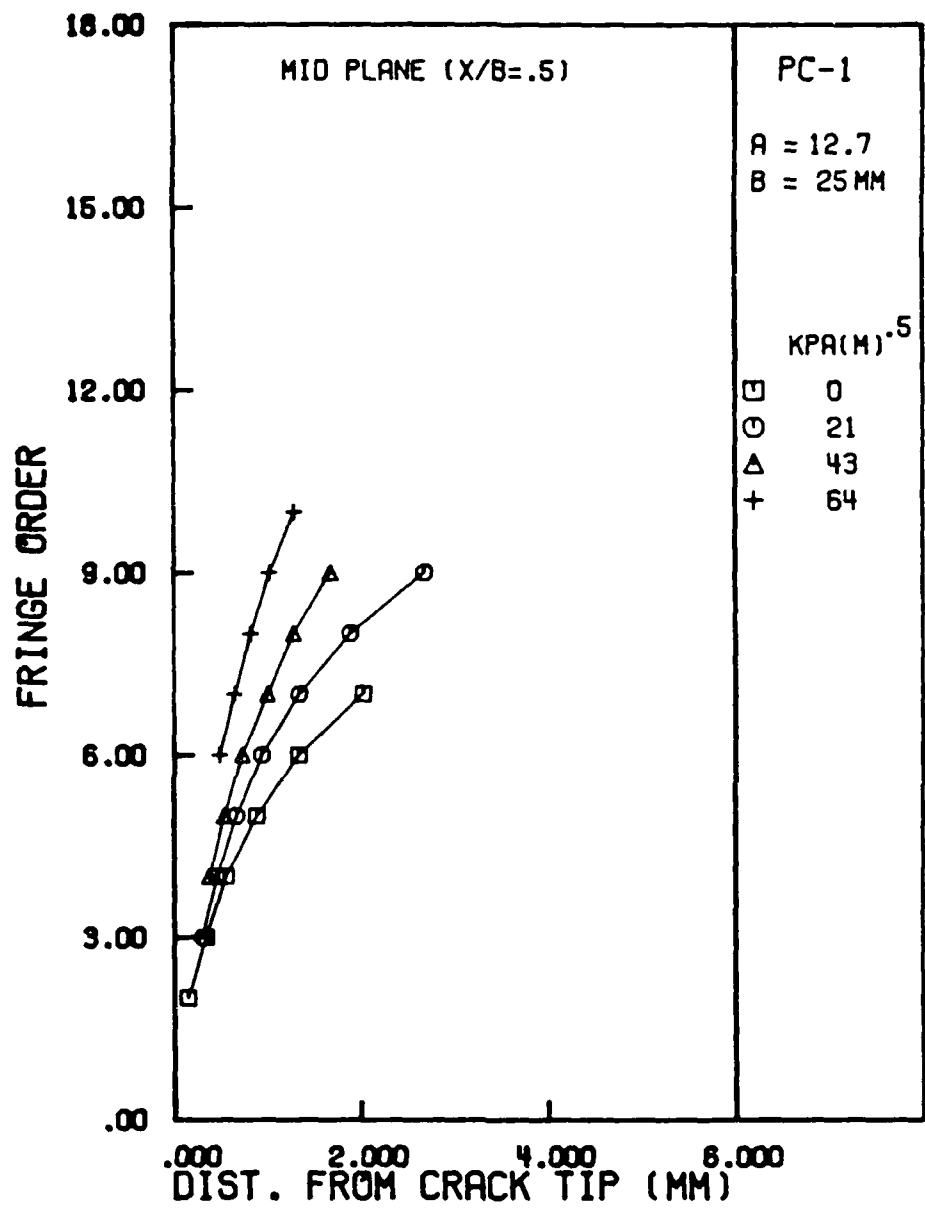


Figure 4.27: Mid-plane crack opening profile for a 25 mm thick PC specimen under steady state cycling.

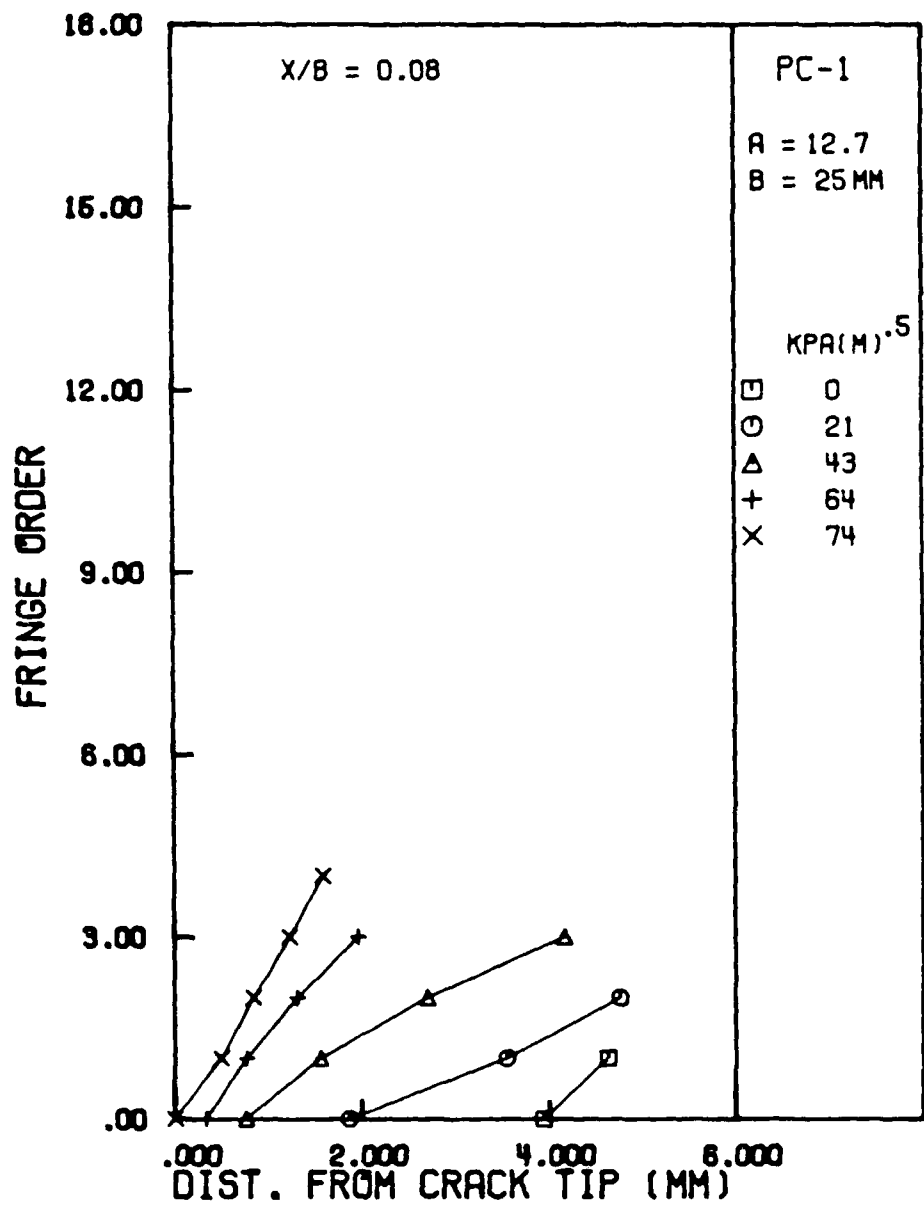


Figure 4.28: Near free surface opening profile for a 25 mm thick PC specimen under steady state cycling.

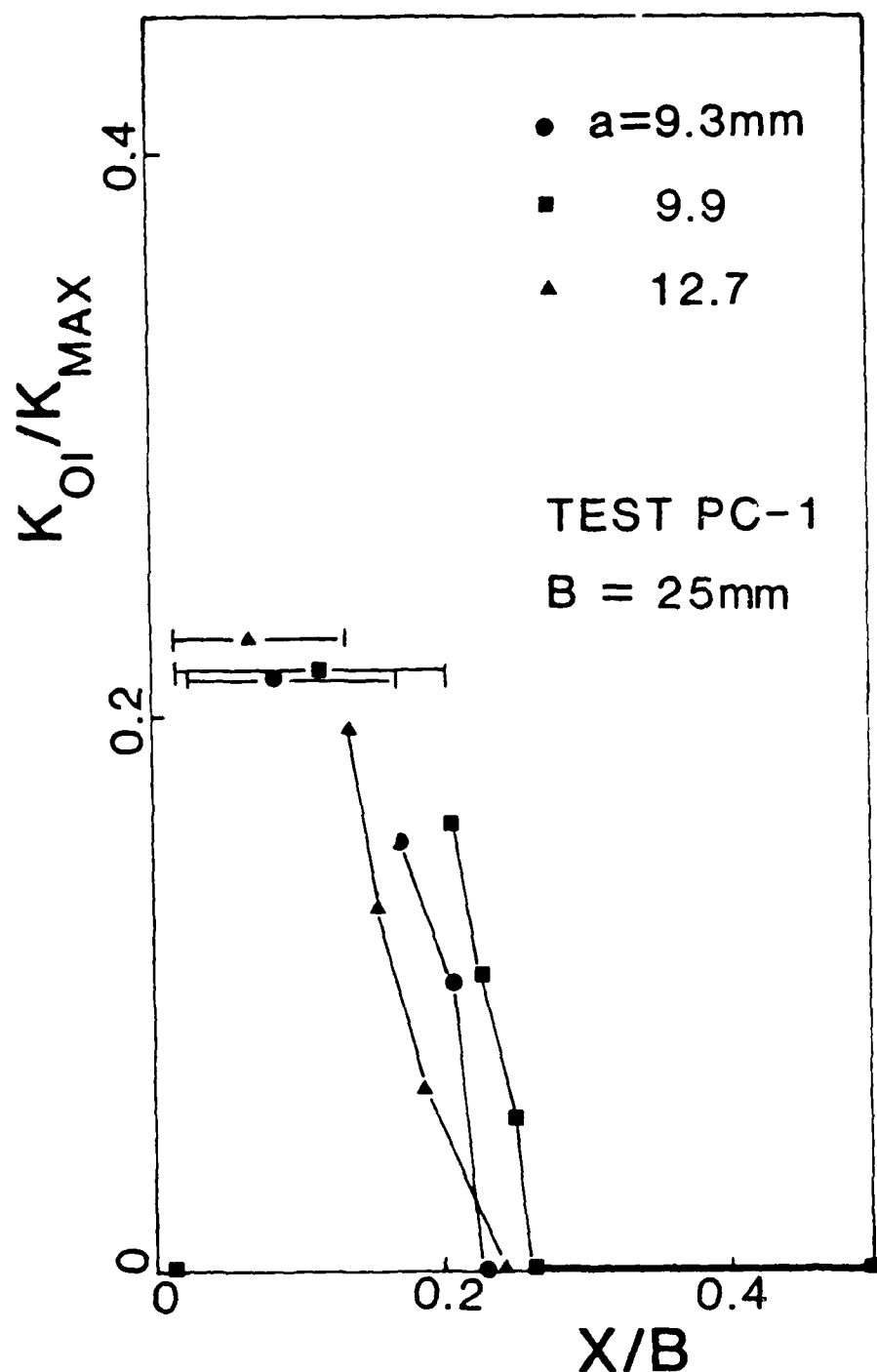


Figure 4.29: Interferometric crack opening load as a function of normalized distance from the free surface for a 25 mm thick specimen.

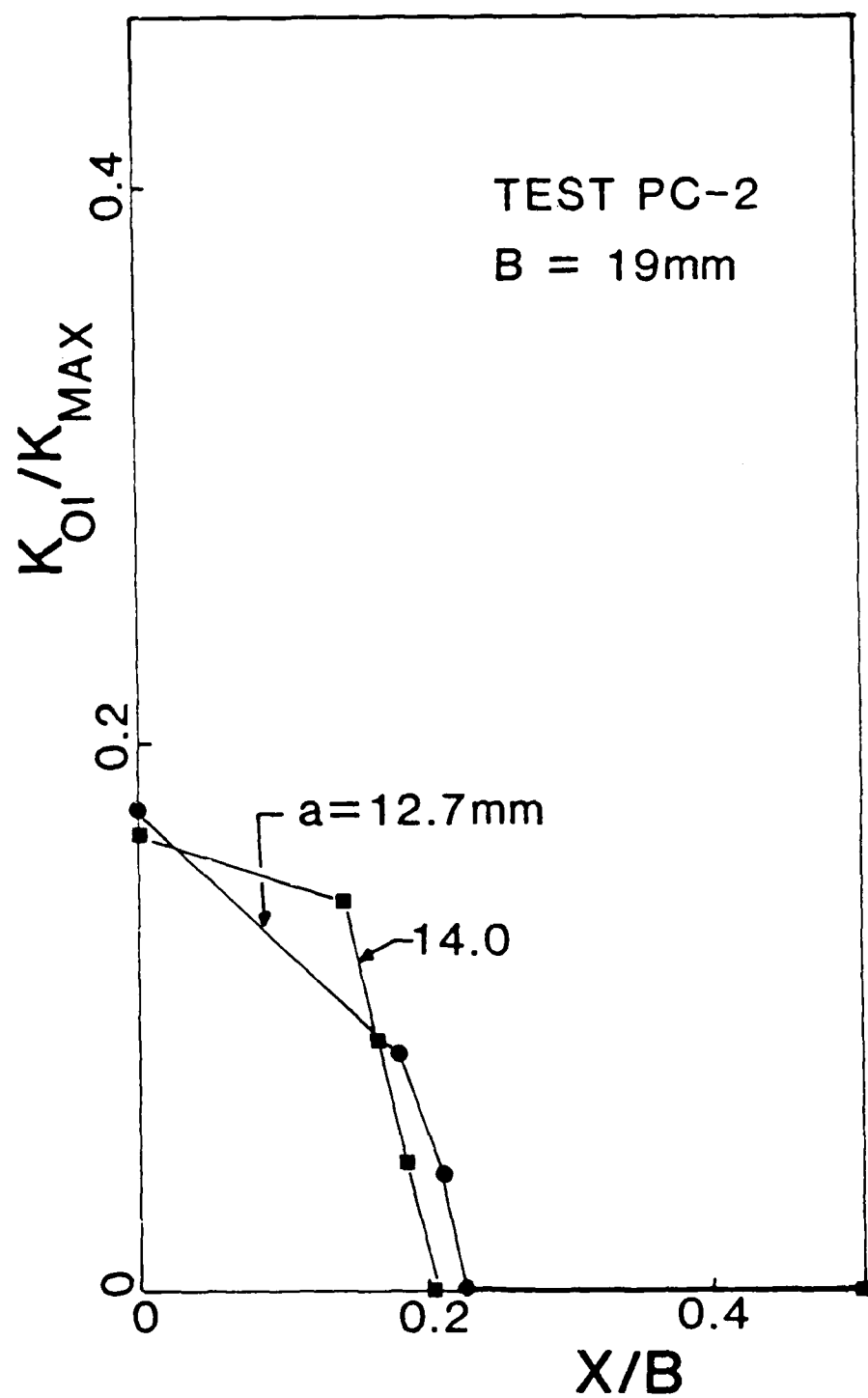


Figure 4.30: Interferometric crack opening load as a function of normalized distance from the free surface for a 19 mm thick specimen.

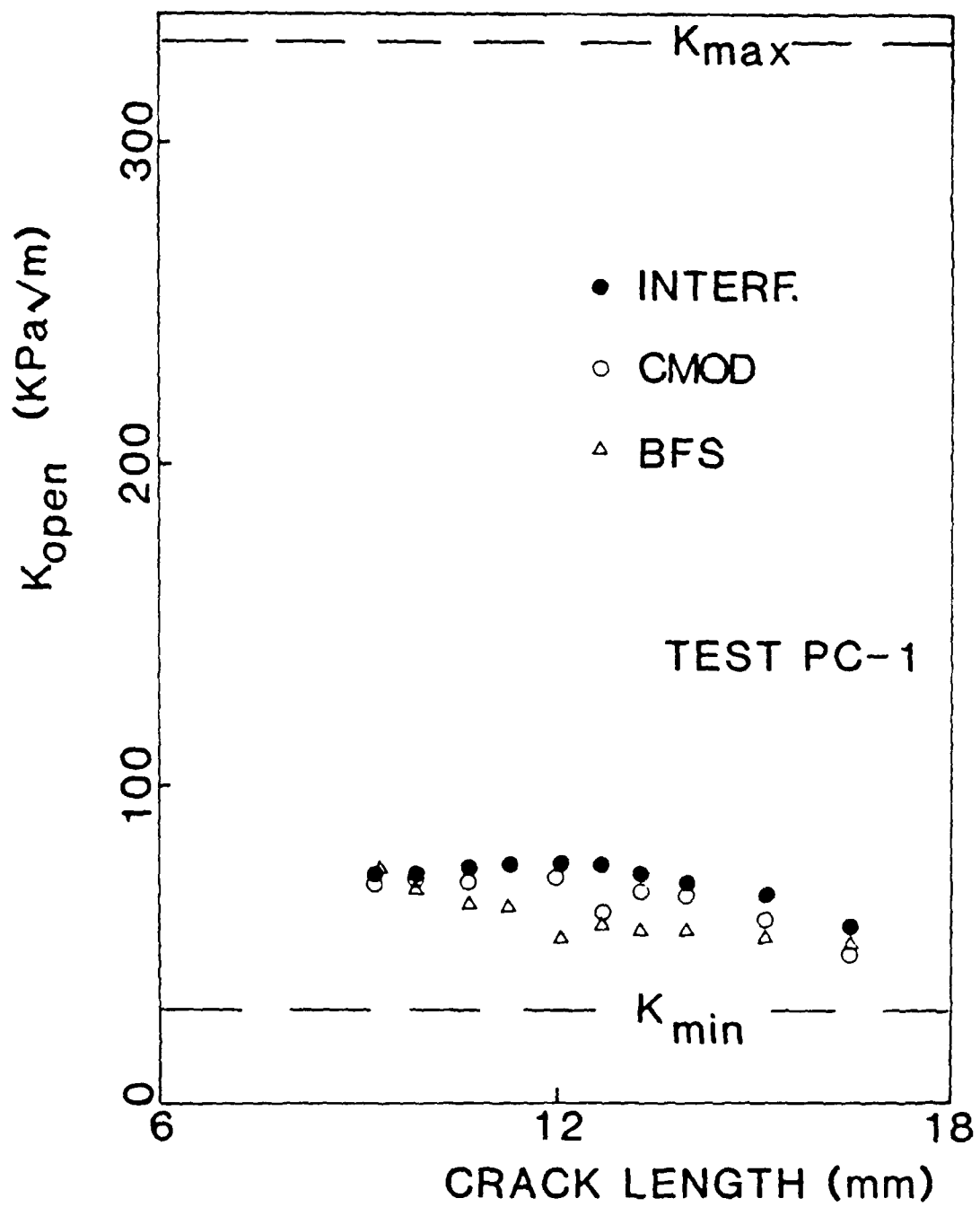


Figure 4.31: Comparison of opening loads obtained from optical interferometry, CMOD, and back face strain measurements for Test PC-1 tested with  $R = 0.1$ .

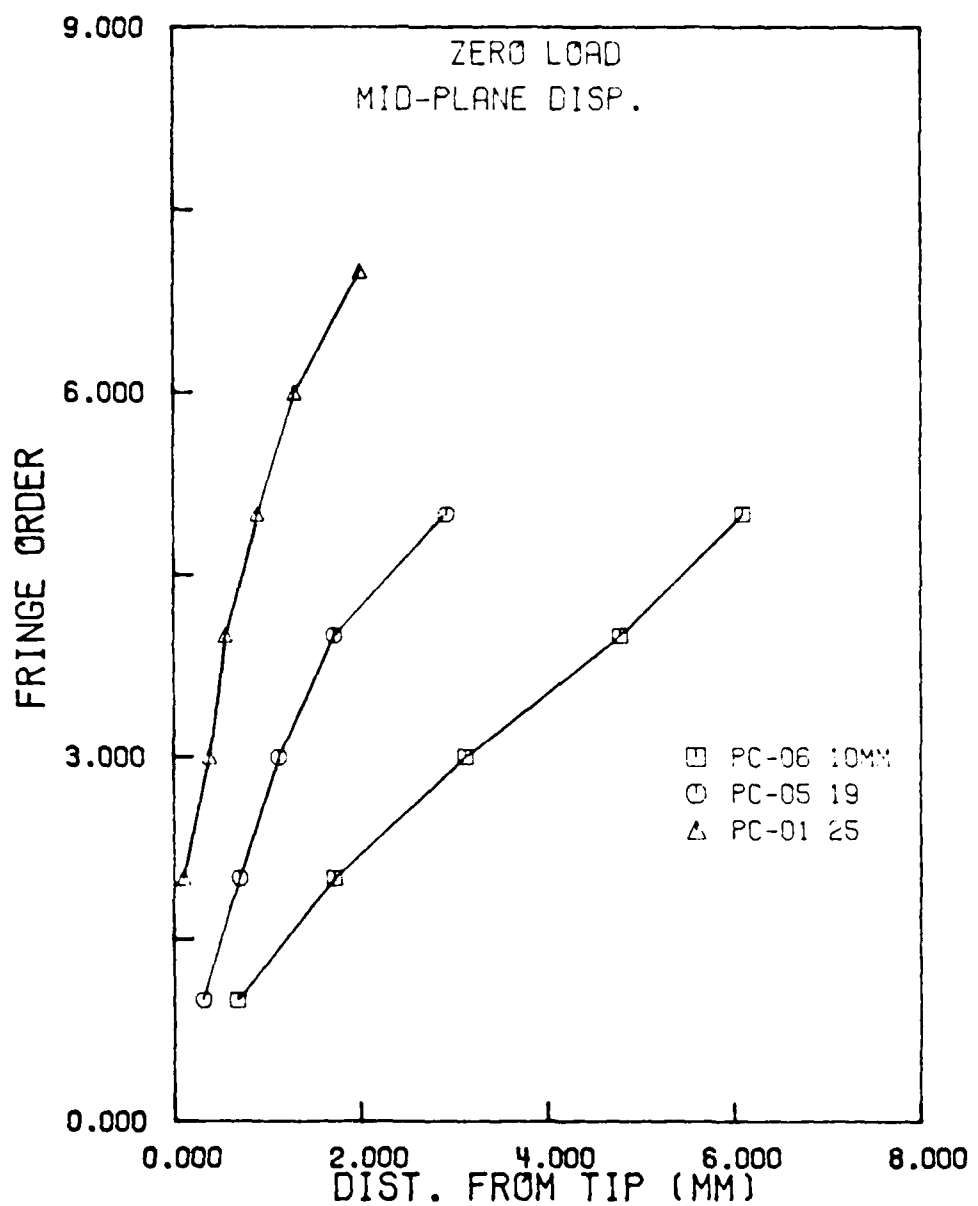


Figure 4.32: Comparison of zero load (residual) mid-plane opening for varying specimen thickness.

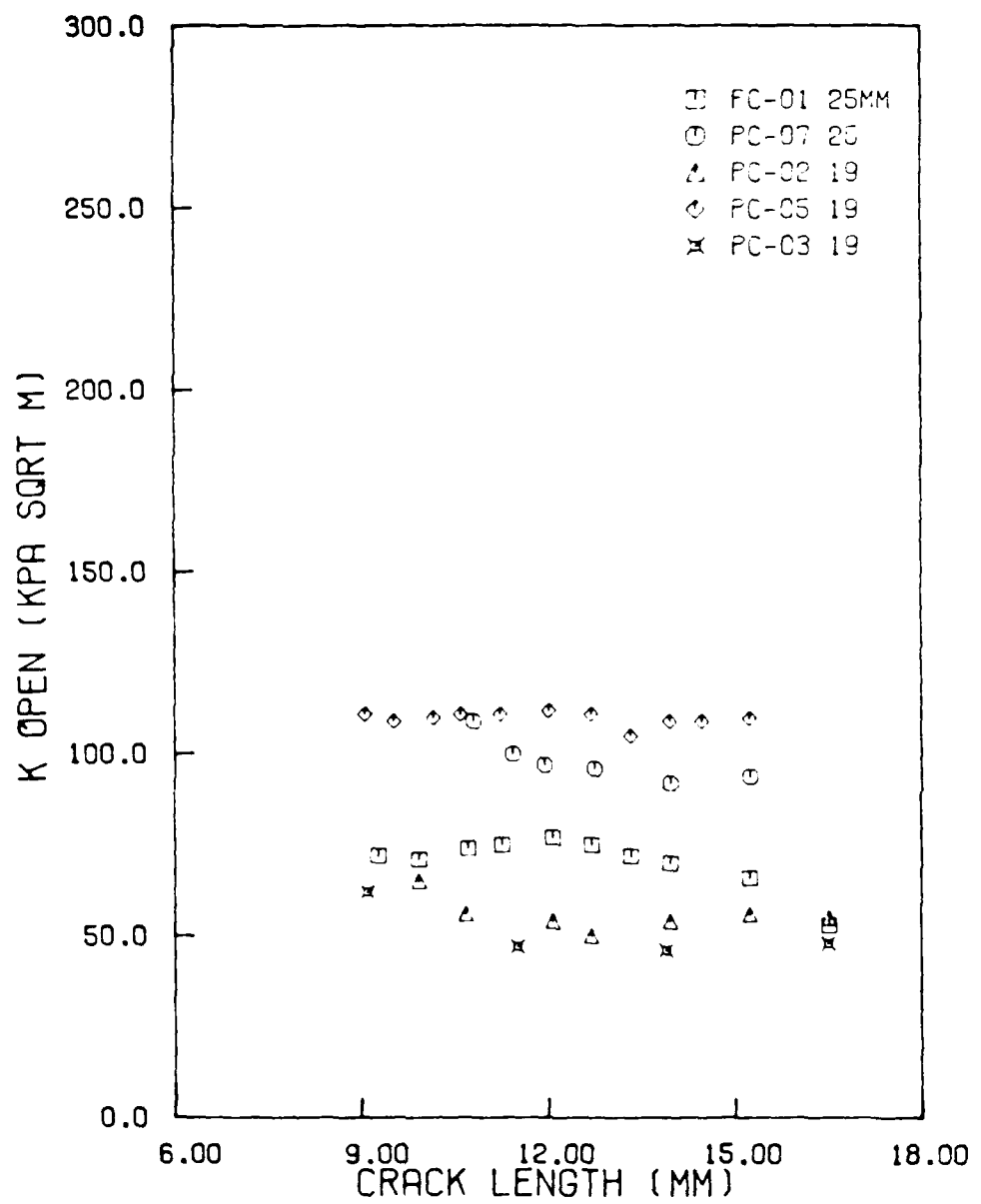


Figure 4.33: Comparison of interferometric free surface opening load for varying specimen thickness.

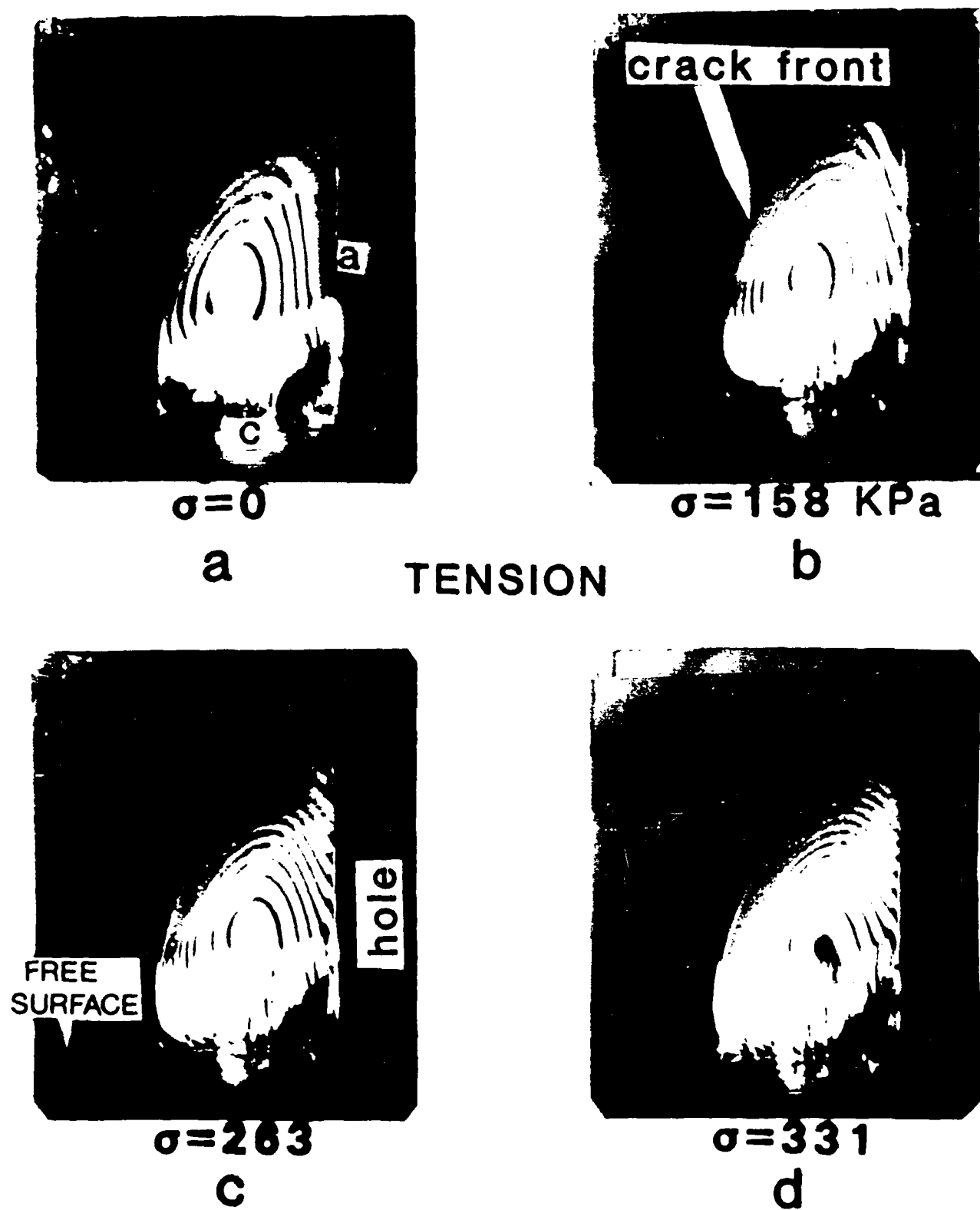


Figure 4.34: Typical interference fringe patterns for various applied remote tensile stresses.

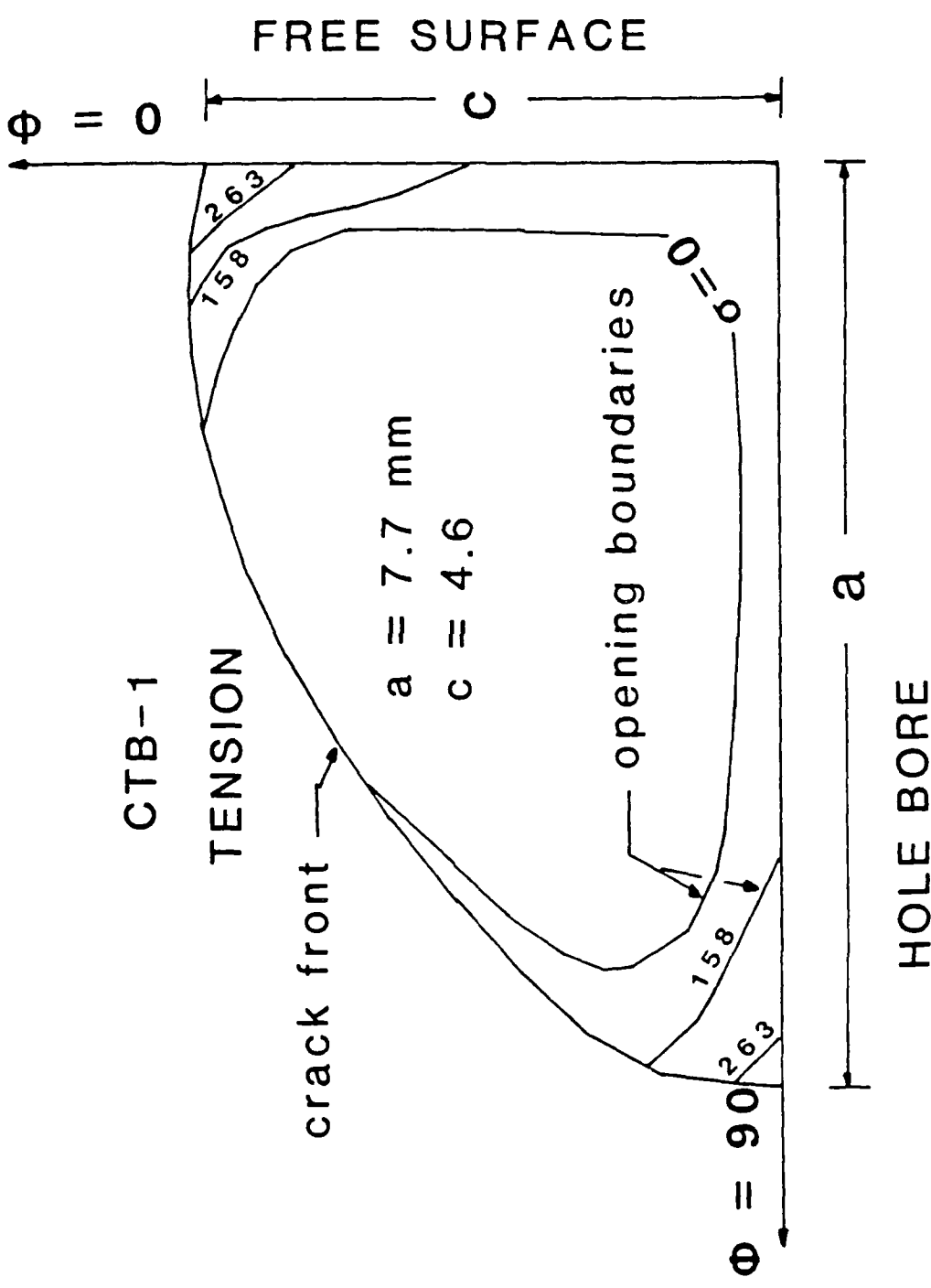


Figure 4.35: Crack opening parameters as a function of applied load, obtained by overlapping the zero order fringe patterns from Figure 4.34.

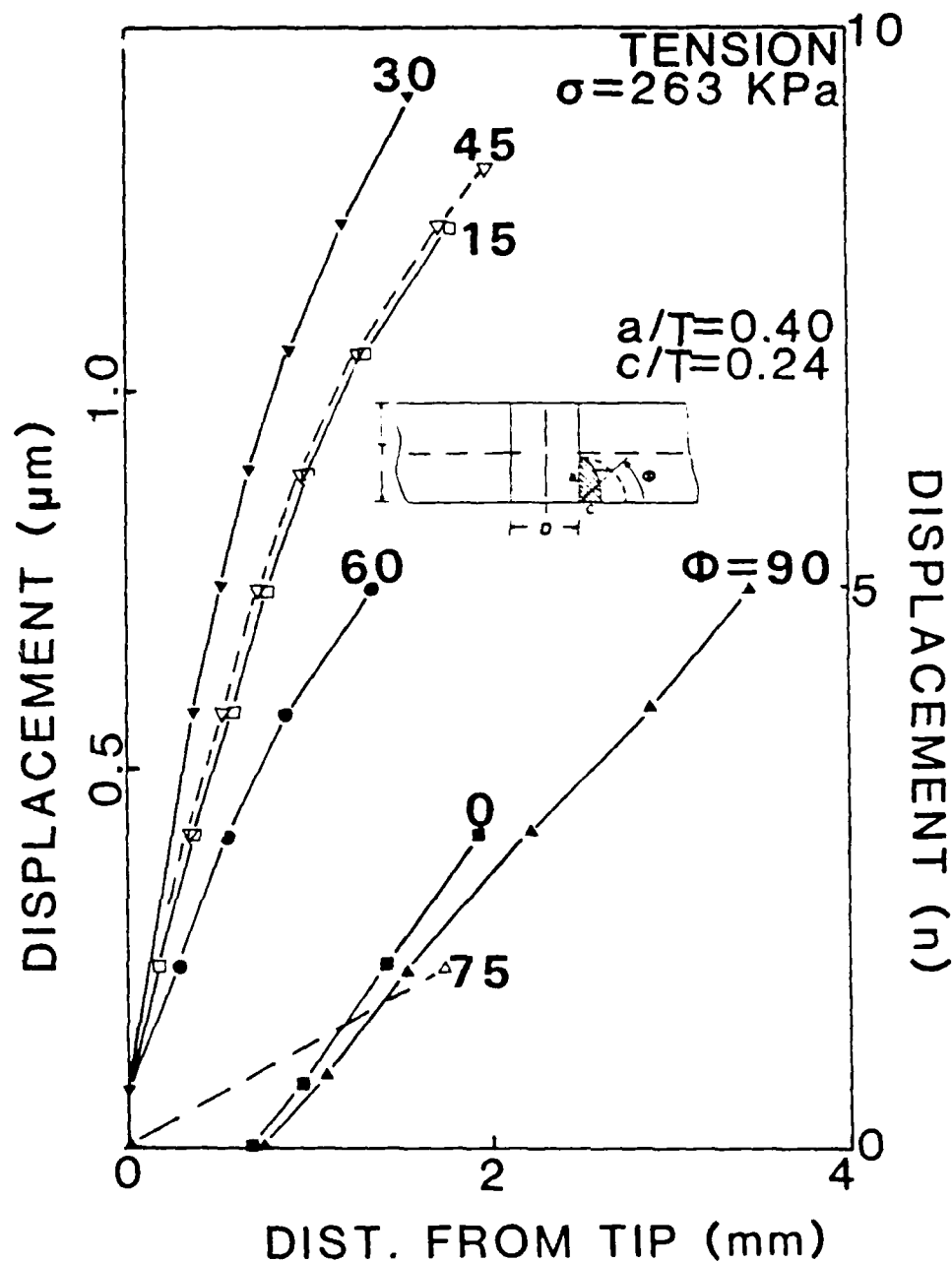


Figure 4.36: Crack opening profiles under a remote tension of 263 KPa for varying parametric angle  $\phi$ .

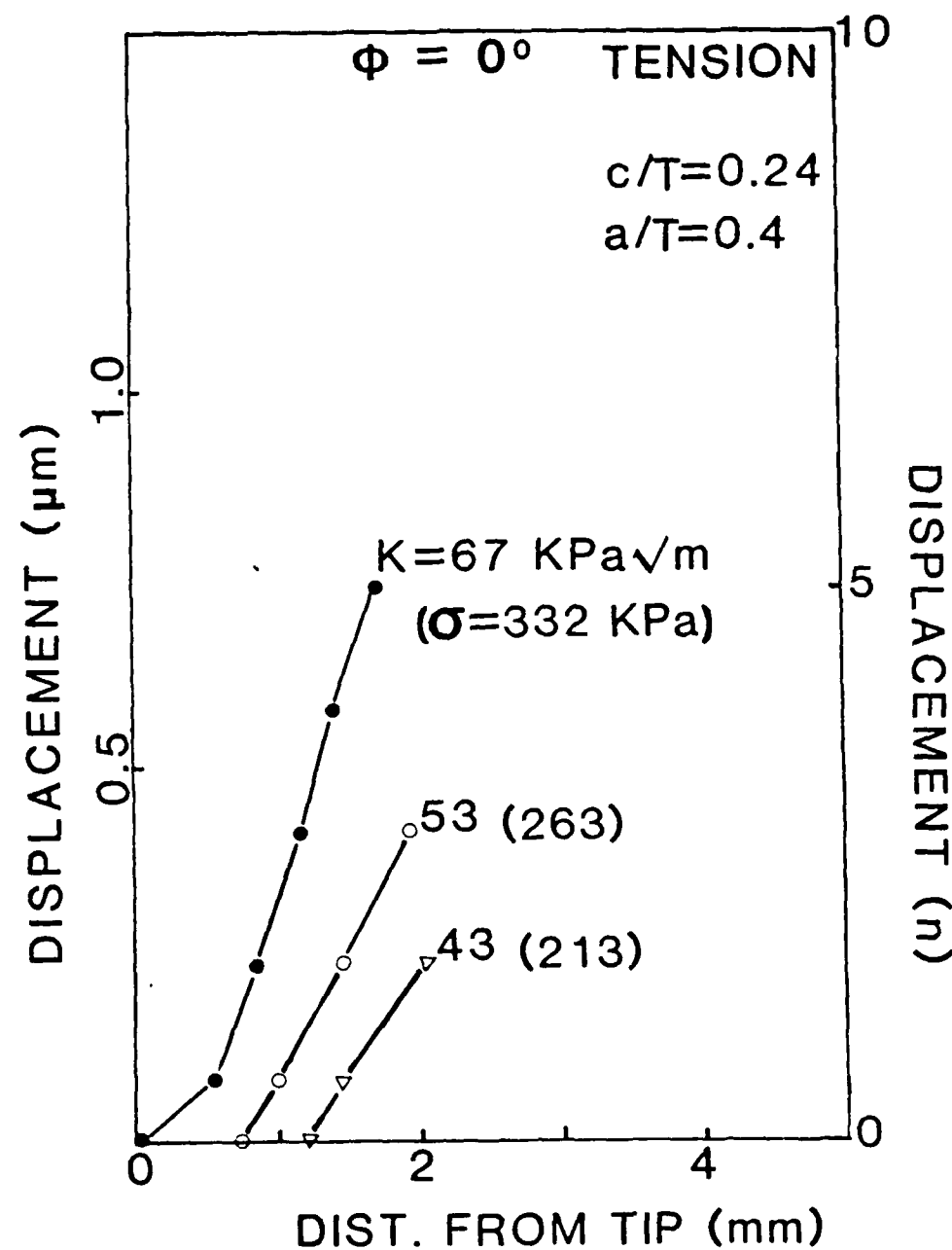


Figure 4.37: Crack opening profiles for varying applied load at the free surface ( $\phi = 0^\circ$ ).

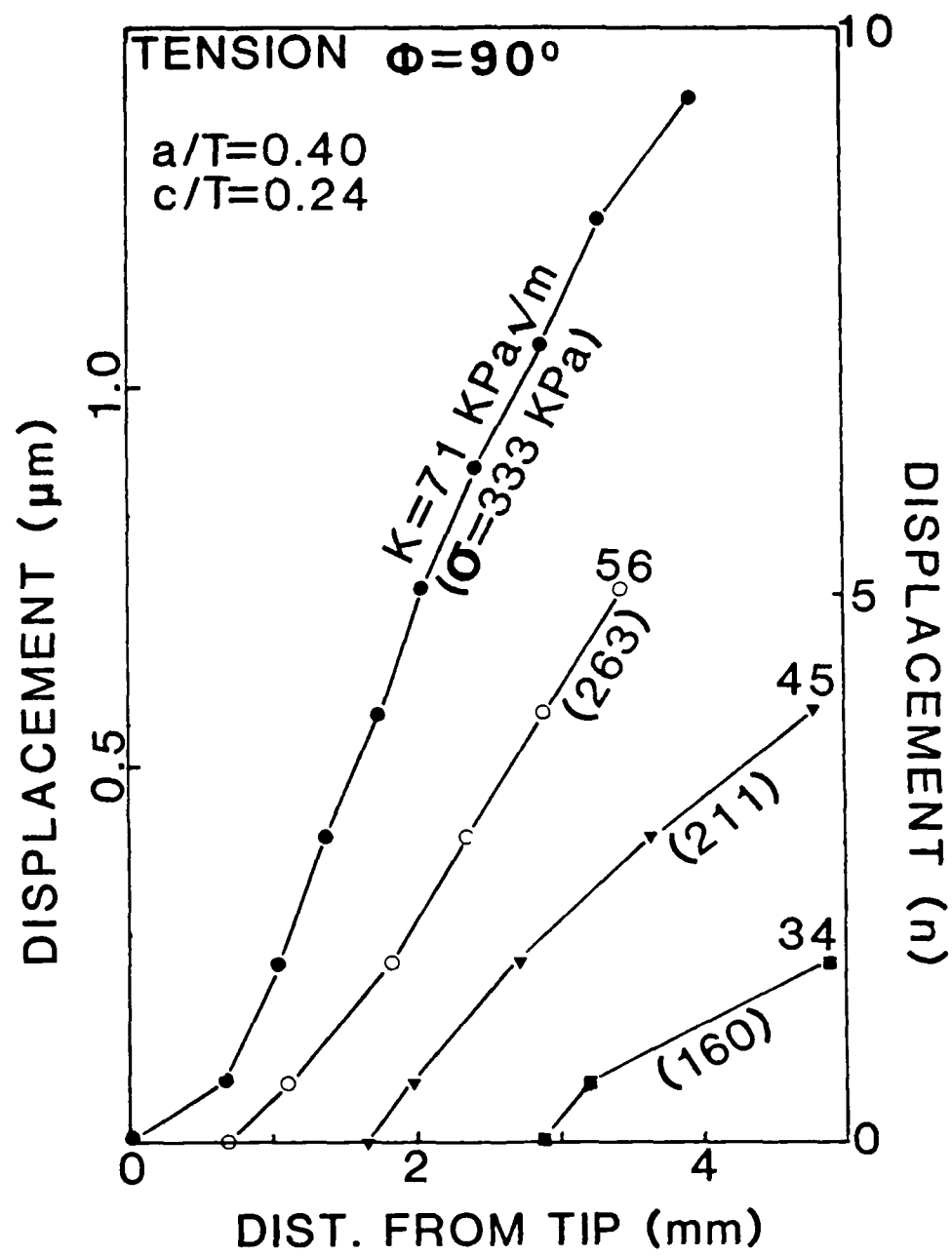


Figure 4.38: Crack opening profiles for varying applied load along the hole bore ( $\phi = 90^\circ$ ).

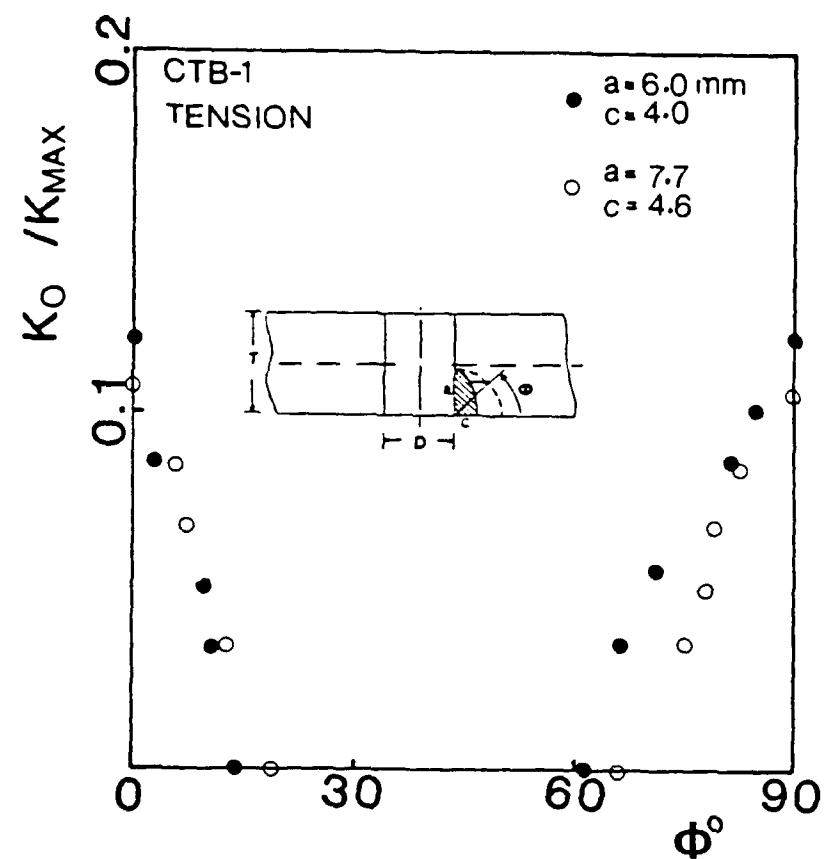


Figure 4.39: Interferometric crack tip opening load as a function of angle  $\phi$  for Test CTB-1.

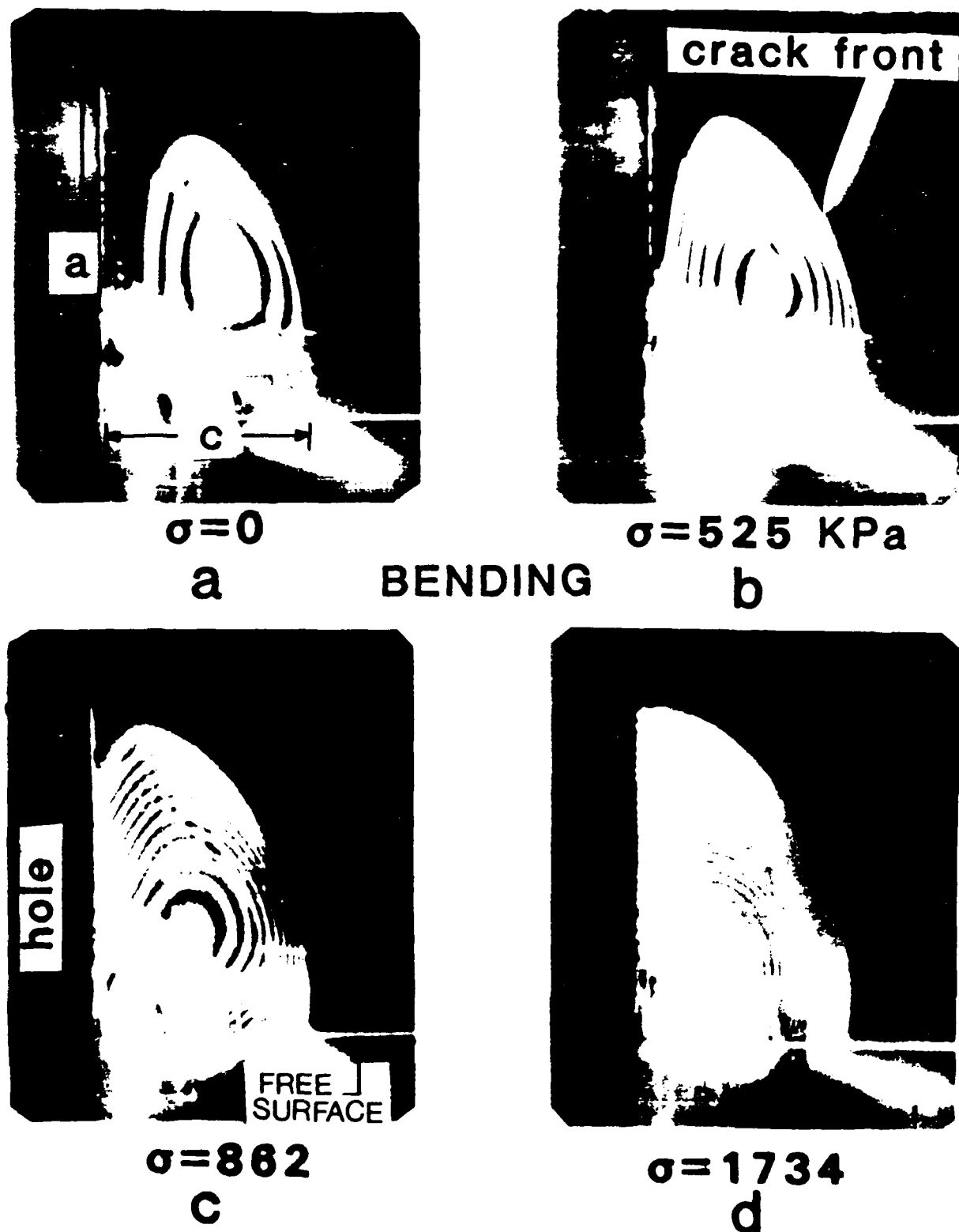


Figure 4-40: Interference fringe pattern photographed during steady state cyclic bending.

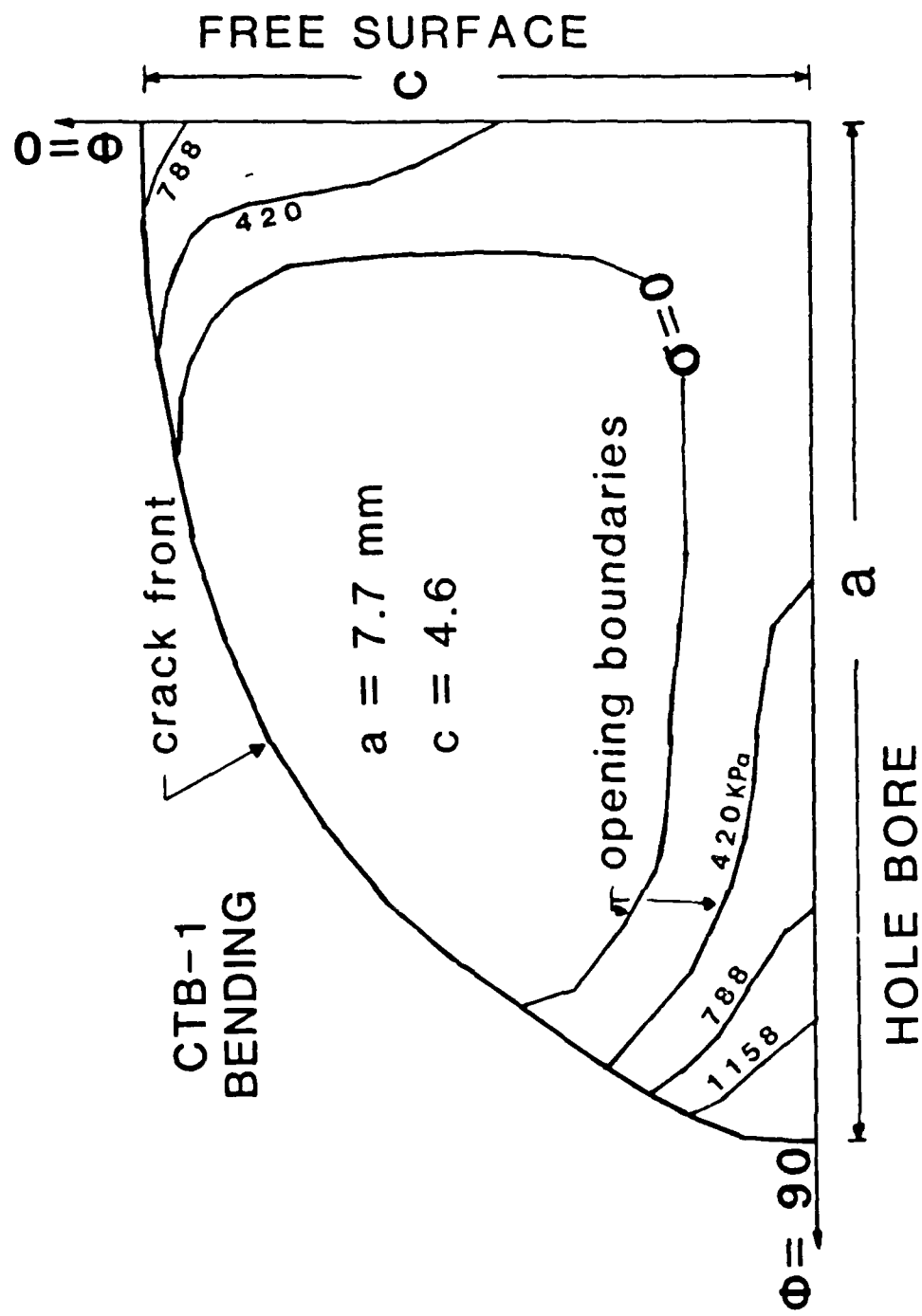


Figure 4.41: Crack opening perimeters as a function of applied bending stress, obtained by overlapping the zero order fringe patterns from Figure 4.40.

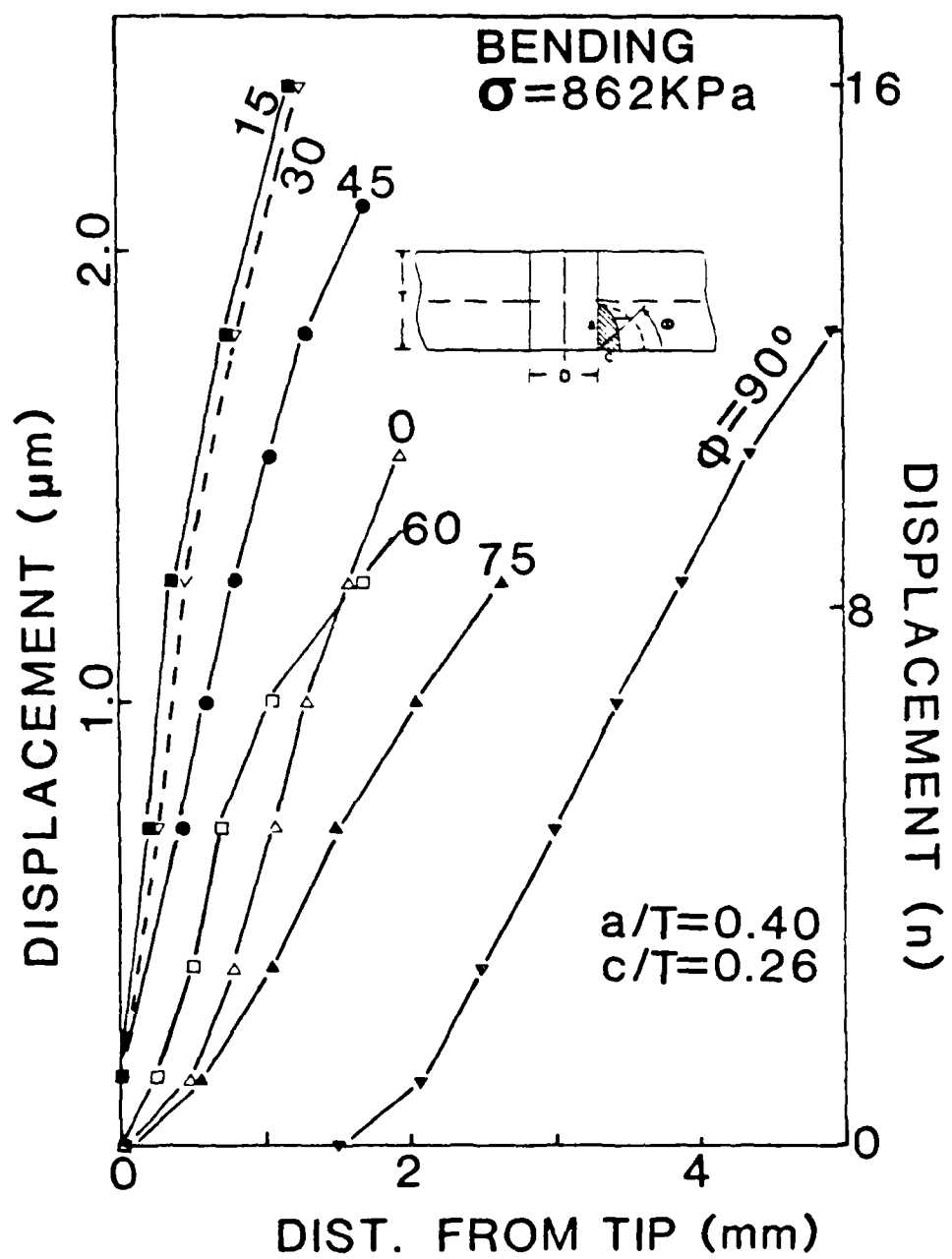


Figure 4.12: Crack opening profile under a remote bending stress of 862 KPa for varying parametric angle  $\phi$ .

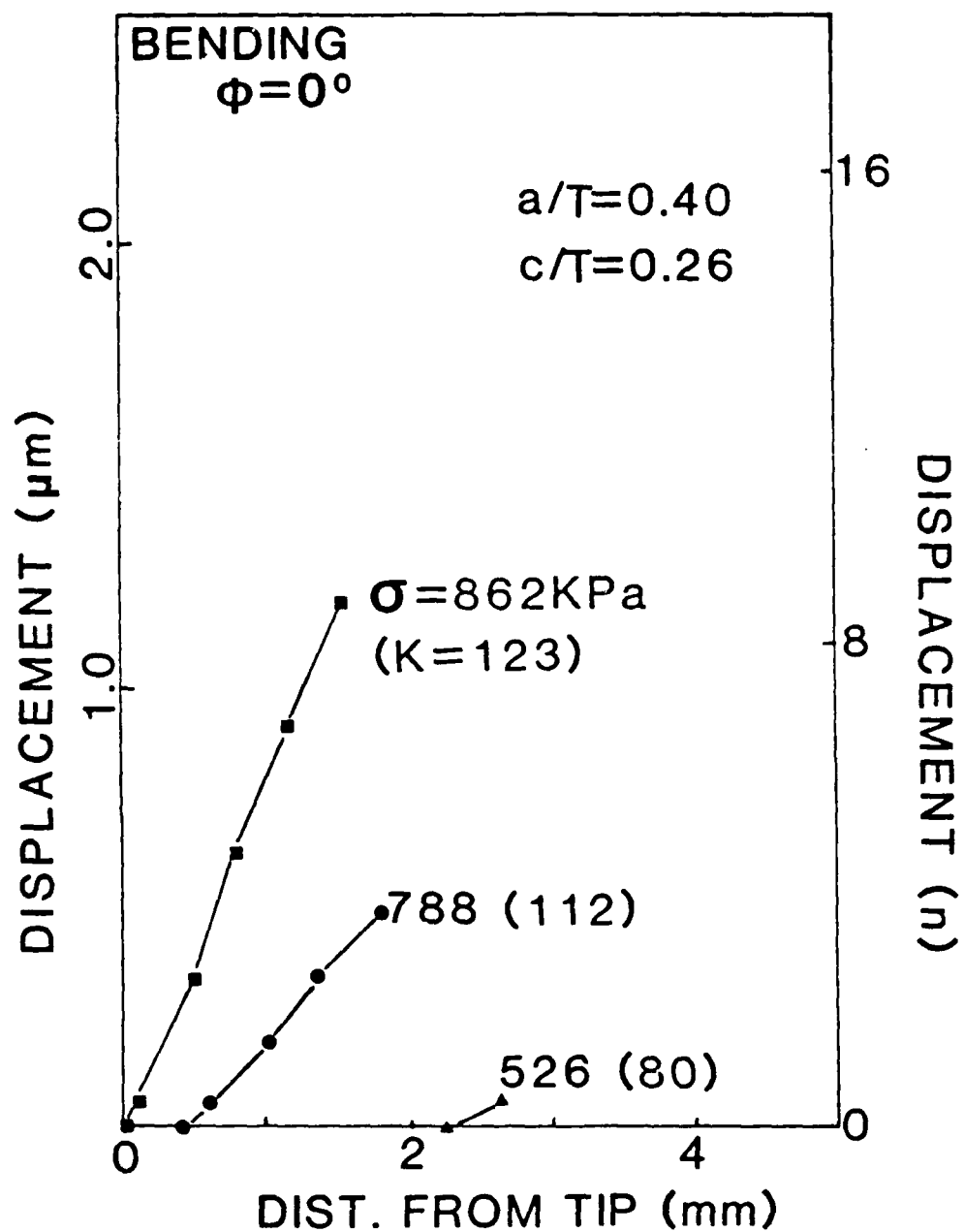


Figure 4.43: Crack opening profiles obtained at the free surface for varying remote stress.

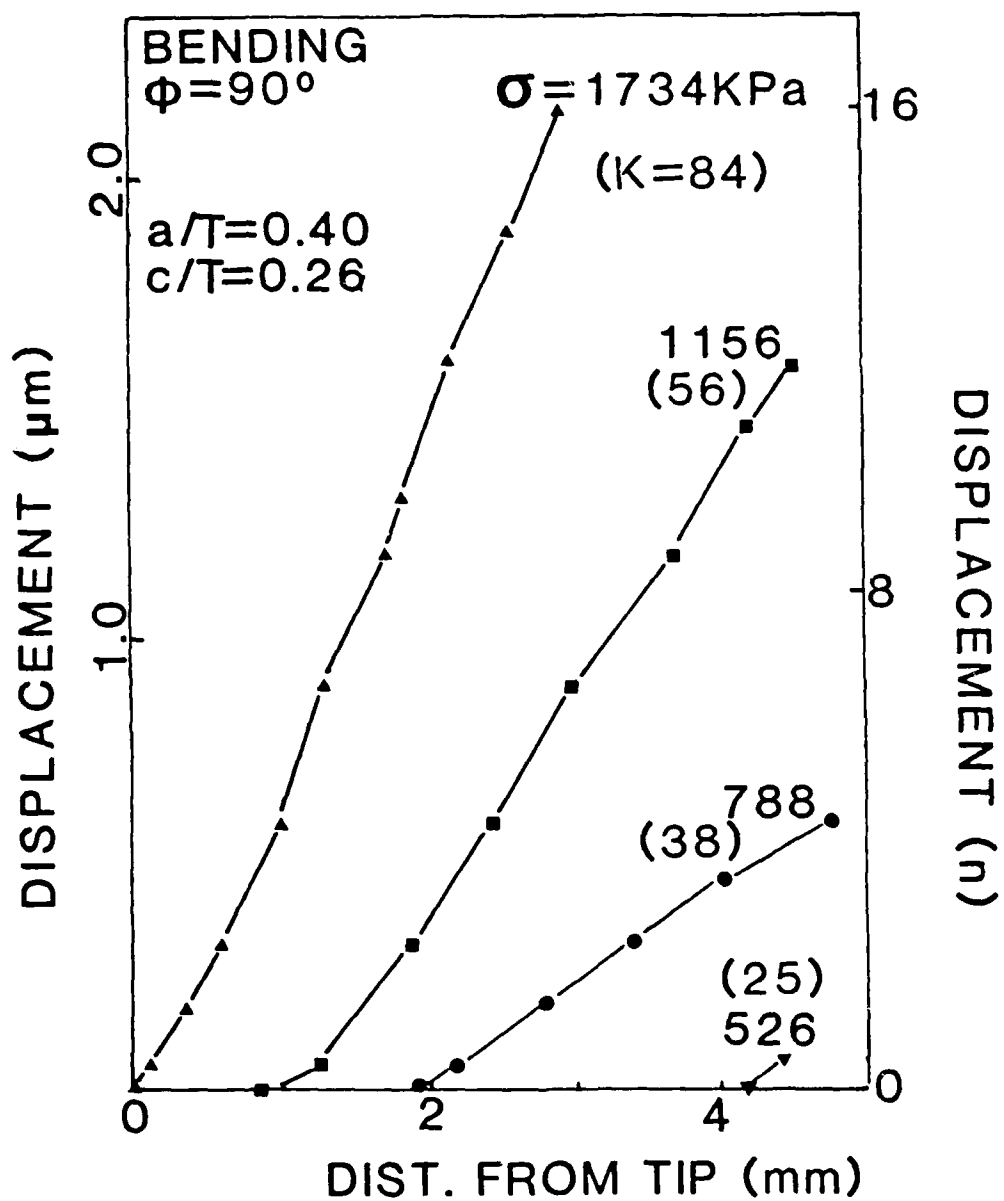


Figure 4.44: Crack opening profile obtained along the hole bore for varying remote bending stress.

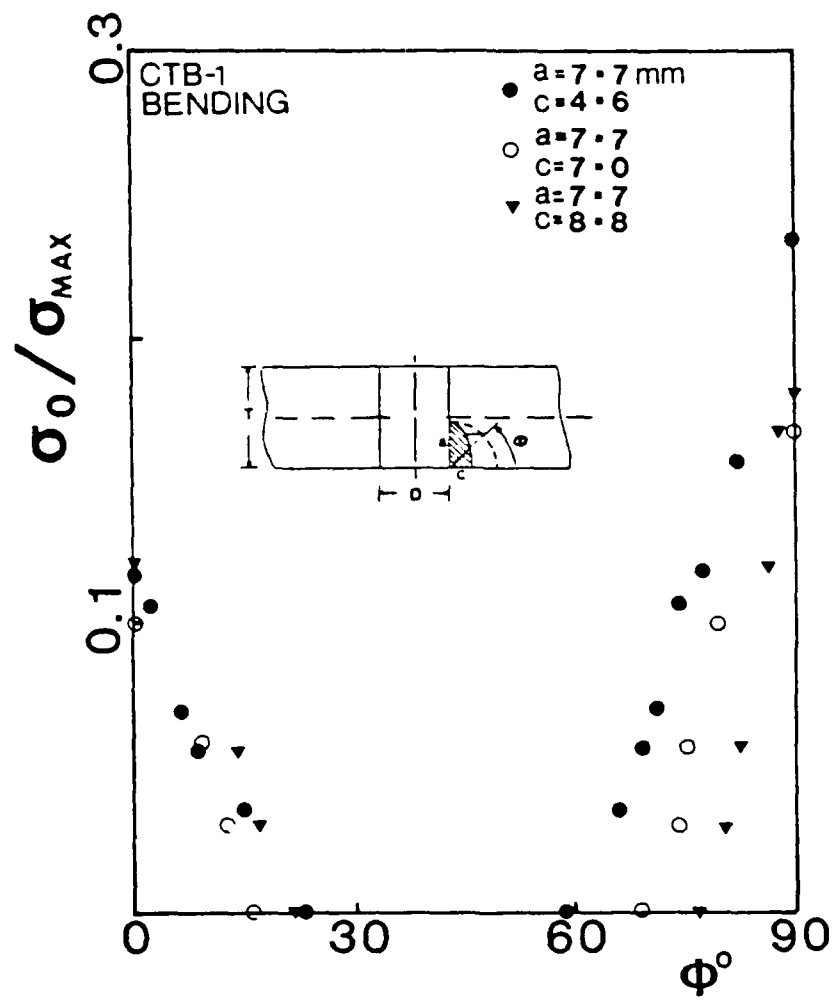


Figure 4.45: Interferometric crack tip opening load as a function of parametric angle  $\phi$  for Test CTB-1.

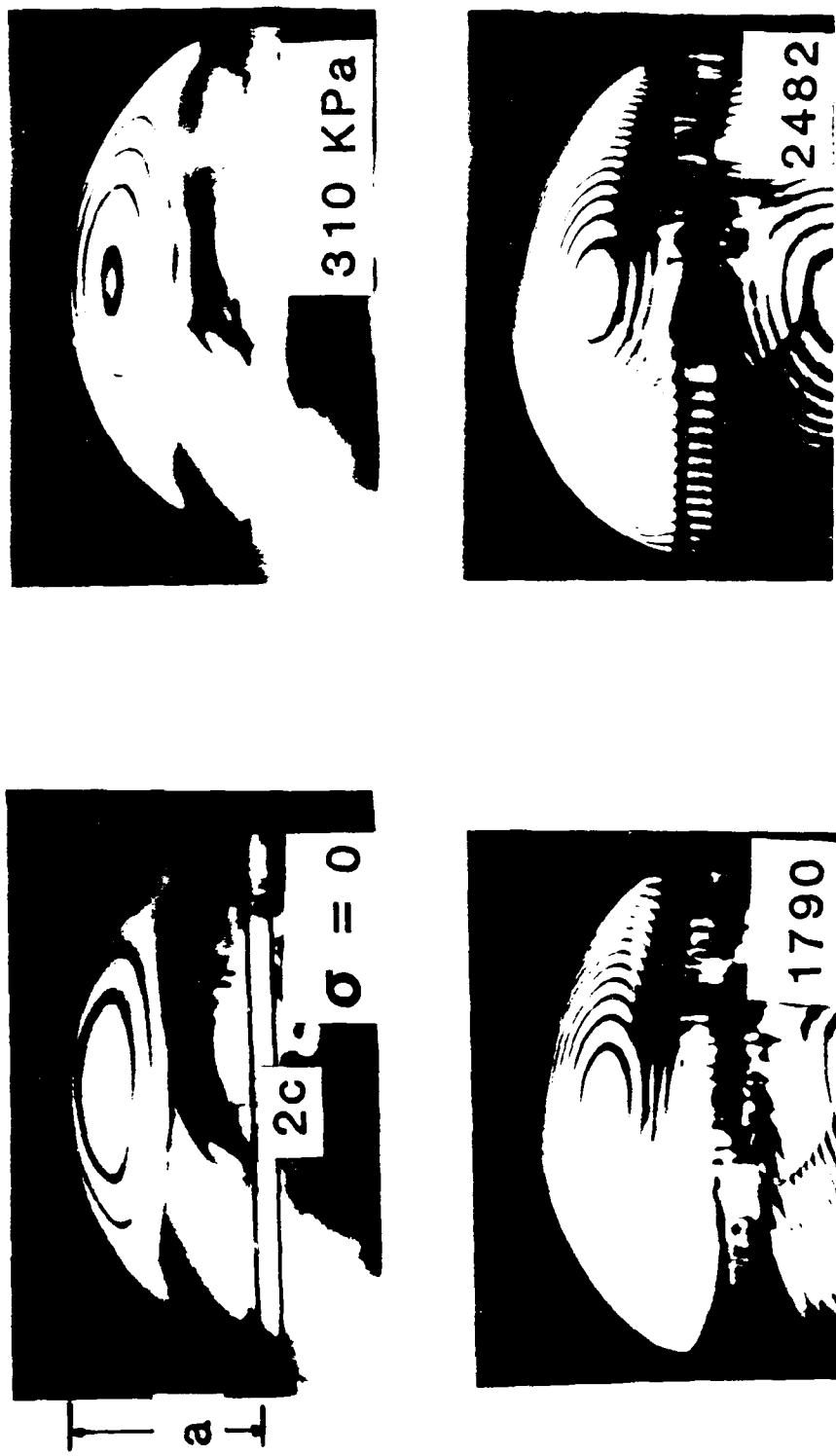


Figure 4.16: Photographs of typical interference fringe patterns for various applied remote bending stresses for specimen SB-1.

## TEST SB 2

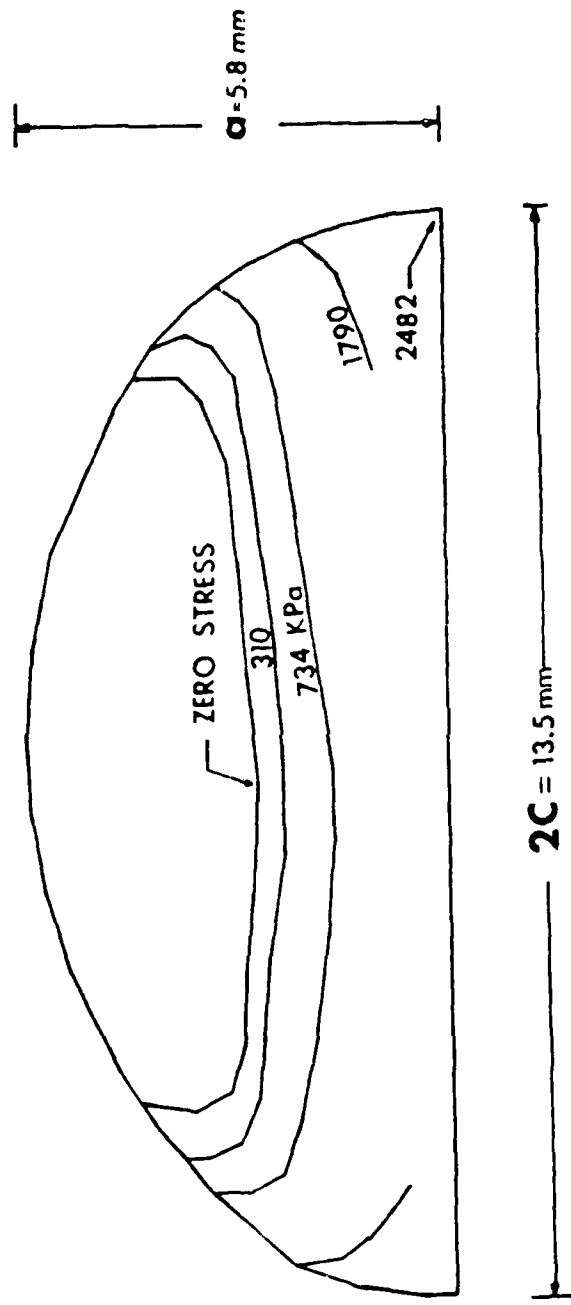


Figure 4.47: Crack opening perimeters as a function of applied load obtained by overlapping the zero order fringe patterns in Figure 4.16.

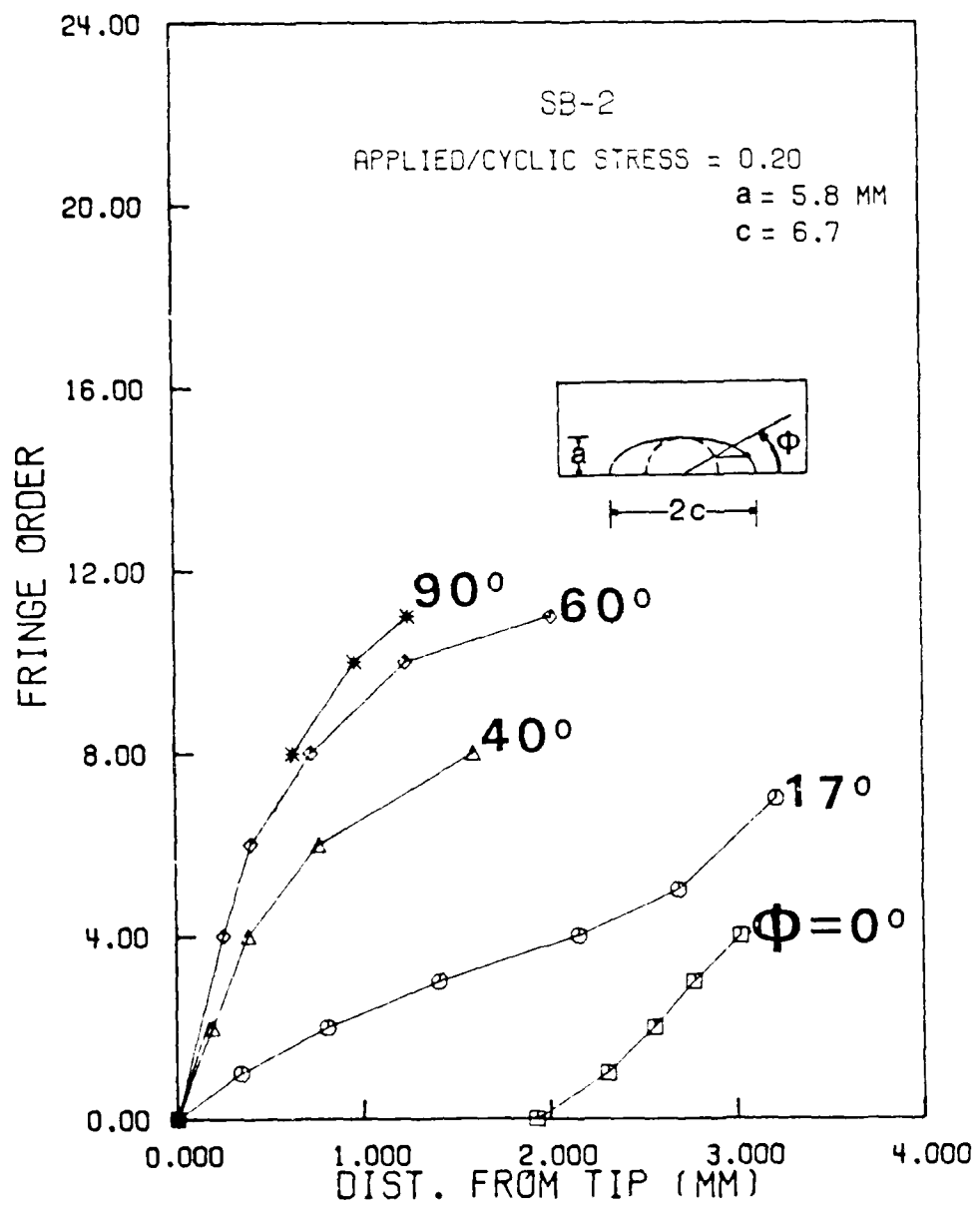


Figure 4.18: Crack opening profiles for various parametric angles  $\phi$  obtained for applied stress of 20% the maximum remote cyclic stress.

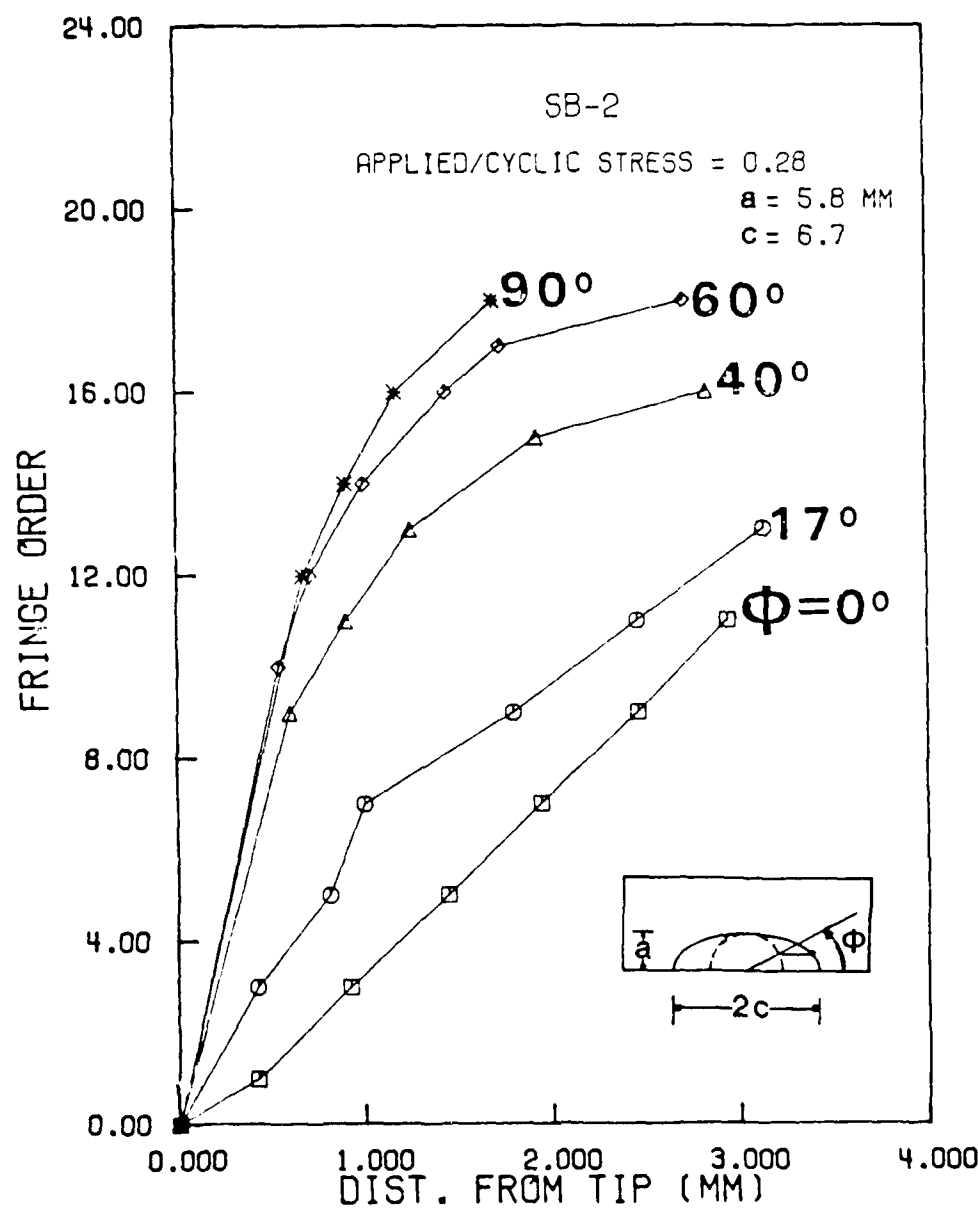


Figure 4.19: Crack opening profiles for various parametric angles  $\phi$  obtained for applied stress of 28% the maximum remote cyclic stress.

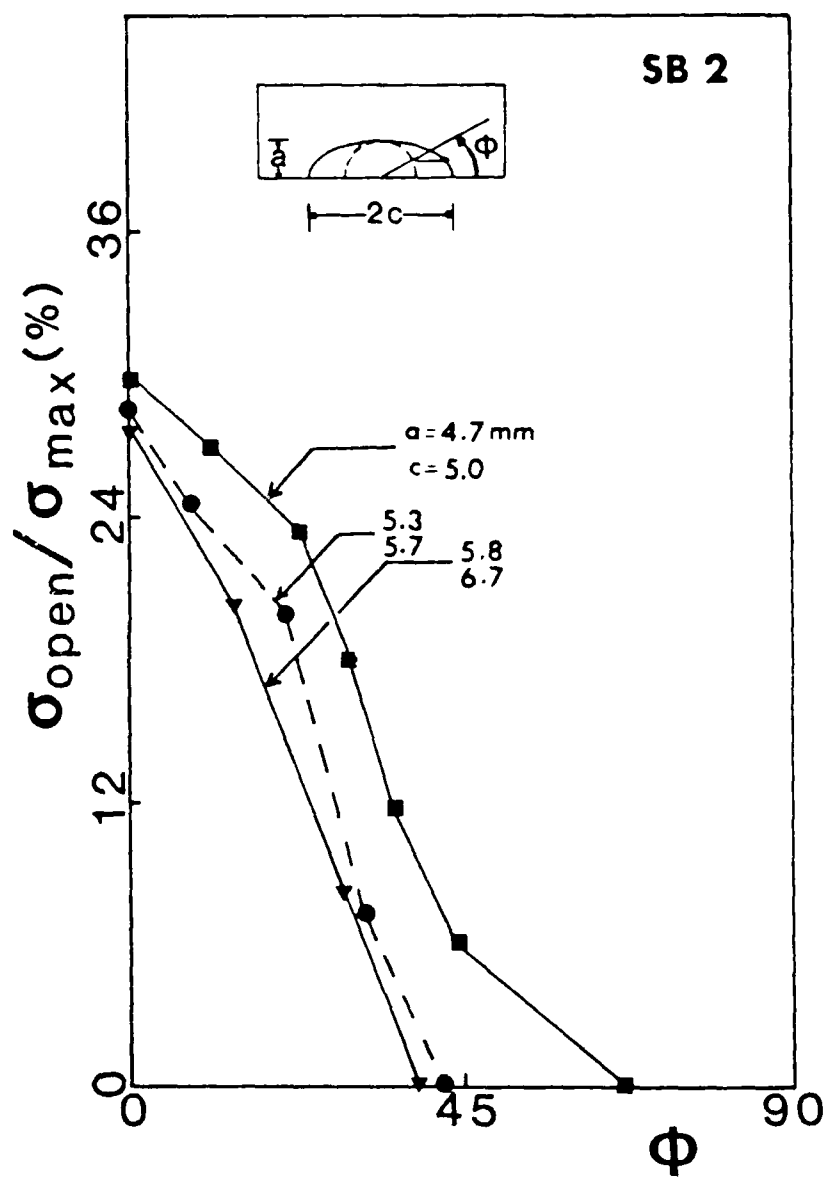


Figure 4.50: Interferometric crack tip opening load as a function of parametric angle  $\phi$  for Test SB-2.

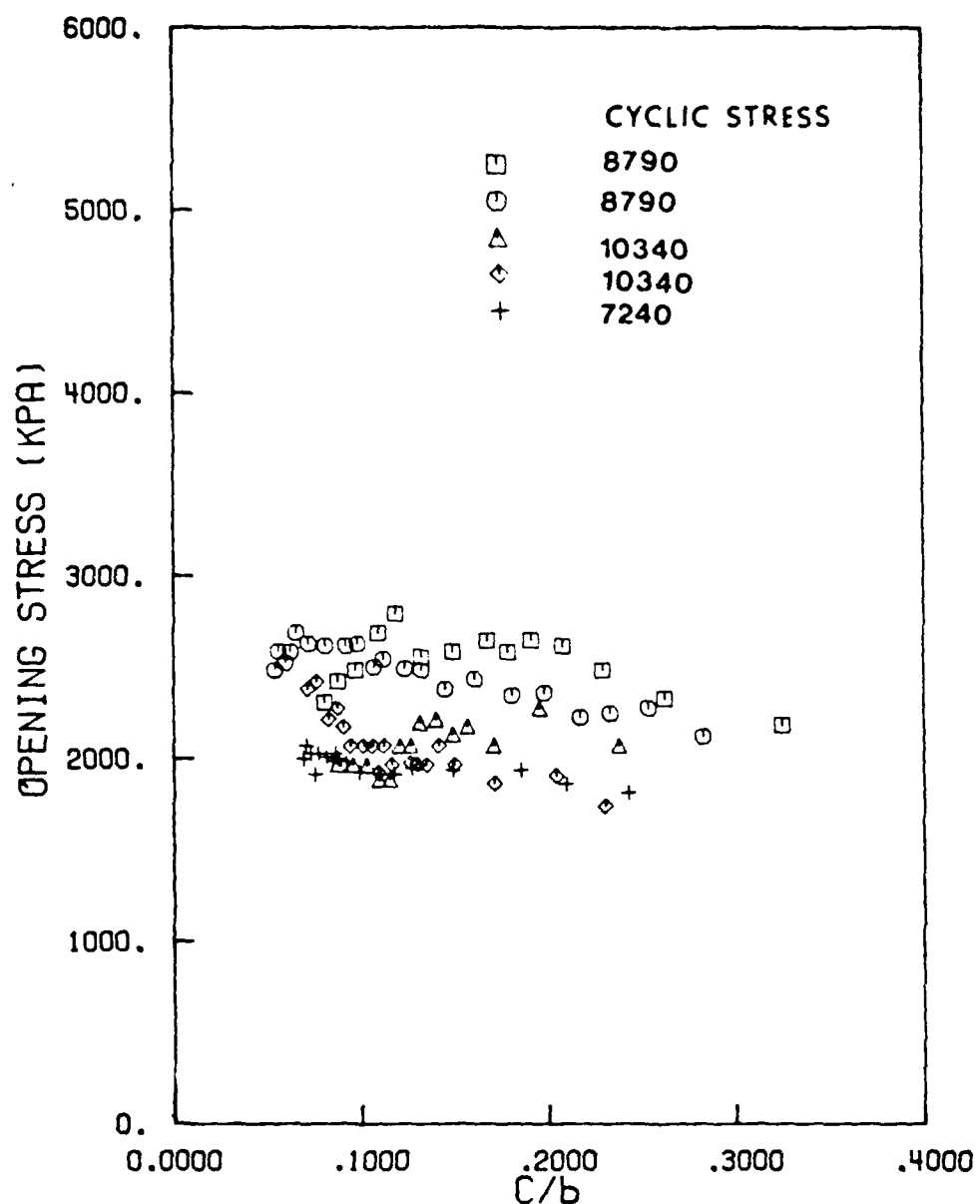


Figure 4.51: Interferometric free surface crack opening stresses as a function of dimensionless crack size for five cyclic bend experiments.

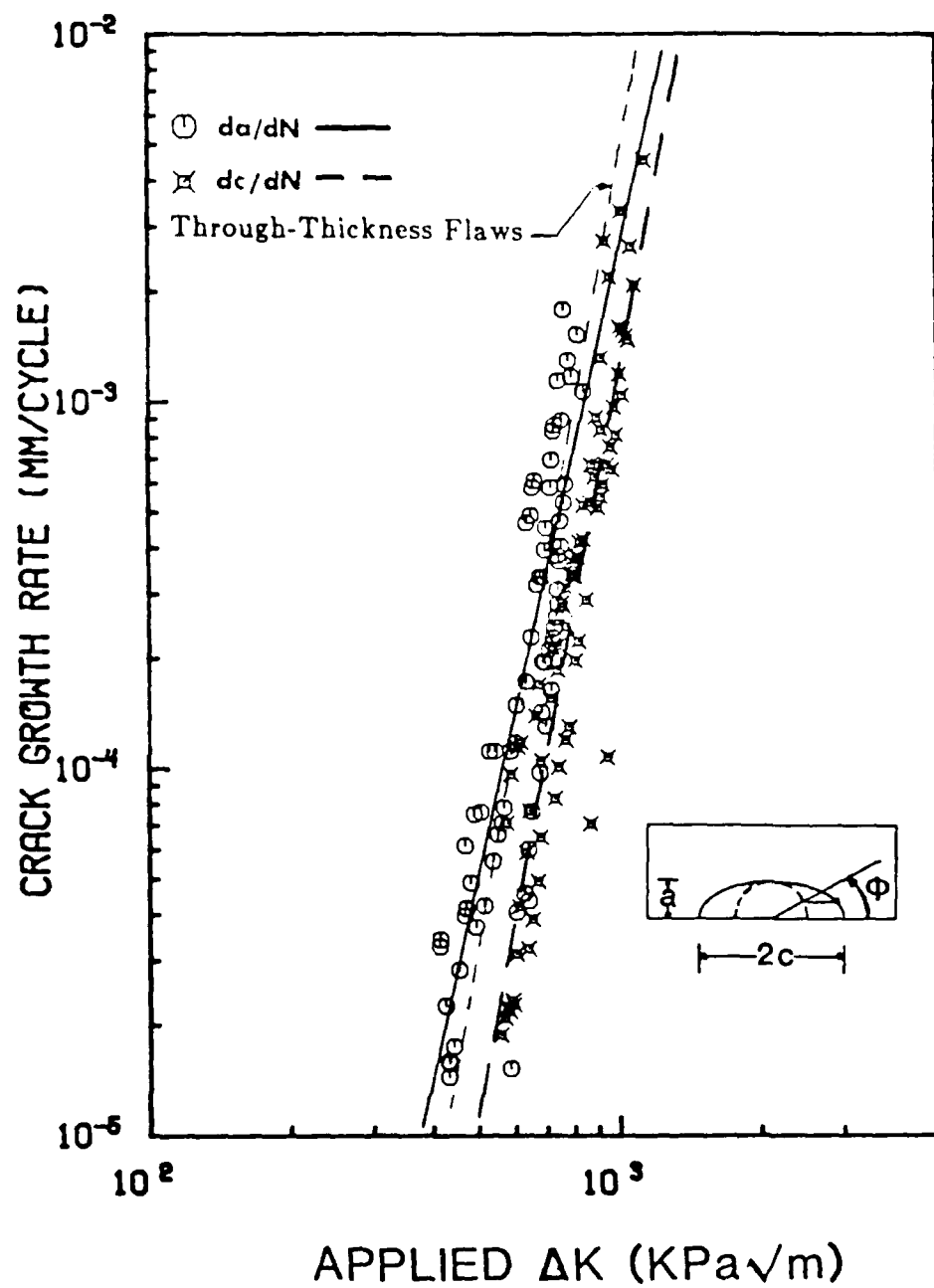


Figure 4.52: Fatigue crack growth rates  $da/dN$  and  $dc/dN$  versus nominal applied  $\Delta K$ .

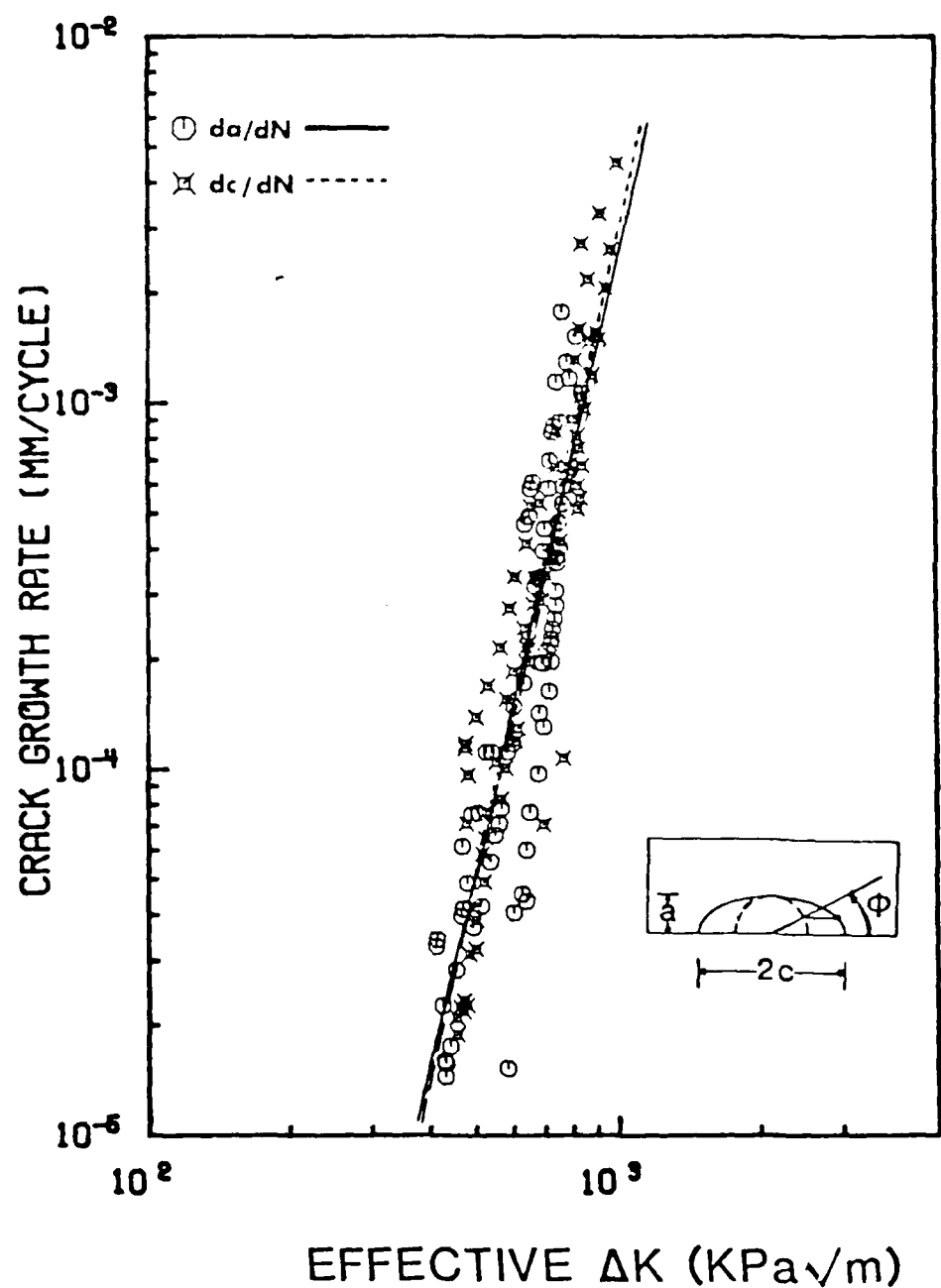


Figure 4.53: Fatigue crack growth rates  $da/dN$  and  $dc/dN$  versus closure corrected effective  $\Delta K$ .

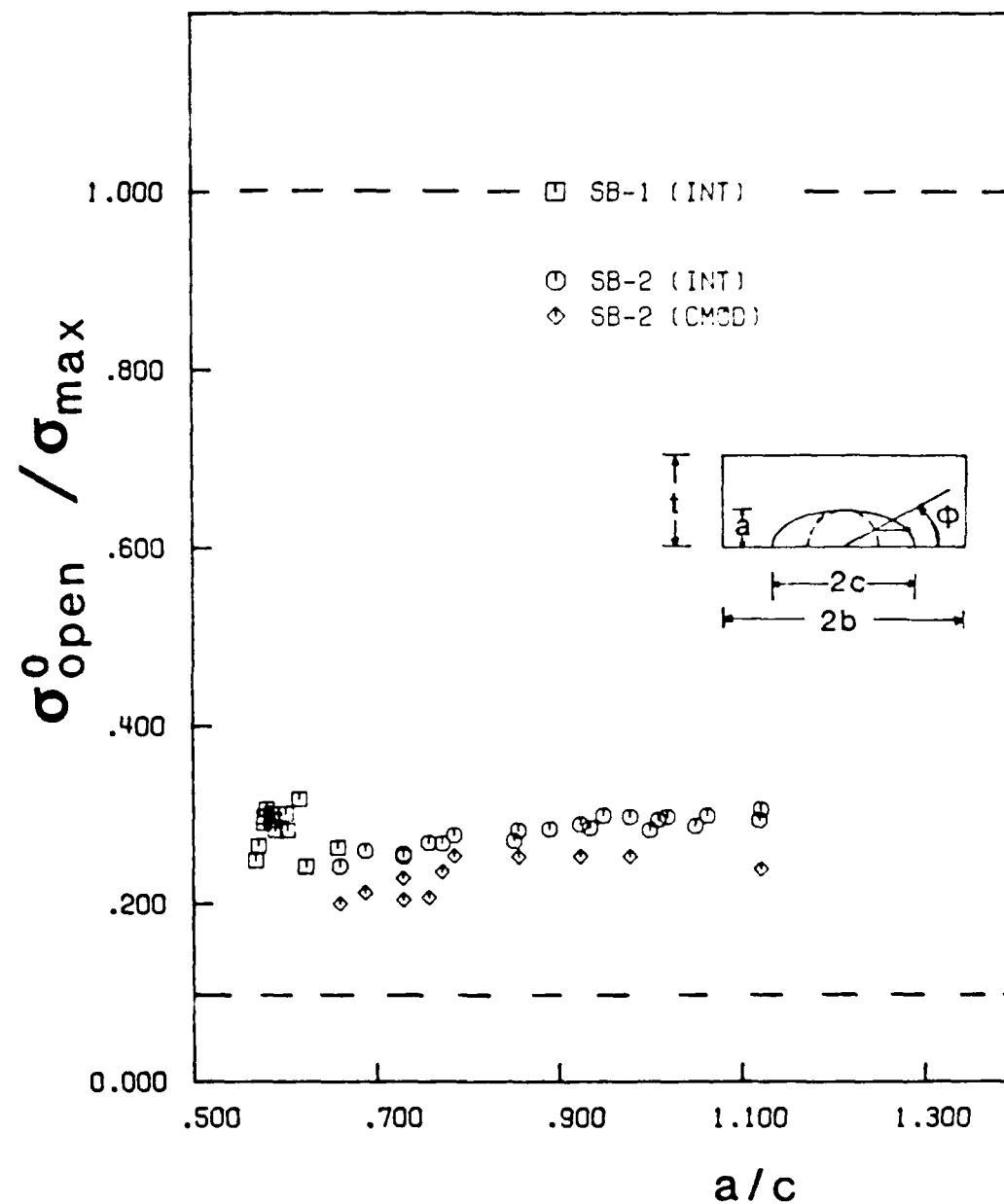


Figure 4.54: Comparison of interferometric free surface opening load with the bulk measurement via crack mouth opening displacement for tests SB-1 and SB-2. The maximum remote cyclic bending stress was kept at 8790 KPa.

## CHAPTER 5

### ANALYTICAL RESULTS

The computer algorithm described in chapter 3 was used to model the 11 different surface flaw experiments which are listed in Table 5.1. The calculation was performed on a Cyber 205 and running times varied from approximately 1000 to 4500 seconds. The running time is dependent upon the applied loads and the amount of total crack growth. The experiments include five bending tests by Ray [50] at three different load levels, four bending tests by Troha [62], and two tension tests by Pope [58]. All tests were performed on polymethylmethacrylate (PMMA) specimens. Sections 5.1 through 5.3 of this chapter will compare some of the experiments with their predicted results. Section 5.4 will examine the sensitivity of the closure model to several different parameters. Section 4.1 of reference [58] reviews the material properties used by the model, which will not be given in this report. Only four models of the surface flaw experiments are summarized in this report. Additional results for the other experiments are given in reference [58].

### 5.1 TESTING BY RAY:

As shown in table 5.1, Ray [50] conducted five bending tests at three different load levels. Optical interferometry was used to determine when closure occurred. All experiments were conducted at an R ratio of 0.1.

The current numerical model predicts significant closure at the interior of the surface cracks, which was not observed in any of the experiments with PMMA. Figure 5.1 shows the predicted interior closure for test SB-1. The model showed good correlation with the experimental results for closure at the free surface for tests SB-1, SB-2, and SB-7 (figure 5.2 shows the predicted free surface closure for test SB-1). These tests were performed at maximum outer fiber bending stresses of 8790 and 7240 Kpa. Tests SB-3 and SB-6 were conducted at loads of 10,340 Kpa and exhibited less closure than the other tests. The free surface closure predictions by the model were considerably higher than the experimentally observed values for tests SB-3 and SB-6 (figure 5.3 shows the experimental and predicted closure for test SB-3) Because of the interior closure calculated by the model, the growth in the a dimension was reduced, and the aspect ratio (a/c) of the modeled crack became less than that of the actual crack. This is shown in figure 5.4 which plots the experimental and calculated aspect ratios for test SB-7.

As the crack grows, the model predicts a slight decrease in closure at the free surface, while closure at the interior decreases and then increases. The reason for the decrease in closure at the free surface appears to be the increase in  $K_{max}$  as the crack length increases. The value of  $K_{op}$  remains nearly constant as the crack grows. The increase in interior closure at high values of  $a/t$  is probably due to the inaccuracy of the weight function

method that was used to calculate  $K_{op}$ . Figures 3.5 and 3.6 show the inadequacy of the method for large cracks ( $a/t > 0.3$ ).

### 5.2 TESTING BY TROHA:

Troha [62] conducted four cyclic bending tests with surface flaws in PMMA specimens. These tests were performed on specimens 76.2 mm wide and 19.05 mm thick, which were machined from a different sheet of PMMA than that studied by Ray. Test 3-11 maintained a constant  $\Delta K$  of 660 Kpa m<sup>(1/2)</sup> at the interior (crack location A) while 3-14 maintained the same  $\Delta K$  at the free surface (crack location C). These constant  $\Delta K$  tests were achieved by appropriate shedding of the applied cyclic moment. A constant cyclic moment of 72.8 N-m was applied to 3-15, while test 3-16 was subjected to block loading (cyclic moments of 72.8, 87.3, 72.8, and 36.4 N-m).

Troha observed phenomena that were not seen by Ray. Troha viewed what he referred to as a "Type II" crack [63]. This type of crack, shown in figure 5.5, exhibits closure at the crack interior, while no contact occurs in the central area of the crack. Troha reported that this type of crack had an aspect ratio ( $a/c$ ) that ranged from 0.75 to 0.65 while  $a/t$  varied from 0.084 to 0.156. As this type of crack grew larger it exhibited the same type of behavior that Ray observed (no interior closure). This type of crack was referred to as a "Type III" crack by Troha, which he defined as a crack that was always open at the interior (point A). In the testing by Ray, the last portion of the crack to open was at the free surface. For Troha's Type III crack, the last point to open was about 12 degrees away from the free

surface (figure 5.6).

Figures 5.7 and 5.8 show experimental and predicted closure for Troha's constant load test 3-15. Figure 5.7 shows good agreement for free surface closure. In figure 5.8 it can be seen that there was some experimentally observed interior closure at small crack sizes. The model predicted much more interior closure than was observed experimentally. Figures 5.9 and 5.10 show experimental and predicted closure for test 3-16, which was subjected to block loading. In figure 5.9 there is a large increase in experimental closure at a  $c/t$  ratio value of approximately 0.4. This is because the specimen experienced a fifty percent decrease in applied moment at this point. The predicted curve does not show this drop because predicted the specimen would fail before the load was reduced. Therefore another computer run was made to analyze test 3-16. In this run crack growth was not predicted by the model, but instead forced to follow the experimentally observed pattern. The results of this run are shown in figure 5.11 as the curve marked "Simulated growth." Although this curve shows the increase in closure at  $c/t=0.4$ , it also shows it decreasing much too rapidly as the crack continues to grow.

### 5.3 TENSION TESTING:

Two cyclic tension tests were performed with surface flawed plates. The specimens were cut from the same sheet of PMMA that was used by Ray, and were oriented so that the cracks grew in the same plane. It was necessary to pre-crack these specimens under bending loads to avoid debonding in the grips. Section 4.4 of reference 58 explains how these

specimens were prepared.

As in the bending tests conducted by Ray, no interior closure was observed for the cyclic tension loading. Considerable closure existed at the free surface. This factor, along with the relative increase in  $K$  at the interior caused the crack to grow much more rapidly in the interior than at the free surface. The  $K$  at the interior during bending was not very high since the bending stress drops off quickly as one moves away from the free surface. Initially, the free surface crack dimension  $c$  grew very slowly in both specimens T-2 and T-3. As observed by Troha and Ray, the point of maximum displacement at minimum load was internal rather than at the free surface. The last point on the crack to open was at the free surface, as Ray observed, rather than at 12 degrees inside the free surface which Troha observed. Figure 5.12 shows that the model did not correctly predict the high free surface closure levels that were observed experimentally when the pre-cracking bending loads were concluded and the tension loads initiated. In these figures  $a/t$  is plotted along the x-axis rather than  $c/t$  because so little growth occurred along the free surface. As in the tests by Ray, the model predicted significant interior closure when none was observed experimentally (figure 5.12).

It is not clear why so much more closure is observed at the free surface than is calculated by the model. The stress distribution under bending load is different from that caused by tension loading (stress under tension loading is constant while stress under bending decreases as distance from the free surface increases), but it is not apparent why this should cause so much closure. The high closure does seem to be a result of the transition from

bending to tensile loading, since closure decreases as the crack grows under tensile load.

#### 5.4 SENSITIVITY ANALYSIS

After the numerical model had been completed and compared with test results, a series of computations were made (see Table 5.2) to determine the sensitivity of closure to several different parameters. These parameters were:

- \* Flow stress
- \* Maximum load
- \* R ratio
- \* Constraint factor alpha
- \* Weight function reference case

Although the modulus of elasticity appears in some of the equations used, it has no effect on the computed closure. Lowering the modulus allows greater displacements of the crack surfaces and the elements that are created are longer, but the contact stresses remain the same, therefore closure remains the same. In his literature survey, Banarjee [5] reports that it has been observed by Fuhring and Seeger [63] that  $K_{op}$  should be independent of the elastic modulus, but this has not been investigated experimentally.

##### 5.4.1 Flow Stress:

Yield stress is used only to determine the convergence limit for the contact stresses. When an iteration causes a change in stress less than two

percent of the yield stress for all elements, the stresses are assumed to have converged. In all other calculations the flow stress, which is the average of the yield and ultimate stress, is used. Case number 1, shown in Table 5.2, was based on Ray's test SB-7. This test had a maximum moment of 79.1 N-m, which corresponds to a maximum outer fiber bending stress of 7240 Kpa (See Table 5.1 for more information.). This experiment was modeled using flow stresses of 13,790, 27,580, 41,370, and 68,950 Kpa (run numbers 2, 3, 1 and 4), and the effect of varying flow stress can be seen in figures 5.13 and 5.14. Note that the effect of flow stress on the closure calculations appears to be negligible. The initially lower values of closure at the free surface for a flow stress of 13,790 Kpa are due to an insufficient amount of pre-cracking. When the flow stress is lowered, several things happen:

- \* The plastic zone becomes larger, and therefore the effective crack length becomes larger.
- \* The elements in the plastic zone and wake become longer.
- \* The maximum stress that develops in the wake is smaller, but contact occurs over a much longer distance

It is the last effect which causes the model to initially predict lower closure values for a flow stress of 13,790 Kpa. Simulated pre-cracking from  $a=2.82$  mm,  $c=3.51$  mm to  $a=3.20$  mm,  $c=3.58$  mm is sufficient for a flow stress of 41,370 Kpa, but not enough for 13,790 Kpa. This is because contact in the 13,790 Kpa flow stress case should extend behind the point where the simulated pre-cracking began. Since the model did not generate any plastic wake in this area (see figure 5.15), it assumes no contact between the crack surfaces. This results in a closure calculation that is too low.

Banarjee [5] reports that while there is some evidence that  $K_{op}$  increases as yield stress decreases, materials with different yield strengths also have different microstructural features. This could result in a variation in surface roughness which might explain the changes in closure associated with yield stress.

#### **5.4.2 Maximum Load:**

According to Newman [19], closure should decrease as the maximum applied load  $S_{max}/\sigma_o$  increases. This effect is most noticeable at higher stress levels and lower R ratios. Taking case number 1 as a baseline, the maximum moment was increased to 158.2 N-m and 237.3 N-m. These runs showed artificially high closure due to the high crack growth rate caused by the high loads. This caused the newly formed elements to exceed the five percent of the plastic zone criterion. Runs that were later made with smaller load increases showed no significant change in closure. Banarjee [5] reports in his literature survey that some investigators have found closure ( $K_{op}/K_{max}$ ) to be independent of  $K_{max}$ , while others have observed a decrease in closure as  $K_{max}$  increases.

#### **5.4.3 R-Ratio:**

Figures 5.16 and 5.17 show the effect of R ratio on crack closure when  $K_{max}$  is kept constant (run numbers 1, 5, 6, 7 and 8), while figures 5.18 and 5.19 show the R ratio effect when a constant cyclic moment is maintained (run numbers 1, 9, 10, 11 and 12). Increasing the R ratio increases the amount of closure because it reduces the compressive yielding in the plastic

wake at minimum load. The compressive yielding shortens the elements in the plastic wake which reduces the contact stresses and therefore closure as well. It should be noted that the amount of pre-cracking required is dependent upon the R ratio. For high R ratios, contact only occurs very near the crack tip, and very little pre-cracking is required. A computer run with an R ratio of -1. was made but the results were unusable because of an insufficient amount of pre-cracking. For figures 5.16 and 5.17 the maximum load for all runs was kept constant. In figures 5.18 and 5.19 the cyclic load was kept constant instead of the maximum load. These figures show the same trend that is evident in figures 5.16 and 5.17. For lower R values, contact occurs over a larger area, and more pre-cracking is required.

According to an early paper (1971) by Elber [3], closure should be related to R ratio in the following manner:

$$K_{op}/K_{max} = 0.5 + 0.1R + 0.4R^2 \quad (5.1)$$

This states that increasing the R ratio should cause an increase in the opening load. This equation also indicates that  $K_{op}/K_{max}$  should have a minimum value of 0.5 for positive R ratios. According to Banarjee [5], values of  $K_{op}/K_{max}$  ranging from 0.15 to nearly 1 have been reported.

#### 5.4.4 Constraint Factor Alpha:

The effect of varying the constraint factor ( $\alpha$ ) was also examined. Alpha is used to simulate the degree of constraint, which affects the amount of closure since more closure occurs under plane stress conditions than under plane strain conditions. In his analysis on aluminum, Newman [19] used  $\alpha=1$  for plane stress and  $\alpha=3$  for plane strain conditions. Because of its

higher poissons ratio,  $\alpha$  was set equal to 5 for plane strain conditions in PMMA. This is explained in more detail in section 4.1 of reference [58]. The degree of constraint around the perimeter was determined by the uniform depth estimation method, which is also explained in section 3.2 of Pope's thesis. Test SB-7 was modeled using three different alpha distributions:

- \* Uniform depth estimation, maximum  $\alpha=5$  (run number 1)
- \* Uniform depth estimation, maximum  $\alpha=3$  (run number 14)
- \*  $\alpha=5$  (plane strain) everywhere (run number 13)

The results of these cases are displayed in figures 5.20 and 5.21 along with the experimentally observed closure loads from Ray's test SB-7. An attempt to model complete plane stress around the crack perimeter ( $\alpha=1$  everywhere) caused  $KOP_a$  to exceed  $KMAX_a$  which resulted in a stoppage of crack growth at A. This caused an arithmetic error to occur in the algorithm. The program is not able to handle cases where the crack completely stops growing at the free surface or the interior.

Figures 5.20 and 5.21 show that closure increases as constraint factor alpha decreases. This is because lowering alpha simulates conditions closer to plane stress and allows greater yielding. Allowing a maximum alpha of 5 seems to correlate better with the test data than a maximum alpha of 3. Increasing alpha increases the maximum stresses ( $\alpha\sigma_0$ ) that can occur in the plastic zone, but it decreases the size of the plastic zone ( $\rho$ ). The net result is that less yielding occurs, and this results in less closure.

#### 5.4.5 Weight Function Reference Case:

The computer algorithm utilizes the weight function method to determine  $K_{cp}$  (see section 3.4 of this report for more detail). This requires the use of a reference case for which the stress intensity factors and crack displacements are known. To test the effect of the reference case on closure calculated by the model, a computer run was made using a tension reference case (case 15) instead of the bending reference case used in all other runs. Comparing calculations 1 and 15 in figures 5.22 and 5.23, it can be seen that the reference case has little effect on closure. The discrepancies that exist between the curves are due to the reference case approximations for the surface crack displacements ( $U_r$ ). The surface crack displacements are necessary to evaluate  $\partial U_r / \partial a$  and  $\partial U_r / \partial c$  in equations 3.2 and 3.3. Initially, the differences in closure loads between runs 1 and 15 are only two percent, but this difference increases as the crack becomes larger. This is consistent with the results shown in figures 3.5 and 3.6. These figures, which compare the results from the algorithm using the bending reference case to the Newman-Raju stress intensity factor solutions, show that the method is less accurate at larger crack sizes. Mattheck et al [60], using a tension reference case, also reported that the method is less accurate at higher  $a/t$  ratios.

In summation, closure predicted by the computer model is affected by certain parameters in the following ways:

- \* Modulus of elasticity has no effect on closure
- \* Flow stress has no significant effect on closure
- \* Increasing the R ratio increases closure
- \* Increasing the constraint factor alpha decreases closure
- \* Maximum load has no significant effect on closure

Table 5.1: Load levels and specimen dimensions of experiments which were modeled numerically

| Experimenter | Cross Section          | Loading | Load Level                                   | Test ID | R Ratio |
|--------------|------------------------|---------|--|---------|---------|
| Ray          | 101.6x23.9 millimeters | bending | 8790 Kpa maximum                             | SB-1    | 0.1     |
| Ray          | 101.6x23.9 millimeters | bending | 8790 Kpa maximum                             | SB-2    | 0.1     |
| Ray          | 101.6x23.9 millimeters | bending | 10,340 Kpa maximum                           | SB-3    | 0.1     |
| Ray          | 101.6x23.9 millimeters | bending | 10,340 Kpa maximum                           | SB-6    | 0.1     |
| Ray          | 101.6x23.9 millimeters | bending | 7240 Kpa maximum                             | SB-7    | 0.1     |
| Troha        | 76.2x19.1 millimeters  | bending | $\Delta K_a = 660$<br>Kpa-m <sup>(1/2)</sup> | 3-11    | 0.035   |
| Troha        | 76.2x19.1 millimeters  | bending | $\Delta K_c = 660$<br>Kpa-m <sup>(1/2)</sup> | 3-14    | 0.035   |
| Troha        | 76.2x19.1 millimeters  | bending | 16,340 Kpa maximum                           | 3-15    | 0.035   |
| Troha        | 76.2x19.1 millimeters  | bending | block loading                                | 3-16    | 0.035   |
| Pope         | 88.9x23.9 millimeters  | tension | 7000-7930 Kpa maximum                        | T-2     | 0.1     |
| Pope         | 88.9x23.9 millimeters  | tension | 7450-6515-5580 Kpa maximum                   | T-3     | 0.1     |

Table 5.2: Summary of sensitivity analysis runs

| Run # | Flow Stress (Kpa) | R Ratio | Alpha               | Maximum Moment (N-m) | Wt. Function Reference Case |
|-------|-------------------|---------|---------------------|----------------------|-----------------------------|
| 1     | 41,370            | 0.1     | Distributed Max = 5 | 79.1                 | Bending                     |
| 2     | 13,790            | 0.1     | Distributed Max = 5 | 79.1                 | Bending                     |
| 3     | 27,580            | 0.1     | Distributed Max = 5 | 79.1                 | Bending                     |
| 4     | 68,950            | 0.1     | Distributed Max = 5 | 79.1                 | Bending                     |
| 5     | 41,370            | 0.      | Distributed Max = 5 | 79.1                 | Bending                     |
| 6     | 41,370            | 0.2     | Distributed Max = 5 | 79.1                 | Bending                     |
| 7     | 41,370            | 0.3     | Distributed Max = 5 | 79.1                 | Bending                     |
| 8     | 41,370            | 0.5     | Distributed Max = 5 | 79.1                 | Bending                     |
| 9     | 41,370            | 0.0     | Distributed Max = 5 | 71.2                 | Bending                     |
| 10    | 41,370            | 0.2     | Distributed Max = 5 | 89.0                 | Bending                     |
| 11    | 41,370            | 0.3     | Distributed Max = 5 | 101.7                | Bending                     |
| 12    | 41,370            | 0.5     | Distributed Max = 5 | 142.4                | Bending                     |
| 13    | 41,370            | 0.1     | = 5 Everywhere      | 79.1                 | Bending                     |
| 14    | 41,370            | 0.1     | Distributed Max = 3 | 79.1                 | Bending                     |
| 15    | 41,370            | 0.1     | Distributed Max = 5 | 79.1                 | Tension                     |

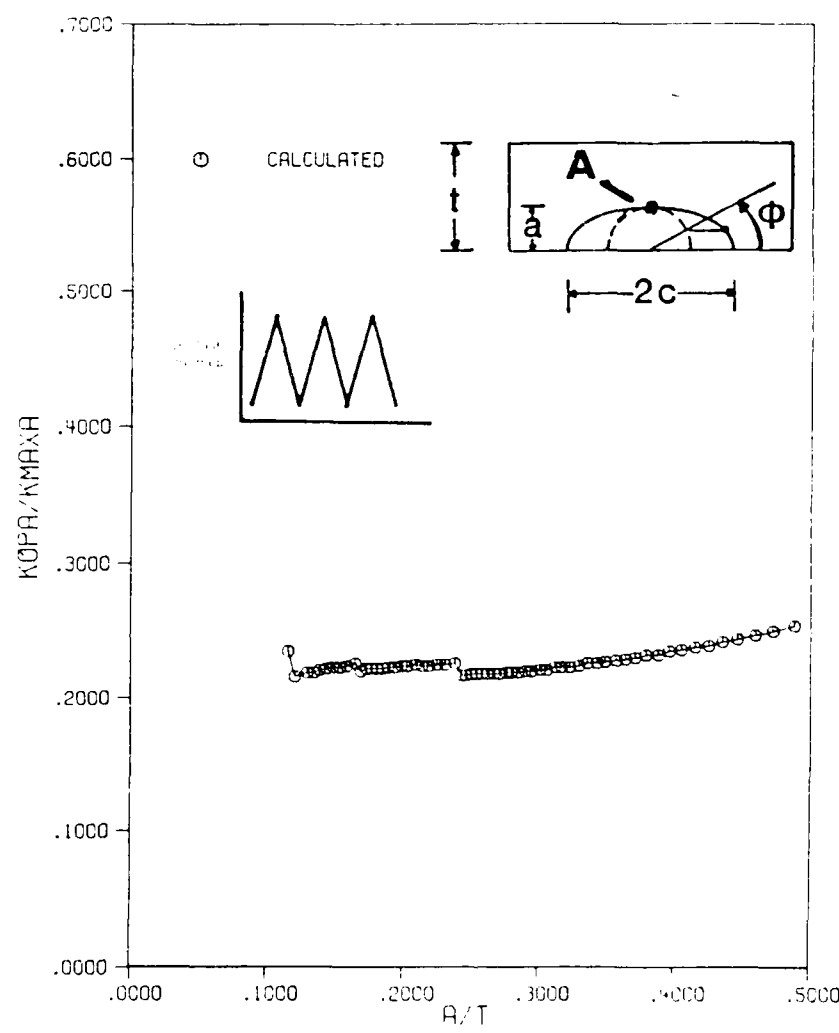


Figure 5.1: Interior closure for test SB-1 max bending stress = 8790 Kpa

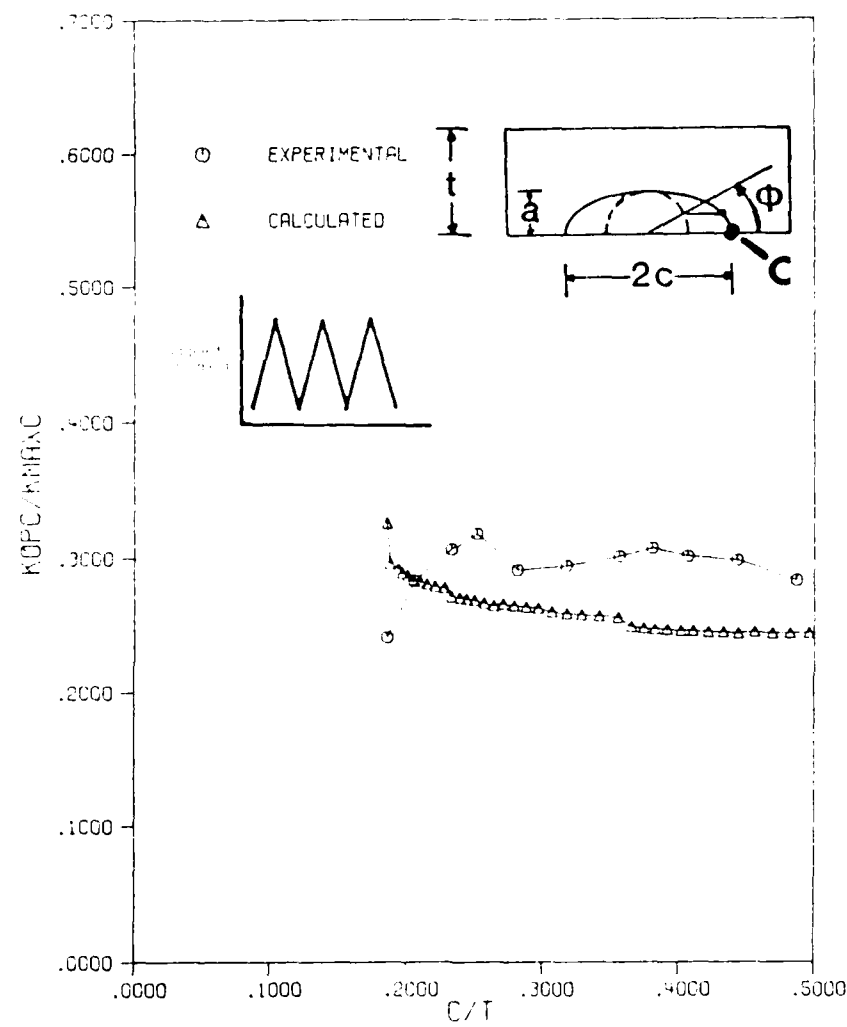


Figure 5.2: Free surface closure for test SB-1 max bending stress = 8790 Kpa

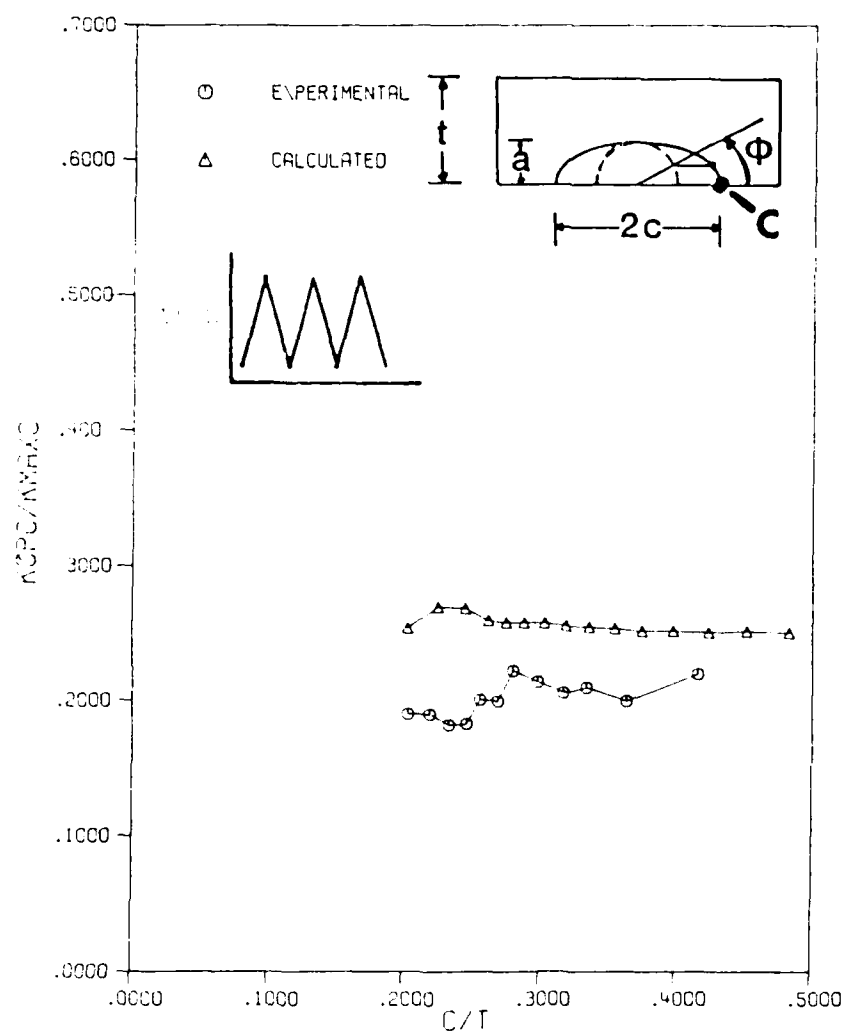


Figure 5.3: Free surface closure for test SB-3 max bending stress = 10,340 Kpa

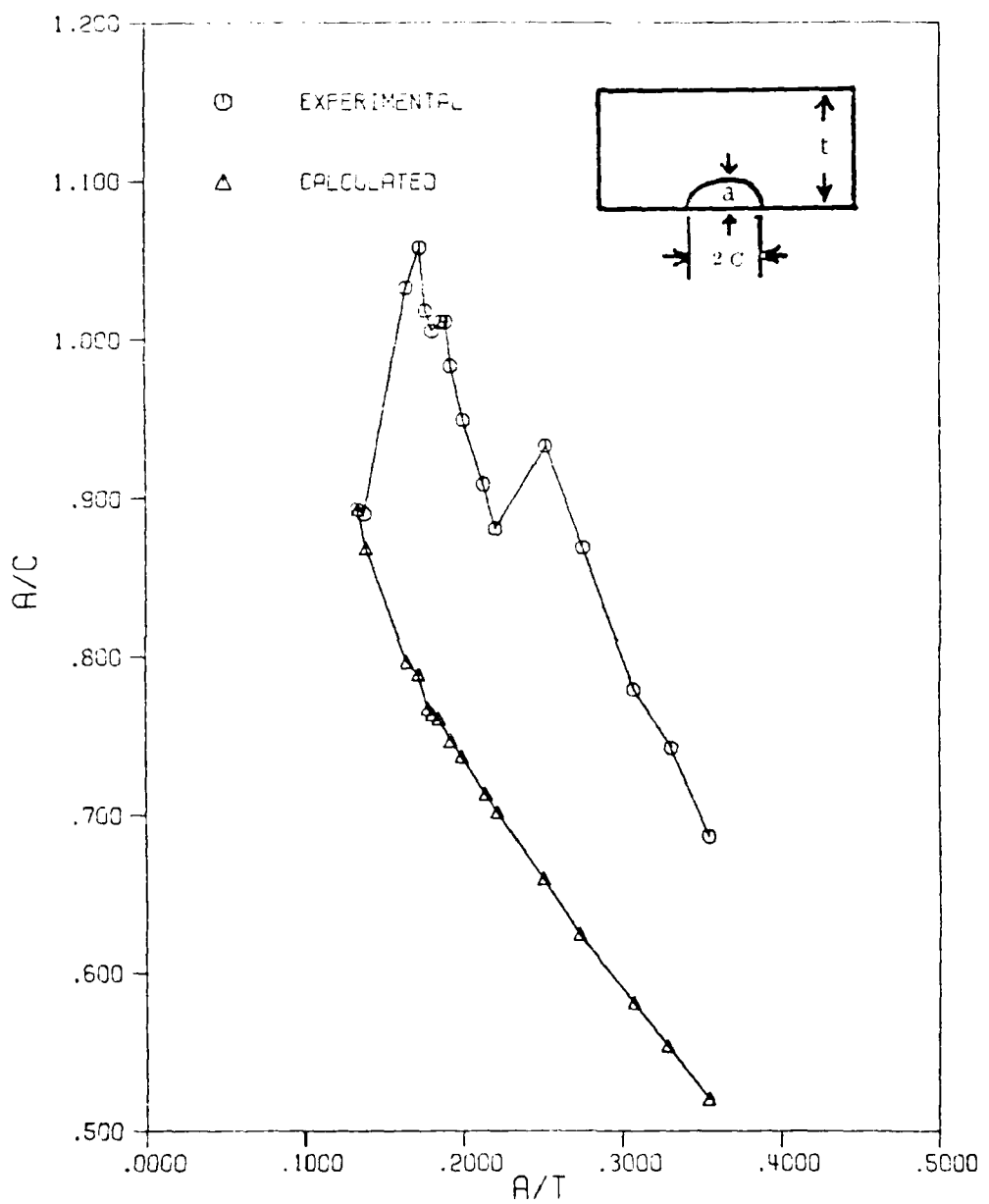


Figure 5.4: Aspect ratios for test SB-7

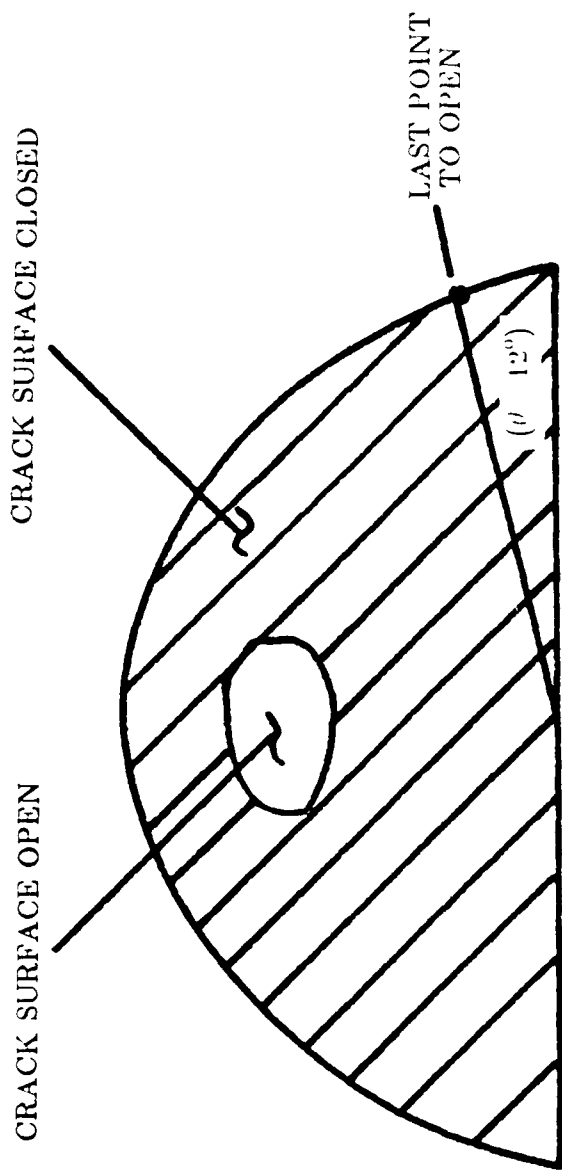


Figure 5.5: Type II crack (reference [63])

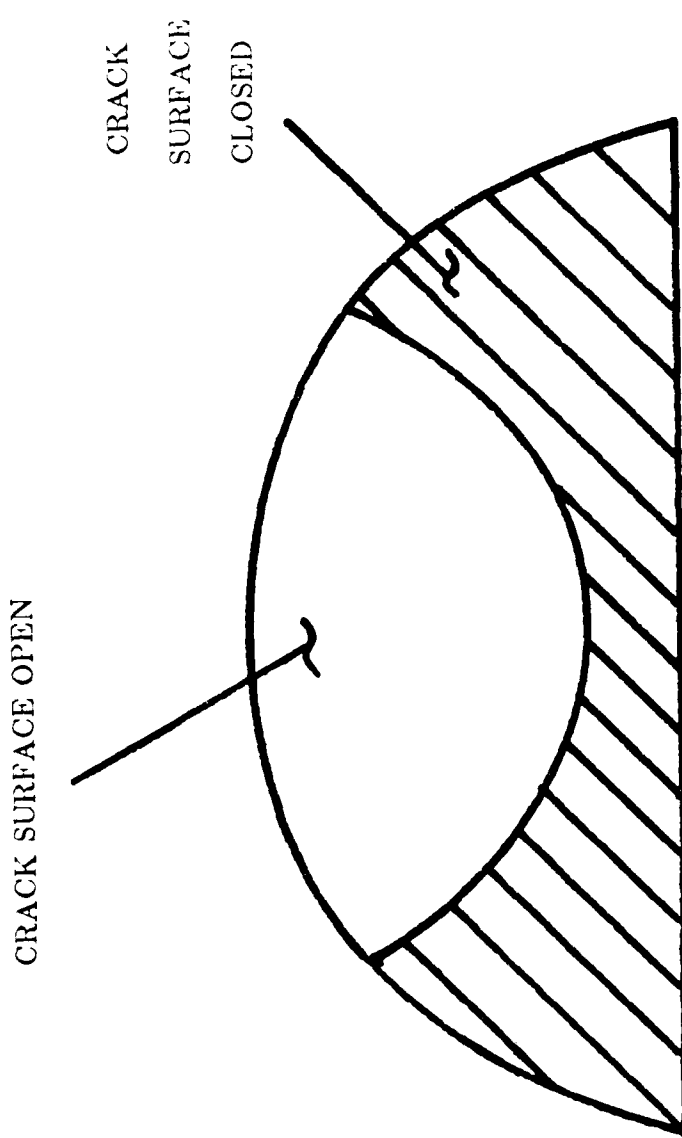


Figure 5.6: Type III crack (reference [63])

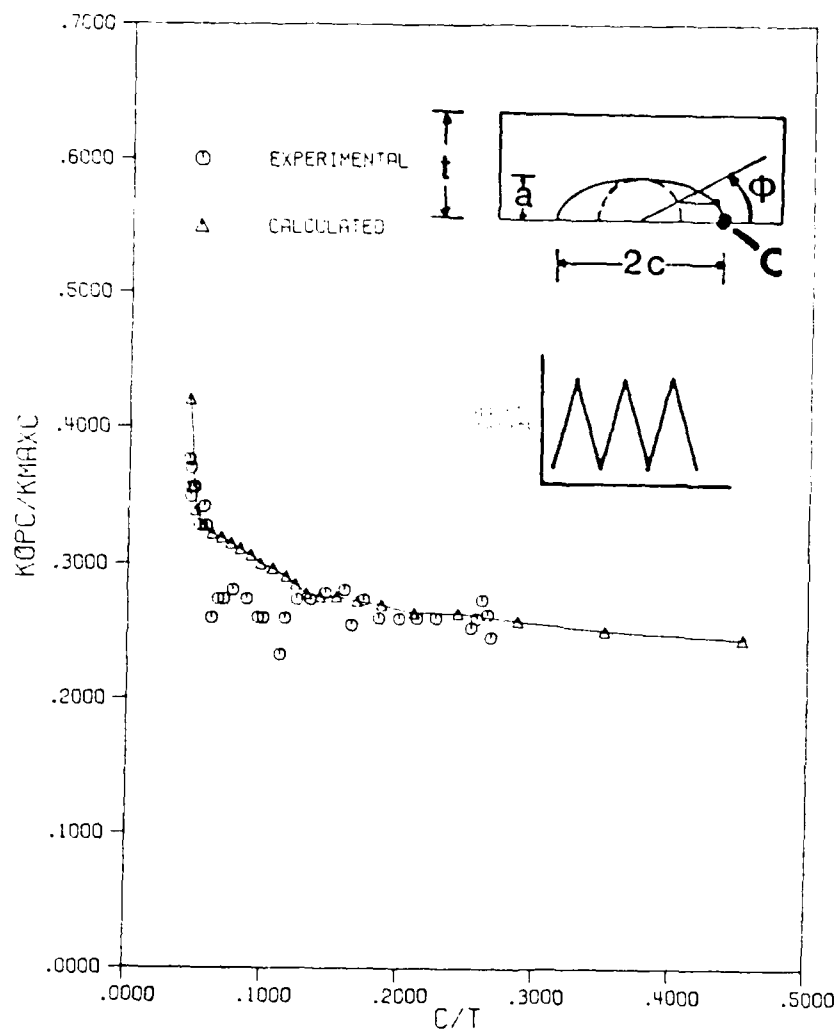


Figure 5.7: Free surface closure for test 3-15 constant load

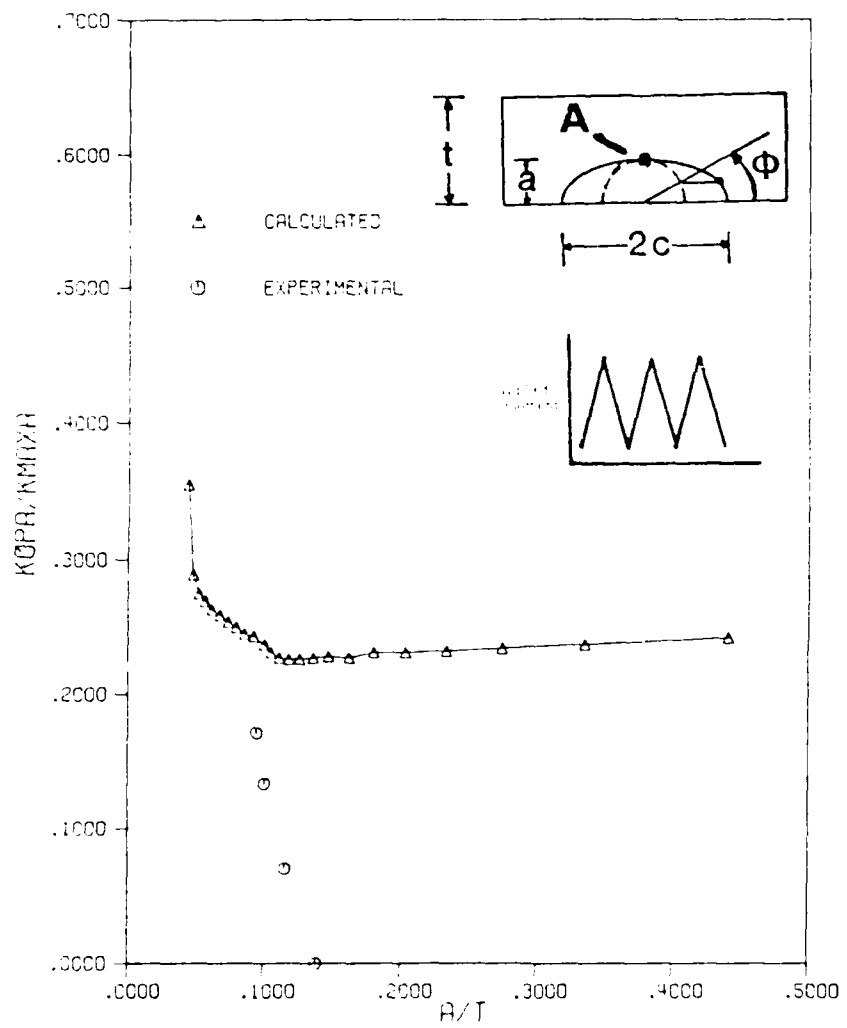


Figure 5.8: Interior closure for test 3-15 constant load

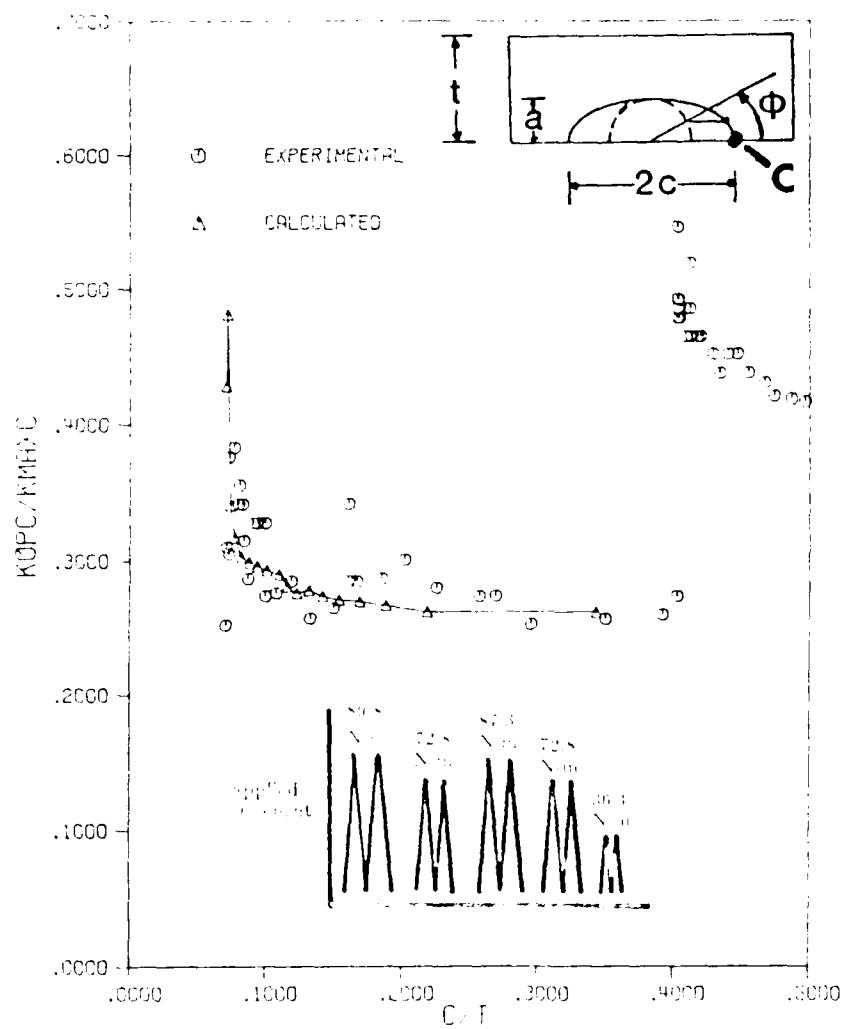


Figure 5.9: Free surface closure for test 3-16 block loading

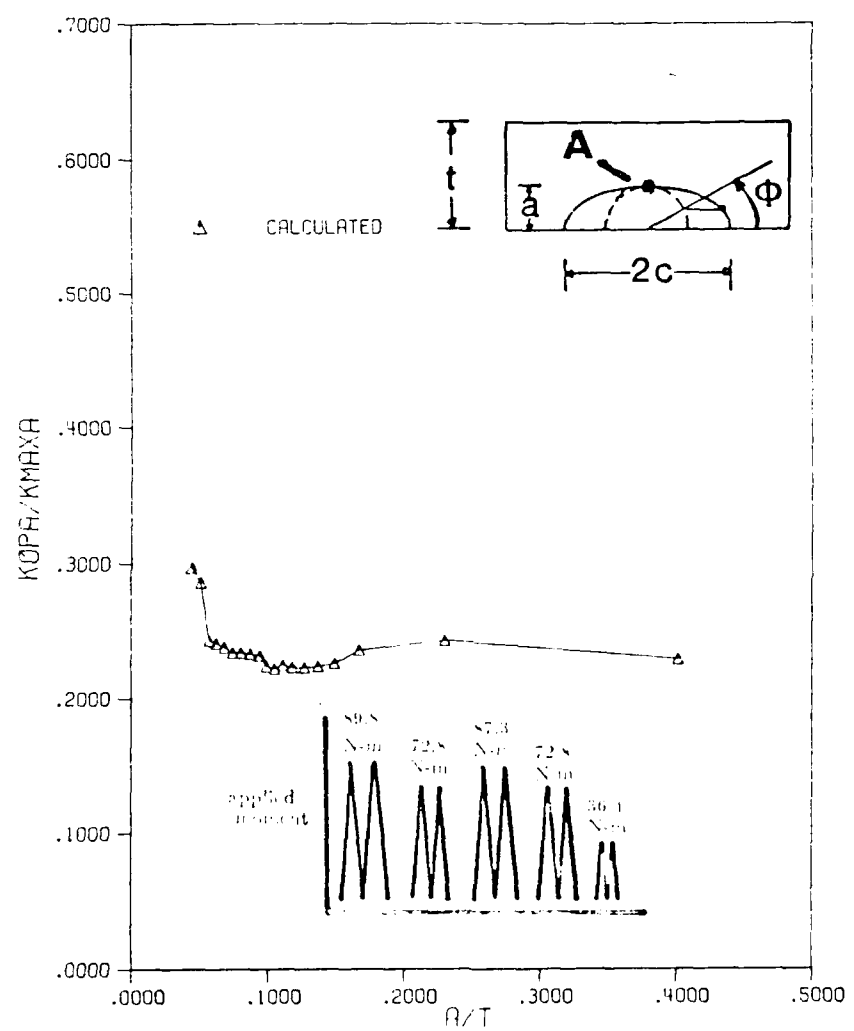


Figure 5.10: Interior closure for test 3-16 block loading

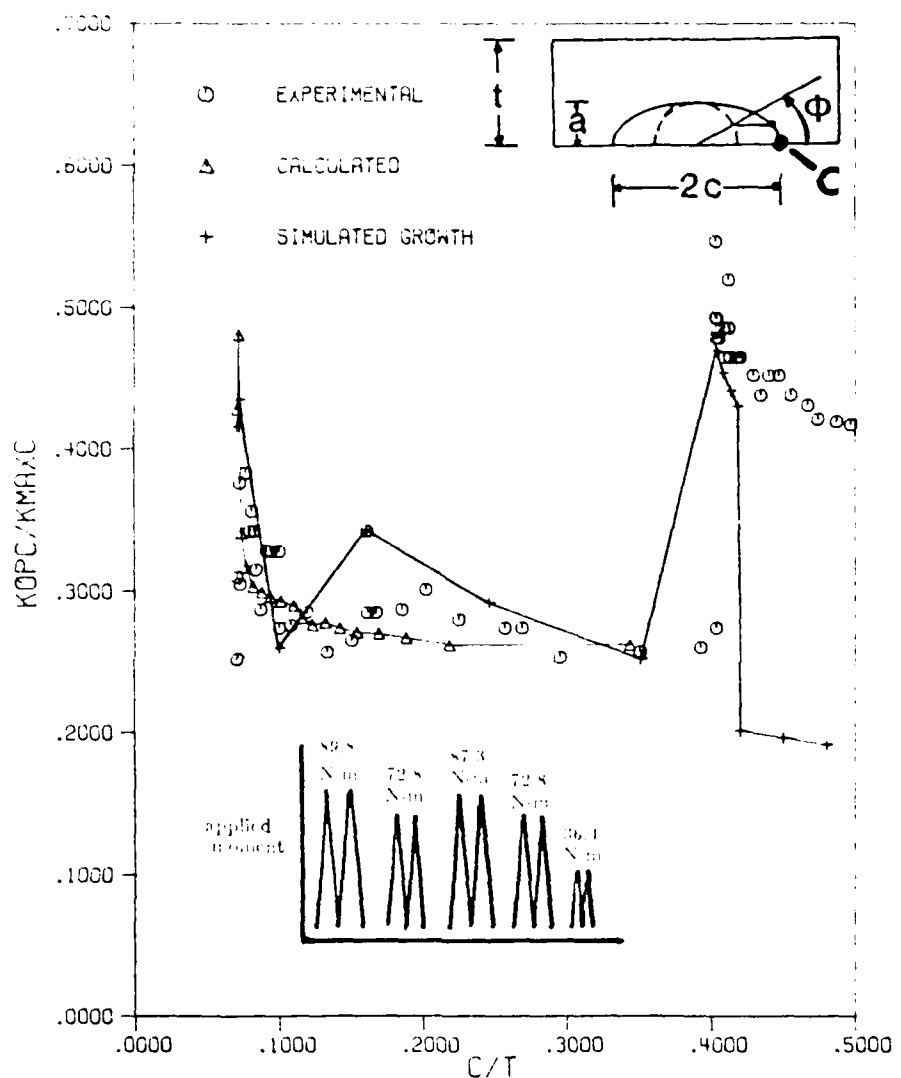


Figure 5.11: Effect of simulated growth on free surface closure for test 3-16

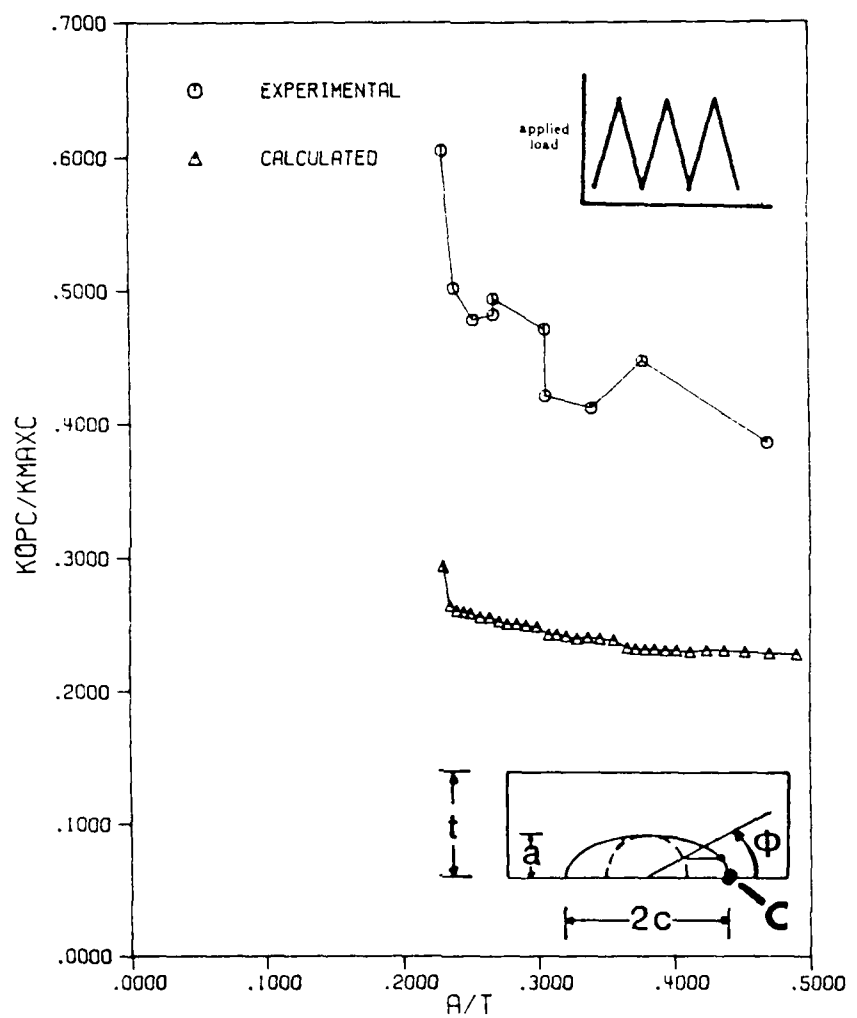


Figure 5.12: Free surface closure for test T-2

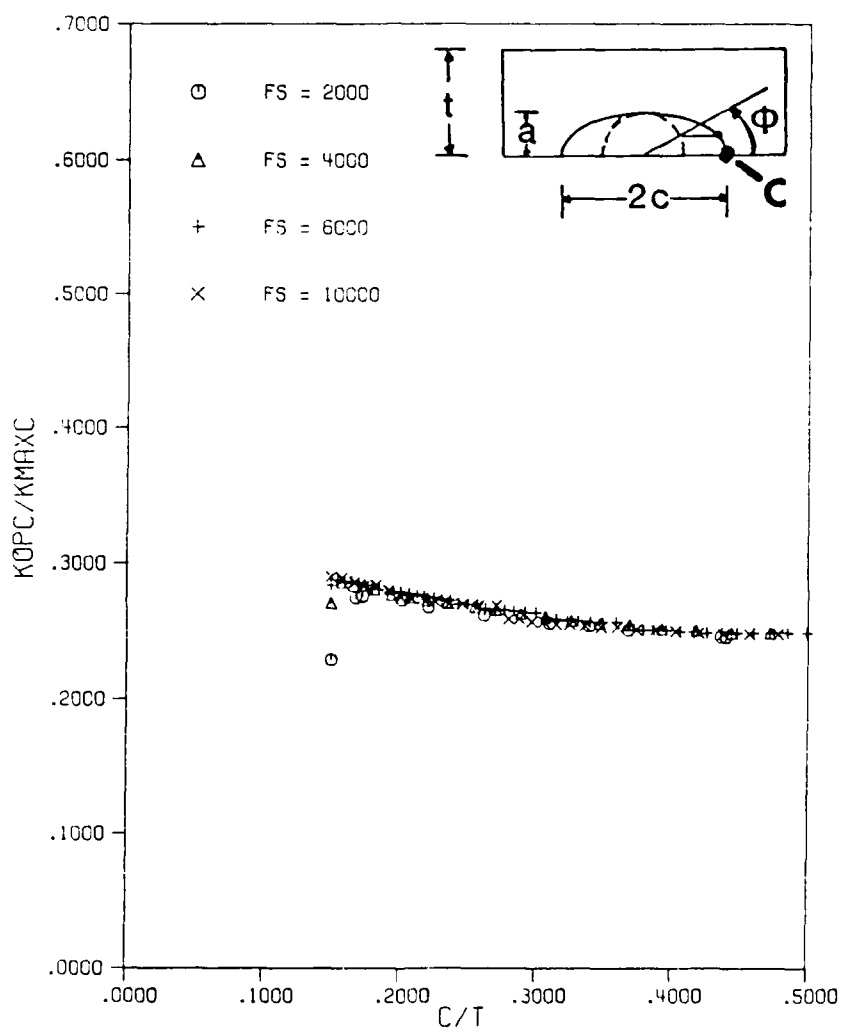


Figure 5.13: Effect of flow stress on closure at the free surface

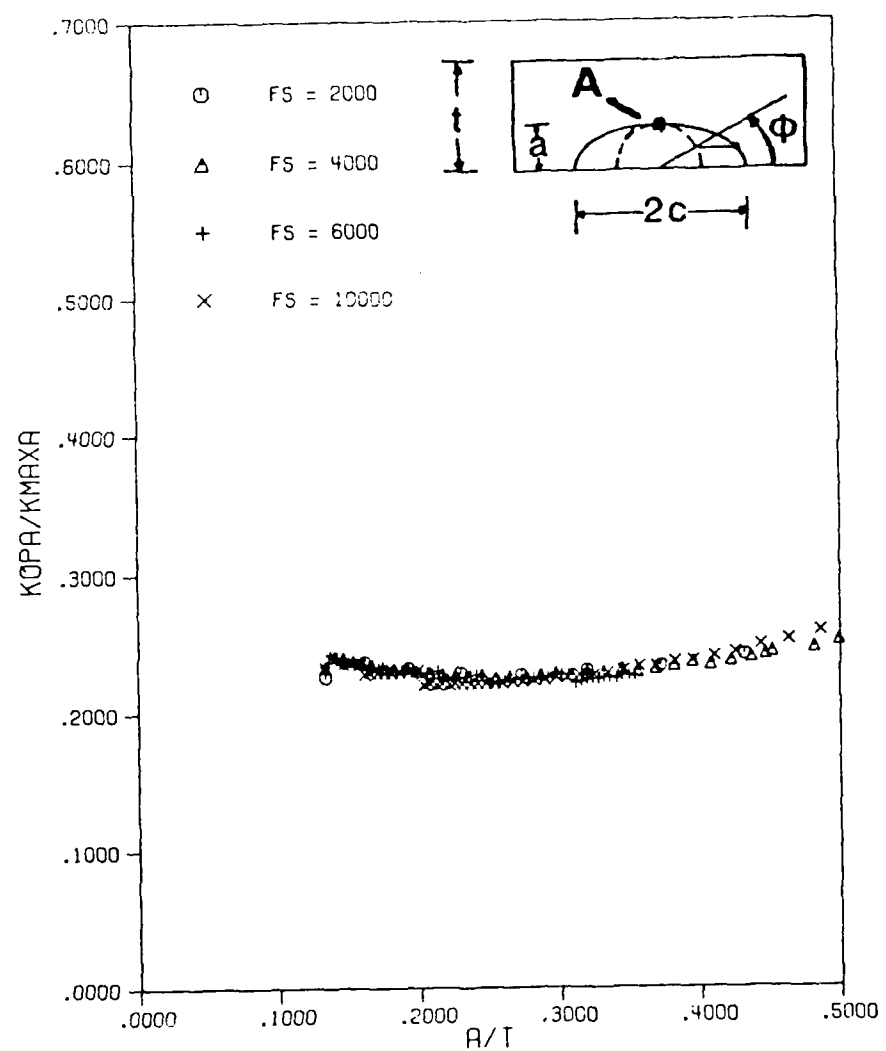


Figure 5.14: Effect of flow stress on closure in the interior

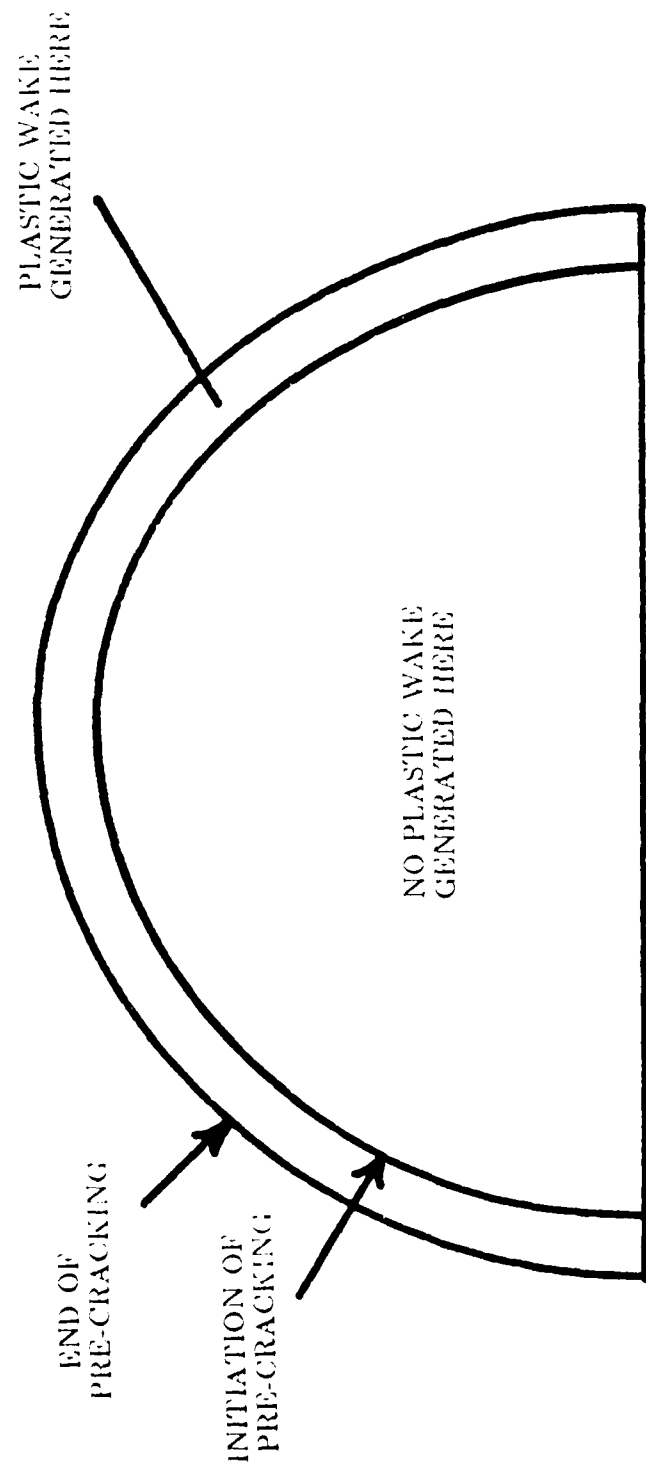


Figure 5.15: Plastic wake due to pre-cracking

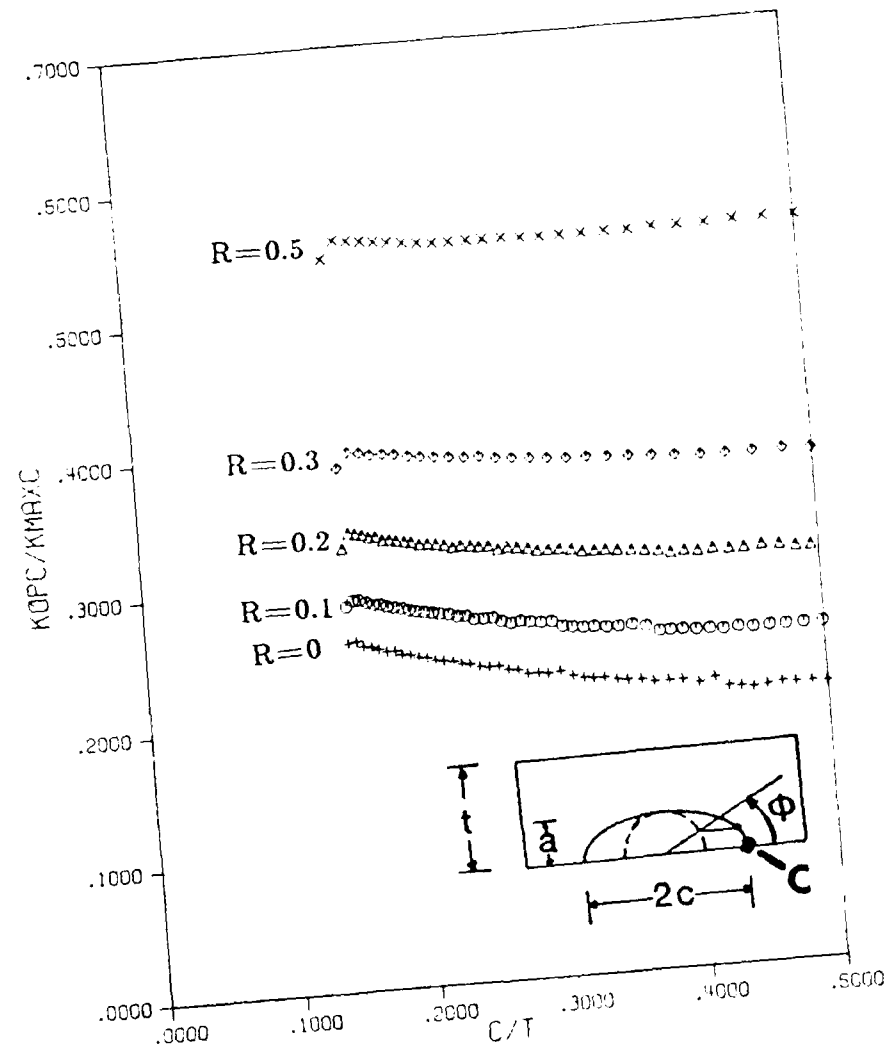


Figure 5.16: Effect of  $R$  ratio on closure at the free surface when  $K_{max}$  is kept constant

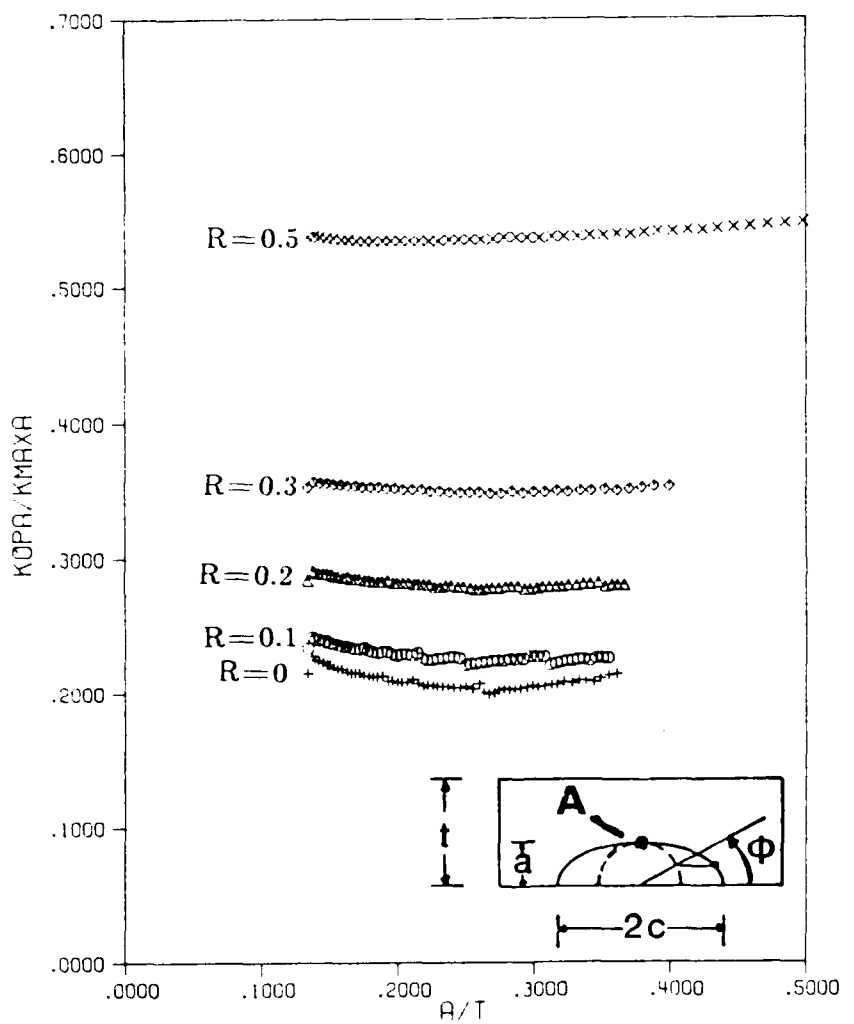


Figure 5.17: Effect of R ratio on closure at the interior when  $K_{max}$  is kept constant

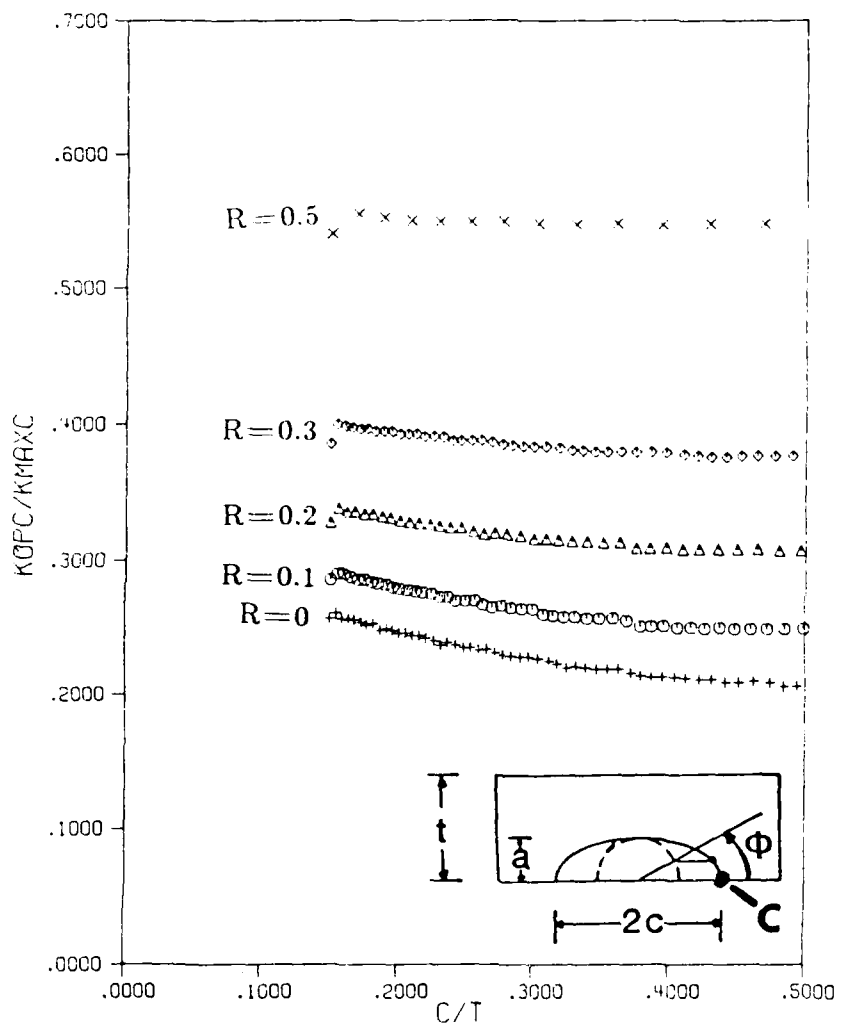


Figure 5.18: Effect of  $R$  ratio on closure at the free surface when  $\Delta K$  is kept constant

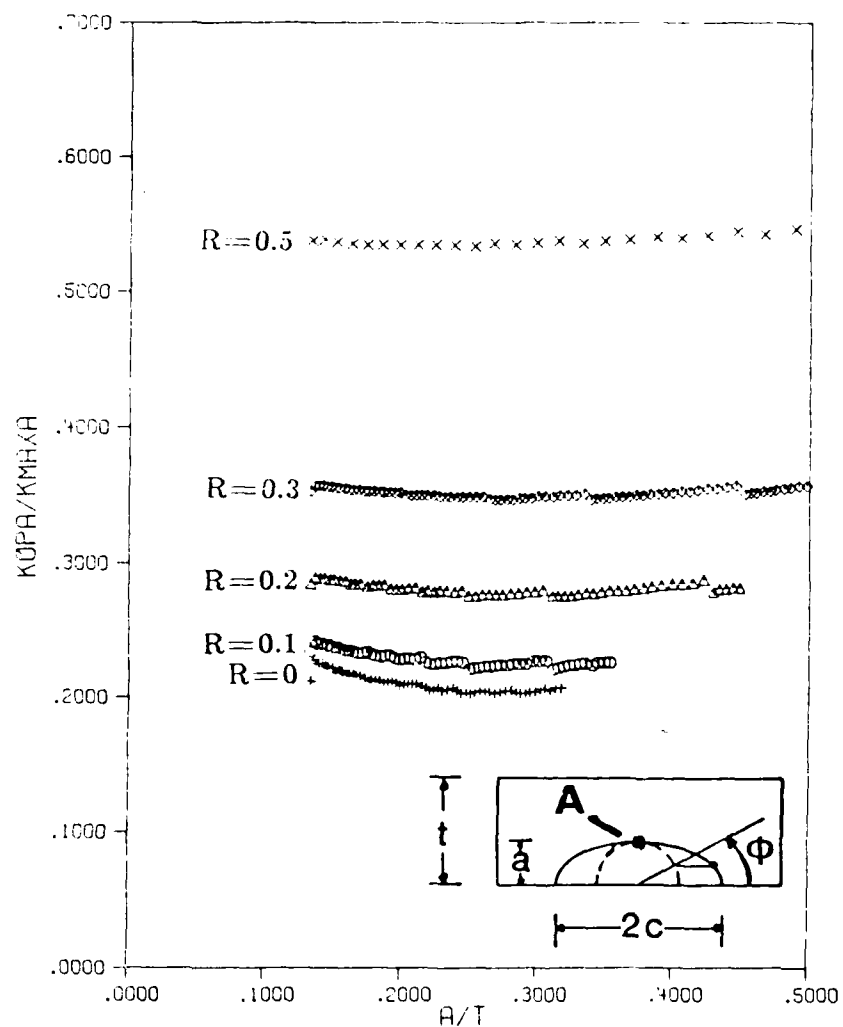


Figure 5.19: Effect of  $R$  ratio on closure at the interior when  $\Delta K$  is kept constant

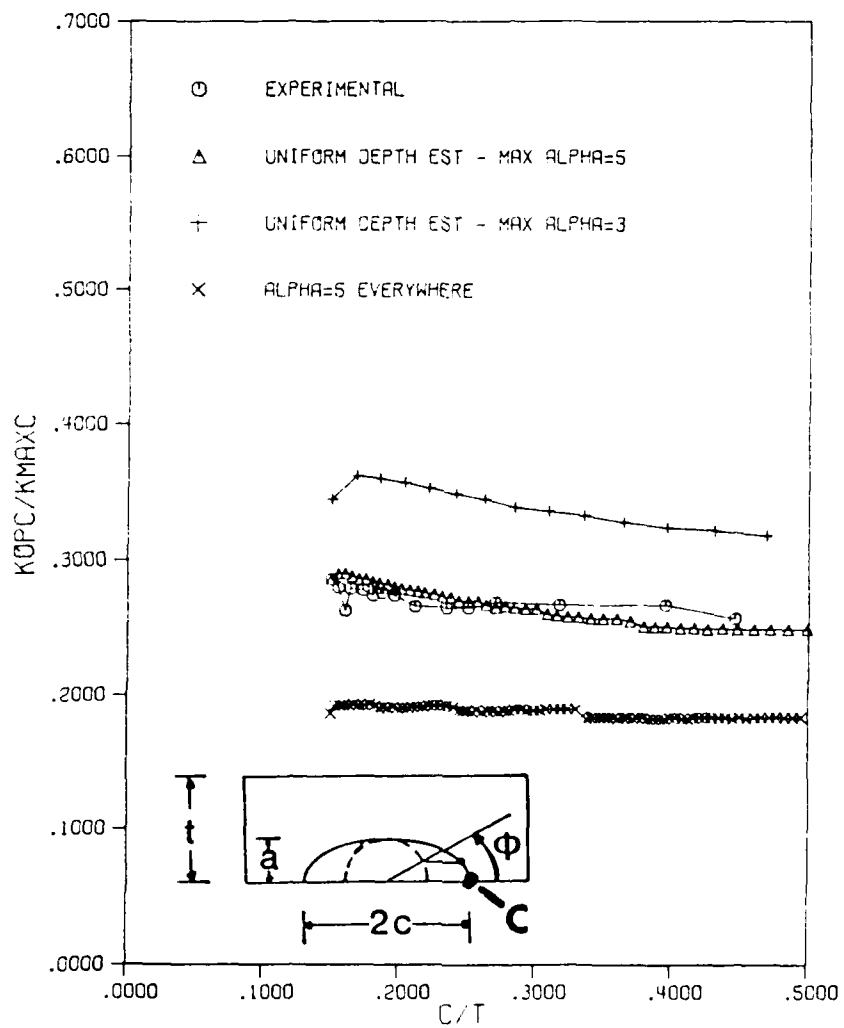


Figure 5.20: Effect of alpha on closure at the free surface for test SB-7

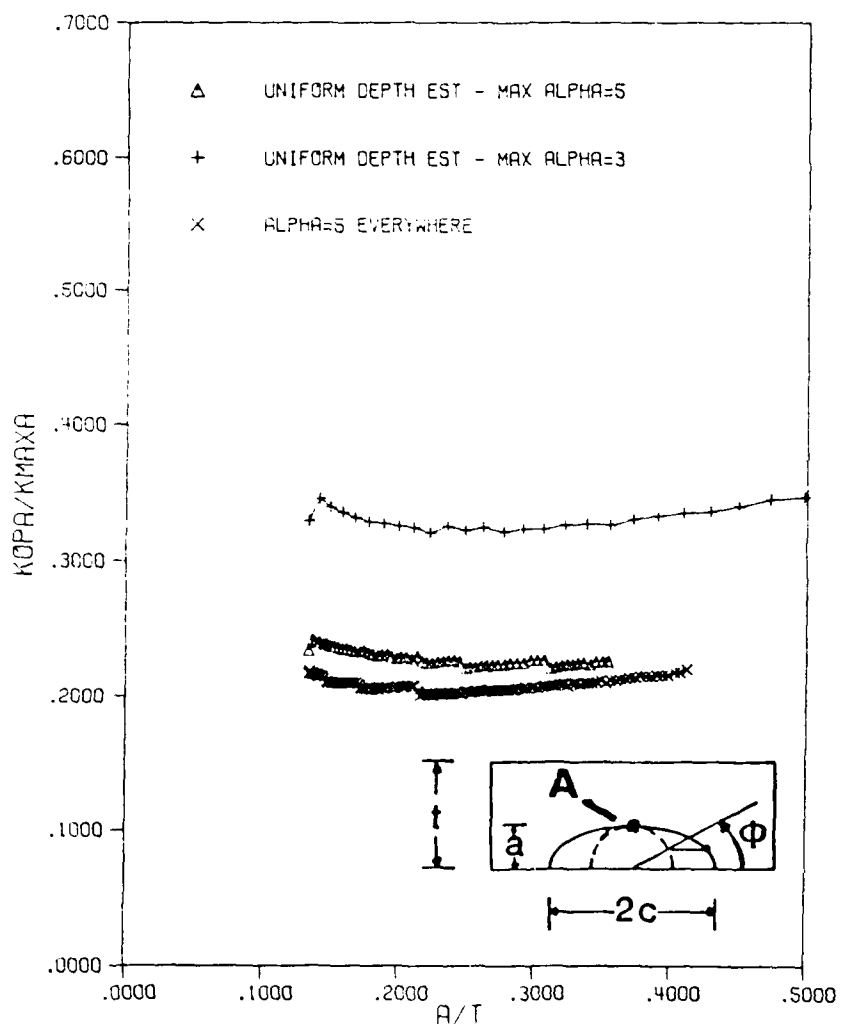


Figure 5.21: Effect of alpha on closure at the interior for test SB-7

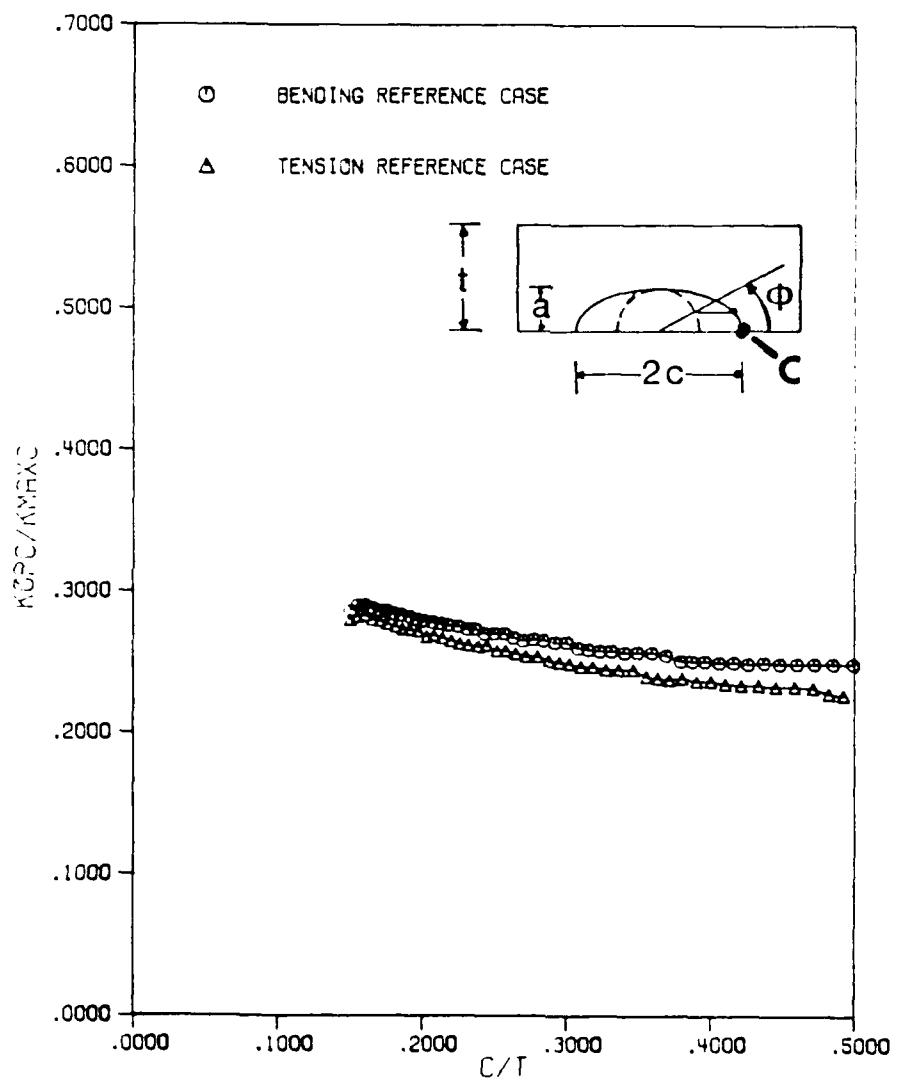


Figure 5.22: Effect of weight function reference case on closure at the free surface

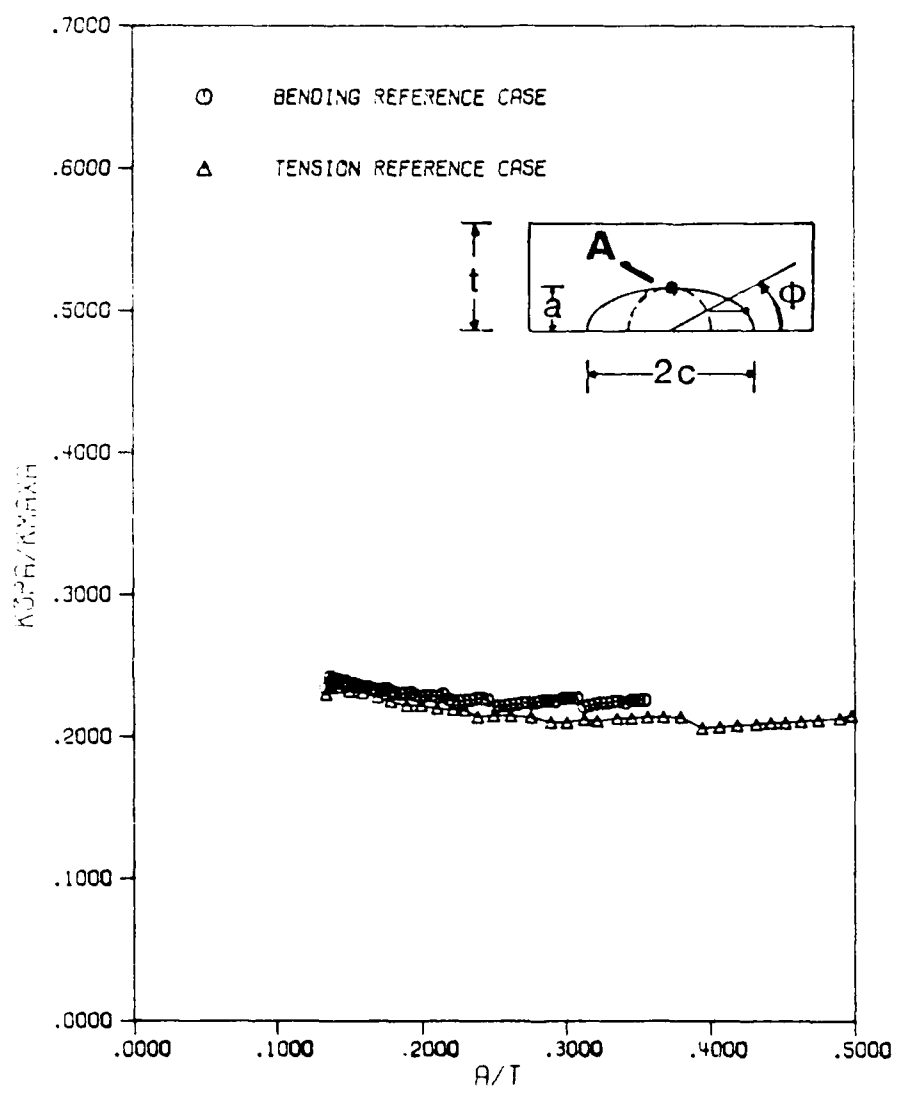


Figure 5.23: Effect of weight function reference case on closure at the interior

## CHAPTER 6

### SUMMARY

The objective of this chapter is to summarize the experimental and analytical results of this project. Section 6.1 summarizes the results obtained from the various through-thickness flaw and part-through flaw experiments conducted with the transparent polymer members. In section 6.2 the polymer crack opening behavior is then examined in context with metal behavior reported by various investigators. The analytical results are summarized in section 6.3.

#### **6.1 SUMMARY OF POLYMER RESULTS:**

Fatigue crack closure experiments were conducted with through-thickness, corner, and surface flaws located in transparent polymer specimens. Optical interference was employed to determine the three-dimensional crack surface displacement field and to characterize local (point-wise) crack closure levels along the crack perimeter. In addition, bulk (average) crack opening loads obtained for certain crack geometries via CMOD and back face strain measurement techniques, were compared with the point-wise measure of crack closure obtained from optical interference.

The optical interference fringe patterns showed that a major portion of the crack surfaces were separated in the thick polymer specimen at zero load. However, a relatively large amount of crack closure was observed at the free surface (plane-stress) locations. Although the crack surfaces in the specimen interior are propped open under zero load, the large level of free surface closure affects subsequent opening at the interior location. For example, in through-thickness cracked members, the mid-plane displacement profile obtained from a numerical elastic analysis agreed well with the experimental results from optical interference, provided that the effect of free surface closure was accounted for. When computing the experimental elastic displacement profile at the specimen's mid-plane, it was necessary to select load levels which caused a major portion of the free surface crack surfaces to remain open (additional details are given in reference [50]).

Although crack tunnelling was observed for various flaw shapes, a quantitative study of the through-thickness flaws showed that the magnitude of crack tunnelling was relatively invariant with crack length. This behavior suggests that the crack growth rate along the specimen's free edge does not vary significantly from the mid-plane crack growth rate, although the closure level at the free surface is significantly higher than the interior location. Thus, the effective cyclic stress experienced at the mid-plane location is not only affected by the closure level at that point, but also by the closure behavior along the free surfaces. This issue is also complicated by the fact that the stress intensity factor for a curved through crack would be expected to vary along the crack perimeter.

Experiments conducted with varying specimen thicknesses showed that crack closure was primarily confined to a strip approximately 2-3 mm wide near each free edge for through flaws in PMMA test members. This transition region (strip) was not significantly affected by specimen thickness or the cyclic  $K_{max}$  level. Thus, a larger percentage of the specimen's thickness was under this transition region for the 'thinner' members. Since the difference in the crack opening behavior between the free surface and the mid-plane was less evident for a thin member, the effective cyclic stress experienced at these two locations did not vary significantly. As a result, the magnitude of crack tunnelling was observed to decrease with a reduction in specimen thickness. Crack tunnelling was also observed with corner flaws located at holes. Here a comparison between the experimental crack front with an assumed quarter-elliptic shape showed that the actual (experimental) crack front in the specimen interior lies ahead of the elliptic shape.

Comparison between the global (average) crack opening loads obtained from CMOD and BFS measurement techniques with the interferometric opening load showed that for a thick member, these bulk opening loads are lower than the free surface opening load. Since a thick member exhibits a significant difference between the free surface and the interior crack opening behavior, these bulk (global) crack opening loads are expected to represent an average quantity for the entire specimen thickness.

## 6.2 CRACK OPENING IN METALS:

The objective here is to compare aspects of the polymer results with the limited amount of information available for experiments conducted by various other investigators with metal members.

Figures 6.1-6.3 present the crack opening loads obtained from various measurement techniques in Rene-95 (a nickel based alloy) specimens. These experiments were conducted with compact tension specimens by Dr. N. E. Ashbaugh, of the University of Dayton Research Institute [49]. Here the metal specimens were subjected to constant cyclic  $K_{max}$  levels. Three different techniques, namely CMOD, BFS, and interferometric displacement gauge (IDG) measurements were employed here to give global and local crack opening load. The IDG method is described in references 35-38 and section 2.2 of reference 50. Recall that the CMOD, and BFS readings reflect a bulk (average) crack opening load, while the IDG measurements provide a local crack opening level for a certain distance behind the free surface crack tip.

Figures 6.1-6.3 compare these various measures of crack opening load. The crack opening loads obtained from the IDG measurements were taken at a point  $7.62 \times 10^{-2}$  mm behind the crack tip on the specimen surface. These figures compare the bulk crack opening (CMOD and BFS) with local free surface (IDG) crack opening for 10, 5, and 2 mm thick specimens.

Note from Figures 6.1 and 6.2 that for relatively thick members, the bulk opening loads fall significantly below the free surface opening loads. This difference in crack opening was also observed with the polymer specimens, and suggests that these thick metal members also exhibit

significant three-dimensional variation in crack opening. On the other hand, Figure 6.3 shows that for a thin member (2 mm thick), the difference between the bulk and free surface opening is not significant, suggesting an uniform crack opening behavior in the thin members.

This variation in crack opening between 'thick' and 'thin' members was also observed with the PMMA through-flaw experiments, where the bulk (average) measure of crack opening load for a thick member was found to be significantly less than the interferometric free surface opening load. Furthermore, interferometric results obtained from polymer experiments conducted with varying specimen thickness showed that crack opening for a thin (5 mm thick) PMMA specimen was uniform across the crack plane, while a 25 mm thick member indicated a large displacement gradient between the mid-plane (interior) and the free edges. Thus the three-dimensional variation in crack opening decreases with a reduction in specimen thickness.

Since the difference in crack opening between the free surface and the mid-plane was less evident for a thin member, the thinner specimens exhibited significantly less crack tunnelling than the thick members. This decrease in crack tunnelling with specimen thickness was also observed in HT80 steel specimens subjected to overloads [9].

Crack closure experiments conducted with other metal members in references [65-67] employing electron fractography showed a difference in the crack opening behavior between the free surface and the mid-plane (interior). Here the specimen's fracture surfaces were marked with a special type of load-sequence, and fractographic studies clearly indicated that the

free surface crack opening load along the free surface of a thick member was significantly larger than the mid-plane crack opening value. Other experiments conducted with a push-rod displacement gage in metal specimens [30-31] also showed similar crack opening behavior, where the crack first opens in the interior followed by subsequent opening along the free edges.

Recently a three-dimensional elastic plastic cyclic finite element analysis of a straight-through crack front [18] predicted the variation in fatigue crack opening load along the flaw perimeter. Here a straight-through crack located in a finite thickness plate was simulated with a tensile cyclic load range between 2.5 and 25% of the material's yield stress. The elastic-plastic finite element analysis was carried out for 10 cycles of load. The crack was allowed to extend one element size (0.03 mm) each cycle, and the opening loads were computed after each load cycle. In this model, as before, the crack first opened in the plane strain interior followed by crack tip opening at the free surface locations as schematically shown in Figure 6.4. Note here that under an applied load of  $0.1 S_{max}$ , the interior portion of the crack starts to open. As the applied load is increased to  $0.36 S_{max}$ , a major portion of the original interior crack tip remains open, while the free surface crack faces are still closed. A load level greater than  $0.56 S_{max}$  is required to separate the crack faces completely along the free edges. Recall that the through-thickness flaw experiments also showed that the crack first opened in the specimen interior followed by free surface opening at a significantly larger load.

Note in Figure 6.4 that unlike the polymer results, where a major portion of the interior crack perimeter remains open under zero load, the numerical analysis in reference [18] shows the crack faces in the specimen interior to be in contact at zero load. However, the contact stresses at the specimen's mid-plane were found to be significantly less than those computed at the plane stress free edges. Furthermore, the numerical study does not include the roughness induced crack closure phenomenon, where the crack surface roughness keeps the crack propped open under zero load. Thus, it is believed here that the initial residual crack opening in the polymer specimen interior may be due to a combination of crack surface roughness and low 'contact stress' level observed at the plane strain interior. Although similar crack surface roughness exists along the free surfaces, the 'large' contact stresses force the free edges to come in close contact, and prevent the crack from opening under a relatively low load at these plane stress locations.

Although a complete three-dimensional experimental investigation of crack opening in metal members may not be possible, the indirect evidence presented above, such as crack tunnelling and fracture surface appearance, clearly suggest a three-dimensional variation in crack opening along the flaw perimeter of a metal specimen. Although it is not known whether the polymer results obtained here describe the crack opening in metal members quantitatively, it is believed that the crack opening behavior in polymer specimens may reflect the corresponding behavior in the metal members qualitatively.

### 6.3 SUMMARY OF ANALYTICAL RESULTS:

Comparison of the closure calculations performed here with the bending tests by Ray and the tension tests performed by Pope reveals a serious deficiency in the model. The model predicts contact between the crack surfaces at the specimen interior where no contact is observed (see figure 6.5). In Troha's experiments, some interior contact was observed, but only for small  $a/t$  ratios (less than 0.156). His experiments were performed with a thinner sheet of PMMA (0.75 versus 0.94 inches) and at a slightly lower  $R$  ratio (0.035 versus 0.1)

Fleck's paper [20] on plasticity-induced plane strain closure may explain this absence of interior contact observed in the experiments. In his study, a center cracked panel and an edge cracked bend specimen were examined with a two-dimensional elastic-perfectly plastic finite element code. Larsson and Carlsson [68] showed the importance of the T-stress (the non-singular stress parallel to the crack plane) for stationary cracks, and Fleck examined its effect on a growing crack under plane strain conditions. Along slice O-6 in figure 3.3, the surface crack may be assumed to act like an edge crack. The T-stress for an edge crack in bending is tensile, which results in a plastic zone at maximum load like that in figure 6.6. Here  $a_0$  is the crack length at which the finite element analysis was initiated, and  $a_f$  is the final crack size. The plastic zones shown in figure 6.6 occur when the crack length is  $a_f$ . The portion of the plastic zone along the crack flank yields in tension in the  $x$  direction. This counteracts the earlier yielding that occurred in the plastic zone ahead of the crack tip and reduces the size of the plastic wake elements. The net result is less closure since there is less

material to wedge the crack open.

All experiments reviewed in this report showed that the maximum displacement did not occur at the crack mouth, as might be expected, but occurred at the crack interior. Fleck's paper also sheds some light on this phenomenon. A crack under plane stress closes continuously, which means that contact first occurs immediately behind the crack tip and then proceeds back toward the crack mouth. In a plane strain situation, discontinuous closure occurs after the crack has grown a short distance from its initial flaw size. Discontinuous closure means that contact first occurs immediately behind the crack tip and next occurs far behind the crack tip as shown in figure 6.7. In this figure, the gap between the crack surfaces at minimum load,  $\delta_{\min}$ , divided by the quantity  $K_{\max}^2/\sigma_y E$  is plotted along the ordinate. The distance behind the crack tip,  $x$ , divided by  $K_{\max}^2/\sigma_y^2$  is plotted along the abscissa. Figure 6.7 shows the displacement profiles for both center cracked panel and bend specimens. Notice that the point of maximum displacement is much closer to the crack tip than the crack mouth. This is the same type of behavior that has been observed in the specimen interior for the surface crack experiments.

Ray conducted experiments at three different stress levels. As expected, the medium stress level exhibited higher free surface opening loads than the lower stress level tests. The highest stressed tests had lower free surface opening loads than the medium stressed tests. The computer model does not predict this trend. As the applied load is increased, the model will always predict higher opening loads. This discrepancy may be due to the effect of the T-stress. Fleck reported that for plane strain conditions, no plasticity-

induced closure would occur if the ratio  $T_{max}/\sigma_{ys}$  is greater than a critical value between 0.035 and 0.070.

In Troha's tests, he noticed that as load was applied, the last point on the crack perimeter to open was not at the free surface but about twelve degrees inside the free surface. Elastic plastic finite element analysis by Trantina [69] on semicircular surface cracks showed that the highest stress occurred at about fifteen degrees from the free surface. This was due to the redistribution in load, and may be responsible for the opening behavior that Troha observed. His specimens were thinner than those of the other experimenters, which may be why this phenomena was not observed by others.

The computational model used in this project is based on the plasticity-induced closure mechanism only. The roughness induced mechanism, which is usually significant only for small crack or near threshold cases, is not accounted for in this model. In most cases analyzed in this paper, the predicted closure is greater than the actual closure, so the inclusion of a roughness induced mechanism would not reduce these discrepancies. Visual inspection of the fracture surfaces of specimen T-2 showed smooth transparent surfaces. Also the interference fringes appeared to be reasonably distinct. In the case of polycarbonate [7], the interference fringes cannot be seen when the crack is grown at high values of  $\Delta K$ , which causes the crack surfaces to become rough.

From this project the following conclusions can be drawn:

1. The free surface closure values predicted by the model correlate well with most of the experiments examined.

2. The model predicts closure in the interior where none or very little is observed.
3. At minimum load the maximum displacement is observed to occur at an internal location, while the model assumes it occurs at the crack mouth.
4. Experiments show that  $K_{op}$  may decrease when load is increased. The model predicts  $K_{op}$  always increases as the load increases.

The basic method of the model appears to be valid, but the equations used to calculate yielding and displacement seem to be inadequate. Since the observed contact is very different from that predicted by the model (figure 6.5), either the calculated displacements of the crack surface or the lengths of the plastic wake elements are incorrect. In the current model, the effect of yielding along the crack faces in the plastic wake is ignored. This could cause elements in the plastic wake to be too large, which would result in erroneously high values of  $K_{op}$ . In determining the displacement of the surface crack under remote loading, it is assumed that the crack displaces along various slices (figure 3.1) like a center cracked panel. This results in the maximum displacement occurring at the crack origin. Under minimum load it is observed that the maximum displacement occurs well inside the crack. This indicates that the displacement of the surface crack is much more complex than the model assumes.

Several recommendations can be made for future research work on surface crack closure modeling:

1. A three-dimensional elastic-plastic finite element analysis of a

growing surface crack should be performed. This type of analysis has already been done for an edge crack by Chermahini [18], and if performed for a surface crack, would give a better understanding of the contact stresses occurring in the plastic wake.

2. A better elastic displacement equation for the surface crack needs to be developed. The method used in the present model incorrectly predicts the location of the maximum displacement.
3. More testing should be performed to determine the effect of specimen thickness on surface crack behavior. Some differences in behavior have been noted between Ray's 0.94 and Troha's 0.75 inch thick specimens.
4. More testing should be performed to determine the effect of load level for constant amplitude loading. Testing by Ray has indicated that  $K_{op}$  can decrease or increase as applied load is increased.

Accomplishing these four items should lead to a better understanding of closure in surface cracks and facilitate improved closure modeling.

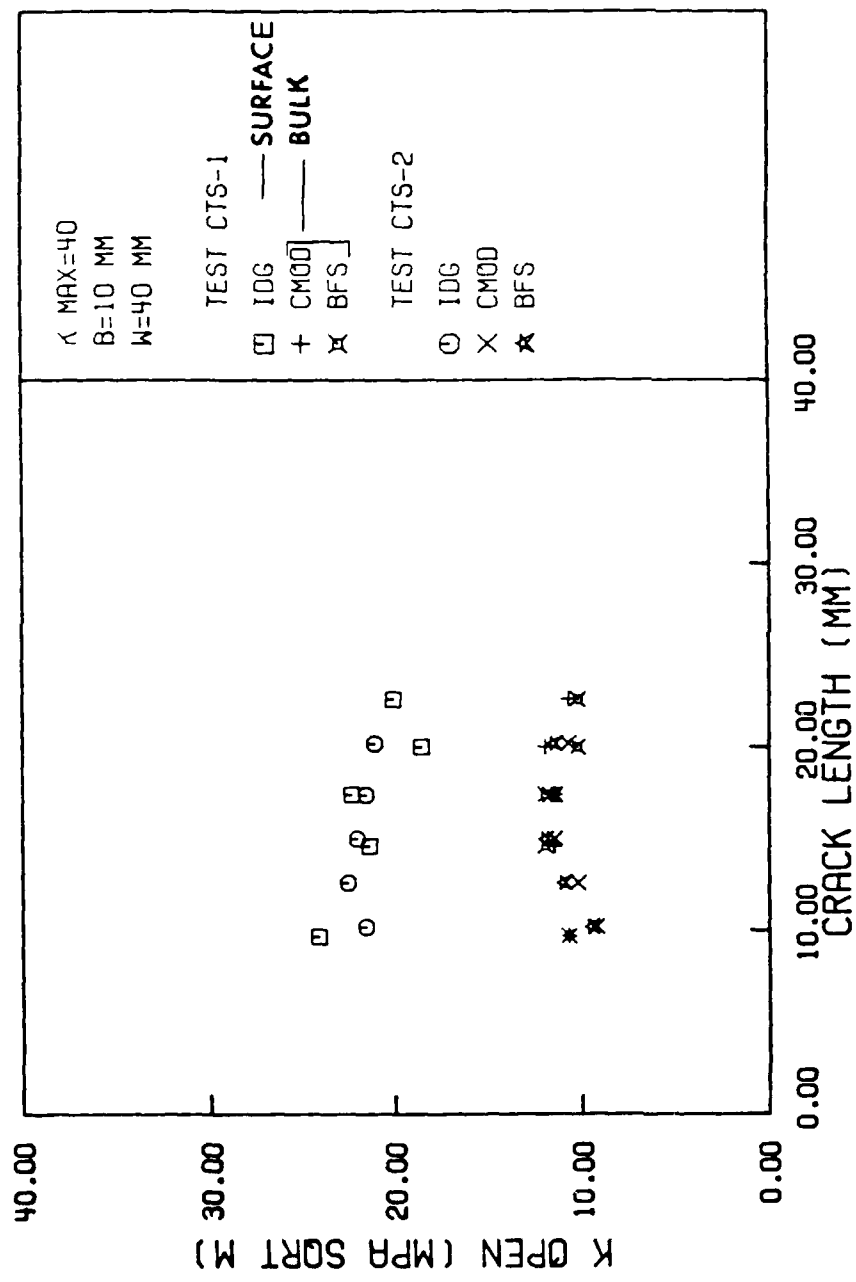


Figure 6.1: Comparison of crack opening loads obtained from IDG, CMOD, and BFS measurements for 10 mm thick Rene 95 specimens as reported in Reference [49].

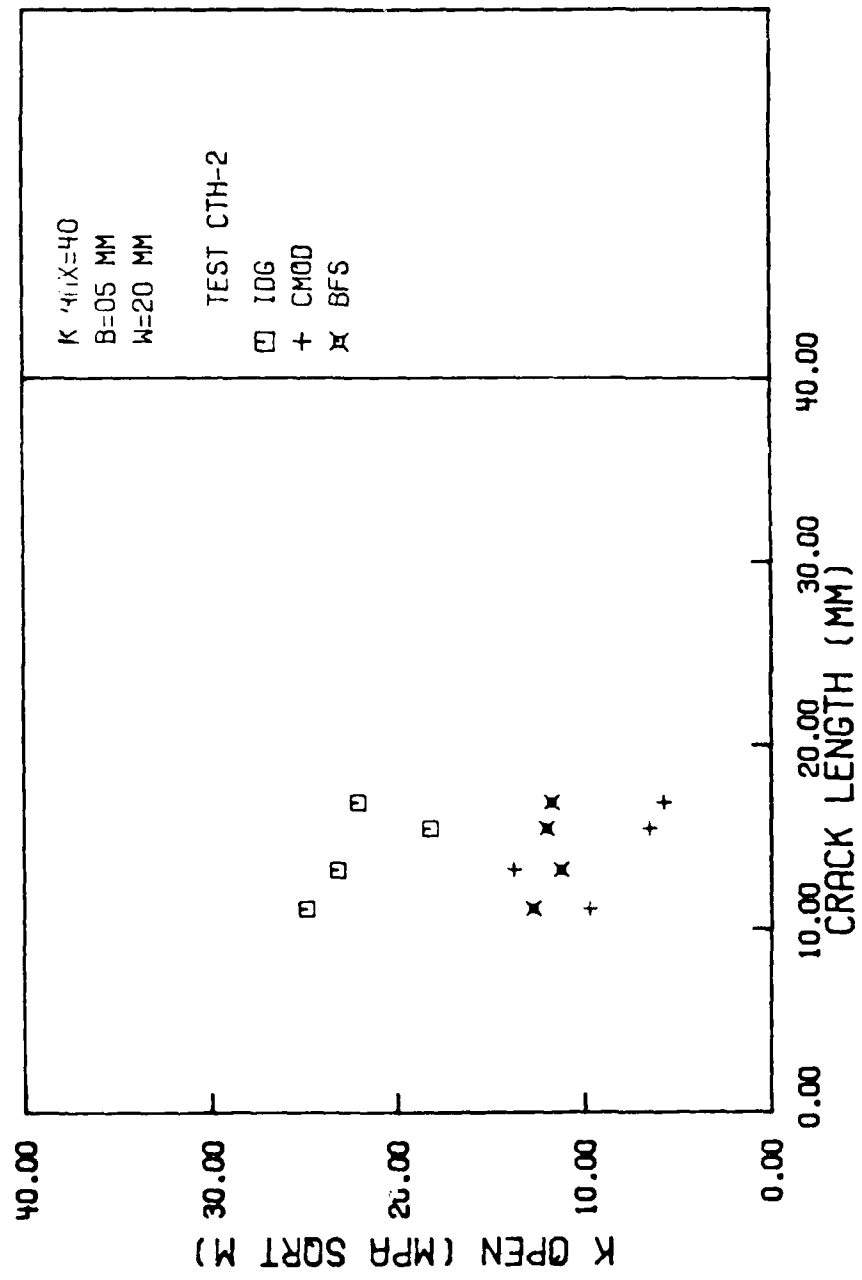


Figure 6.2: Comparison of crack opening loads obtained from IDG, CMOD, and BFS measurements for a 5 mm thick Rene 95 specimen as reported in Reference [49].

RD-R192 296

THREE-DIMENSIONAL ASPECTS OF FATIGUE CRACK CLOSURE (U)  
PURDUE UNIV LAFAYETTE IN SCHOOL OF AERONAUTICS AND  
ASTRONAUTICS A F GRANDT ET AL. FEB 98 AAE-98-1

3/3

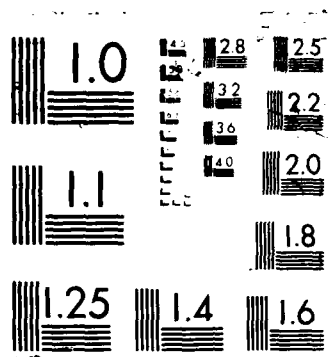
UNCLASSIFIED

AFOSR-TR-98-0266 AFOSR-95-0186

F/G 20/11

NL

1 H.D.  
1600 ft  
2.5%  
1000 ft  
100 ft



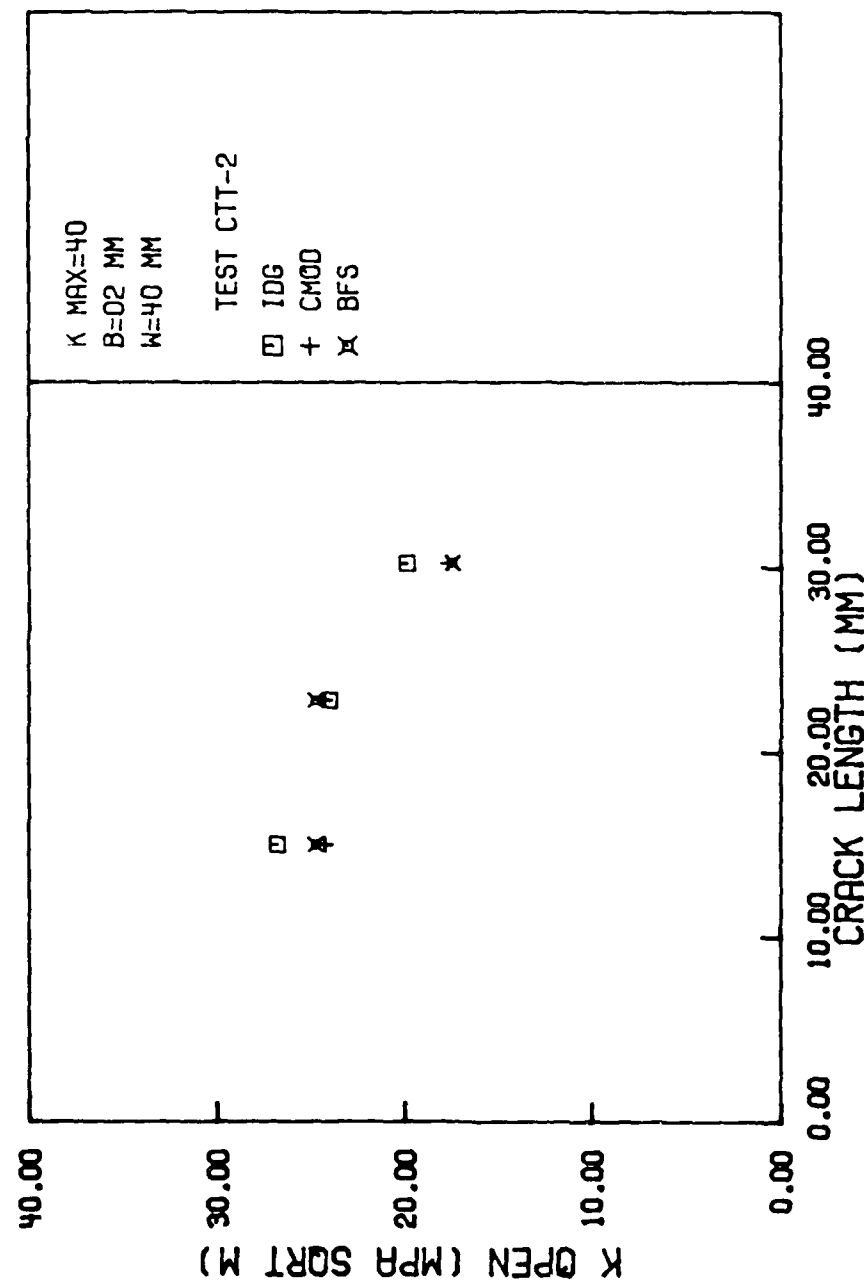


Figure 6.3: Comparison of crack opening loads obtained from IDG, CMOD, and BFS measurements for a 2 mm thick Rene 95 specimen as reported in Reference [49].

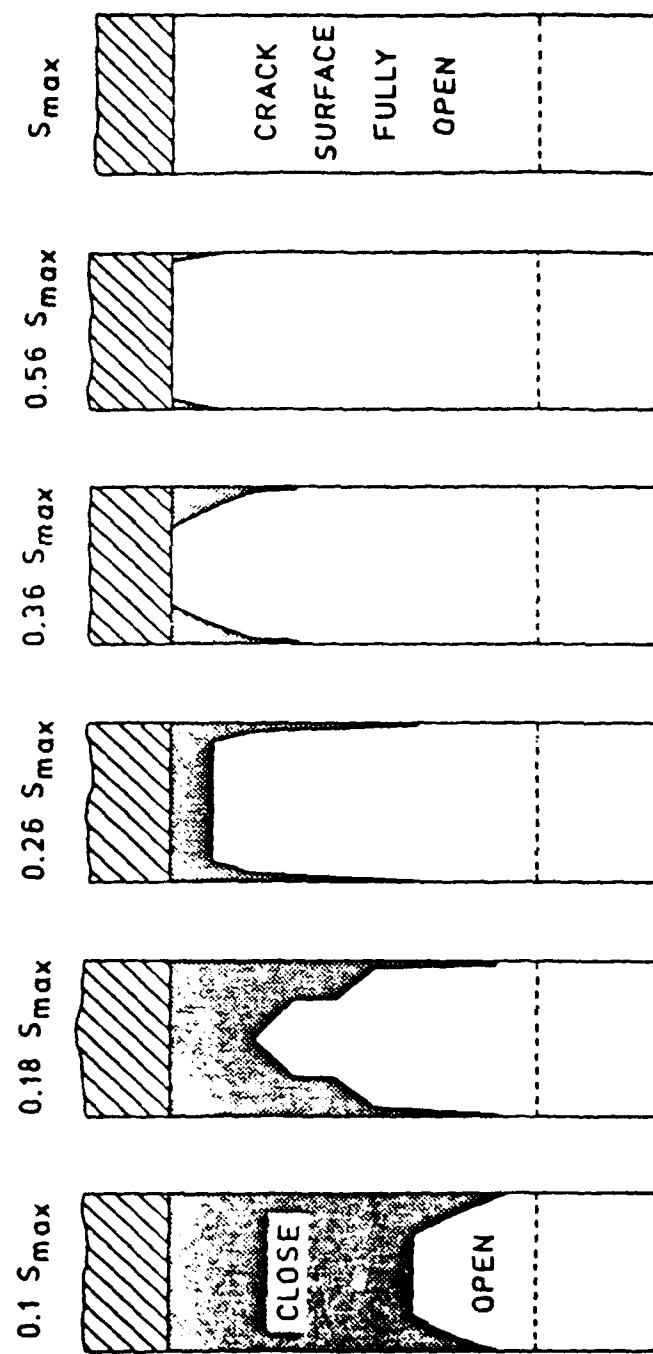


Figure 6.4: Crack plane view showing the opening perimeters as a function of increasing load obtained from Reference [18].  $S_{\max}$  represents the maximum cyclic stress.

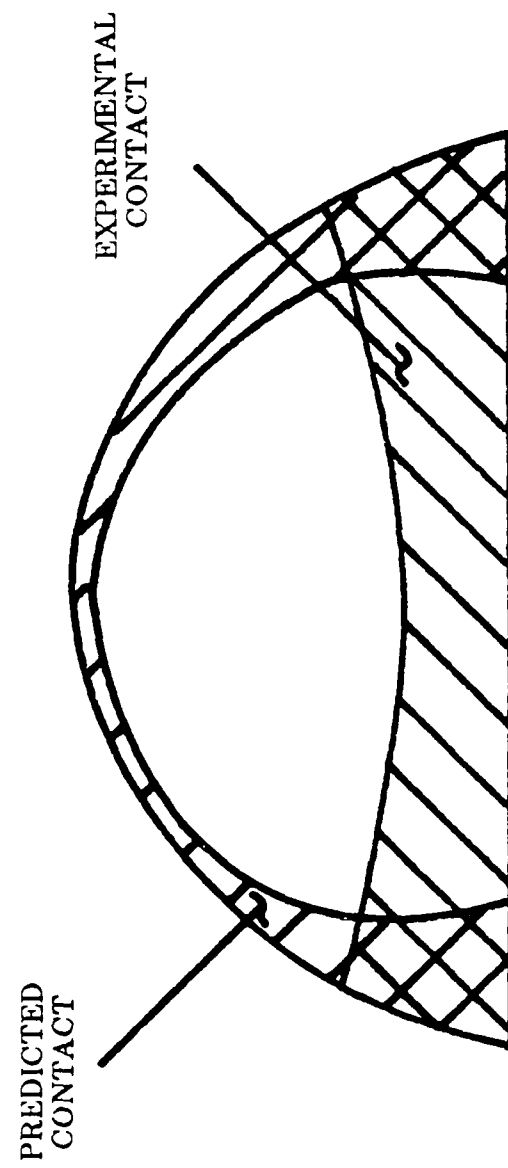


Figure 6.5: Experimental and predicted contact of crack surfaces

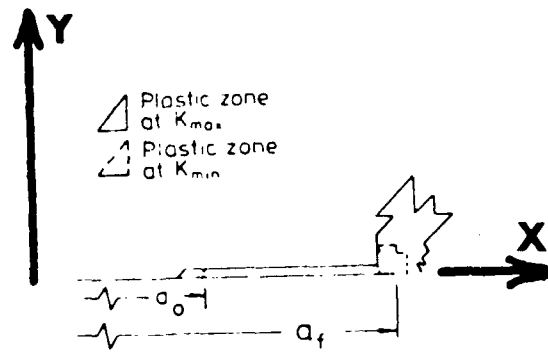


Figure 6.6: Plastic zone for an edge crack (reference [20])

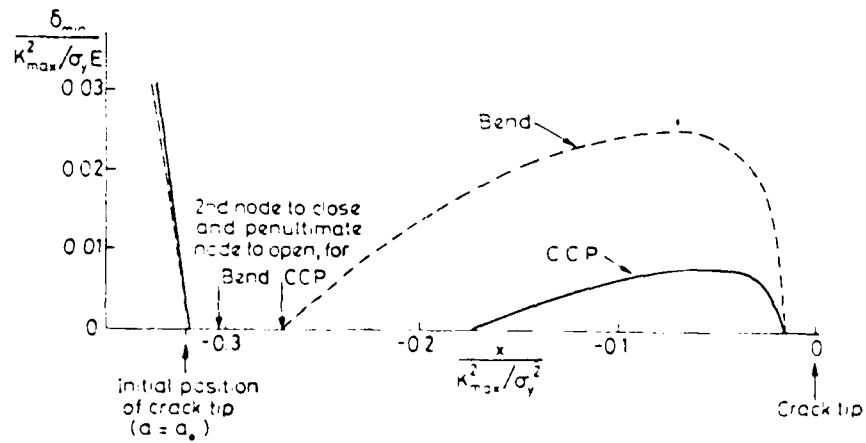


Figure 6.7: Discontinuous closure (reference [20])

## LIST OF REFERENCES

- [1] Elber, W., "Fatigue Crack Propagation," *Ph.D Thesis, 1968*, University of New South Wales.
- [2] Elber, W., "Fatigue Crack Closure Under Cyclic Tension," *Engineering Fracture Mechanics*, Vol. 2, No. 1, 1970, pp. 37-45.
- [3] Elber, W., "The Significance of Fatigue Crack Closure," *Damage Tolerance in Aircraft Structures*, ASTM STP 486, 1971, pp. 230-242.
- [4] Paris, P.C., "Twenty Years of Reflection on Questions involving Fatigue Crack Growth," *Fatigue Thresholds, Fundamentals and Engineering Applications*, Vol. I, ed. J. Bachland, A. Blom, and C. Beevers, Proc. of an International Conference, Stockholm, June 1981, pp. 3-32.
- [5] Banerjee, S., "A Review of Crack Closure," *Technical Report AFWAL-TR-84-4031*, AFWAL Material Laboratory, WPAFB, Ohio, January 1984.
- [6] Suresh, S., and Ritchie, R.O., "Near-Threshold Fatigue Crack Propagation: A Perspective on the Role of Crack Closure," *Fatigue Crack Growth Threshold: Concepts*, D.L. Davidson, and S. Suresh, Eds., TMS-AIME, Warrendale, PA, 1984, pp. 227-261.
- [7] Fuchs, H.O., and Stephens, R.I., *Metal Fatigue in Engineering*, John Wiley & Sons, 1980, pp. 46-48.
- [8] Mills, W.J., and Hertzberg, R.W., "The Effect of Sheet Thickness on Fatigue Crack Retardation in 2024-T3 Aluminum Alloy," *Engineering Fracture Mechanics*, Vol. 7, No. 4, 1975, pp. 705-711.

- [9] Matsuoka, S., and Tanaka, K., "Influence of Sheet Thickness on Delayed Retardation Phenomenon in Fatigue Crack Growth in HT80 Steel and A5083 Aluminum Alloy," *Engineering Fracture Mechanics*, Vol. 13, No. 2, 1980, pp. 293-306.
- [10] Saff, C., "F-4 Service-Life Tracking Program (Crack Growth Gages)," *Technical Report AFFDL-TR-79-3148*, Air Force Flight Dynamics Laboratory, WPAFB, Ohio, 1979.
- [11] Hess, J.P., Grandt, A.F., Jr., and Dumanis, A., "Effect of Side-Grooves on Fatigue Crack Retardation," *Fatigue of Engineering Materials and Structures*, Vol. 6, No. 2, 1983, pp. 189-199.
- [12] Walker, W., and Beevers, C.J., "A Fatigue Crack Closure Mechanism in Titanium," *Fatigue of Engineering Materials and Structures*, Vol. 1, 1979, pp. 135-148.
- [13] Morris, W.L., James, M.R., and Buck, O., "A Simple Model of Stress Intensity Range Threshold and Crack Closure Stresses," *Engineering Fracture Mechanics*, Vol. 18, No. 4, 1983, pp. 871-877.
- [14] Minakawa, K., and McEvily, A.J., "On Crack Closure in Near-Threshold Region," *Scripta Metallurgica*, Vol. 15, 1981, pp. 633-636.
- [15] Ritchie, R.O., Suresh, S., and Moss, C.M., "Near-Threshold Fatigue Crack Growth in 2 1/2 Cr-Mo Pressure Vessel Steel in Air and Hydrogen," *Journal of Engineering and Material Technology*, Transaction of ASME, Series H, 102, 1980, pp. 293-299.
- [16] Suresh, S., Zamiski, G.F., and Ritchie, R.O., "Oxidation and Crack Closure, An Explanation for Near-Threshold Corrosion Fatigue Crack Growth Behavior," *Metallurgical Transaction*, 12A, 1981, pp. 1435-1443.
- [17] Newman, J.C., Jr., "A Finite-Element Analysis of Fatigue Crack Closure," *Mechanics of Crack Growth*, ASTM STP 590, 1976, pp. 281-301.

- [18] Chermahini, R.G., "Three-Dimensional Elastic-Plastic Finite Element Analysis of Fatigue Crack Growth and Closure," *Ph.D Thesis, Old Dominion University*, August, 1986.
- [19] Newman, J.C., Jr., "Prediction of Fatigue Crack Growth Under Variable-Amplitude and Spectrum Loading using a Closure Model," *Design of Fatigue and Fracture Resistant Structures*, ASTM STP 761, 1982, pp. 255-277.
- [20] Fleck, N.A., "Finite Element Analysis of Plasticity-Induced Crack Closure Under Plane Strain Conditions," *Engineering Fracture Mechanics*, Vol. 25, No. 4, 1986, pp. 441-449.
- [21] Fleck, N.A., "An Investigation of Fatigue Crack Closure," *CUED/C-MATS/TR.104, Ph.D Thesis, Engineering Department, Cambridge University*, May 1984.
- [22] Minakawa, K., Newman, J.C., Jr., and McEvily, A.J., "A Critical Study of the Crack Closure Effect on Near-Threshold Fatigue Crack Growth," *Fatigue of Engineering Materials and Structures*, Vol. 6, No. 4, 1983, pp. 359-365.
- [23] Irving, P.E., Robinson, J.L., and Beevers, C.J., "A Study of the Effects of Mechanical and Environmental Variables on Fatigue Crack Closure," *Engineering Fracture Mechanics*, Vol. 7, 1975, pp. 619-630.
- [24] Gan, D., and Weertman, J., "Crack Closure and Crack Profile Rates in 7075 Al," *Engineering Fracture Mechanics*, Vol. 15, No. 1-2, 1981, pp. 87-106.
- [25] Blom, A.F., and Holm, D.K., "An Experimental and Numerical Study of Crack Closure," *Engineering Fracture Mechanics*, Vol. 22, No. 6, 1985, pp. 997-1011.
- [26] Frandsen, R.V., Inman, R.V., and Buck, O., "A Comparison of Acoustic and Strain Gauge Techniques for Crack Closure," *International Journal of Fracture*, Vol. 11, 1975, pp. 345-348.

- [27] Bouami, D., and de Vadder, D., "Detection and Measurement of Crack Closure and Opening by an Ultrasonic Method," *Engineering Fracture Mechanics*, Vol. 23, No. 5, 1986, pp. 913,920.
- [28] Fleck, N.A., "The Use of Compliance and Electrical Resistance Techniques to Characterize Fatigue Crack Closure," *CUED/MATS/TR.89, Engineering Department, Cambridge University*, 1982.
- [29] Bachmann, V., and Munz, D., "Fatigue Crack Evaluation with the Potential Method," *Engineering Fracture Mechanics*, Vol. 2, 1979, pp. 61-71.
- [30] Fleck, N.A., and Smith, R.A., "Crack Closure-Is it Just a Surface Phenomenon?" *International Journal of Fatigue*, Vol. 4, No. 3, 1982, pp. 157-160.
- [31] Fleck, N.A., Smith, I.F.C., and Smith, R.A., "Closure Behavior of Surface Cracks," *Fatigue of Engineering Materials and Structures*, Vol. 6, No. 3, 1983, pp. 225-239.
- [32] Turner, C.C., Carman, C.D., and Hillberry, B.M., "Fatigue Crack Closure Behavior at High Stress Ratios," Presented at *International Symposium on Fatigue Crack Closure*, Charleston, SC, 1986.
- [33] Carman, C.D., "Fatigue Crack Closure Behavior During Constant Loading Conditions," *M.S. Thesis, School of Mechanical Engineering, Purdue University, West Lafayette, IN, 47907*, 1986.
- [34] Sharpe, W.N., Jr., and Grandt, A.F., Jr., "A Preliminary Study of Fatigue Crack Retardation Using Laser Interferometry to Measure Crack Surface Displacements," *Mechanics of Crack Growth*, ASTM Stp 590, 1976, pp. 302-320.
- [35] Sharpe, W.N., Jr., "Interferometric Surface Strain Measurement," *International Journal of Nondestructive Testing*, Vol. 3, 1971, pp. 56-76.

- [36] Macha, D.E., Sharpe, W.N., and Grandt, A.F., Jr., "A Laser Interferometry Method for Experimental Stress Intensity Factor Calibration," *Cracks and Fracture*, ASTM STP 601, 1976, pp. 490-505.
- [37] Bar-Tikva, D., Grandt, A.F., Jr., and Palazotto, A.N., "An Experimental Weight Function for Stress-Intensity Factor Calibrations," *Experimental Mechanics*, Vol. 21, No. 10, 1981, pp. 371-378.
- [38] Sharpe, W.N., Corbly, D.M., and Grandt, A.F., Jr., "Effects of Rest Time on Fatigue Crack Retardation and Observation of Crack Closure," *ASTM STP 595*, 1976, pp. 61-80.
- [39] Sunder, R., and Dash, P.K., "Measurement of Fatigue Crack Closure Through Electron Microscopy," *International Journal of Fatigue*, Vol. 4, 1982, pp. 97-105.
- [40] Bowels, C.Q., "An Experimental Technique for Vacuum Infiltrating of Cracks with Plastic and Subsequent Study in the SEM," *Technical Report LR-249*, Department of Aeronautical Engineering, Delft University of Technology, 1977.
- [41] Macha, D.E., Corbly, D.M., and Jones, J.W., "On the Variation of Fatigue Crack-Opening Load with Measurement Location," *Experimental Mechanics*, June, 1979, pp. 207-213.
- [42] Ohta, A., Kosuge, M., and Sasaki, E., "Change of Fatigue Crack Closure Level with Gauge Location Along the Crack Line," *International Journal of Fracture*, Vol. 15, 1979, pp. R53-R57.
- [43] Pitoniak, F.J., Grandt, A.F., Jr., Montulli, L.T., and Packman, P.F., "Fatigue Crack Retardation and Closure in Polymethylmethacrylate," *Engineering Fracture Mechanics*, Vol. 6, 1974, pp. 663-670.
- [44] Ray, S., "Three-Dimensional Crack Closure Measurements in Polycarbonate," *M.S. Thesis, School of Aeronautics and Astronautics, Purdue University*, West Lafayette, IN, 47907, December, 1984.

- [45] Ray, S., Grandt, A.F., Jr., and Andrew, S., "Three-Dimensional Measurements of Fatigue Crack Closure and Opening," ASTM STP Devoted to Symposium on Fundamental Questions and Critical Experiments on Fatigue (in Press).
- [46] Ray, S., and Grandt, A.F., Jr., "Comparison of Methods for Measuring Fatigue Crack Closure in a Thick Specimen," Accepted for Publication in ASTM STP devoted to the International Symposium on Fatigue Crack Closure, Charleston, SC, May 1986.
- [47] Ray, S., Perez, R., and Grandt, A.F., Jr., "Fatigue Crack Closure of Corner Cracks Located at Holes Loaded in Tension or Bending," Accepted for Publication in *Fatigue and Fracture of Engineering Materials and Structures*, 1986.
- [48] Troha, W.A., Nicholas, T., and Grandt, A.F., Jr., "Three-Dimensional Aspects of Fatigue Crack Closure in Surface Flaws in a Transparent Material," Accepted for Publication in ASTM STP devoted to the International Symposium on Fatigue Crack Closure, Charleston, SC, May 1986.
- [49] Private consultation with Dr. N. E. Ashbaugh, currently associated with University of Dayton Research Institute. Experiments conducted at Air Force Wright Aeronautical Materials Laboratories, Wright Patterson Air Force Base, Dayton, Ohio, March 1987.
- [50] Ray, S.K., Phd. thesis, Purdue University, August 1987, "A Three-Dimensional Investigation of Steady State Crack Closure Behavior for Through-Thickness and Part-Through Flaws."
- [51] Packman, P.F., "The Role of Interferometry in Fracture Studies," *Experimental Techniques in Fracture Mechanics*, SESA Monograph 2, ed. A.S. Kobayash, 1975, pp. 59-87.
- [52] Crosley, P.B., Mostovoy, S., and Ripling, E.J., "An Optical Interference Method for Experimental Stress Analysis of Cracked Structures," *Engineering Fracture Mechanics*, Vol. 3, 1971, pp. 421-433.

- [53] Liechti, K.M., and Knauss, W.G., "Crack Propagation at Material Interfaces: I. Experimental Technique to Determine Crack Profiles," *Experimental Mechanics*, Vol. 22, No. 7, 1982, pp. 262-269.
- [54] Sommer, E., "An Optical Method for Determining the Crack Tip Stress Intensity Factor," *Engineering Fracture Mechanics*, Vol. 1, 1970, pp. 705-718.
- [55] Doll, W., "Optical Interference Measurements and Fracture Mechanics Analysis of Crack Tip Craze Zones," *Advances in Polymer Science*, 52153, Kausch, H.H., 1983, pp. 105-168.
- [56] Halliday, D., and Resnick, R., *Physics Part II*, John Wiley & Sons, Third Edition, 1978, pp. 1006-1012.
- [57] Newman, J.C., Jr., and Raju, I.S., "Stress-Intensity Factor Equations for Cracks in Three-Dimensional Finite Bodies Subjected to Tension and Bending Loads," *NASA Technical Memorandum 85798*, April 1984.
- [58] Pope, J.E., Phd. thesis, Purdue University, December 1987, "A Three-Dimensional Model of Fatigue Crack Growth Incorporating Crack Closure."
- [59] Newman, J.C., and Raju, I.S., "An Empirical Stress-Intensity Factor Equation for the Surface Cracks," *Engineering Fracture Mechanics*, Vol. 15, No. 1-2, 1981, pp. 185-192.
- [60] Mattheck, C., Morawietz, P., and Munz, D., "Stress Intensity Factor at the Surface Crack and the Deepest Point of a Semi-elliptical Surface Crack in Plates Under Stress Gradients," *International Journal of Fracture*, Vol. 23, 1983, pp. 201-212.
- [61] Petroski, H.J. and Achenbach, J.D., "Computation of the Weight Function from a Stress Intensity Factor," *Engineering Fracture Mechanics*, Vol. 10, 1978, pp. 257-268.

- [62] Private consultation with W.A. Troha, currently associated with AFWAL Aero Propulsion Laboratory, Wright-Patterson Air Force Base. Experiments conducted at AFWAL Materials Laboratory, Wright-Patterson Air Force Base, Dayton, Ohio, July 1987.
- [63] Troha, W.A., Nicholas, T., and Grandt, A.F. Jr., "Three-Dimensional Aspects of Fatigue Crack Closure," Presented at ASTM International Symposium on Fatigue Crack Closure, Charlseston, South Carolina, May 1986., Accepted for publication in ASTM Special Technical Publication devoted to conference proceedings.
- [64] Fuhring, H. and Seeger, T., "Dugdale Crack Closure Analysis of Fatigue Cracks Under Constant Amplitude Loading," *Engineering Fracture Mechanics*, Vol. 11, 1979, pp. 99-122.
- [65] Pelloux, R.M., Faral, M., and McGee, W.M., "Fractographic Measurements of Crack-Tip Closure," *Fracture Mechanics: Twelfth Conference*, ASTM STP 700, 1980, pp. 35-48.
- [66] Sunder, R., "Fatigue Crack Propagation Under Spectrum Loading," *National Aeronautical Laboratory*, Vol. 14, No. 1, January 1986, Bangalore, India.
- [67] Anandan, K., and Sunder, R., "Closure of Part Through Cracks at the Notch Root," *Document MT 8625, National Aeronautical Laboratory*, Bangalore, India.
- [68] Larsson, S.G. and Carlsson, A.J., "Influence of Non-Singular Stress Terms and Specimen Geometry on Small-Scale Yielding at Crack Tips in Elastic-Plastic Materials," *J. Mech. Phys. Solids*, Vol. 21, 1973, pp. 263-277.
- [69] Trantina, G.G., deLorenzi, H.G., and Wilkening, W.W., "Three-dimensional Elastic-plastic Finite Element Analysis of Small Surface Cracks," *Engineering Fracture Mechanics*, Vol. 18, No. 5, 1983, pp. 925-938.

## APPENDIX A

**Summary of Personnel, Publications, and Presentations**

A.F. Grandt, Jr. served as principal investigator for Grant Number AFOSR-85-0106. He was assisted during the three-year grant period by the following graduate students from the Purdue University School of Aeronautics and Astronautics: G. Kistler, R. Perez, J.E. Pope, S.K. Ray, and W.A. Troha. Mr. Troha is an AFWAL Propulsion Laboratory employee who is conducting his Ph.D. dissertation in absentia at the AFWAL Materials Laboratory. Although Mr. Troha was not supported directly by AFOSR Grant Number 85-0106, his research efforts were closely coordinated with those conducted on the Purdue campus. Mr. Troha's work at AFWAL employed laboratory facilities under the direction of Dr. T. Nicholas.

The following technical publications and presentations resulted from work sponsored by this grant.

**Publications**

- [1] S.K. Ray, R. Perez, and A.F. Grandt, Jr., "Fatigue Crack Closure of Corner Cracks Located at Holes Loaded in Tension or Bending," *Fatigue and Fracture of Engineering Materials and Structures, The International Journal*, Vol. 10, No. 3, 1987, pp. 239-250.
- [2] R. Perez, S.K. Ray, and A.F. Grandt, Jr., "Application of a Weight function Method to Predict the Fatigue Life of Corner Cracked Holes Loaded in Bending," *Engineering Fracture Mechanics*, vol. 28, No. 3, 1987, pp. 283-291.
- [3] S.K. Ray and A.F. Grandt, Jr., "Comparison of Methods for Measuring Fatigue Crack Closure in a Thick Specimen," *Symposium on Fatigue Crack Closure*, ASTM Special Technical Publication 982 (in press).
- [4] W.A. Troha, T. Nicholas, and A.F. Grandt, Jr., "Three-Dimensional Aspects of Fatigue Crack Closure in Surface Flaws in a Transparent Material," *Symposium on Fatigue Crack Closure*, ASTM Special Publication 982 (in press).
- [5] S.K. Ray and A.F. Grandt, Jr., "Fatigue Crack Closure of Surface Flaws Loaded in Pure Bending," *Experimental Mechanics* (in press).
- [6] S.K. Ray and A.F. Grandt, Jr., "Thickness Effect on Fatigue Crack Closure in Polymethylmethacrylate," *Proceedings of Twentieth Midwestern Mechanics*

*Conference, Purdue University, August 1987.*

- [7] R. Perez, *Stress Intensity Factors for Fatigue Cracks at Holes under Cyclic Stress Gradients*, Ph.D. Thesis, Purdue University, W. Lafayette, Indiana, May 1986.
- [8] S.K. Ray, *A Three-Dimensional Investigation of Steady State Fatigue Crack Closure Behavior for Through-Thickness and Part-Through Flaws*, Ph.D. Thesis, Purdue University, W. Lafayette, Indiana, August 1987.
- [9] J.E. Pope, *A Three-Dimensional Model of Fatigue Crack Growth Incorporating Crack Closure*, Ph.D. Thesis, Purdue University, W. Lafayette, Indiana, December 1987.

#### **Presentations**

- [1] S.K. Ray and A.F. Grandt, Jr., "Comparison of Methods for Measuring Fatigue Crack Closure in a Thick Specimen," presented at ASTM International Symposium on Fatigue Crack Closure, Charleston, South Carolina, May 1986.
- [2] W.A. Troha, T. Nicholas, and A.F. Grandt, Jr., "Three-Dimensional Aspects of Fatigue Crack Closure in Surface Flaws in a Transparent Material," Presented at ASTM International Symposium on Fatigue Crack Closure, Charleston, South Carolina, May 1986.
- [3] S.K. Ray and A.F. Grandt, Jr., "Thickness Effect on Fatigue Crack Closure in Polymethylmethacrylate," presented at Twentieth Midwestern Mechanics Conference, Purdue University, August 1987.
- [4] R. Perez, A.F. Grandt, Jr., and C.R. Saff, "Tabulated Stress Intensity Factors for Corner Cracks at Holes Under Stress Gradients," to be presented at ASTM/SEM Symposium on Surface Crack Growth: Models, Experiments and Structures, 25th April 1988, Las Vegas, NV. Paper also submitted for publication in ASTM STP devoted to conference.

END  
DATE  
FILMED

6-1988

DTIC